UNIVERSITÀ
DEGLI STUDI
DI TRIESTE

Università degli Studi di Trieste

Dipartimento di fisica

XXXVI Ciclo del Dottorato di Ricerca in Fisica

In-depth characterisation of diamond detectors for the Belle II experiment

Settore scientifico-disciplinare: FIS/04

Candidato:
Alice Gabrielli

Coordinatore:
Prof. Francesco Longo

Supervisore di tesi:
Prof. Lorenzo Vitale

ANNO ACCADEMICO 2022–2023

Contents

Introduction **1**

1 Belle II at SuperKEKB **3**
1.1 B factories . . . 3
1.2 SuperKEKB collider . . . 4
1.3 Belle II detector . . . 6
1.4 Beam induced background . . . 11
1.4.1 Background sources . . . 11
1.4.2 Background mitigation and monitors . . . 14

2 Belle II Vertex Detector **16**
2.1 Vertex detector . . . 16
2.1.1 Beam pipe chamber of the interaction point . . . 18
2.1.2 Pixel Detector . . . 20
2.1.3 Silicon Vertex Detector . . . 22
2.1.4 VXD CO_2 cooling system . . . 25
2.2 Radiation damage to silicon detectors . . . 25
2.2.1 Radiation-induced defects . . . 25
2.2.2 Effects on detector properties . . . 27
2.2.3 VXD vulnerabilities to beam-background . . . 28
2.3 Long Shutdown 1 . . . 29
2.3.1 LS1 beam pipe . . . 29
2.3.2 PXD2 and VXD reinstallation . . . 29

3 Radiation and environmental monitoring **32**
3.1 Radiation monitoring and beam abort . . . 32
3.1.1 Diamond detectors for radiation monitoring . . . 33
3.1.2 Diamond radiation monitor and beam abort system . . . 36
3.1.3 Diamond Control Unit . . . 37
3.2 VXD environmental monitoring . . . 39
3.2.1 Temperature monitoring . . . 40
3.2.1.1 NTC system . . . 40
3.2.1.2 FOS system . . . 42
3.2.2 Humidity monitoring . . . 44
3.3 VXD Hardwire Interlock system . . . 47

4 Assembly, characterisation and installation of diamond detectors **50**
4.1 Description of the sensor under study . . . 50
4.2 New production of ten diamond detectors for LS1 . . . 52

4.2.1 Assembly procedure and preliminary tests . . . 52
4.2.2 Characterisation procedure . . . 54
4.2.3 Radiation sources used in the characterisation procedure . . . 55
4.3 Characterisation with α radiation . . . 57
4.3.1 Experimental setup . . . 57
4.3.2 Characterisation of the experimental setup . . . 59
4.3.3 Data taking and analysis of the detector response . . . 61
4.3.4 Analysis of charge carrier properties . . . 64
4.3.5 Average energy to create an electron-hole pair . . . 65
4.4 Characterisation with β radiation . . . 71
4.4.1 Experimental setup and measurements methods . . . 71
4.4.2 Current stability and current-voltage characteristic . . . 73
4.4.3 Current-to-dose calibration . . . 77
4.5 Characterisation with X radiation . . . 84
4.5.1 Experimental setup and measurement methods . . . 84
4.5.2 Current-to-dose rate calibration . . . 85
4.6 Summary of the characterisation results and installation on the new beam pipe . . . 92

5 Transient response of diamond detectors to sub-picosecond high-intensity electron bunches 95
5.1 Introduction . . . 95
5.2 Experimental setup . . . 98
5.2.1 Beam facility . . . 99
5.2.2 DUT test station . . . 102
5.2.3 Setup optimisation . . . 103
5.2.4 Instrumentation and data collection . . . 104
5.3 Measurement overview . . . 106
5.4 Electron beam optimisation . . . 107
5.4.1 Diamond response as a feedback . . . 107
5.4.2 Fluorescent screen downstream DUT . . . 110
5.4.3 Fluorescent screen on DUT support . . . 113
5.5 Beam parameters . . . 114
5.6 Detector signals . . . 119
5.6.1 Signals amplitude and shape . . . 119
5.6.2 Detector bias-voltage scan . . . 123
5.6.3 Bunch charge scan . . . 125
5.6.4 Beam size scan . . . 128
5.7 Summary . . . 129

6 Simulation of the diamond-detector response to ultra-short and intense high-energy electron pulses 131
6.1 Introduction . . . 131
6.2 TCAD simulation of the diamond response . . . 132
6.2.1 Sentaurus Technology CAD . . . 132
6.2.2 Diamond detector model . . . 133
6.2.3 Electron beam simulation . . . 138
6.2.4 Signal formation . . . 139
6.3 LTspice readout circuit . . . 141

6.3.1 Diagram of the circuit 143
6.3.2 Diamond resistance 144
6.4 Validation of the simulation approach 146
6.5 Comparison of the simulation results with the experimental data 148
6.6 Summary and future developments 151

Summary **152**

Acknowledgements **154**

Bibliography **155**

Introduction

The Belle II particle-physics experiment studies electron-positron collisions produced by the SuperKEKB collider in Japan since 2018. Its targets are high precision measurements of the properties of the heavy quarks and the tau lepton. Now and over the next decade, Belle II is at the forefront of the intensity frontier. This involves performing precision experiments to test the Standard Model of particle physics, with the potential of discovering anomalies that could indicate the presence of unexpected and novel phenomena. To achieve this goal, the SuperKEKB accelerator, a new-generation high-luminosity asymmetric e^+e^- collider, is targeting the unprecedented peak luminosity of $6.3 \times 10^{35}\,\mathrm{cm}^{-2}\mathrm{s}^{-1}$, 30 times larger than that of its predecessor. In June 2022, SuperKEKB set a new record by reaching a luminosity of $4.7 \times 10^{34}, \mathrm{cm}^{-2}\mathrm{s}^{-1}$, the highest luminosity ever achieved by any collider. The machine continues to make steady progress towards its designed luminosity target.

To achieve the high luminosity required, high beam intensities and strong focusing at the interaction point are necessary, at the cost of producing high radiation backgrounds. These backgrounds have the potential to cause permanent damage and reduce the performance of the Belle II sub-detectors. The heart of Belle II is its state-of-the-art silicon vertex detector, which precisely tracks the paths of the charged particles. To ensure optimal performance, the detector must operate in an environment with controlled radiation backgrounds from the accelerator. To protect the detector in a harsh radiation environment and to ensure that the accelerator operates at peak performance, a monitoring system based on single-crystal synthetic diamond sensors was designed, developed and installed by the Belle II Trieste group. This system continuously monitors radiation doses in the vicinity of the interaction region and triggers protective measures if necessary. It has proved to be a key element in ensuring the safe and successful operation of the accelerator. Taking advantage of a long-term shutdown (LS1) in 2022 to install the innermost layers of the vertex detector, the radiation monitoring system was also upgraded. In February 2023 I installed new diamond sensors on a new beam pipe.

This thesis describes the work I made to achieve a comprehensive characterisation of the diamond detectors used in the radiation monitoring and beam abort system of Belle II. The main goal of this work is a detailed account of the entire process involved in the production and test of these diamond detectors, including their assembly, characterisation and calibration using different radiation sources, and their installation in the Belle II detector. Of particular importance is the determination of the current-to-dose-rate calibration factor, a crucial parameter for the use of these detectors as dosimeters in the radiation monitor. This calibration factor is derived under steady β and X irradiation conditions using a comparison method with a silicon diode as a reference. This method significantly reduces the systematic uncertainties associated with the radiation source. Under steady irradiation, our diamonds exhibit a linear response over a wide current range. However, in the context of the SuperKEKB interaction region, where significant beam losses occur, the radiation field can generate very large signals. Rapidly fluctuating or non-uniform irradiation fields

can induce transient space charge and create non-uniform electric fields within the diamond, leading to non-linear effects. Unlike the well-calibrated steady state radiation for our diamond detectors, dose rate estimation for bursts of radiation with spike-like temporal profiles can be subject to non-linear effects, potentially resulting in an underestimated dose value. To investigate the transient response under fast and intense bursts, a sub-sample of diamond detectors is irradiated with 1 GeV ultra-short, high-intensity electron bunches from the linac of the FERMI free electron laser. This experimental setup is devoted to the study the detector response under extreme conditions. A two-step numerical simulation approach is used to quantitatively model the signal formation under these extreme conditions, providing valuable insights into the complex dynamics governing these detectors in such challenging environments.

The thesis is structured as follows. Chapter 1 provides a brief overview of the SuperKEKB accelerator and the Belle II detector. It discusses the main sources of beam-induced background that can potentially damage the detector and degrade its performance. In Chapter 2 a more detailed look is given at the innermost part of the interaction region, with the interaction point beam pipe and the vertex detector. It also presents a brief overview of the major improvements made during LS1. Chapter 3 gives a comprehensive description of the radiation and environmental monitoring systems for the vertex detector. Chapter 4 is dedicated to the complete assembly, characterisation and calibration procedures and installation of eight diamond detectors for the LS1 upgrade. Chapter 5 covers further testing of the diamond detectors transient response to sub-picosecond high intensity electron bunches. This chapter includes discussions of setup design, optimisation of beam conditions, measurement procedures and results. Chapter 6 details the two-step numerical simulation designed to quantitatively model the signal formation in the diamond under the conditions described in the previous chapter. A summary is drawn at the end of the document.

Chapter 1

Belle II at SuperKEKB

In this Chapter I briefly introduce the B factories (Section 1.1), focusing in particular on the Belle II experiment at the SuperKEKB collider. An overview of the SuperKEKB and the main challenges to reach an higher luminosity is given in Section 1.2, then Section 1.3 briefly describes the Belle II detector. A higher luminosity corresponds to a higher beam-induce background in which the machine and the detector must operate. Section 1.4 reports an overview on the main background sources in SuperKEKB and the main countermeasures used to prevent and reduce radiation damages.

1.1 B factories

In 1973 Kobayashi and Maskawa [1] pointed out that $\mathcal{CP}$ violation could be naturally incorporated into the Standard Model (SM) as an irreducible complex phase in the weak interaction quark-flavor-mixing matrix if the number of quark flavors was six. This is remarkable because at that time only the existance of three quarks of the original Gell-Mann and Zweig (1964) quark model [2] (*i.e.* the u-, d- and s-quarks) was experimentally confirmed. By 1980, after the discovery of c-quark at Brookhaven [3] and SLAC [4] and the discovery of the b-quark at Fermilab [5], the Kobayashi-Maskawa proposal, embodied in the Cabibbo-Kobayashi-Maskawa (CKM) quark flavor mixing matrix [1, 6], was accepted as a component of the Standard Model.

$\mathcal{CP}$ violation was expected to be observable in neutral B meson decays to $\mathcal{CP}$ eigenstates, such as $B^0 \to J/\Psi K_s^0$, but, in the early 1980's no such decays had been observed. The turning point arrived after the evidence of a large B meson lifetime from experiments at SLAC in 1983 and the discovery by the ARGUS experiment at DESY in 1987 of a substantial rate for $B^0 - \overline{B}^0$ mixing, both indicating that the CKM-matrix parameters were in an experimentally accessible range. The problem, at that time, was that the available sample of B mesons was three orders of magnitude less than the one required to observe $\mathcal{CP}$ violation in B decays.

The need for a larger data sample originated the idea of the so called "B factories" [7], e^+e^- colliders capable of producing more than one million $B^0 - \overline{B}^0$ mesons pairs per day, which, compared with CESR at Cornell or DORIS II at DESY that were able to produce nearly 30 $B^0 - \overline{B}^0$ pairs per day, was an improvement of 5 orders of magnitude in less than 30 years. The development of B factories was accompanied by progress in the capabilities of the detectors, in the data acquisition systems, to deal with the large amount of data produced, in tracking and vertexing performance, in software, and data storage technology.

In 1987 Pier Oddone proposed the concept of an asymmetric e^+e^- circular collider

that would operate at the $\Upsilon(4S)$ resonance and produce B mesons pairs with a lab-frame boost sufficient for time-dependent measurements of the $\mathcal{CP}$ asymmetry. Intense beams of electrons and positrons are brought to collision at the energy corresponding to the $\Upsilon(4S)$ meson mass, which is just above the $B\overline{B}$ production kinematic threshold. The enhancement in production rate of $\Upsilon(4S)$ mesons, which predominantly decay to $B\overline{B}$ pairs, gives a favourable ratio of signal to backgrounds, which are mainly due to competing non-resonant hadron production. In addition, the annihilation of point-like particles gives a precise knowledge of the collision energy, which sets stringent constraints on the final-state kinematic properties, resulting in further background suppression. Because the $\Upsilon(4S)$ mesons are produced at threshold, in an energy-symmetric collider they would be nearly at rest in the laboratory frame. Hence, the resulting B mesons would too be produced with low momentum ($\approx 10\,\mathrm{MeV}/c$) in the laboratory, because of the $21\,\mathrm{MeV}/c^2$ difference between $\Upsilon(4S)$ and $B\overline{B}$ pair masses. With such low momenta they would travel approximately $1\,\mu$m before decaying. The 10 μm typical spatial resolution of vertex detectors would not be sufficient to separate B-decay vertices and study the decay time evolution for measurements involving mixing. Asymmetric beam energies are used to circumvent this limitation, because they boost the collision centre-of-mass along the beam in the laboratory frame, thus achieving B-decay vertices separation.

Among the B factories projects that were proposed during the 1980s, only PEP-II at SLAC and KEKB at KEK were realized. Both projects included an instantaneous luminosity higher than $10^{33}\mathrm{cm}^{-2}\mathrm{s}^{-1}$ and a boost of the centre-of-mass sufficient to observe the time evolution of B mesons decays. The excellent performances of PEP-II (operated in 1999-2008) and KEKB (operated in 1999-2010) allowed the respective BaBar and Belle detectors to verify the Cabibbo-Kobayashi-Maskawa (CKM) theory of $\mathcal{CP}$ violation, together with many other measurements and discoveries.

The emphasis in particle physics has now shifted to the search for physics beyond the Standard Model in flavor physics. An upgrade of the Belle experiment, Belle II, plays a central role for the next round of investigations at the next generation electron-positron B-factory SuperKEKB [8].

1.2 SuperKEKB collider

SuperKEKB, illustrated in Figure 1.1, is an upgrade of the KEKB accelerator [9], and has been operational since 2016.

It is a 3 km-circumference energy-asymmetric electron-positron (e^+e^-) double-ring collider [10], with a centre-of-mass (CM) energy of $\sqrt{s} = 10.58\,\mathrm{GeV}$, which correspond to the mass of the $\Upsilon(4S)$ resonance. The SuperKEKB collider complex consists of a high-energy ring (HER) of 7 GeV electrons, a low-energy ring (LER) of 4 GeV positrons and an injection linear accelerator (linac) equipped with a damping ring (DR) to reduce spread in position and momentum (emittance) of positrons. Electrons and positrons are injected from the linac into the main ring at full energy. Since the beam lifetime is much shorter than an hour, top-up injections are continuously performed during data taking. The two beams of electrons and positrons, circulating in the HER and LER respectively, collide at the interaction point (IP), and the collision products travel from the interaction point (IP) through the volume of the detector, where various final states can be detected.

The design peak luminosity of SuperKEKB was initially set to $8 \times 10^{35}\,\mathrm{cm}^{-2}\mathrm{s}^{-1}$, 40 times higher than that achieved by KEKB, and it aims at accumulating an integrated luminosity of $50\,\mathrm{ab}^{-1}$. However, after the first years of operations a number of technological and scientific challenges have slowed SuperKEKB performance compared to the designed

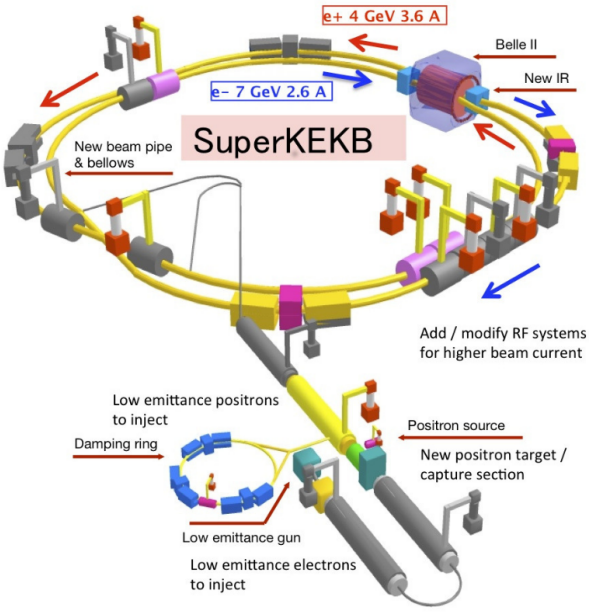

Figure 1.1: Simplified scheme of the SuperKEKB collider.

profile of increasing luminosity. The SuperKEKB now (2023) is targeting a peak luminosity of $1 \times 10^{35}\,\mathrm{cm}^{-2}\mathrm{s}^{-1}$ after the long-term shutdown 1 (LS1, from July 2022 to the end of 2023) and $6.3 \times 10^{35}\,\mathrm{cm}^{-2}\mathrm{s}^{-1}$ after a second long-term shutdown (LS2), scheduled for 2027 [11, 12].

The luminosity can be expressed as

$$\mathcal{L} = \frac{\gamma\pm}{2er_e}\left(1+\frac{\sigma_y^*}{\sigma_x^*}\right)\left(\frac{I_\pm\xi_{y\pm}}{\beta_y^*}\right)\left(\frac{R_L}{R_{\xi_{y\pm}}}\right), \tag{1.1}$$

where "+" denotes positrons and "−" denotes electrons, r_e is the classical electron radius and γ is the Lorentz factor. All the other terms in the equation are related to beam: $\sigma_{x,y}^*$ are the beam size at the IP in the horizontal and vertical plane, I is the beam current, β_y^* is the vertical beta function at the IP, $\xi_{y\pm}$ is the vertical beam-beam parameter and R_L and $R_{\xi_{y\pm}}$ are reduction factors for the luminosity and the beam-beam parameter [13]. It is assumed that vertical beta function and transverse beam size of the positron beam are the same as the electron beam. The parameters of the horizontal beta function at the IP, the horizontal emittance, the bunch length, and the crossing angle between two beams, which are not included in the equation, contribute to the luminosity through the beam–beam parameter and the reduction factors.

To achieve high luminosity, SuperKEKB utilises the so-called nano-beam scheme [13]. The crucial elements of this plan involve reducing through squeezing and implementing a substantial horizontal crossing angle at the interaction point (IP). In order to squeeze the vertical and horizontal beam size at the IP, it is necessary to reduce the vertical betatron function at the interaction point (IP) by minimising the longitudinal size of the overlap-region of the two beams at the IP. These two parameters are related by equation

$$\sigma(s) = \sqrt{\epsilon\beta(s)}\,, \tag{1.2}$$

where $\sigma(s)$ is the transverse beam size, ϵ is the emittance and $\beta(s)$ is the betatron function, which describes the dispersion effects as a function of the position s along the nominal beam trajectory. However, when the betatron function at the interaction point (β^*) approaches the bunch length, not all particles collide at the minimum of the transverse beam size. This phenomenon is called *hourglass effect* [14] and can reduce the luminosity. By increasing the beam crossing angle and reducing the emittance and horizontal betatron function at the IP, the overlap region of the two beams is reduced, and the hourglass effect becomes negligible.

By design, the vertical and horizontal beam sizes at the IP should be squeezed down to $\sim 50\,\mu$m and $\sim 10\,\mu$m respectively, while the horizontal crossing-angle has been increased up to 83 mrad. For this purpose the final-focusing superconducting-quadrupole magnets [15] (QCS) have been located nearer to the IP than those of KEKB, thanks to the relatively large crossing angle. Figure 1.2 and Table 1.1 highlight the main differences between KEKB and SuperKEKB, showing both the design parameters and the ones achieved. The reduction of the luminous volume size in the initial design to about 5% with respect to the predecessor KEKB, combined with doubling beam currents, was expected to yield a factor 40 gain in luminosity.

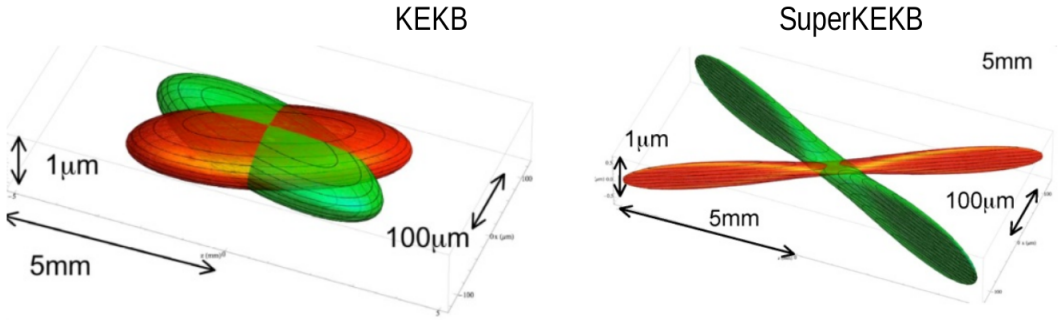

Figure 1.2: Three dimensional sketch of the bunch geometry at the interaction point for KEKB (left) and initial design of SuperKEKB (right). The positron (electron) bunches are shown in red (green).

In June 2020, the machine achieved a significant milestone by surpassing and subsequently doubling the peak luminosity of KEKB, all while using similar or even lower beam currents. This accomplishment led to a world record luminosity of 4.7×10^{34},cm^{-2}s^{-1} in June 2022. However, the goal is to increase the luminosity by another order of magnitude in the coming decade, with an updated target luminosity of $6.3 \times 10^{35}\,\mathrm{cm}^{-2}\mathrm{s}^{-1}$ after LS2.

1.3 Belle II detector

The design of a new collider, capable of delivering an instantaneous luminosity increasingly higher than that of KEKB, also meant new requirements for the detector, which had to be significantly upgraded to cope with the new machine conditions. The Belle II detector aims at maintaining the same level of performance of Belle, even with the reduced centre-of-mass boost, while operating in a much higher background environment.

While the detector fits in the same volume of its predecessor, keeping the superconducting solenoid magnet and the return iron yoke, Belle II replaced or upgraded its components in order to satisfy the new requirements, keeping a good hermiticity of the detector. Com-

	KEKB Achieved		SuperKEKB May 1st, 2020		SuperKEKB June 22nd,2022		SuperKEKB Design	
	LER	HER	LER	HER	LER	HER	LER	HER
E [GeV]	3.5	8.0					4.0	7.0
I_{beam} [A]	1.637	1.188	0.438	0.517	1.363	1.118	3.6	2.6
# of bunches	1585		783		2249		2500	
I_{bunch} [mA]	1.033	0.7495	0.5593	0.6603	0.606	0.497	1.440	1.040
β_y^* [mm]	5.9	5.9	1.0	1.0	1.0	1.0	0.27	0.30
ξ_y	0.100	0.060	0.024	0.022	0.040	0.028	0.069	0.061
$\mathcal{L}$ ($\times 10^{34}\,\text{cm}^{-2}\text{s}^{-1}$)	2.11		1.57		4.71		80	
$\int \mathcal{L}dt$ [ab^{-1}]	1.04		0.03		0.424		50	

Table 1.1: Comparison between KEKB and SuperKEKB main parameters. * indicates values at the IP. [12]

pared to Belle, the Belle II detector will be taking data at an accelerator with up to 40 times higher luminosity, and thus has to be able to operate at much higher event rates and background rates. To maintain the excellent performance of the spectrometer, the critical issue is to mitigate the effects of higher background levels, which lead to an increase in occupancy and radiation damage, as well as to background hits and pile-up noise in the electromagnetic calorimeter, and to neutron-induced hits in the muon detection system. The mitigation of the background level can be pursued with a better background events rejection from the detector and reducing the background rates on the detector using collimation systems and dedicated radiation monitors that can give feedback to the machine operators. Higher event rates also require substantial modifications of the trigger scheme, data acquisition system and computing.

The Belle II detector [16] has a cylindrical geometry with a central body, named barrel, and two endcap sections that close the forward (FWD) and backward (BWD) sides. From the interaction point to the outer regions, as shown in Figure1.3, the apparatus consists of various detector layers:

- The vertex detector (VXD), whose main purpose is the reconstruction of charged particles tracks, providing a good vertex resolution. It consists of two devices, the silicon pixel detector (PXD) and silicon vertex detector (SVD), with a total of six layers around the beam pipe. A more detailed description is given in Chapter 2.
- The central drift chamber [17] (CDC) involved in tracking at large radii and particle identification. Information from the CDC is also used for the trigger signal.
- The charge particle identification system, composed of a time of propagation [18] (TOP) counter and an aerogel ring imaging Cherenkov [19] (ARICH) counter, both designed to discriminate pions, muons and electrons using Cherenkov light.
- The electromagnetic calorimeter [20] (ECL) to measure energy of photons and electrons and to separate electrons from hadrons.
- The K_L^0 and muon system [21] that detect muons and K_L^0 escaping from the internal region.

A superconductive solenoid is located between the ECL and the KLM providing an axial magnetic field of 1.5 T. All the Belle II components and their specifications are summarised in Table 1.2.

Belle II employs a right-handed Cartesian coordinate system with origin in the interaction point. The z-axis is parallel to the electron-beam direction, which is parallel to the magnetic field within the solenoid; the y-axis points vertically upward, and the x-axis is horizontal and pointing outward of the accelerator tunnel.

The commissioning and data taking phases of SuperKEKB and Belle II can be summarised as:

- *Phase 1:* 2016, beams without collisions with dedicated background detectors around the future interaction area.
- *Phase 2:* 2018, beams collisions with Belle II detector, except VXD. Only a VXD sector and other dedicated background detectors in the rest of the VXD volume.
- *Phase 3, run 1:* 2019-2022, beams collisions with the full Belle II detector except the second layer of PXD.
- *Phase 3, run 2:* starting on 2024-, beams collisions with refurbished Belle II detector, such as full PXD, additional shielding, replacement or fixing of inefficient parts.

During *Phase 3*, in the period of time between *run 1* and *run 2*, called *Long Shutdown 1* (LS1), the detector has been upgraded with the installation of a complete pixel detector (PXD) mounted on a modified beam pipe with extra shielding and 8 new diamond detectors; moreover, several minor improvements in other subsystems were put in place. After *Phase 3 run 2* a middle term upgrade of the Belle II detector [22] is planned after 2027, with an upgrade of the interaction region (IR) required to reach a peak luminosity of $6.3 \times 10^{35}\,\mathrm{cm}^{-2}\mathrm{s}^{-1}$. A new vertex detector might be required to cope with the new IR design.

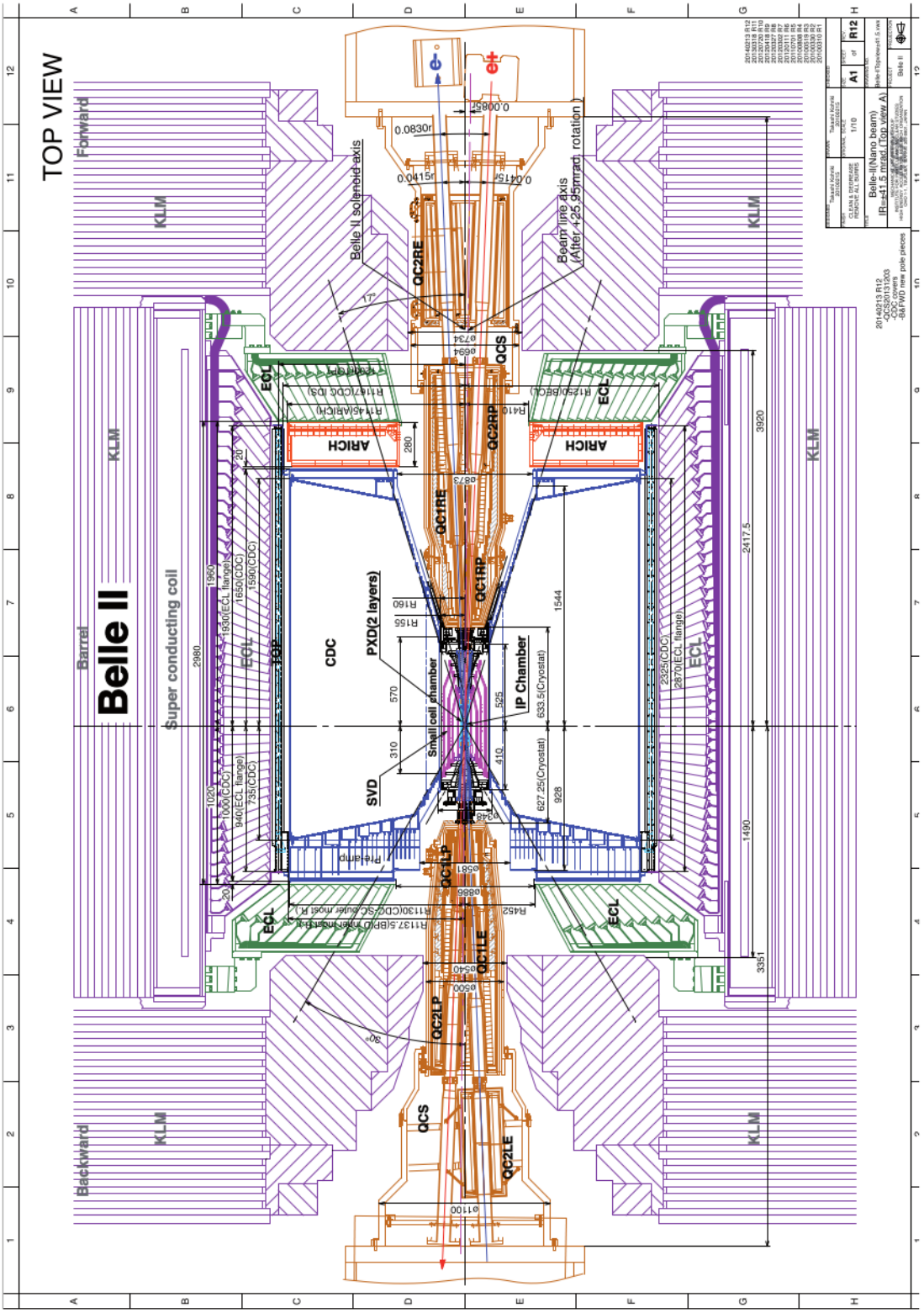

Figure 1.3: Belle II top view [16].

Purpose	Name	Component	Configuration	Readout channels	θ coverage
Beam pipe		Beryllium	Cylindrical, inner radius 10 mm, 10 μm Au, 0.6 mm Be, 1 mm paraffin, 0.4 mm Be		
Tracking	PXD	Silicon pixel (DEPFET)	Sensor size: 15×(L1 136, L2 170) mm^2, Pixel size: 50×(L1a 50, L1b 60, L2a 75, L2b 85) μm^2; two layers at radii: 14, 22 mm	10^6	[17°;150°]
	SVD	Silicon strip	Rectangular and trapezoidal, strip pitch: 50(p)/160(n) - 75(p)/240(n) μm, with one floating intermediate strip; four layers at radii: 38, 80, 115, 140 mm	2.45×10^5	[17°;150°]
	CDC	Drift chamber with He-C_2H_6 gas	14336 wires in 56 layers, inner radius of 160mm outer radius of 1130 mm	1.4×10^5	[17°;150°]
Particle ID	TOP	RICH with quartz radiator	16 segments in ϕ at $r \approx 120$ cm, 275 cm long, 2cm thick quartz bars with 4×4 channel MCP PMTs	8×10^3	[31°;128°]
	ARICH	RICH with aerogel radiator	2×2 cm thick focusing radiators with different n, HAPD photodetectors	7.8×10^4	[14°;30°]
Calorimetry	ECL	CsI(Tl)	Barrel: $r = 125-162$cm, endcap: $z = -102 - +196$cm	6624 (Barrel), 1152 (FWD), 960 (BWD)	[12.4°;31.4°], [32.2°;128.7°], [130.7°;155.1°]
Muon ID	KLM	barrel:RPCs and scintillator strips	2 layers with scintillator strips and 12 layers with 2 RPCs	θ 1.6×10^4, ϕ 1.6×10^4	[40°;129°]
	KLM	end-cap: scintillator strips	12 layers of (7-10)×40 mm^2 strips	1.7×10^4	[25°;40°], [129°;155°]

Table 1.2: Summary of the Belle II components and specifications.

1.4 Beam induced background

Beam backgrounds [23] are sources of radiation not coming from collisions in the interaction point and one of the key challenges at SuperKEKB and Belle II. In the SuperKEKB and Belle II designs, it was already estimated that several sub-detectors would be subject to close-to-tolerable backgrounds at peak luminosity. The most vulnerable sub-detectors are TOP and CDC, whose particle identification and charged tracks reconstruction performances are strongly affected by high beam losses in the IR.

Given the importance of beam background mitigation to the success of the experiment, background studies have been extensively performed since the early phases of SuperKEKB operation and continued to be performed routinely. Modern e^+e^- colliders are subject to many sources of background, that can be divided in single beam backgrounds and luminosity backgrounds. Backgrounds from luminosity processes, which are expected to dominate at target luminosity, have been slightly (up to 20%) lower than expected, while backgrounds from single beams are currently dominating and a factor of 4 higher than expectations. This is in line with the size of typical machine systematics involved, such as unknown machine errors, beam instabilities, beam-beam effects, modelling accuracy of machine component and detector surroundings.

The diamond radiation monitoring and beam abort system, that will be described in Chapter 3, continuously monitor the beam losses around the VXD during all SuperKEKB operations: initial injection, physics runs, continuous injection, machine and background studies.

1.4.1 Background sources

Beam particles deviated from the nominal orbit can be lost by hitting the beam pipe inner wall or other machine apparatus. If their loss position is close to the detector, generated shower particles might reach the detector. Fake hits generated by the background hits may deteriorate the detector's physics resolution. Radiation dose by gammas or neutrons originated by background events damages the detector components, especially silicon devices. Below a description of different types of beam background sources at SuperKEKB [24] is given.

Touschek scattering is a single electromagnetic scattering between two particles of the same bunch. The momentum transferred in the collision may deviate one or both particles outside the momentum acceptance [25], resulting in their loss. Touschek collisions are possible because, due to the momentum and energy spread of particles within the same bunch, particles undergo betatron and synchrotron oscillations during their motion. Given the Touschek scattering probability [26], the total scattering rate (r_T) is proportional to the number of filled bunches (n_b), the square of the bunch current (I_b), the inverse of the horizontal and vertical bunch sizes (σ_x and σ_y), the inverse of the bunch length (σ_z), and the inverse third power of accelerated-particle energy (E),

$$r_T \propto \frac{n_b I_b^2}{\sigma_x \sigma_y \sigma_z E^3} \,. \tag{1.3}$$

Higher beam currents along with a smaller beam size imply a large increase of Touschek scattering in SuperKEKB with respect to its predecessor KEKB. Particles lost due to Touschek scattering hit the beam pipe inner wall, producing electromagnetic showers. If this occurs near the interaction point, the shower products can reach the detector, generating signals not related to collisions. Movable collimators are used to

mitigate the effects of Touschek scattering. These devices stop off-trajectory particles, not allowing them to reach the interaction region. During the accelerator design it has been decided to increase the LER energy with respect to KEKB to 4 GeV: this choice reduces the Touschek LER background.

Beam-gas scattering is a scattering of beam particles with residual gas molecules in the beam pipe. The particle-molecule interaction may occur through two different processes: Coulomb scattering, which changes the direction of the beam particle; and bremsstrahlung scattering, which also reduces the energy of the beam particle, through photon emission. Beam-gas scattered particles are lost by hitting the beam pipe inner wall while they propagate around the ring. The beam-gas scattering rate (r_{BG}) is proportional to the beam current (I) and to the pressure (P) inside the beam pipe.

$$r_{BG} \propto IP = p_0 I + p_1 I^2 \tag{1.4}$$

Two components contribute to the pressure, a pressure without beams (p_0), and a dynamical component that depends on the total beam current (p_1). This second term is related to desorption effects: previously absorbed gas molecules can be re-emitted by the beam pipe walls. An improvement of the vacuum quality is usually achieved by *baking* and *vacuum-scrubbing.* During *baking*, sections of the beam pipe are heated up and the released gas molecules are extracted using vacuum pumps. *Vacuum-scrubbing* consists in letting the beams circulate without collisions to stimulate the re-emission of molecules absorbed by the beam pipe walls and their extraction by vacuum pumps. The beam-gas background is reduced by tuning the collimator positions.

Synchrotron radiation is the emission of photons by accelerated charged particles. The power emitted (W_S) is proportional to fourth power of the beam energy (E) and the inverse square of the curvature radius (ρ) [27].

$$W_S \propto \frac{E^4}{\rho^2} \tag{1.5}$$

Given the proportionality to the beam energy squared, the HER beam is the main source of this background. Since the sources of SR background are the accelerated particles, the photon emission rate is proportional to the beam current. The energy spectrum of SR photons ranges from a few keV to tens of keV. In order to protect the first layer of the vertex detector from SR-induced damage, the shape of the beam pipe in the interaction region is designed to avoid direct SR hits at the detector and its inner surface is coated with a gold layer to absorb SR photons. However, during the accelerator commissioning in *Phase 2* SR-component in the particle energy spectrum was detected by dedicated sensors placed around the IP.

Radiative Bhabha process is an electron-positron scattering process where a photon is present in the final state, in addition to the initial particles, $e^+e^- \rightarrow e^+e^-\gamma$ (Figure1.4). Radiative Bhabha photons can interact with the iron of the accelerator magnets, producing low-energy gamma rays and neutrons. Low-energy gamma rays contribute to the background for the CDC and for the barrel particle identification systems. Neutrons are the main background source for the outermost detectors like KLM. Neutron shielding is used in the accelerator tunnel to reduce their flux. By emitting a photon, electrons and positrons lose energy and may then hit the beam pipe walls, producing electromagnetic showers. Bhabha scattering is also important for luminosity measurements. The Bhabha cross section is large and dominated by

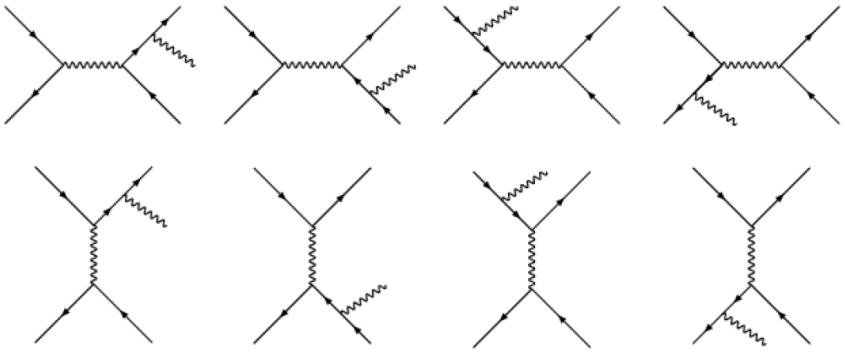

Figure 1.4: Leading-order Feynman diagrams that contribute to the radiative Bhabha process.

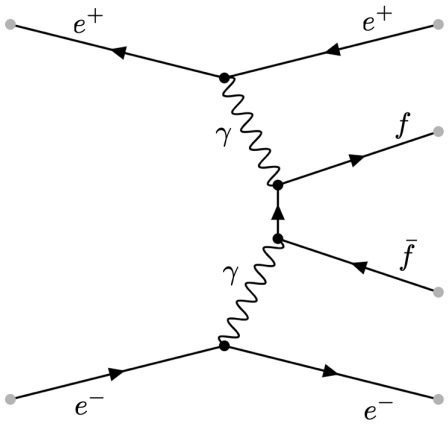

Figure 1.5: Leading-order Feynman diagram for the two-photon process.

electromagnetic interactions. Therefore it is possible to use perturbative QED and predict the cross section with high accuracy.

Two photon process is the QED process $e^+e^- \to e^+e^-e^+e^-$. Low momentum electron-positron pairs can spiral around the magnetic field lines of the Belle II solenoid leaving multiple hits in the inner Belle II detectors. The primary particles that lose a large amount of energy or scatter at large angles can be lost inside the detector, as with radiative Bhabha. As the background particles interact with the inner detector, they increase the hit multiplicity, making tracking more difficult.

Injection background is caused by charge injection in a circulating beam bunch. The main difference between the stored particles and injected particles is the oscillation amplitude around the bunch center. Injected particles oscillate with larger amplitudes and can be lost in the interaction region, becoming a source of background for the Belle II detector. After each injection the bunch is perturbed and a higher background rate is observed in the detector for few milliseconds after the injection. A veto signal, whose duration can be adjusted according to the background conditions, is applied to Belle II detector and data acquisition trigger to prevent the detector readout during each injection.

Sudden beam loss The stored beam sometimes becomes very unstable and can cause

catastrophic or so-called sudden beam losses. These losses have already caused quenches of QCS superconductive magnets, and sometimes they damaged sensitive components of Belle II and SuperKEKB collimators, significantly slowing down planned luminosity increase. A possible cause of these events is dust traps in the beam pipe, but this is not yet fully understood. Detailed analysis of beam abort and other related studies are still ongoing.

All these backgrounds strongly depend on the beam optics. According to preliminary estimates, the PXD total integrated dose may range from about 150 to about 180 kGy (15 to 18 Mrad) during the projected lifetime of Belle II at the design integrated luminosity (50 ab^{-1}). For the inner and less exposed layers of the SVD approximately 4.5 Mrad are expected to be integrated during the same Belle II activity period [28]. These estimates have been used to approximately determine a projection for the dose budget, needed to prevent the vertex detector from integrating radiation doses significantly higher than the design values.

1.4.2 Background mitigation and monitors

Background countermeasures [29], such as beam collimation and specialised shielding, are used to mitigate radiation damage, gradual deterioration, or reduced Belle II reconstruction performance, due to higher occupancy, fake hits and pile-up noise in the electromagnetic calorimeter, neutron induced hits in the muon detection system.

Movable collimators are installed along the SuperKEKB rings to stop deviated beam particles before they reach the interaction region and leave background hits in Belle II detector. However, a fraction of beam particles can still be lost inside the interaction region. To protect the inner detectors from background showers, tungsten shields are installed just outside the IP beam pipe and inside the vertex detector. In addition, thick tungsten shields were also installed during LS1 around QCS, where the beam loss rate is estimated to be the highest due to the large betatron function. Also the IP beam pipe of the SuperKEKB is designed to reduce the synchrotron radiation background. Most of the SR from upstream of the IP is stopped by the tapered collimation part of the incoming pipe so that SR will not hit the beryllium part of the central IP beam pipe. The reflected SR also should not reach the central IP beam pipe thanks to the ridge structure on the tapered surface of the incoming beam pipe.

Anyway, since not all beam losses can be fully avoided, the beam instrumentation is essential to monitor beam parameters and provide safe machine and detector operation. Various detectors to measure dose rates in the IR and accelerator tunnel are in use:

- The main one in the IR is based on diamond detectors, studied in this thesis. The system measures the radiation dose rate in the IR, provides quick beam abort signal and records the dose rate. The diamond radiation monitoring system is described in detail in Chapter 3.

- The sCintillation Light And Waveform Sensors (CLAWS) detector system, which is based on plastic scintillators and silicon photomultipliers. It monitors beam-induced backgrounds synchronised with the SuperKEKB injection. This system also provides a beam abort signal since 2021, but it is not able to record the dose rate.

- Time Projection Chambers (TPCs), compact gaseous detector filled with a He (70%)+ CO_2 (30%) gas mixture, measure the *fast* neutron flux in the accelerator tunnel from both sides of Belle II.

- ^3He tube detectors, installed around Belle II, count *thermal* neutrons with kinetic energy below about 0.025 eV.
- PIN photo-diodes, installed next to each collimator, monitors fast beam losses around the movable jaws.
- 5 m long ion chambers, mounted on the outer wall along the tunnel, measure beam losses in the accelerator tunnel.
- New loss monitors, based on CsI-crystals with photo-multiplier tubes (PMTs) and electron-multiplier tubes (EMTs), have been installed during LS1 near SuperKEKB collimators. These new system with good time synchronisation capabilities will be used to pin down the location of high beam losses around the rings.

SuperKEKB has a beam-abort system, which has been upgraded from KEKB [9]. Beam-abort requests from more than one hundred loss monitors around the ring are collected locally and delivered to the central control room of the accelerator. Logical ORs of these signals, separately for LER and HER, trigger kicker magnets, that quickly dump the beams in a controlled way. The two kicker triggers are also sent back to the Belle II control room and other locations, to save detailed beam loss data locally and allow a "post-abort" analysis of the beam losses that immediately preceded the occurrence of a given abort.

The diamond and CLAWS systems are integrated into the SuperKEKB abort system to provide abort signals which are essential to protect the Belle II detector and the QCSs final focus superconductive magnets. A detailed description of the diamond radiation monitor and beam abort system is given in Chapter 3.

Chapter 2

Belle II Vertex Detector

In this chapter I describe the Belle II vertex detector. The vertex detector plays a central role in measuring the decay vertices of B mesons. It consists of two sub-detectors: the innermost pixel detector (PXD), described in Section 2.1.2 , and the silicon vertex detector (SVD), described in Section 2.1.3. In Section 2.2 I report the effects of the main sources of damage related to radiation in semiconductor devices and the major vulnerabilities of PXD and SVD to backgrounds. Section 2.3 gives a brief overview of the improvements to the interaction region (IR) made during Long Shutdown 1, with the installation of the full PXD on a re-designed beam pipe. This installation required a new production of diamond detectors for the radiation monitoring and beam abort system that I will describe in Chapters 3 and 4.

2.1 Vertex detector

An excellent vertex resolution is essential for measuring the decay vertices of B mesons. Typical momenta of the decay products are ranging from a few tens of MeV to a few GeV and multiple scattering has a significant impact on the vertex resolution. For this reason the innermost vertex detector has to minimise as much as possible the material inside the acceptance region.

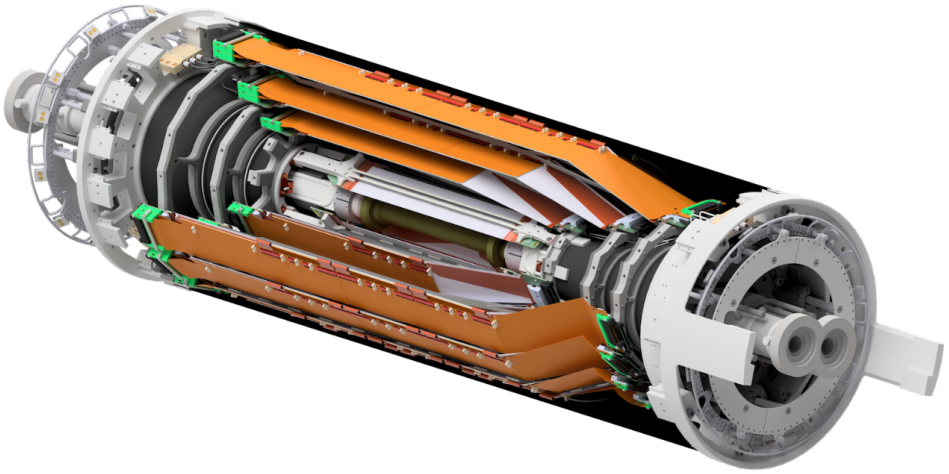

Figure 2.1: The Belle II VerteX Detector (VXD), made by pixel detectors (PXD) in the two inner layers and double-sided silicon strip (SVD) detectors in the four outer layers.

The Belle II VerteX Detector (VXD) consists of two devices, the silicon PiXel Detector (PXD) and the Silicon Vertex Detector (SVD), arranged altogether on six layers (Fig.2.1). The main features about the VXD layers are summarised in Table 2.1, while the layout is shown in Figure 2.2.

	PXD		SVD			
	L1	L2	L3	L4	L5	L6
Radius [mm]	14	22	39	80	104	135
N. ladders	8	12	7	10	12	16
N. sensor/ladder	2	2	2	$2+1^*$	$3+1^*$	$4+1^*$
N. sensors	16	24	14	30	48	80
ϕ pitch [μm]	50	50	50	75, 75 to 50*		
z pitch [μm]	60	80	160	240		
Sensor thickness [μm]	75		320	320, 300*		
Mat. budget [X_0]	0.19%		0.70%	0.70%		
N. channels/sensor	768×250		$768+768$	$768+512$		
N. channels	3M	4.6M	22k	38k	61k	102k

Table 2.1: Summary table of the main features of the VXD layers. Fields with an * are relative to the trapezoidal, slanted sensors of SVD. For SVD, the readout pitch is indicated.

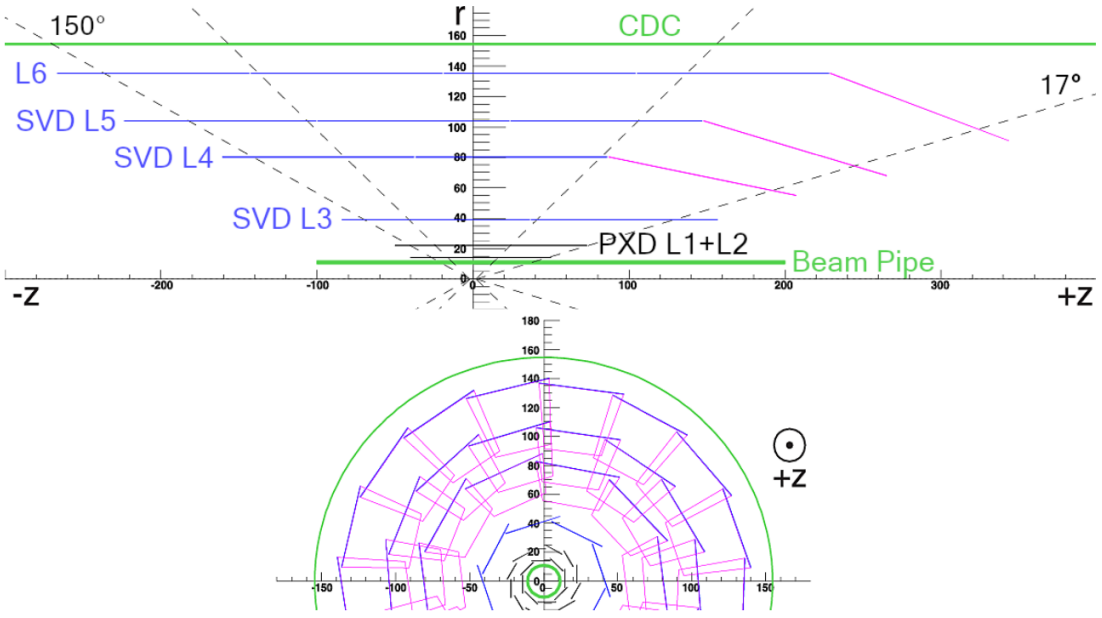

Figure 2.2: Schematic side view (top) and front view (bottom) of the VXD. The axis scales are in mm.

The VXD is designed to sample the trajectories of charged particles in proximity of the interaction point (IP) and therefore infer the decay position of long-lived particles. However, due to the small distance from the IP, the vertex detector has to withstand high backgrounds. A smaller distance from the interaction point helps vertex reconstruction,

leads to harsher operation conditions with higher background and increased occupancy, *i.e.* the fraction of channels hit in each triggered event.

In the following I describe the Belle II interaction region (IR) and in particular the beam pipe design. Subsequently a description of PXD and SVD design and main characteristics are given.

2.1.1 Beam pipe chamber of the interaction point

The SuperKEKB interaction region (IR) extends for ± 4 m from the interaction point (IP), and includes the whole final focusing system integrated on the Belle II detector itself. For the upgrade from Belle to Belle II detector, the interaction region has been re-design in order to achieve higher luminosity through the nano-beam scheme. The main improvements introduced in the new interaction region are the final focusing superconductive magnets (QCS) larger than Belle and located closer to the interaction point (IP). In the vertex detector two additional layers of pixel detectors were introduced close to the IP. Moreover, the beam pipe design has been changed, to meet the nano-beam scheme requirements and to reduce the background which can damage the detector. For this purpose an heavy metal shielding has been integrated. Figure 2.3 shows the layout of QCSs in the SuperKEKB interaction region.

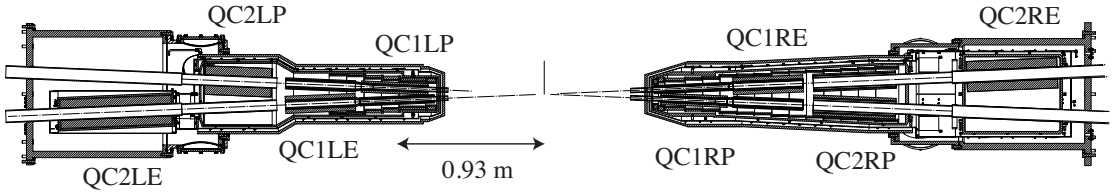

Figure 2.3: Schematic view of a longitudinal section of the SuperKEKB interaction region (IR), with the final focusing superconductive magnets.

The IR beam pipe, shown in Figure 2.4, consists of a beryllium (Be) straight central part and two tantalum (Ta) crotch parts, the latter connecting the IP to the QCS final magnets. All the components have been chosen in order to have less material as possible within the detector acceptance and more material outside of the acceptance, in order to reduce background by particle showers.

Each crotch part consists of two pipes, respectively for the incoming and outgoing beams. The incoming pipe is characterised by a taper, to reduce the number of photons entering into the central part, and ridges on the internal surface, to keep the direction of the scattered photons away from the Be central chamber. Moreover, the polarity of the last bend of SuperKEKB is designed so that the SR fan from the bend does not directly hit the central part of the IP chamber. Therefore, contrary to KEKB, there is no mask structure, since the SR is blocked by the crotch.

The central IP chamber, which has a length of 230 mm, consists of two coaxial pipes with a central part 71 mm long of beryllium (Be) and two lateral part of titanium (Ti). Ti was chosen since it has similar coefficient of linear expansion of Be. The two pipes have diameters of 20 mm and 24 mm respectively, with a 1 mm gap between them. A coolant flows through the gap between two beam pipe walls. The radius of the IP chamber is the same as that of the QCS beam pipe, in order to avoid a resonant cavity structure. The central pipe has a $\sim 20\,\mu$m thick gold coat sputtered inside, which can absorb the

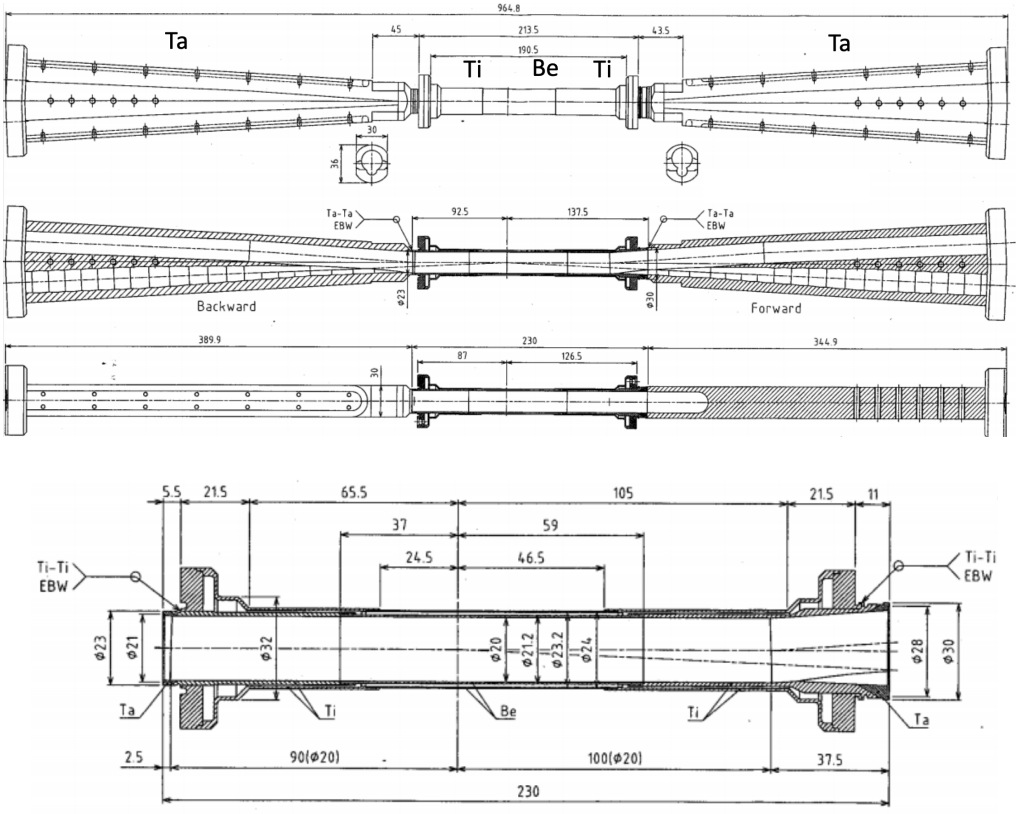

Figure 2.4: Belle II beam pipe: the top picture shows three different views of the IP beam pipe; the bottom picture shows the design of the central chamber.

synchrotron radiation photons. The connection between the crotch parts and the QCS is made by bellows pipes made of CrCu, which are flexible to allow an easy connection. Beam-position monitors are mounted on the bellows for fast and precise beam feedback.

To keep a stable temperature is important both for the fragile thin beryllium tubes, and also for the PXD mechanics: the cooling system has a central role. There are three main heat sources: the beam-induced Higher Order Mode (HOM) [27], wall currents and synchrotron radiation (SR) hits [30]. The HOM is induced by beam bunches run through a pipe with a sudden variation of diameter. The electromagnetic field attached to the beam bunch is scattered or trapped in the cavity, and the trapped component can work as a heat source. This heat source affects the crotch parts, and especially the outgoing pipes. This source has been minimised with a smooth transition from the crotch to the beryllium part. The wall current is instead related to charged particles that drag charge on the surface of the beam pipe, inducing an image current. The energy loss by image current can heat up the pipe. The largest heat source in this section is caused by the image current.

The central beryllium part and crotch tantalum parts are cooled with paraffin and water, respectively. Since beryllium is reactive, cooling by water was avoided for the central part. Instead, a normal paraffin liquid such as $C_{10}H_{22}$ has been used. As the heat capacity of $C_{10}H_{22}$ is around 2 J/K/g, a flow of about 300 cm^3/min of paraffin is needed to keep the temperature rise below 10°C. To ensure a safety margin, the cooling system can support a paraffin flow up to 1000 cm^3/min. In addition, the pressure drop of the liquid should be less than 0.1 MPa to avoid breakdown of the cylinder. For monitoring the

temperature pt100 sensors are distributed over the chamber. An interlock system has been implemented to monitor both paraffin flow and temperature during accelerator operations, with the goal of preventing fatal accidents. An heavy metal shielding, made of Tungsten, is integrated around the crotch pipes and their connection to the central IP chamber, in order to reduce background by particles showering.

2.1.2 Pixel Detector

Thanks to the reduced beam pipe radius (10 mm instead of 15 mm of Belle beam pipe), the innermost layers of the VXD can be placed closer to the interaction point, which is advantageous for vertex resolution. However, in this way an higher occupancy, *i.e.* fraction of channels hit during an event, is expected: for this reason pixel sensors were chosen over strip sensors, as they have many more readout channels and, thus, much smaller occupancy.

The Pixel Detector (PXD) [31, 32] design includes two coaxial layers of sensors with radii at 14mm and 22mm, as shown is Fig.2.5, for a total of around 8 million pixels. The polar acceptance ranges from 17° to 150°. Its final design consists of 40 modules, which are glued end-to-end in pairs of two, forming eight inner and twelve outer ladders. In *Phase 3 run 1* detector, a reduced PXD with 10 ladders and 19 functional modules was installed, corresponding to all eight ladders of layer 1 and two ladders of layer 2. Each module in the first (second) layer is made up of a large $1.5 \times 6.8\,(8.5)\,\mathrm{cm}^2$ silicon structure with an integrated DEPFET [33] (Depleted Field Effect Transistor) sensor.

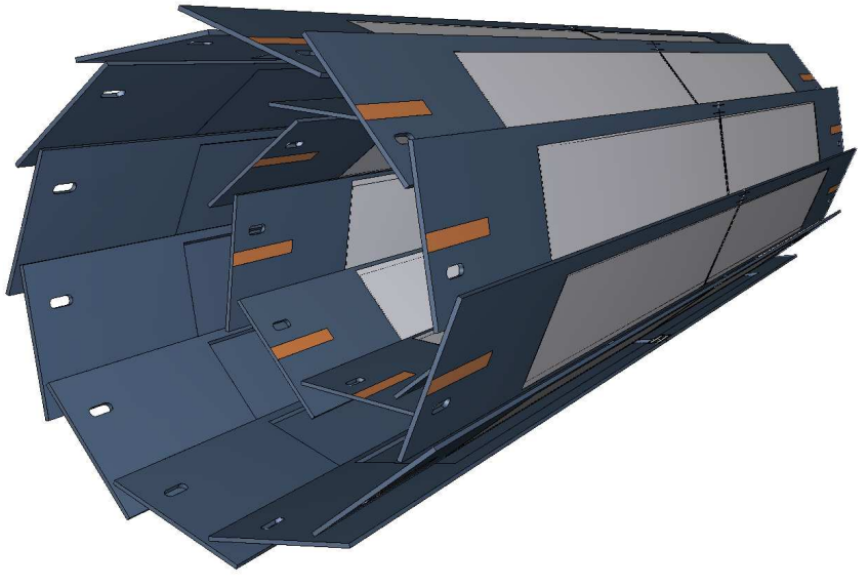

Figure 2.5: Schematic view of the geometrical arrangement of the PXD sensors. The light grey surfaces are sensitive DEPFET pixels [16] thinned to 75 μm.

The DEPFET sensor consists of a p-channel MOSFET integrated onto a silicon substrate, which is fully depleted applying a suitable voltage. A schematic of a DEPFET is show in Figure 2.6.

Incident particles generate electron-hole pairs within the fully depleted bulk. The electrons drift in the electrical field generated by the bias voltage, to the *internal gate* where they are collected. The current circulating through the FET (from the *drain*, connected

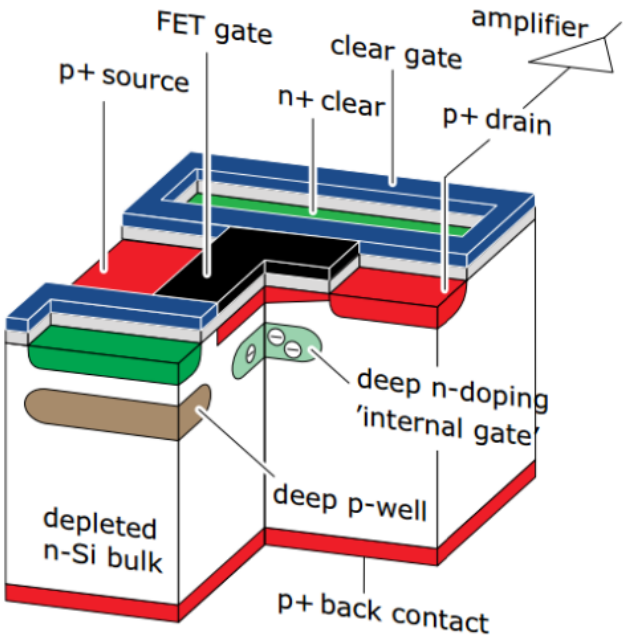

Figure 2.6: Schematic of the DEPFET-based pixels of PXD.

to the amplifier, to the *source*) is modulated by the voltage on the *gate*: a voltage needs to be applied to the gate in order to have a current. However, since the internal gate is capacitively coupled to the gate, the current also depends on the accumulated charge. The accumulated charge remains in the internal gate until removed by applying a positive voltage to the clear gate. Columns of pixels can be read by multiple amplifiers, one row at the time, using the so called rolling shutter readout scheme.

The sensor consists of a 250×768 matrix of DEPFET pixels. It is thinned to $75\,\mu$m to reduce the average material budget to $\simeq 0.2\% X/X_0$ per layer inside the tracking acceptance. The silicon bulk can be thinned to a few tens of μm without affecting sensor performance, but mechanical aspects must also be taken into account, such as the effect on the glide of the sensor due to thermal movements. The electronics is integrated with the sensor, allowing the amplification of the signal charge just above the position of its generation. The remaining readout electronics, which needs cooling, are located out-side the acceptance region and will not contribute to the multiple scattering material budget. The electronics is mounted on the Support Cooling Block (SCB), which is cooled by a two-phase CO_2 cooling system at $[-30°\mathrm{C}, -20°\mathrm{C}]$, described in Section 2.1.4. Active cooling is also used for the DEPFET matrix by utilising carbon tubes around the detector with nitrogen N_2 flow, used also to keep the detector volume dry.

This detector is a low power device, since pixels are "on" only during the readout, and no active cooling is necessary for the pixel itself. The total power consumption for the full PXD is about 360 W. Moreover, these sensors have a very small capacitance, resulting in a very low noise performance even at room temperature. The detector has a spatial resolution of 20 μm. To reach that, the position of the traversing charged particle is obtained by weighting the different amounts of charge measured in neighbouring pixels. The smaller separation between B vertices in an event due to the smaller Belle II boost

with respect to Belle is compensated by a reduced radius of the first detector layer.

Large backgrounds are associated with high data rates, equivalent to about 20 Gbit/s at 3% occupancy. Data is reduced using information from SVD. The distinction between physics and background hits relies on the extrapolation of tracks reconstructed in the SVD and propagated back to the PXD. Around each intersection point of a track with the PXD, a region of interest (ROI) is defined. If a fired PXD pixel lies inside the ROI, it is kept and readout; otherwise, it is discarded.

2.1.3 Silicon Vertex Detector

The Silicon Vertex Detector (SVD) [34] completes the VXD with four more layers of double-sided silicon strip detectors (DSSD), placed at radii between 39 and 135 mm. The VXD, together with the CDC, are the tracking system of the Belle II detector. The SVD has a stand alone vertex reconstruction capability, which is also used to define ROIs in the PXD to reduce the readout data rates. Moreover, it is able to accurately reconstruct the vertices of particles that decay outside the volume of PXD, such as K^0_S. Finally, it also provides dE/dx information, used for particle identification.

Since a lower particle background rate than in the PXD is expected, double-sided silicon strip detectors (DSSD) allows to achieve similar vertex-detection performance of PXD but with a much smaller number of readout channels. Furthermore this technology provides precise track information while keeping low the material budget.

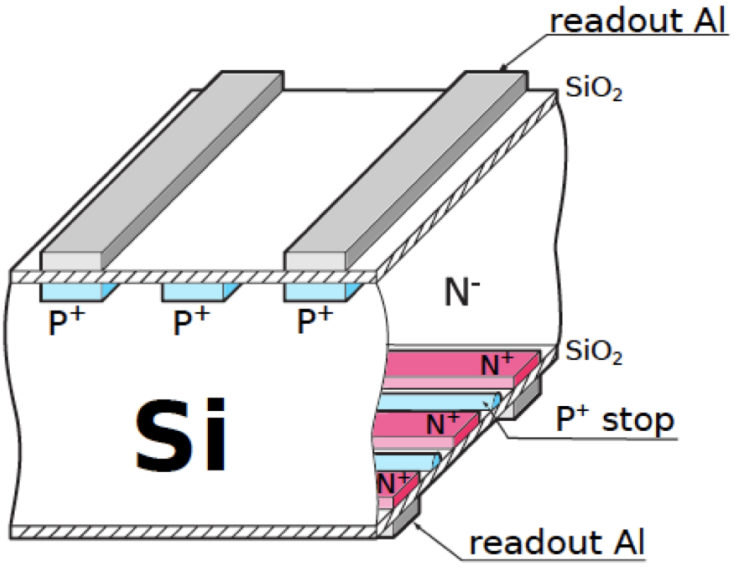

Figure 2.7: Schematic view of the double-sided silicon detector.

The double-sided silicon strip sensor consists of an n-type silicon substrate $\sim 300\,\mu$m thick with p^+ strips implanted on one side, and orthogonal n^+ strips implanted on the other side (Figure 2.7). As p-n junction, when a reverse bias voltage of O(100V) is applied between p and n strips the depletion region is extended to the volume of the whole substrate, which corresponds to the sensitive (or active) volume. A charged particle crossing the substrate generates electron-hole (eh) pairs which drift to the n and p strips, respectively, due to the electric field. The drift of charge carriers induces a current in the strips that can be measured by the readout electronics, through AC-coupled connections. The latter are

formed by aluminium strips placed above a layer of silicon oxide (SiO_2), in correspondence of p and n strips.

An intermediate floating strip is placed between two readout strips to improve the resolution without increasing the number of readout channels: the signal induced in the floating strip is shared between the neighbouring readout strips. The SiO_2 layer contains fixed positive charges that are trapped either during fabrication or by radiation damage after production. These positive charges attract electrons forming an e^- accumulation layer in the silicon bulk, which effectively short-circuits the n strips. To avoid this, a p^+ implant, called p-stop, is put between two n strips, pushing away the electrons and insulating n strips when a sufficient bias voltage is applied.

The SVD consists of four coaxial layers made by ladders mounted on a lantern-shape barrel. Each ladder is made of a support structure hosting 2 to 5 sensors with their readout chips and cooling support. The sensors are arranged around the beam direction with a windmill-like structure that causes a partial overlap of the sensor active regions (between 2% and 8% depending on the layer). The polar angular acceptance ranges from 17° to 150°. It is asymmetric to account for the forward boost originated from the asymmetric-energy collisions. To cope with the inclination of the forward tracks as well as to minimise the material traversed in the forward part, a lantern-like geometry was adopted for the forward end of the three outer layers of SVD, whose detectors are inclined with respect to the cylinder axis.

In order to accommodate the different geometry of the layers, three different types of sensors are used: small rectangular sensor for the innermost layer (L3), large rectangular sensors for the outermost layers (L456) and trapezoidal sensors for the forward region of the outermost layers (L456). Rectangular sensors are produced by Hamamatsu Photonics, trapezoidal ones by Micron. Figure 2.8 shows the three different types and dimensions of the sensors, whose main features are summarised in Table 2.2.

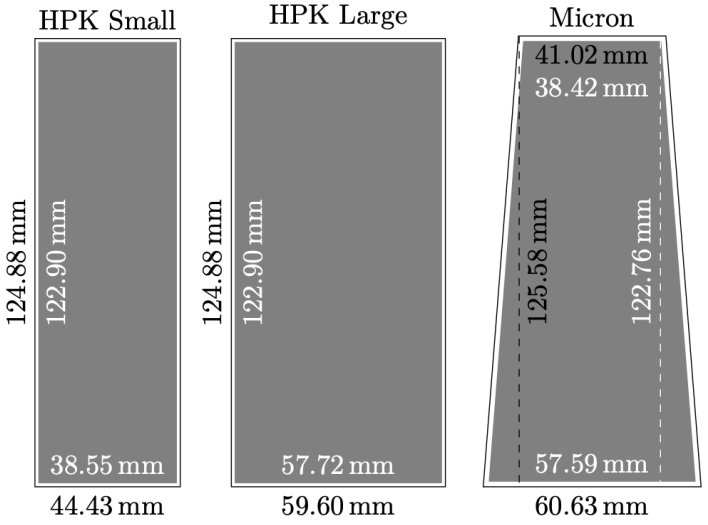

Figure 2.8: The dimensions of the three types of DSSD used in SVD and their active area (to scale).

Figure 2.9 show a picture of the different ladders of SVD. Layer 3 has has 7 planar ladders with two rectangular small sensors. Layers 4, 5 and 6 respectively, have 10/12/16 ladders with two/three/four rectangular large sensors and one trapezoidal sensor. The latter is placed on the forward side, and is tilted towards the z axis by 11.9°/17.2°/21.1°.

	Rectangular small	Rectangular large	Trapezoidal
Number of p-strips	768	768	768
p-strip pitch [μm]	50	75	75 to 50
Number of n-strips	768	512	512
n-strip pitch [μm]	160	240	240

Table 2.2: Summary of the main features of the three types of sensors used in SVD.

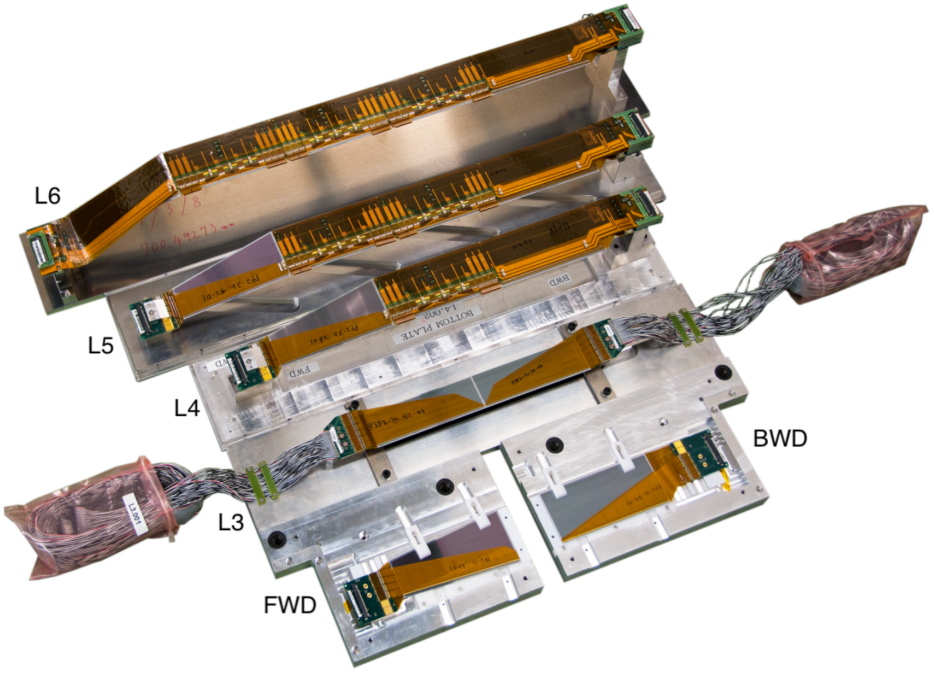

Figure 2.9: From top to bottom: Ladders of L6, L5, L4 and L3 placed on their transport frames, in the very front the forward and backward sub-assemblies are shown on their transport containers.

The ladders are mounted on two supports, one FWD and one BWD, called end-rings. The detector structure is then completed by 1 mm thick Carbon Fiber Reinforced Plastic (CFRP) cylinder (outer cover), which is 898 mm long with a 152.8 mm radius and provides mechanical support. To ensure a proper ground connection, a 0.1 mm thick aluminium sheet is glued on the external surface of the outer cover.

The readout electronics for the L3 backward and forward sensors is placed at each end of the ladders on dedicated PCBs, while that for the central sensors is placed on the so called "origami" [35] above the sensor itself, thus requiring a cooling pipe to placed on top of those sensors.

The high particle rate due to beam-induced background requires a readout chip with a fast shaping time. For this reason the APV25 chip [36], originally developed for the tracking detector of CMS, was chosen: it contains low-noise preamplifiers and shapers for 128 channels, and has a shaping time of 50 ns, crucial to minimise the hit occupancy due to the high particle rate from beam-induced background.

A 1 mm layer of Airex foam acts as thermal and electrical insulator between the sensor and the origami circuit. A planar pitch adapter connects the strips on the top side to the

chips, while the strips on the bottom side use a flexible pitch adapter wrapped around the edge of the sensor. Having all the chips on one side of the sensors allows to use a single cooling pipe for the APV25 chips of each layer, minimising the material budget.

In total 1748 APV25 chips are installed, with a power consumption of 700W. The SVD shares with PXD the cooling system, described in Section 2.1.4, used for the cooling of the APV25 chips. The sensor front-end is connected via hybrid cables to the junction boards (JBs), which provide the connection to the data cables to the Flash ADC (FACD) [37] and to the power cables to the power supplies. The junction boards are located in the so called "DOCK boxes", placed on the CDC wall on both sides. In addition to SVD DOCK boxes, also the PXD ones and the one used for cooling are hold on the CDC wall.

For the SVD, each DOCK box contains six junction boards and has a water cooling pipe at its bottom. The water flow in the cooling is provided by a chiller situated on the top of the E-hut. Patch panels for the connection of environmental sensors like the temperature NTC sensors, the diamond radiation sensors and optical fibers (Section 3) are mounted onto some of the SVD DOCK boxes.

2.1.4 VXD CO_2 cooling system

The cooling CO_2 plant, called *IBBelle* [38], supplies a two phase CO_2 to the VXD system (SVD and PXD) up to a rate of 30 g/s. The CO_2 has been chosen as cooling fluid for the following reasons:

- The liquid CO_2 has a large latent heat, allowing a the cooling with a lower flow compared to water.
- The viscosity of the liquid CO_2 is small and allows the use of small-diameter tubes for coolant circulation. For the SVD, the inner tube diameter is only 1.5 mm.
- A wall thickness of 0.05 mm provides sufficient pressure margin, keeping low the material budget.

During *Phase 3 run 1 IBBelle* was operated at a temperature of $-20°$C. However, in *Phase 3 run 2*, the system might require lower temperatures, in the range of [$-30°$C, $-20°$C], to compensate for the increased power consumption of the PXD2.

2.2 Radiation damage to silicon detectors

All background sources described in Section 1.4.1 can damage the VXD sensors, deteriorating its tracking performances as the absorbed dose increases. For proper charged particle pattern recognition the signal-to-noise ratio of the silicon vertex detector has to remain above 10 during the whole duration of Belle II data taking. In order to protect the inner detectors, whose tracking capabilities are essential for the Belle II physics program, a radiation monitoring and interlock system, described in Section 3.1 has been implemented and installed in the IR. In this section the main sources of damage related to radiation in semiconductor devices are presented. Changes in the macroscopic behaviour are traced back to microscopical lattice structure changes [39].

2.2.1 Radiation-induced defects

Depending on the type and energy of the radiation, the interaction may involve the electrons of the silicon crystal or the Si nuclei in the lattice. Typically, the interaction with the

electrons is a transient effect and is used to detect particles. The interaction with the nuclei, on the other hand, can cause permanent damage. High-energy particles, such as hadrons and higher-energy leptons, displace silicon atoms from their lattice positions, creating vacancies (empty lattice sites) and interstitials (atoms between regular lattice sites), called primary knock-on atoms (PKA). This is known as *bulk damage*. These defects introduce new energy levels in the band gap of the silicon and, if not annealed, lead to degradation of the electrical properties of the detector, including increased leakage current and carrier trapping. An incident particle must transfer a recoil energy of at least 25 eV to a silicon atom to displace it from its lattice site; if the energy is sufficient, at the end of the path the atom will displace several other atoms in a small volume, producing a cluster defect. For recoil energies below 2 keV, isolated defects are created. On a microscopic scale, defects have several effects. They act as recombination generation centres, as they can capture and emit electrons and holes; they are also trapping centres, where electrons and holes are captured and re-emitted with some time delay; they can also be charged, affecting the spatial charge density in the depletion region.

The type and energy of the incident radiation determines the probability of forming a primary knock-on atom and the maximum elastic recoil energy transferred to the atom. The "non-ionising energy loss" (NIEL) hypothesis provides a model for the displacement damage cross section $D(E)$, which gives the average recoil energy released by a particle of energy E per unit particle fluence ϕ, taking into account all possible interactions and the distribution of the energy lost to displacement. Figure 2.10 shows the displacement damage cross section for different particles.

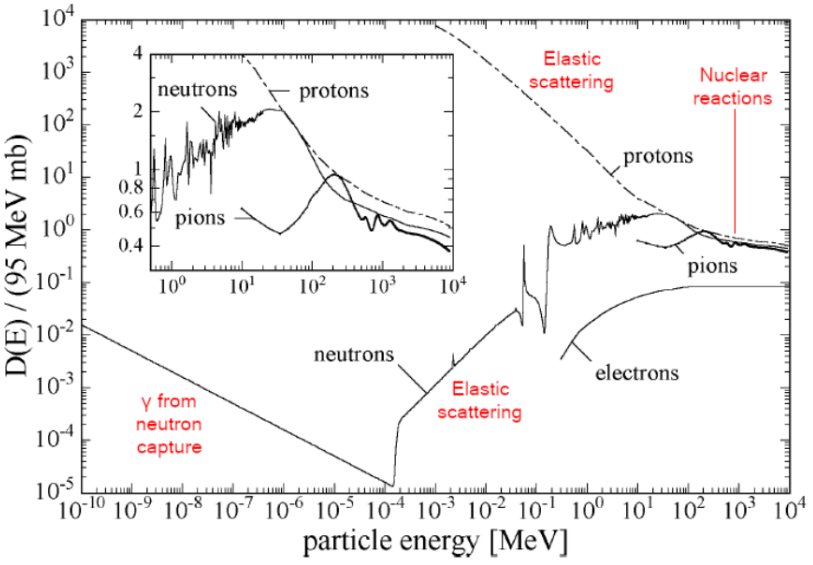

Figure 2.10: The displacement damage cross section in silicon for different particles as a function of their kinetic energy, relative the NIEL cross-section of a 1 MeV neutron in silicon, which is by definition 95 MeV mb. The main process responsible for displacement is indicated.

In addition to displace silicon atoms, radiation can also affect the dielectric layers present in silicon devices and the interfaces between them and the silicon. The main effects are a charge build-up in the oxide and an increase in the interface trap density. This is called *surface damage*.

2.2.2 Effects on detector properties

The microscopic lattice defects induce several changes in the properties and operating parameters of a detector.

Operating voltage: radiation damage can change the space charge density in the silicon depletion region. As a consequence, the bias voltage necessary to deplete the bulk changes. Radiation-originated defects can interact with dopants such as phosphorus present in n-type substrates used for the SVD sensors, changing their charge state and preventing them from fulfilling their role as donors (donor removal). In addition they act as effective acceptors. The effective doping decreases as the impinging particle fluence (number of particles that intersect a unit area of the detector) increases until an intrinsic-like condition is achieved. Increasing furthermore the fluence brings to a type inversion of the n-type silicon substrate. During Belle II data taking, the SVD sensors are expected to suffer from donor removal, as the absorbed dose increases. Hence the applied voltage could be changed to obtain the best detector performances.

Reverse-bias current: defects can emit electrons and holes, causing the generation of a reverse-bias current in the depleted volume. The major contributions to this current come from defects whose energy levels are near the band-gap centre. Since the defect generation is proportional to the impinging-particle fluence, a linear relation between the leakage current increase and the fluence exists. Bulk defects and interface traps increase the reverse-bias current in depleted volume and surface respectively. The reverse-bias current increases the detector noise level, deteriorating the Signal-to-Noise Ratio (SNR).

Trapping of signal charge: the trapping probability for charge carriers per unit time is approximately proportional to the trap concentration, which is increased by radiation-induced damage. Unlike reverse-bias current, where only energy levels close to mid-gap contribute significantly, all the defects are able to trap charge carriers. Trapped charge carriers are released after some time and only if they are released early enough they can fall in the time window needed for charge collection. Otherwise, trapping decreases the charge collection efficiency of the detector, defined as the ratio between the collected and the created charge due to an impinging particle. Like reverse-bias current, charge trapping also lowers the detector SNR, this time by reducing the signal.

Radiation effects, respectively from the surface and bulk damage, are usually parameterised in terms of the total ionising dose released in the sensor (TID) and with the non-ionising energy loss (NIEL), expressed as a function of the 1-MeV neutron equivalent fluence. The damage sources described so far depend on the particle fluence accumulated over time on the detector. However spike-like intense and rapid energy releases may also produce additional damage. During short, intense irradiation, a very high density of carriers can be created. The silicon then behaves more like an electrical conductor, causing the applied voltage to drop across the dielectric layer of the AC coupling capacitors integrated in the SVD sensors. High voltage difference across the oxide can lead to dielectric breakdown, thus shorting the AC capacitors. Radiation damage not only affects sensors, but also their readout electronics which is located in the same volume. However, the use of thin high-quality gate oxides in CMOS technology has reduced the effects of radiation damage [40] on readout circuits, which makes these effects less relevant with respect to the sensors.

2.2.3 VXD vulnerabilities to beam-background

Different beam-backgrounds described in Section 1.4.1 might deteriorate the detector performance. Here I describe the main VXD sub-detectors vulnerabilities to beam-background.

PXD is the innermost detector and its expected dominating background originates from irreducible two-photon process. Also sudden beam losses are of particular concern as the passing particles not only damage the detector by creating dead pixels or inefficient regions but they can deposit significant dose shortening the detector's lifetime. Moreover, as the closest detector to the interaction point, the PXD is also uniquely sensitive to the back-scatter of low-energy synchrotron radiation photons. Since it is the closest detector to the IP, the first limitation is on occupancy. Assuming 30 kHz trigger rate operation, some data loss will start to occur once the mean PXD occupancy exceeds 3%. For this value of occupancy also the offline performance will degrade significantly because of cluster merging and a higher probability to associate wrong hits to the track. Another limit is given by the detector degradation due to radiation damage.

The device is deemed safe for an integrated dose rate of 2 Mrad/smy[1] in 10 years of operation, while the type inversion is not expected to occur before reaching a 1-MeV neutron equivalent fluence of 1×10^{14} neq/cm^2. This results is obtained from a dedicated X-ray irradiation campaign [41]. During *Phase 2* and the first run of *Phase 3*, the current average occupancy was always below 0.3% in the PXD, suggesting that background levels may be kept under control. However, in May 2021 there was a significant beam loss, where one module of PXD first layer was damaged by SR, making the replacement with the new two-layer PXD during LS1 of particular value.

In the SVD, the beam background increases the hit occupancy and causes radiation damage on the sensors, degrading the tracking performances. In particular, radiation damages can affect the sensor leakage current, strip noise, and the full depletion voltage of sensors. Therefore, it is relevant to evaluate the detector performance over the entire lifetime of the experiment.

Effects due to surface damage are saturating after a relatively low integrated dose, at about 100 krad, while bulk effects are expected to dominate the SVD radiation damage in the long range. The most restrictive limit on the SVD beam background levels is due to the degradation of the tracking performance, which limits the hit occupancy of the SVD innermost layer (Layer 3) to about 5%, with a rejection of background hits based on the hit-time. A deterioration of the SVD performance is expected after an integrated dose of about 6 Mrad, corresponding to about 1.4×10^{13} neq/cm^2 of 1-MeV neutron equivalent fluence, due to a sizable reduction in the SNR. As for changes in the effective doping concentration and depletion voltage, no significant performance degradation is expected even after bulk type inversion and up to about 2.5×10^{13} neq/cm^2 total 1-MeV equivalent neutron fluence. This limit is based on the results of sensors used in the BaBar experiment [42], similar to the SVD ones, that were confirmed to be fully functional after irradiations up to this level.

During the operation in 2021, the hit occupancy averaged among the Layer 3 sensors was 0.5% at maximum, well below the occupancy limit of about 5%. In the three-year operation of the SVD, from 2019 to 2021, the first effects of radiation damage have been measured, compatible with the expectations, and with no degradation of the SVD performance [43].

[1] The unit smy stands for a Snowmass year (1×10^7 s), which is typical operation time of an accelerator facility.

2.3 Long Shutdown 1

Following the *Phase 3 run 1* data taking period, a long-term shutdown period, LS1, began in July 2022, during which the completeness and robustness of present Belle II has been improved. As mentioned before, the PXD installed for *run 1* was incomplete. In addition, it has experienced unforeseen damage due to beam losses, deteriorating significantly the overall hit efficiency by 2.5%. Although its performance is still within the nominal requirements, the expected increase in luminosity could deteriorate the tracking efficiency without the second layer in place. Therefore, the main reason for this long shutdown was the completion of the vertex detector with two full layers of pixel detectors. However, taking advantage of the installation of the new detector, a new improved beam pipe has been manufactured, as described below. In addition, in view of the long period of non-operation of the collider, other work was planned, such as the replacement of part of the photomultipliers (PMT) of the TOP detector, maintenance work on the CDC and a new data acquisition system common to all subsystems. Below is a brief description of the improvements made to the new beampipe and the installation of the new pixel detector (PXD2).

2.3.1 LS1 beam pipe

During bad HER injection, PXD observed synchrotron radiation, which may damage the detector. To mitigate the effects of synchrotron radiation on the PXD, the decision was taken to produce a new beam pipe for the PXD2. To reduce the SR, the straight section was shortened on each side by 1cm on the FWD and 0.5cm on the BWD. With respect to the first beam pipe, an additional layer of $10\,\mu$m of gold (Au) was sputtered onto the IP inner tube to absorb SR photons and the bump shape of the crotch section was reduced to mitigate photon scattering. Preliminary simulation of the new beam pipe design showed a reduction in photon hit rate of $\sim 50\%$.

In addition, during *Phase 3 run 1*, the temperature measurement between the IP cooling flange and the PXD mounting block reached approximately $45\,^{\circ}$C on the FWD side, which may be a problem for PXD stable operation. The crotch part heating is proportional to the LER beam current and should be reduced for PXD stable operation. The crotch cooling has been modified to provide more effective cooling contact with the water pipe: a new heat sink with good thermal paste has been used. Figure 2.11 shows images of two consecutive steps in the assembly of the new beam pipe.

Due to the construction of a new beam pipe, the eight diamond detectors used for the radiation monitoring and beam abort system described in Section 3.1 and installed on the first beam pipe were also replaced with new ones. It was decided to build eight new detectors, instead of using the ones already installed on the old beam pipe, in order to reduce the installation time of the new vertex detector. The new diamond detectors have the same geometry as the old production, and the assembly, characterisation and installation are described in the Chapter 4.

2.3.2 PXD2 and VXD reinstallation

The PXD2 is using the same design as PXD, described in Section 2.1.2. The schedule from production to the final assembly of PXD2 with all the necessary tests has been long, due to the complexity of the system itself and to several mechanical and thermal constrains and many issues requiring further investigation and testing. One of the main problems is excessive bending ($\sim 1\,$mm) of the modules due to malfunction of the detector's

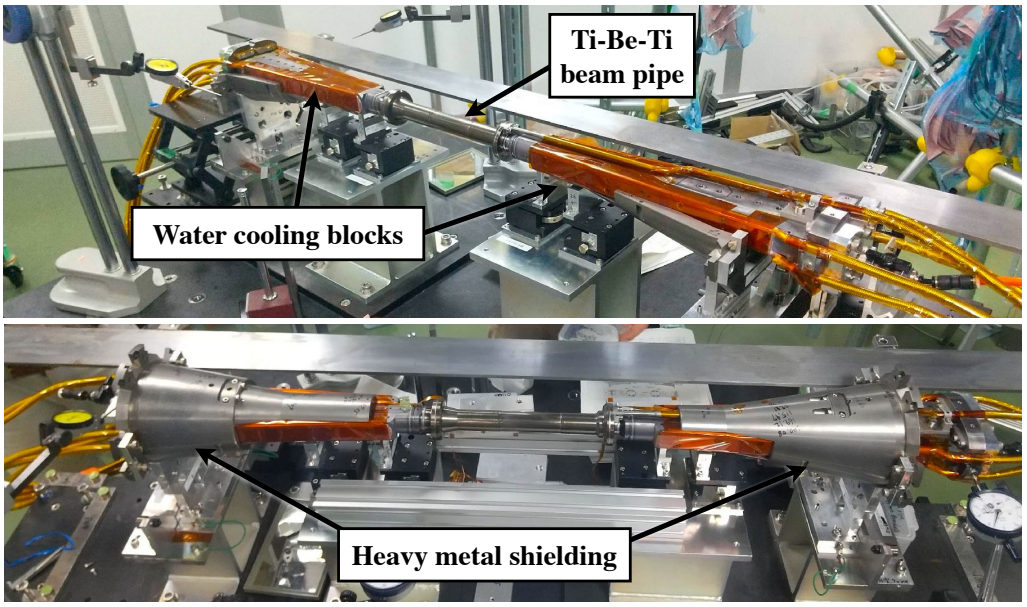

Figure 2.11: Two sequential steps of beam pipe assembly: (top) installation of the water cooling blocks on the crotch parts, (bottom) heavy metal shielding integration on the crotch parts.

sliding system, which allow movements due to thermal contractions and expansions. For this reason, keeping the temperature within defined ranges is essential not only for the performance of the PXD, but also for its mechanical stability. The detector was mounted on the new beam pipe in March 2023. Figure 2.12 shows the detector after installation.

The PXD2 was first installed on the new beam pipe and thoroughly tested to ensure the proper functioning of the entire detector. Subsequently, the VXD was carefully extracted from Belle II detector and SVD was detached from PXD. After the stand-alone commissioning of PXD2 and SVD, SVD was married to PXD2, as shown in Figure 2.13. This complex process spanned several months and involved a multitude of sequential steps and extensive testing of the detectors and the environmental monitoring system discussed in Section 3.2. Notably, the process involved two successive commissioning phases of the VXD, one prior to and another subsequent to its installation in the Belle II detector.

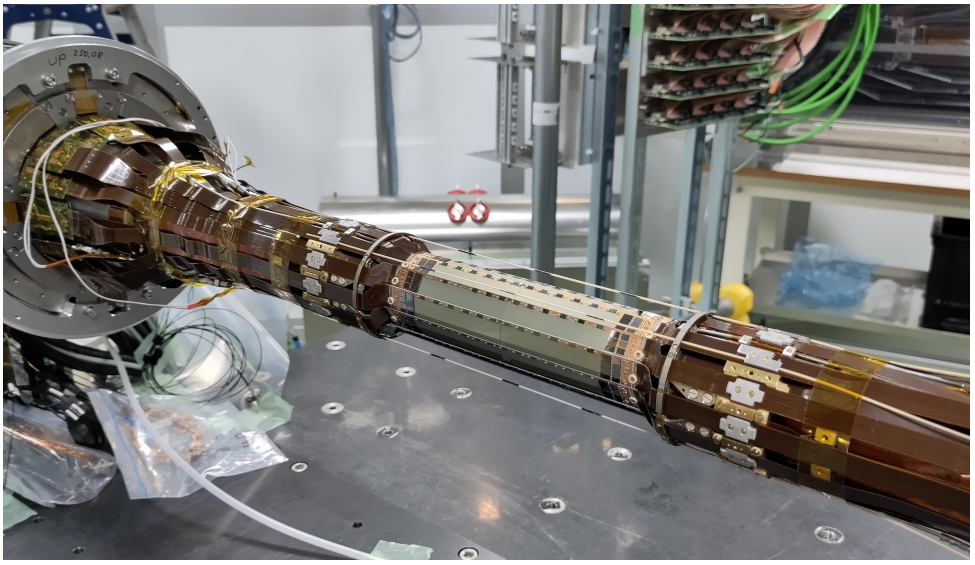

Figure 2.12: PXD2 after the installation on the beam pipe.

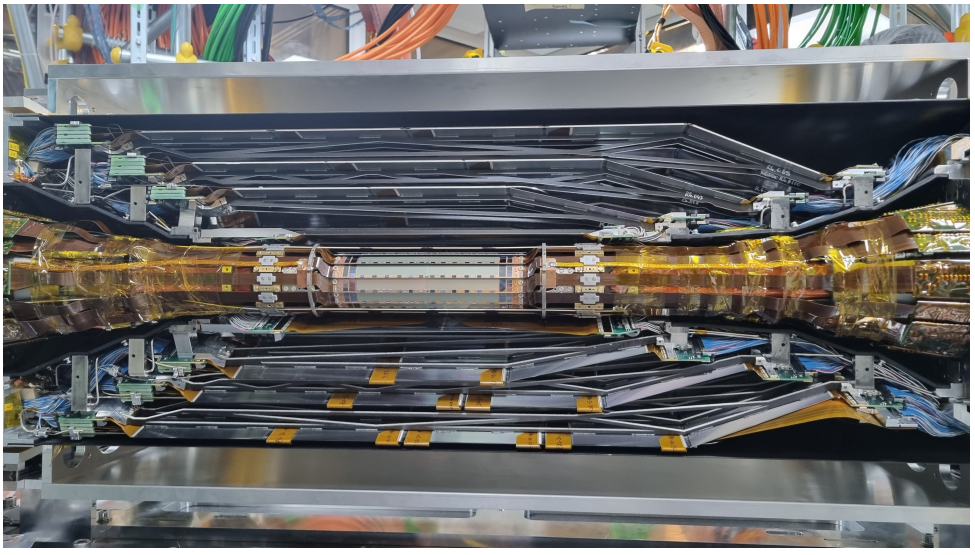

Figure 2.13: First half of SVD attached to PXD2.

Chapter 3

Radiation and environmental monitoring

In this Chapter I briefly describe the SVD radiation and environmental monitoring systems. Since some parts of the monitoring systems are common to the PXD detector and were developed together, they are also called VXD radiation and environmental monitors. All environmental parameters such as radiation levels, temperature and humidity must be constantly monitored and, if certain conditions are met, immediate action must be taken, such as interlocking the power supply or sending an abort signal to the SuperKEKB collider. The radiation monitoring and beam abort system is described in Section 3.1, while in Section 3.2 both the temperature and humidity monitoring system are described. The last Section 3.3 describes the VXD local hardwire interlock (VLHI), crucial for safe operation of the detector. During my PhD I also worked on the hardware of the environmental system, in particular during the LS1. Additionally, I held the responsibility for firmware development and contributed to various hardware enhancements of the VLHI project during LS1. Part of the material presented in this Chapter is sourced from Ref. [34] and the internal documentation of SVD.

3.1 Radiation monitoring and beam abort

Excellent vertex detector tracking is fundamental to achieve the Belle II flavour physics objectives, and the construction of a new vertex detector took up to three or four years at considerable effort and cost. An efficient and reliable protection system is therefore needed to safeguard the vertex detector from high radiation doses and to extend its lifetime as much as possible with limited impact on its performance. Since the protection system measures radiation levels, it is also essential to monitor beam losses and correlate them with SuperKEKB parameters. The radiation system must operate smoothly and without severe performance degradation throughout Belle II lifetime: as the SuperKEKB parameters are optimised to achieve high luminosities, the radiation system will continue to be fundamental.

Primary requirements for radiation-monitor detectors are:

- to rapidly measure sudden intense radiation bursts so as to allow immediate countermeasures;
- to reliably measure integrated radiation dose for long-term studies of detector degradation;

- to be radiation resistant;
- to contribute low additional material in the detector volume, in order not to interfere excessively with the particle-reconstruction performance.

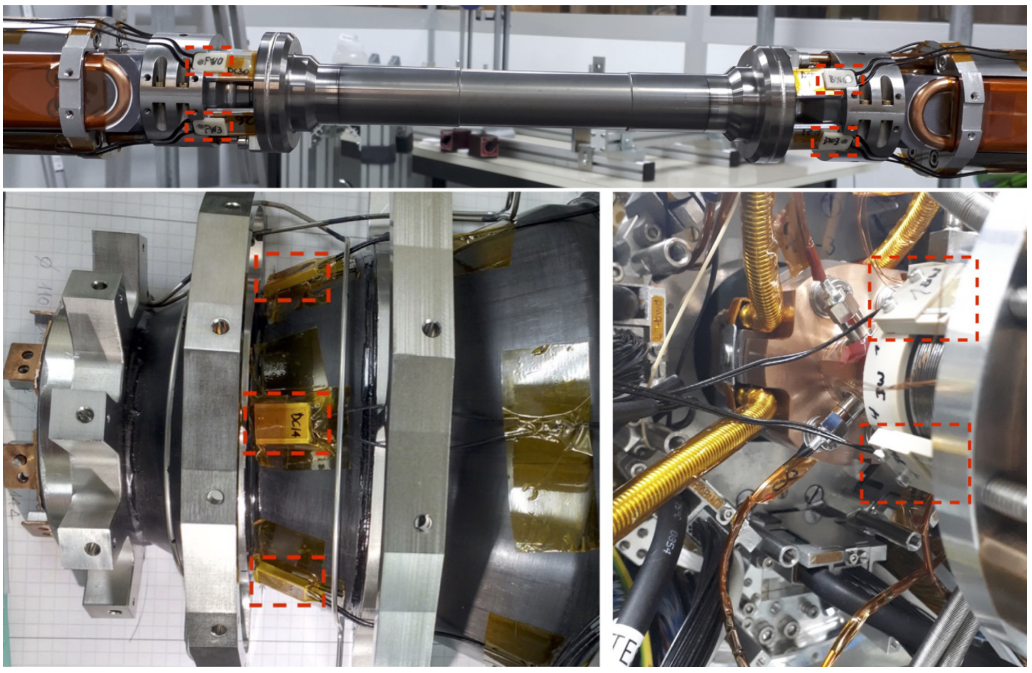

Figure 3.1: Photographs of diamond detectors (red dashed boxes) mounted on the beam pipe (top), on the backward SVD support cone (bottom left), and on the bellows close to the backward QCS (bottom right)

The Belle II radiation monitoring and beam abort system consists of 28 diamond detectors, 8 mounted on the beam pipe (BP) near the interaction point (IP), 12 on the SVD support cones, and 8 on the so called "QCS bellows" near the QCS magnets, which join the beam pipe to the accelerator rings, as shown in Figure 3.1. Figure 3.2 shows the location of the installed diamonds in the Belle II detector.

The original plan for the radiation system consisted on 20 sensors. After the accelerator pilot run in 2018, on request of SuperKEKB, eight more diamonds were installed on the QCS bellows. In these positions, they help protecting the QCS magnets from quenches in case of large beam losses, thus extending the original purpose of the system. The system was installed in 2018 and has been in operation since then. It serves for both physics data acquisition (*Phase 3 run 1*) with the complete Belle II apparatus and for any beam-related activity on the SuperKEKB accelerator.

3.1.1 Diamond detectors for radiation monitoring

Over the past few decades, various detectors have been developed for radiation monitoring and beam loss detection at accelerator facilities. Gas ionisation chambers are the most commonly employed instruments, especially in areas where there is sufficient space without interfering with the experimental apparatus, such as along the accelerator ring. Closer to the interaction region, where space is limited and the amount of material should be minimised, silicon PiN diodes have often been used [44–46]. However, these sensors have some serious drawbacks: their reverse bias current, which measures the instantaneous radiation

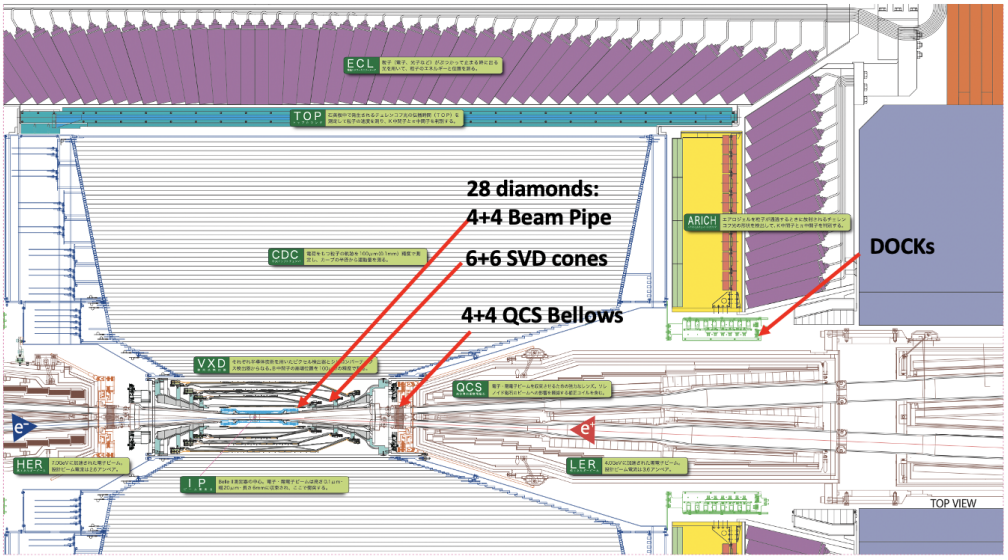

Figure 3.2: Part of the longitudinal section of the Belle II detector, with the positions of the 28 diamond detectors composing the Belle II radiation monitor system. Also the location of the DOCKs is shown.

dose rate, is highly temperature dependent. The dark leakage current rises unceasingly as radiation damage accumulates with the integrated dose and it can be measured only in the absence of radiation. As a result, they require frequent re-calibration and subtraction of a dominant dark leakage term, introducing large systematic errors.

Belle II chose diamond sensors [47, 48] as radiation monitors because of their superior performance in harsh radiation environment over competing technologies, such as the silicon PiN diodes mentioned above. Table 3.1 shows a comparison between the main properties of diamond and silicon: high purity diamond crystals can be considered as a "wide-gap intrinsic semiconductor" with interesting properties compared to silicon.

Property	Diamond	Silicon
Number of atoms density N [10^{22} cm^{-3}]	17.7	5.0
Mass density ρ [g cm^{-3}]	3.53	2.33
Band gap E_g [eV]	5.47	1.12
Resistivity ρ_c [Ω cm]	$> 10^{12}$	2.3×10^5
Electron mobility μ_e [cm^2 V^{-1} s^{-1}]	1800	1350
Hole mobility μ_h [cm^2 V^{-1} s^{-1}]	1200	480
Electron saturation velocity v_e^s [10^6 cm s^{-1}]	26	10
Hole saturation velocity v_h^s [10^6 cm s^{-1}	16	7
Thermal conductivity k [W cm^{-1} K $^{-1}$]	21.9	1.5
Energy to create e-h pair $\epsilon_{e/h}$ [eV]	13	3.6
Displacement energy E_d [eV/atom]	42	15

Table 3.1: Comparison between diamond and silicon main properties at T=300K.

The high displacement energy and extreme thermal conductivity ensure the radiation resistance and negligible temperature dependence of diamond sensors [49]. These properties are particularly suitable for operation in high radiation environments. A description of radiation damage in silicon and other semiconductors is given in Section 2.2. Diamond detectors are considered to be more radiation tolerant than silicon detectors due to their higher displacement energy of $\sim 42\,\text{eV}$, making the creation of a defect less likely [50]. It is expected to be several times more radiation tolerant against protons up to several MeV, and an order of magnitude more tolerant above several hundred MeV. In addition, the NIEL for neutrons is expected to be lower by more than an order of magnitude due to reduced damage from recoil atoms and fission fragments due to the light element composition. The amount of defects created by radiation damage reduces the mobility and lifetime of the charge carriers, and hence the charge collection efficiency.

The large bandgap allows operation with low leakage current. The high thermal conductivity makes diamond an interesting material for applications where active detector cooling is impractical, such as in the confined volumes around the interaction regions of collider experiments. The high carrier mobility allows fast signal collection. Despite these very interesting properties, the widespread use of diamond for large area applications in tracking devices has been limited by the costs of producing high quality crystals, the difficulty of making them available on large wafers and by the availability of mature detector technology based on silicon wafers with microstrip or pixel electrodes [51, 52]. The ratio of cost to sensor area is much higher for diamond detectors than for silicon. The size of single crystal diamond wafers is also limited to a few cm^2, which limits the range of applications. One of the most effective techniques developed to grow detector-quality diamond crystals is chemical vapour deposition [53] (CVD), which is also used to grow the diamonds used for Belle II.

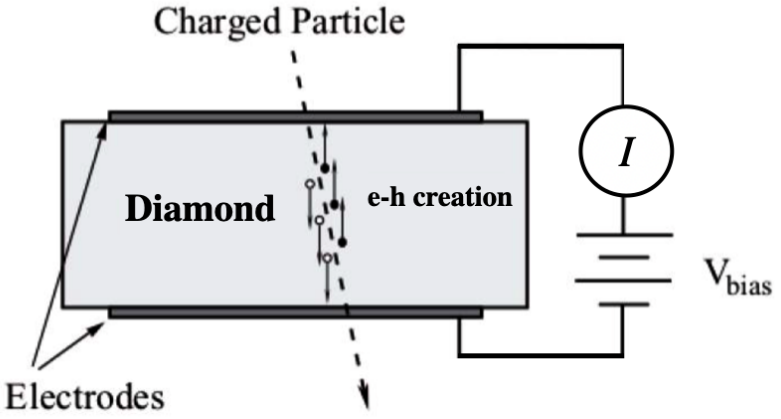

Figure 3.3: Schematic layout of a diamond sensor. The charge carriers produced by an impinging charged particle are collected by applying an external electric field via a bias voltage V_{bias}. The induced current is read by a picoammeter in the readout circuit.

Figure 3.3 outlines the mechanism of charged-particle detection by diamond sensors with a planar geometry. The energy released in the diamond bulk by an impinging charged particle produces pairs of charge carriers, electrons (e) and holes (h), through ionisation. The same mechanism is present in semiconductor materials, where an electron is promoted from the valence band to the conduction band after absorbing enough energy. This transition generates two oppositely charge carriers, an electron in the conduction band and

a hole in the valence band [54]. The energy needed for the promotion from a lower to a higher band depends on the forbidden energy gap that separates the two bands and on the fraction of transferred energy that excites other degrees of freedom. Electrons and holes are then collected by applying an external electric field in which the charge carriers drift in opposite directions. The electric field in the diamond bulk is generated by applying to the metallic contacts a bias voltage V_{bias} from few to hundred volts. The drift of charges inside the diamond bulk induces a current that is read by an external picoammeter.

Diamond detectors also have the capability to detect neutral particles, such as photons and neutrons. However, the probability of detecting a neutron is relatively low due to the small volume of the diamond and the limited material within the diamond sensor. Additionally, the diamond detectors used in the Belle II radiation monitor cannot distinguish between neutral and charged-particle interactions.

A detailed description of the diamond detectors employed in the radiation monitor and the characterisation procedure performed for each detector is given in Chapter 4. To use these detectors as dosimeters, the current measured with the diamond detector must be converted into a dose rate, making the current-to-dose rate calibration a pivotal aspect.

3.1.2 Diamond radiation monitor and beam abort system

The diamond radiation monitoring system is part of a broader set of systems used to monitor the environmental conditions within the vertex detector volume. The main goal of the diamond system is to monitor the radiation near the interaction point and to trigger protective actions if radiation rates exceed the safety thresholds. The system can operate in two ways.

Continuous radiation monitoring at 10 Hz: the dose rate collected by the diamond sensors is read and archived with a 10 Hz sampling frequency. The radiation level (instantaneous dose rate) is made available online and used as a reference for the beam background during accelerator-tuning operations, such as collimator adjustments and beam-optic tuning. The decision to power the inner sub-detector is also based on diamond dose-rate measurements. The archived dose rates are also used to estimate the total integrated doses absorbed by the silicon detectors (offline analysis).

Beam abort request with 2.5 μs granularity: the diamond system aborts the beams if the radiation level near the interaction point exceeds a programmable threshold. This functionality uses data readout at 400 kHz. In the initial design it was set to 100 kHz to match the beam revolution frequency, but later at the end of 2019 it was increased to 400 kHz to have a faster beam abort cycle of 2.5 μs. If a potentially damaging beam-loss is detected, the abort signal is generated within one quarter of a beam revolution period (10 μs). Each threshold is determined by two values: the integration interval, which identifies the time gate for data collection, and the threshold value, which is the mean dose-rate threshold beyond which an abort request is generated.The threshold values are adjusted empirically, taking into account the specific requirements of the Belle II sub-detectors and striving to minimize any potential interference with the normal operations of the accelerator.

The comparison between the dose-rate measured and the threshold is performed within a running window that has a gate equal to the integration interval. Every 2.5 μs a new value is added to the running window and the oldest value is subtracted. Another parameter relevant for the abort configuration is the sensor multiplicity: it establishes the minimum fraction of diamond sensors that have to yield a signal over threshold to generate an abort

request. Figure 3.4 shows the on-line display of dose rates measured by diamonds used by both Belle II and SuperKEKB operators.

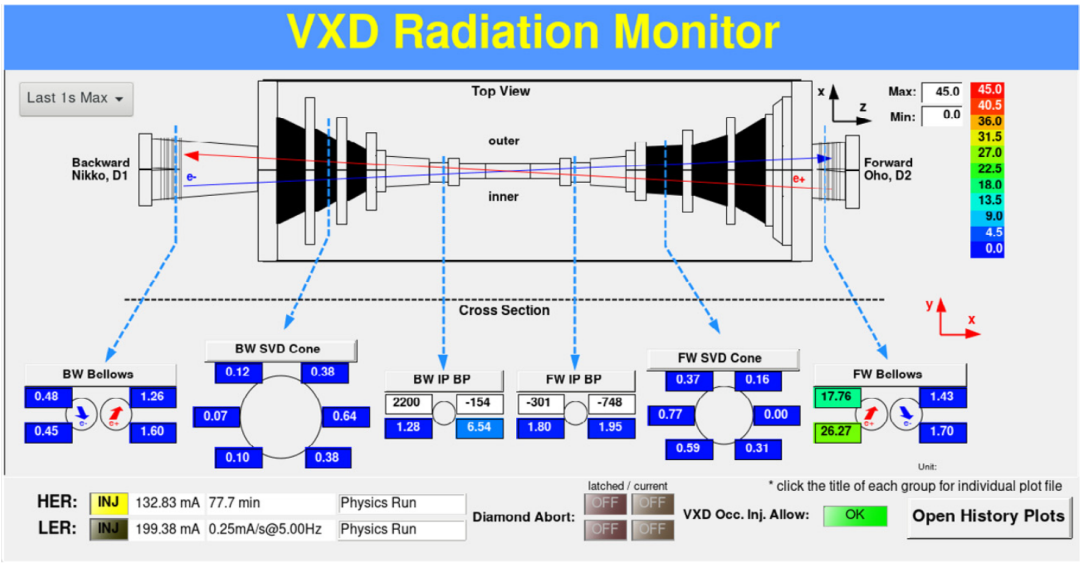

Figure 3.4: Sketch of the location of the 28 diamond detectors on the beam pipe, the SVD support cones, and the beam pipe bellows and their monitored dose rates, as shown by the on-line display of dose rates. This panel is available both to Belle II and SuperKEKB operators.

3.1.3 Diamond Control Unit

The 28 diamond detectors are controlled by seven diamond control units (DCU). Each DCU pilots four diamond detectors as sketched in the block diagram of Figure 3.5 .

The digital core is a board hosting a Cyclone V FPGA by Intel [55], which receives commands via an Ethernet interface, drives four HV modules independently through a DAC, and accepts input data from an analogue module with amplifiers and ADC conversion. The DCU is also able to deliver VXD abort requests separately for the electron higher-energy ring (HER) and the positron lower-energy ring (LER), and receives the SuperKEKB abort signals. The HV modules EMCO CA10 [56] provide positive bias voltages range from 0 to 1 kV with a maximum output current of 1 mA.

The diamond currents are amplified by transimpedance amplifiers, digitised by a 16-bit ADC [57] at 50 Msamples/s, and processed by FPGAs in the DCUs. The FPGA firmware stores sums of 125 ADC samples every 2.5 μs at 400 kHz in a large revolving buffer memory. Further sums of five million ADC values can be read out at 10 Hz. The online control software converts these values from ADC to dose-rate units after subtracting pedestals; these data are archived and used for continuous monitoring. From the archived values, accompanied by time stamps, integrated doses are computed. Three amplifier gain values can be selected by resistors in the feedback loop of the front-end operational amplifier [58], to provide three different current measurement ranges: 36 nA, 9 μA, and 4.5 mA, which are called range 0, 1 and 2 respetively. The first range allows precise monitoring of relatively small beam losses, while the third range avoids saturation in the detection of large radiation spikes, and is used for beam abort. The intermediate range may be used for background and injection studies, both at 10 Hz and 400 kHz, and also in the future, with increasing dose rates.

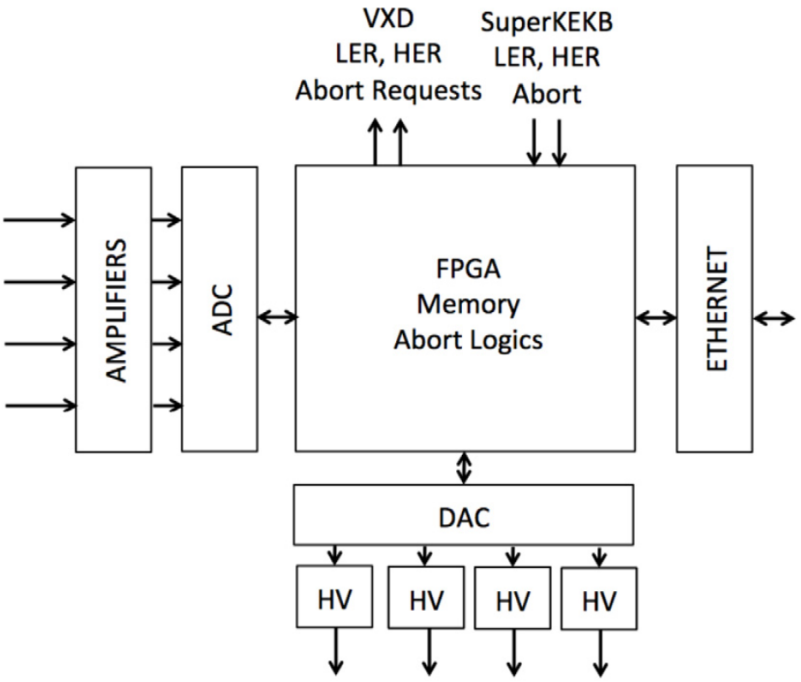

Figure 3.5: Diamond control unit (DCU) block diagram. Arrows on the left side indicate currents from diamond sensors.

For each diamond detector, two moving sums of 400 kHz data are computed by the DCU firmware. The moving sums are updated at each 2.5 μs cycle, by subtracting the oldest added value and adding the newest one. The two moving sums, representing integrated doses, are compared with programmable thresholds. If a moving sum exceeds the corresponding programmed dose threshold, a logical signal is generated; in total, eight signals are available per DCU, two for each diamond detector. The resulting eight logical signals can be combined using programmable logic to produce an abort request, if the DCU is enabled to do so. In the present configuration of seven DCUs connected to the 28 detectors, only one DCU, controlling four detectors located on the beam pipe, is enabled to deliver abort requests. Individual masks can be applied to exclude noisy channels, if needed. “Abort request" signals are generated separately for LER and HER then sent to SuperKEKB, when a programmed minimum number of unmasked signals above threshold is reached. When the abort kicker magnets complete an abort that either originated from this system or from other sources, two "SuperKEKB abort" timing signals (HER and/or LER) are broadcast and received by the DCUs. These signals stop the buffer memory writing. The 400 kHz data can then be read out and used for a "post-abort" analysis of the beam losses preceding the abort.

In the default configuration during *Phase 3 run 1*, 24 diamond detectors were dedicated to monitoring at 10 Hz, and the corresponding DCUs preset on the most sensitive current measurement range 0. Four detectors mounted on the beam pipe were dedicated for the abort function, with range 2 selected in the corresponding DCU. Occasionally one of the DCUs that reads 4 QCS bellows diamond detectors was set to range 1 or 2 respectively for injection background or large beam losses studies.

Saturation effects in continuous injection

During standard operation the current measured with the diamond detectors is of the order of $0.1-10$ nA, which corresponds to a dose rate of about $3.5-350$ mrad/s. In the continuous injection mode of SuperKEKB, the intensities of the circulating beam bunches are topped up repeatedly over short time intervals, at a frequency of up to 25 Hz. Immediately after each injection, beam losses in the interaction region grow until the beam oscillations due to the injection perturbation are dumped away. As a result, beam losses and diamond detector signals vary in time; a significant part of the radiation dose is delivered during short time intervals, typically $100 - 200\,\mu$s, adding up to a few μA per second, *i.e.* above range 0 upper limit current, depending on the specific injection pattern and frequency. The dose-rate monitor at 10 Hz and the total dose computation are based on digital sums of the 50 MHz ADC data over 100 ms time intervals. If saturation of the current signals occurs in range 0 over much shorter time intervals, it becomes partially hidden by averaging in 10 Hz data, leading to an underestimate of radiation dose rates and integrated doses. This observation suggests to switch to range 1 for some DCUs in future operations, to avoid saturation at higher beam currents; an upgrade of the electronics towards expanding the dynamic range is also considered in the long term [59].

3.2 VXD environmental monitoring

In addition to the radiation monitoring system, the VXD employs an environmental monitoring system, which allows to safely operate the detector. The system is designed to measure environmental parameters such as temperature and humidity.

The power dissipation by the PXD DEPFETs and their front-end electronics amount to about 18 W per module, 360 W in total expected for the 20 modules of full PXD. On the other hand, the SVD front-end chips consume in total about 700 W in full operation. While the PXD has not a cooling system on the sensors, it uses the nitrogen used to establish the dry volume to blow the heat outward, the SVD detector has a cooling system based on heat exchange with a dual-phase CO_2 fluid at a temperature of $[-30\,^\circ\text{C}, -20\,^\circ\text{C}]$ circulating in thin pipes with good thermal contact with the heat dissipation sources. To prevent condensation or ice formation on parts of the SVD cooling system, the whole volume of the PXD/SVD is kept dry by a flux of nitrogen.

Both humidity and temperature are steadily monitored by the complementary systems described in Sections 3.2.1 and 3.2.2 respectively. Moreover, a hardwired interlock system has been implement, describer in Section 3.3, which protects both SVD and PXD by orderly shutdown their power supplies when local and general Belle II environmental conditions exceed acceptable limits. All readout instrumentation of the environmental monitoring system is located outside the Belle II detector in Electronic hut (E-hut), close to the detector, but accessible during operation.

All the values measured by the monitoring system are displayed on a dedicated monitoring panel, which is visible to the shift operators during normal operation. In addition to the hardwired interlock, the system has a software interlock that sends a warning alarm when values are in a critical zone. Figure 3.6 shows the monitoring panels for the temperature monitoring systems. Similar display panels are available also for the humidity monitoring system.

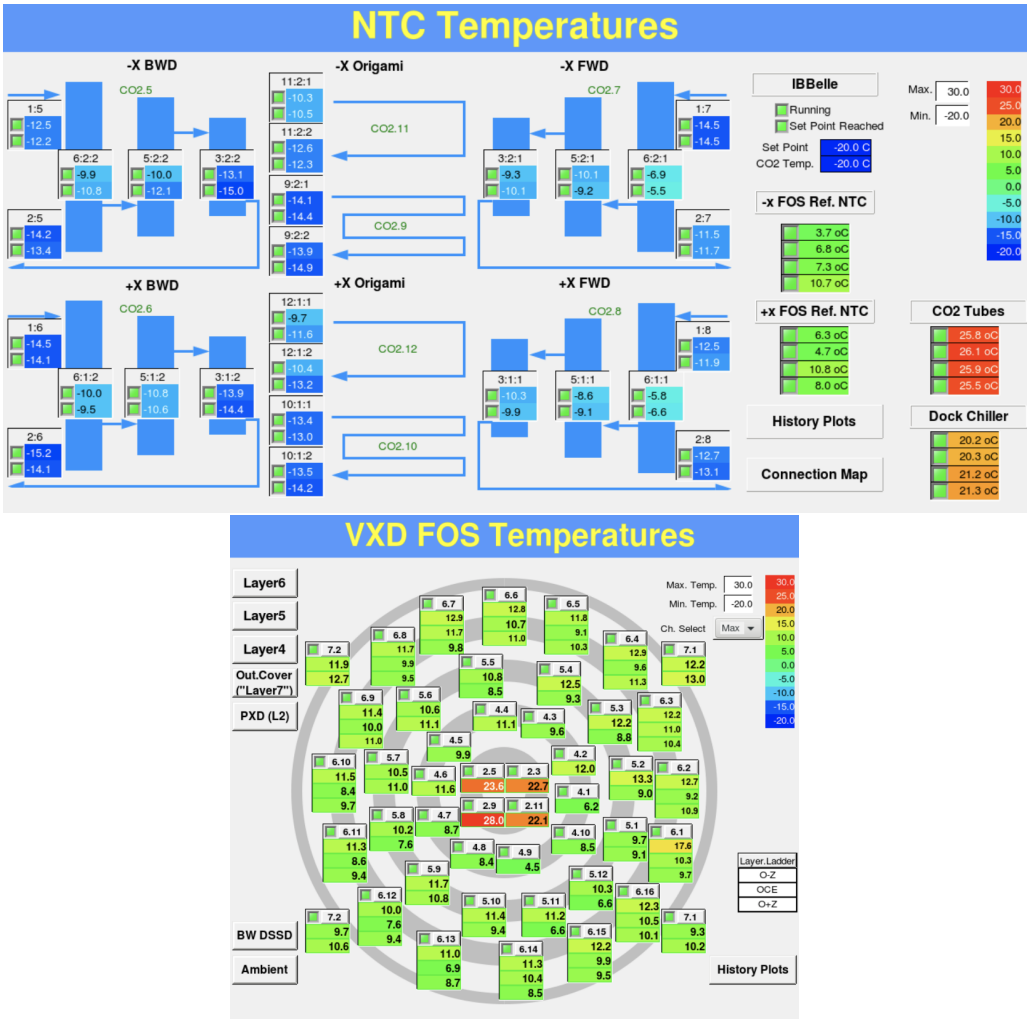

Figure 3.6: Monitoring panels of the environmental temperature monitoring system, accessible by the SVD shifters during the detector operation.

3.2.1 Temperature monitoring

Temperature monitoring is therefore important to ensure proper operation of the cooling system, with a required absolute accuracy of 1°C and a resolution of 0.1°C. It is composed of two subsystems. Temperature is monitored by Negative Temperature Coefficient (NTC) thermistors and by Bragg-type Fiber Optic Sensors (FOSs).

3.2.1.1 NTC system

The system consists of a total of 96 NTC sensors to monitor the temperature in several locations:

- 12 pairs of NTC thermistors are mounted on the outer surface of the SVD support end-rings (one sensor on each of the six half-rings), for FWD and BWD respectively;
- 16 pairs if sensors on the cooling pipes (one for each inlet and outlet);
- additional 20 pairs of sensors are installed on the CO2 transfer lines, in the docks chiller cooling system, and at cross-reference points with the FOS sensors.

The location of NTC installed of the end-rings and the cooling pipes is shown in the scheme of Figure 3.7.

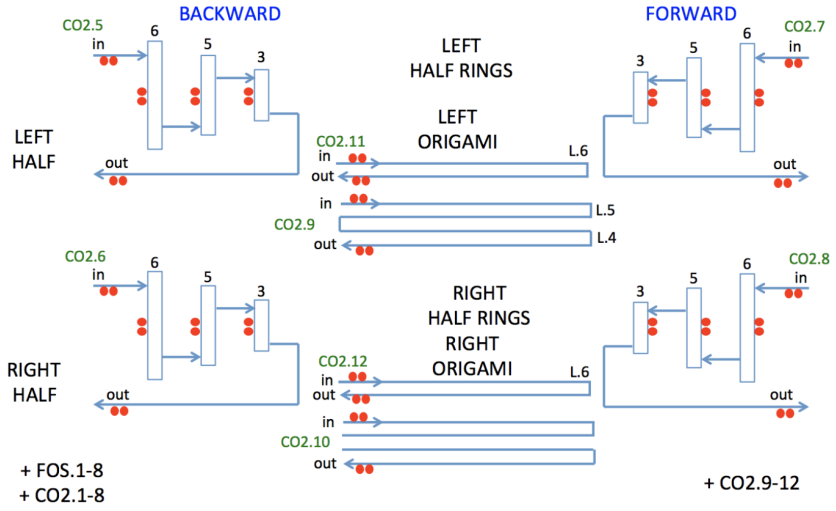

Figure 3.7: Physical layout of the NTC system installed on SVD: the red dot pairs represent NTC sensors placed on half end-rings and on the inlets and outlets of cooling pipes.

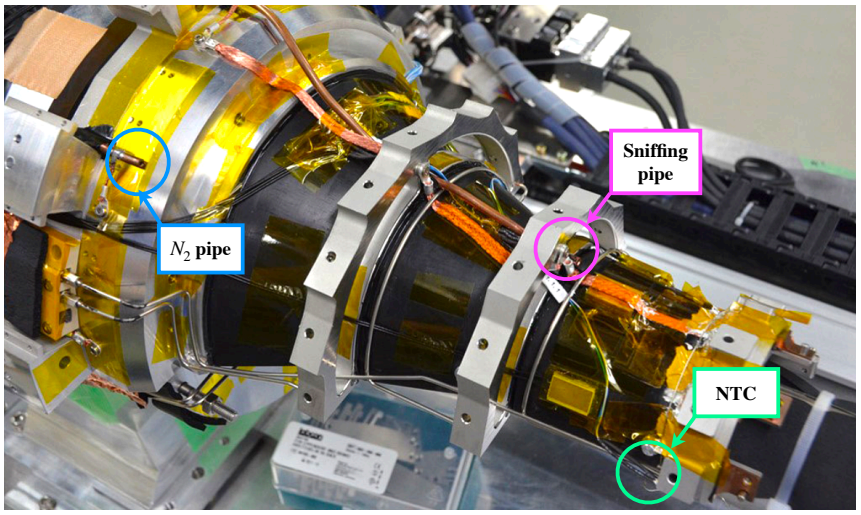

Figure 3.8: Picture of NTC, N_2 and sniffing pipes installed of the +x FWD half-cone of SVD.

Figure 3.8 shows an example of the installed NTCs on the +x FWD SVD end-ring.

The NTC thermistors used in the monitoring system, with 10 kΩ resistance at 20°C, are radiation-resistant and halogen-free [60] and have accuracy better than 1°C. They require only two wires per sensor, since their resistance can be chosen to be much higher than that of connecting cables. The readout of NTC sensors is performed by a custom-designed system, built by INFN Trieste, which is based on the Embedded Local Monitor Board (ELMB), designed and used in large numbers at CERN [61]. Each ELMB has an ADC multiplexed to 64 input channels: half measure the voltage drop across the NTC thermistors while the remaining are connected to reference resistors to optimise the accuracy. When the temperature surpasses a predefined threshold, established within comparators featur-

ing adjustable thresholds through trimmers, these signals trigger the hardware interlock system. The readout system consists of three motherboards with their ELMBs mounted together with power supplies, providing 96 input channels, and 12 interlock outputs in total. The main features of the NTC readout system are shown in Figure 3.9.

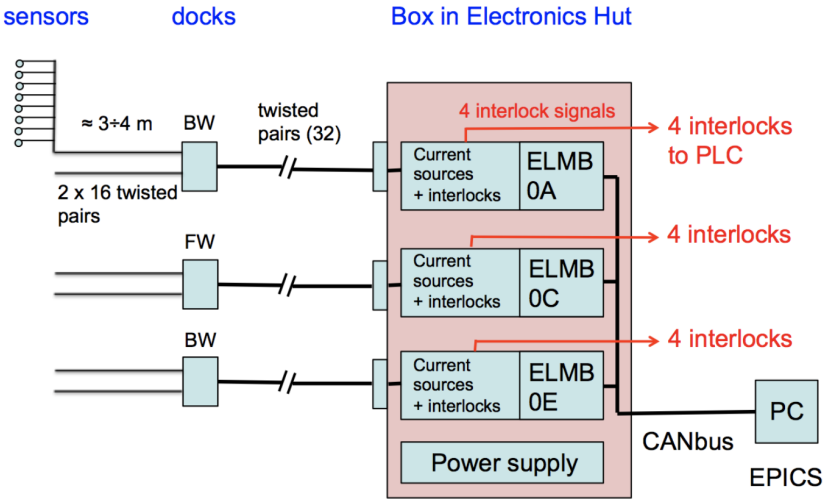

Figure 3.9: Block diagram of the NTC system readout: each readout unit accommodates one ELMB card and four interlock lines. The interlock signals are then sent to VLHI PLC (Section 3.3).

Halogen-free flat twisted-pair cables are used to connect the sensors to intermediate patch panels at the VXD DOCKs and finally to the readout unit in the E-hut. Two spare readout units were built and used in parallel during construction and commissioning: one for the ladder-mount setup and the other for the SVD commissioning setup. Since it's important to know the absolute value of the temperature, a conversion factor between the voltage drop and the temperature is needed. The calibration of the NTCs is obtained by measuring their resistance at -30°C, 10°C and 50°C, and fitting the Steinhart-Hart coefficients [62]. With this calibration an accuracy better than $\pm$ 1°C is obtained, which is sufficient for our purpose.

3.2.1.2 FOS system

Close to the SVD heat sources (the APV25 chips) the temperature is monitored with an accuracy better than 0.6°C by FOS, optical fibers equipped with sensors realised by Bragg gratings coated with temperature-sensitive acrylate [63]. The optical fibers are inserted in channels prepared in the Airex foam only for the SVD layers from 4 to 6. Each fiber has several 10 mm long sensors, whose position has been decided in order to be roughly in correspondence of the front-end chips on the origami boards (Section 2.1.3). Two more fibers, each with 4 temperature sensors, are glued on the SVD inner surface of the carbon fiber half cylinders that constitute the SVD outer cover. Figure 3.10 shows a picture of a fiber installed on one of the SVD L6 ladders.

Moreover four fibers are installed between PXD layer 2 and SVD layer 3, as shown in Figure 3.11. These fibers constitute the only temperature sensors for monitoring the PXD temperature. In LS1, the PXD fibres were replaced at the same time as the PXD2 was installed. Four new calibrated fibers were installed in the exact positions of the fibers previously placed on PXD.

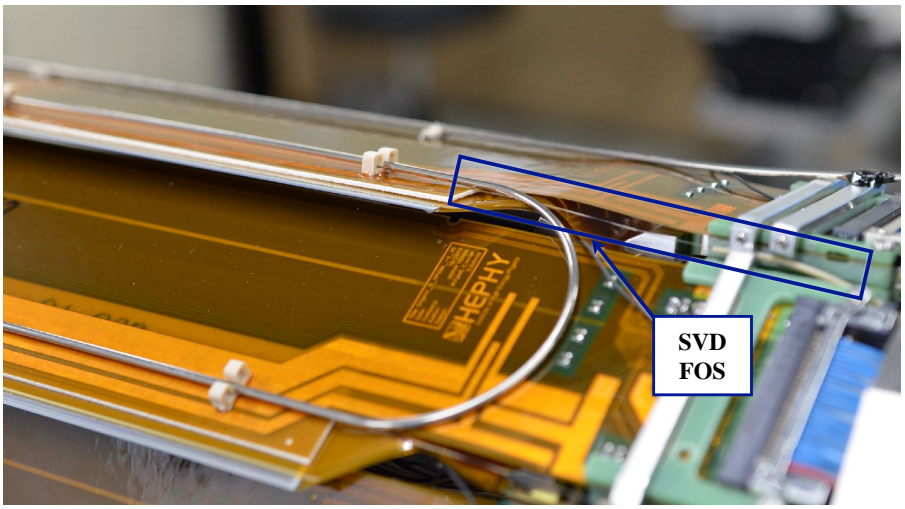

Figure 3.10: FOS installed on one of the SVD ladders of L6.

The external part of the fiber is protected by a peek tubing, which is radiation resistant and halogen-free. Each sensor on a fiber is made by a Fiber Bragg Grating (FBG) with a characteristic reflection wavelength, mechanically shifted by temperature-sensitive acrylate coating. By the measurement of shifts in reflection wavelength, it is possible to determine the temperature with an accuracy better than 0.6 °C. The system consists of 44 fibers with in total 260 sensors and a nominal wavelength at 20°C between 1522 and 1573 nm. Twelve sensor are distributed on PXD fibers, while the remaining 248 are on SVD layers and outer cover. The separation in nominal wavelength between contiguous FBG sensors is in steps of 3 nm. For the purpose of cross-calibration, a subset of eight fibers includes an additional sensor positioned outside the Airex foam channel, thermally coupled with an NTC thermistor.

The readout of FBG sensors uses an "optical sensing interrogator" [64], equipped with an integrated high-power, low-noise swept-wavelength laser. This interrogator is located in the E-hut and features a total of 16 input channels and an internal 4×4 passive multiplexer. Since the number of readable fibers exceeds this capacity, an external multiplexing solution is provided through the use of 16 1×4 splitter/coupler modules. To ensure efficient use of the available resources, the assignment of fibers to the external multiplexers and interrogator input channels is optimised to prevent any overlap of nominal FBG wavelengths at the same input. A schematic overview of the readout system for SVD fibers is depicted in Figure 3.12.

A dedicated analysis software [65] provides a comprehensive suite of tools for handling data acquisition, computation and analysis of optical sensor networks. This software is used for calibrations and debugging of the system. Also for the fibers an accurate calibration of the sensors is fundamental. Each FOS was calibrated in a climatic chamber by determining the coefficients of a polynomial fit to the measured temperature-wavelength relation. Additionally, numerous tests were conducted at different stages of the assembly, commissioning, and installation processes to ensure the system's reliability and accuracy.

The FOS system has no hardware interlock signal in output, but a software interlock has been implemented to prevent the temperature from exceeding predefined limits. The temperature trend over time is monitored from the shifter monitoring panel, allowing a direct comparison with the hybrid current trend of the SVD sensors.

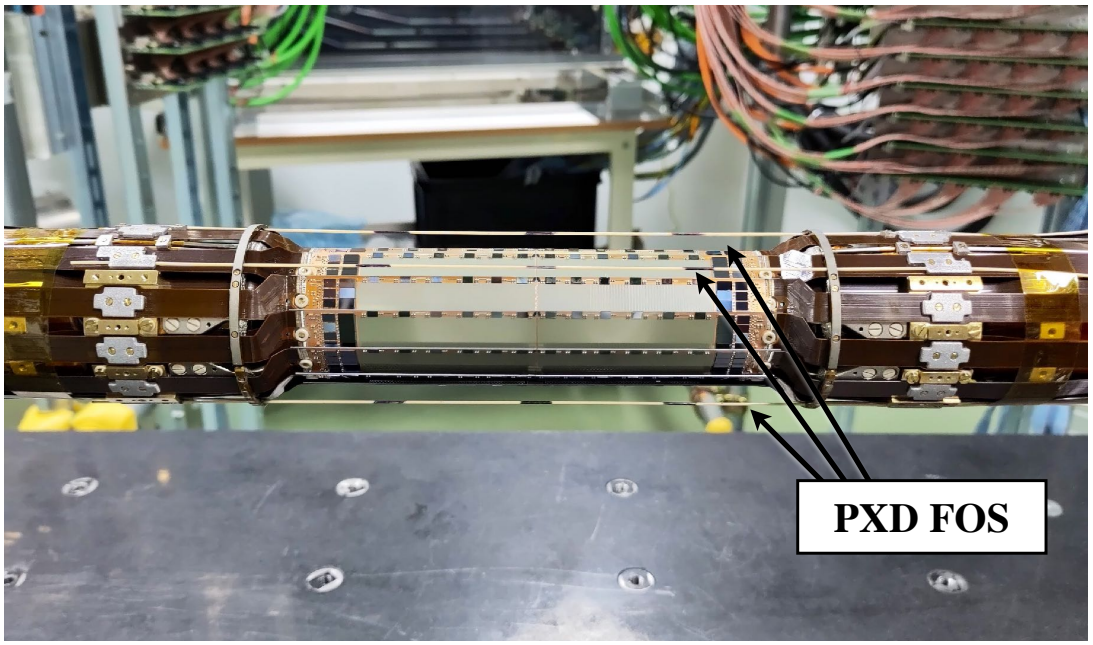

Figure 3.11: FOS installed between the Layer 2 and Layer3. The black marks on the fibers correspond to the position of the sensors. The fourth PXD fiber is situated on the other side of detector.

3.2.2 Humidity monitoring

To prevent condensation of water vapour and ice formation on the cooling pipes and other cold components, it is crucial to maintain an extremely low humidity level within the entire volume of the VXD. This is achieved by continuously flowing dry nitrogen throughout the VXD volume. The VXD volume is closed by the insertion of the QCSs, both forward (FWD) and backward (BWD), which have a sealing ring around the metal structure. The atmosphere inside the VXD volume needs to be kept at a dew point below -30°C. During the *Phase 3 run 1*, the measured dew point temperature was approximately -80°C. Due to radiation concerns, the miniature humidity sensors available on the market are not sufficiently radiation-hard to be installed inside the interaction region. Additionally, replacing these sensors during operation is not a practical option. Therefore, to monitor the dew point, samples of the circulating gas are steadily extracted from the VXD dry volumes and channelled to humidity monitor units located in the E-hut via copper pipes, so called sniffing pipes. Figure 3.8 shows an example of one of the copper pipes installed inside VXD inner volume.

In total four copper pipes were installed in the forward and backward sides of the inner and outer dry volumes of the VXD. The inner volume, called "cold" volume, corresponds to the volume inside VXD, closed by the outer cover. Instead the two outer volumes, called "warm" volumes, are the volumes inside the CDC cone, between the VXD end-ring and the ring of the DOCK boxes, respectively for FWD and BWD. Even if the inner cold volume is unique, two sniffing pipes, inserted on the forward and backward sides, are used for redundancy.

Figure 3.13 illustrates the configuration of the various lines and sensors within the humidity monitoring unit. There are four lines, and each of them is connected to a humidity measurement unit. Two electro-valves enable the connection of each fully equipped line to either the VXD dry volumes or a calibration gas source. These four lines converge into

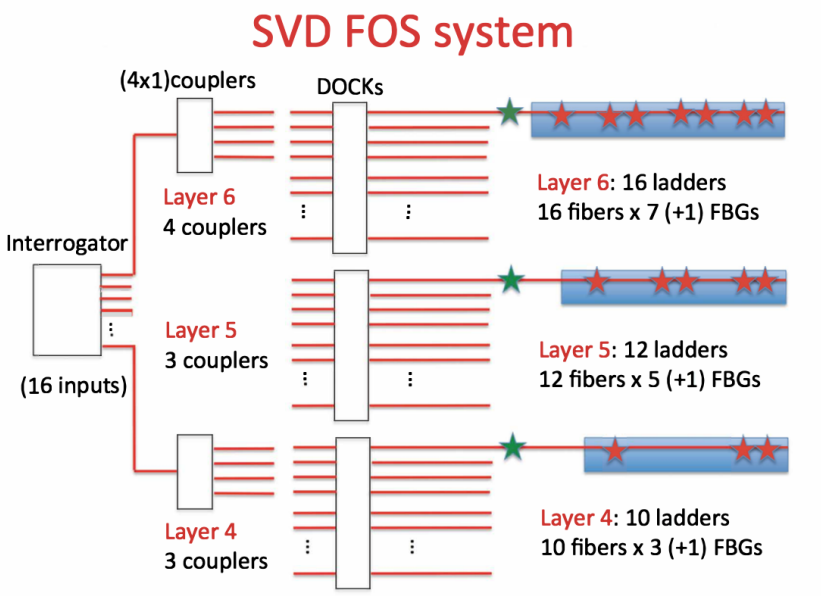

Figure 3.12: Readout scheme of FBG sensors for SVD: within layers 4, 5, and 6, each ladder accommodates one fiber, as indicated by the sensor count. These fibers are organised in groups of four, connected through (4×1) couplers to one of the 16 inputs on the interrogator.

a vacuum pump, allowing the extraction of gas from the dry volumes. The suction flow for each line can be precisely regulated using manual flow regulators and monitored using information from a mass flow meter. In terms of redundancy, an additional vacuum pump is included, and the switching of pumps is automatically controlled by motor protection switches. An alarm LED on the front panel serves as an indicator in case a pump switch occurs. The two remaining lines, which are not connected to the suction pump, are connected to a pressure transmitter. These lines are responsible for monitoring the pressures within the warm dry volumes.

The original system was equipped with miniature dew point transmitters, Vaisala DMT143 [66]. These transmitters are capable of measuring the dew point within a range from-80°C to +20°C with an accuracy of ±2°C in both air and nitrogen. Initially, they were well-suited to the expected dew point range of about -60°C to -70°C. However, it was discovered that the humidity levels were even lower, resulting in a dew point below -80°C. As a consequence, after a few months of operation, the sensors frequently entered a self-calibration state, leading to error conditions. Subsequently, these sensors were replaced with dew point transmitters Vaisala DMT152, which have a measurement range from -100°C to 0°C keeping the same level of accuracy.

The DMT152 provides both analog (4 - 20 mA signal) and digital (RS485) readout. The analog current outputs of the Vaisala sensors are connected to loop-powered seven-segment displays of type Nokeval 302 [67], which compare the measured values to a programmable range and provide two relay outputs for upper and lower alarms whenever the measured value is out of range. The range for these alarms can be configured separately for the four input lines and was selected based on the observed conditions during operation The alarm relays are directly connected to the VXD hardware interlock system. However, the sensors are also read out via the RS485 bus, and a USB interface is used to facilitate efficient data

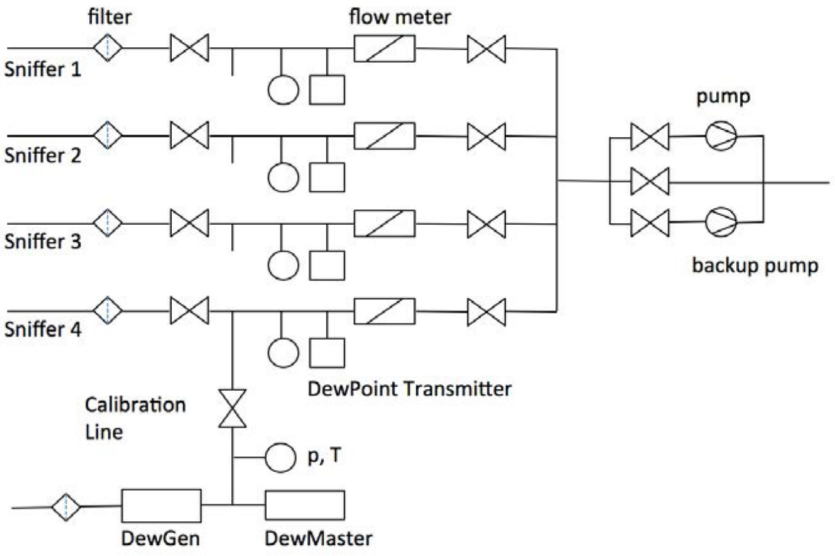

Figure 3.13: Schematic of the sniffing lines and sensors installed in the humidity monitoring system.

communication and sensor monitoring.

Figure 3.14: Humidity monitoring system installed in E-hut.

Furthermore, an extended system with enhanced redundancy for ensuring safe long-term operation was designed and constructed at INFN Trieste. I installed this system in parallel with the existing one during LS1, as shown in Figure 3.14. This new system includes an additional spare measurement line, bringing the total to five. Each line features redundant dew point measurements with two different sensors: the Alpha Moisture Systems Model AMT [68]with a range of -120°C to +20 °C and the Michell Systems Easydew [69] with a range of -110 °C to +20 °C. Mass-flow meters and pressure sensors are of the same type as those used in the original system. Each line is managed by a dedicated processor board, providing both USB and Ethernet readout for improved interfacing. Unlike the first

system, where the threshold can only be selected on the Nokeval panel, the new system allows the threshold to be defined in the firmware and can be remotely changed through a customised procedure.

3.3 VXD Hardwire Interlock system

A prompt shutdown of the PXD and SVD power supplies must be executed in response to various critical conditions, which are triggered by hardwired signals. These signals must operate independently of the control network and software.

An effective and widely adopted solution is to employ industry-standard programmable logic controllers (PLCs). PLCs offer reliability, programmability, and the flexibility to expand with both digital and analog input/output modules, handling various digital and analog input signals in order to make them adaptable to evolving interlock conditions.

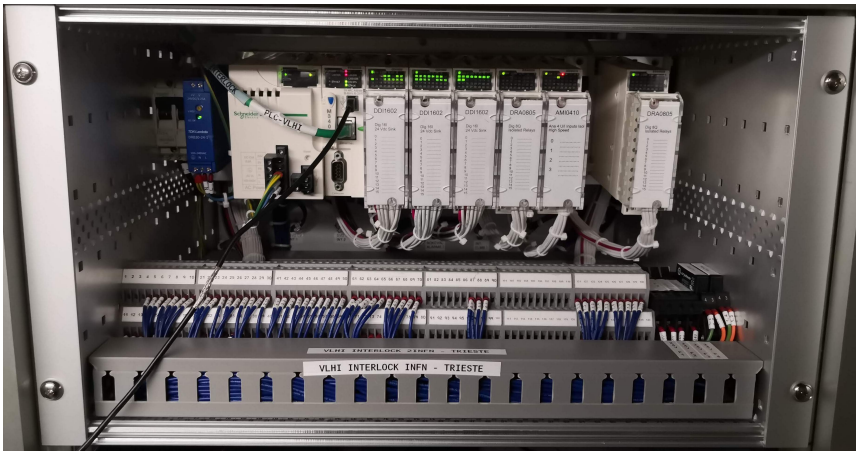

Figure 3.15: VLHI PLC installed in E-hut.

The VXD Local Hardwired Interlock (VLHI) is implemented using a Programmable Logical Controller (PLC), shown in Figure 3.16. VLHI uses PLC Modicon M340 from Schneider Electric [70], together with several analog and digital I/O modules which can be configured according to the specifications and are easily expandable to cope with future needs. While the digital I/O modules are discrete that send or receive an "enable" signal, the analog modules are 4-input industrial measurement devices, which perform monitoring, measurement, and continuous process control functions.

The VLHI system receives digital input signals and alarms from:

- 12 groups of NTC temperature sensors;
- 8 dew point sensors, 4 for each humidity system;
- the DOCK chiller (alarm in case of system malfunctioning);
- the waterleak monitoring system of the DOCK chiller;
- the paraffin cooling system of the beam pipe;
- the CO2 cooling system;
- the KEK beam control when there is a beam abort;

- the manual stop of the VXD operation;
- the central Belle II interlock system (solenoid, water leak, e-hut power, environmental monitors).

Under normal (non-interlock) conditions, each of these systems should provide "enable" currents to the corresponding PLC inputs (positive logic). The interlock condition ("disable": no current to the PLC input) is equivalent to a missing connection; in other terms, the system is a "default-OFF interlock". Furthermore, the system also receives two additional analog current signals from the DOCK chiller flow meters, specifically for the forward (FWD) and backward (BWD) cooling lines. These current signals, measured in milliamperes [mA], are then converted into flow rates [l/min] based on the flow meter specifications. Within the VLHI firmware, a threshold is defined to trigger an interlock when the flow falls below a predetermined value. Such a drop in flow could indicate a potential leak in the cooling system.

The firmware includes logic for generating interlock output signals when a disable signal is received from one of the aforementioned input sources. The following interlock output signals are activated based on combinations of the input signals:

- SVD low voltage (LV) and high voltage (HV) power supplies;
- PXD power supplies;
- SVD DOCK chiller;
- CO_2 cooling system;
- central Belle II interlock system.

Figure 3.16 displays the monitoring panel, illustrating all the input and output signals. In this representation, a red box indicates an interlock or disable state, while a green box signifies an enable state. This visual representation helps operators quickly identify the system's status and take necessary actions.

Two VLHI systems were assembled and the PLC programmed at INFN Trieste. A test box is used to simulate all the input signals with the agreed protocols and their electrical properties. The PLC firmware was thoroughly tested and debugged in the laboratory, before the shipment to KEK. All tests were then repeated for each input and output, in the VXD commissioning phase before the start of physics data taking. During my PhD, I focused on implementing the paraffin and dock chiller inputs in the VLHI firmware and hardware. This work was prompted by the SuperKEKB requirements to establish an interlock signal for the PXD power supplies and IBBelle related to the beam pipe cooling system, and the installation of a new DOCK chiller system during LS1.

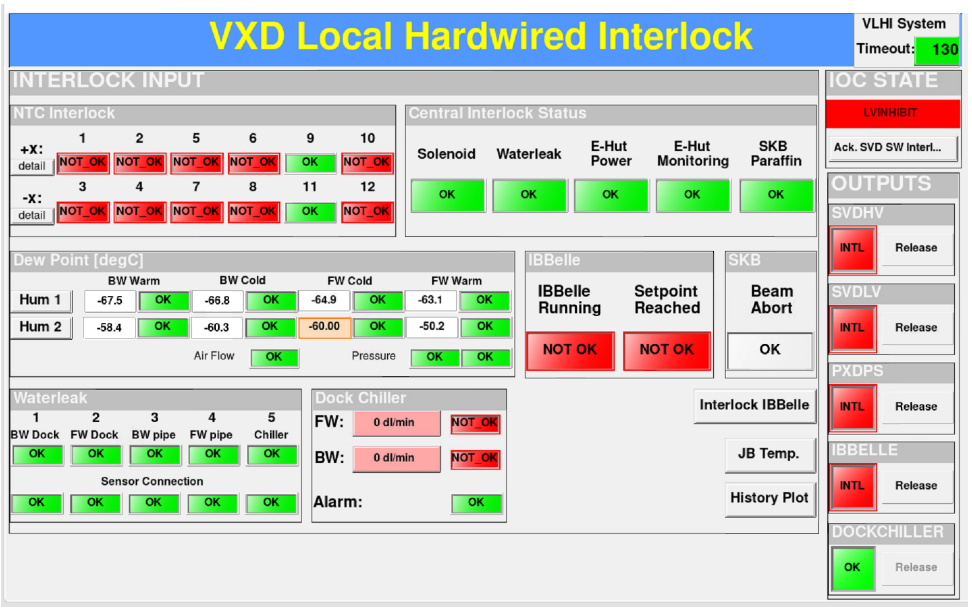

Figure 3.16: VLHI monitoring panel. The red "NOT_OK" boxes correspond to an interlock signal.

Chapter 4

Assembly, characterisation and installation of diamond detectors

This chapter describes assembly and characterisation of the diamond detector used in the Belle II radiation monitoring and beam abort system. I have assembled and tested ten diamond detectors which were installed in February 2023 on the new Belle II beam pipe, described in Section 2.3. The chapter contains a detailed description of the assembly, characterisation procedure and calibration performed with different radiation sources for each of the ten detectors. In Section 4.6 a summary of the characterisation results and the installation procedure of the diamond detectors on the new beam pipe are reported. I presented the work presented in this Chapter at the conference [71]. Furthermore, the characterisation procedure was published in the paper [72], and the performance of these detectors in both Phase 2 and Phase 3, Run 1, can be found in the paper [73].

4.1 Description of the sensor under study

Our sensors are based on $(4.5 \times 4.5 \times 0.5)$ mm^3 high-purity electronic grade sCVD diamond crystals from Element Six [74], with two $(4.0 \times 4.0)\,\mathrm{mm}^2$ electrodes on opposite faces, made of Ti+Pt+Au layers, (100+120+250) nm thick. The electrodes are processed by CIVIDEC [75], which performed several quality controls upon our tight specifications. The electrodes are radiation-resistantand can withstand temperatures up to 400°C. The sensors are mounted in radiation-hard multi-layer printed circuit boards (PCB) [76], as shown in Figure 4.1.

The *back*-side electrode is glued to a mounting pad of the PCB, while the $front$-side electrode is connected to the second pad by two ball-bonded gold wires. The outer gold layer on the electrodes facilitates wire bonding. Two miniature coaxial cables, each 2.5 m long, have their inner conductor soldered to the PCB pads, while the outer conductor is electrically and mechanically connected to the PCB by conductive glue. Finally, the package hosting the diamond sensor is shielded by an aluminium cover, shown in Figure 4.2, thinned to $240 \pm 5\mu$m in front of the sensor. A total of 20 aluminium covers were manufactured using a computer numerically controlled (CNC) milling machine. I assign a maximum systematic error of 5 μm to the measured thickness, taking into account the observed surface variations. A Kapton tape measuring $(12 \times 9), \mathrm{mm}^2$ is applied in the thinned section of the aluminium cover to prevent discharges between the wire bonds and the cover. Before installing the detectors on the new beam pipe, the cover was fixed with Kapton tape, as shown in Figure 4.2 (right), providing also the electrical isolation of the

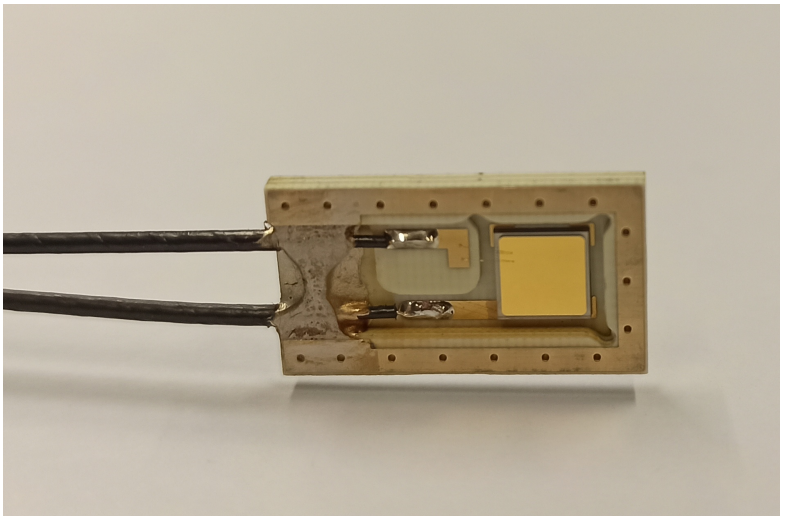

Figure 4.1: The diamond sensor is placed in a printed-circuit board (PCB) package, with the back-side electrode attached with conductive glue to a mounting pad and the front-side electrode connected to a smaller pad by two ball-bonded gold wires. Two miniature coaxial cables are soldered to the PCB pads for signal transmission and high voltage supply.

detector. A second set of tests was performed after fixing the cover on each sensor by Kapton tape, to complete the detector package.

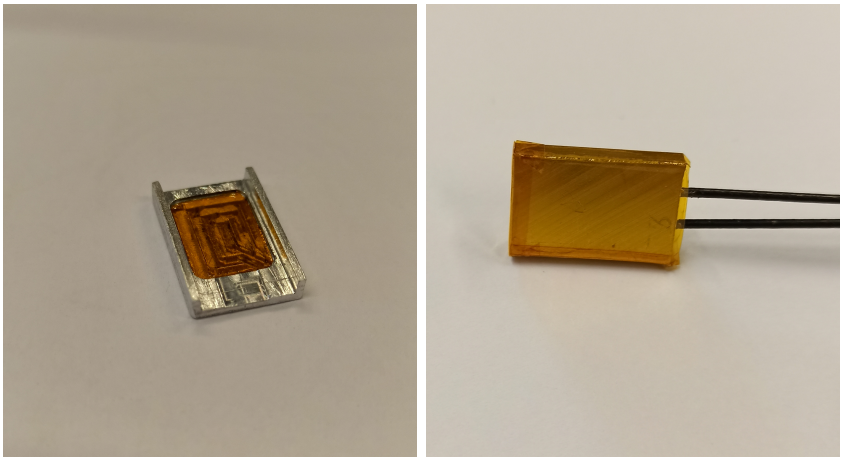

Figure 4.2: (left) The aluminium cover with a $(12 \times 9)\,\mathrm{mm}^2$ Kapton tape is placed in its thinned part. (right) I used Kapton tape to fix the aluminium cover on diamond PCB and give electrical isolation of the detector surface.

The sensor acts as solid-state ionisation chambers when a bias voltage is applied to the electrodes. The full volume of the diamond can be considered active in terms of energy deposition. The electron-hole pairs, created in the diamond bulk by the radiation, drift toward the electrodes and induce a current in the polarisation circuit.

4.2 New production of ten diamond detectors for LS1

From January 2021 to mid 2022, ten new diamond detectors have been assembled and tested to be used in the LS1 upgrade (see Section 2.3). A full characterisation of each detector was carried out using different radiation sources as described below. The results of the characterisation are also summarised in Section 4.6.

4.2.1 Assembly procedure and preliminary tests

Several steps are required to assemble the complete diamond detector in all its parts. First, two customized SMA connectors are assembled onto a 5 m long micro-coaxial cable [1], which will be used to bias the diamond detector and carry the output signal. The cable is tested by applying a bias of up to 800 V between the central conductor and the surrounding shield and measuring the current. The main aim is to ensure that there is no contact between the two and that a very good insulation is provided. The leakage current between the inner and outer conductors is typically much lower than 1 pA at the operating coltage of 100 V. It is also possible to determine the insulator resistance from the slope of the I-V curve, with typical values between 80 TΩ and 100 TΩ.

Following this test, the cable is divided into two equal 2.5 m-long segments, with one SMA connector retained for each part. The central conductors of the two wires are soldered to the left and right pads of the PCB, as shown in Figure 4.1. The two outer conductors are glued with conductive glue to the metallised ceramic-like package, which provides an electrical shield. The electrical connection is re-tested on the PBC after cable assembly to check for any contribution from leakage current through the detector package.

Before assembling the detectors, I measured the thickness of each diamond crystal using an optical microscope. The average thickness measured for the ten diamonds is $541.2 \pm 6.1 \mu$m and 9 out of 10 diamond thicknesses are consistent among each other withing 6 μm. Only one diamond has a thickness 9% lower than the other diamonds of the same sample. The average value is about 10% higher than the nominal thickness of 500 μm given by the manufacturer. The knowledge of thickness plays a crucial role in determining the properties of charged carriers, as explained in Section 4.3, and is essential for estimating the calibration factor. This is because the measured value is employed in the simulation of the device within FLUKA [77]. Furthermore, the thickness is a factor in the estimation of systematic uncertainty associated with the calibration procedure.

Then the diamond is mounted on the central pad of the ceramic-package with conductive epoxy glue, cured by heating it up to 80 °C for at least 3 hours. A pre-printed path on the package established the electrical connection between the back-side diamond electrode and the right-side cable. The electrical connection between the front-side electrode and the other cable is made by two ball bondings with a 25 μm diameter gold wire (two bondings for redundancy). These connections allow to apply a bias voltage across the diamond sensor, while measuring the output current.

For each detector I obtained the current-voltage characteristic, with the aim of measuring the currents in absence of radiation (*dark currents*) and so verifying that the signal current with irradiation is distinguishable from the noise current. The measurements are performed by applying a bias voltage up to 800V to one side electrode via the coaxial cable, while the other electrode is connected to ground. Both the currents flowing into and from the sensor are read. The test is performed in twice, providing a positive bias voltage to

[1] Miniature coaxial cable with polyimide insulation and 50 Ω impedance. Both the cable and the SMA connectors used on our detectors are halogen free, an essential requirement for safe operation in a high radiation environment.

the front-side or the back-side electrode, in order to detect possible differences in current flow, that can be tracked down to contributions by leakage current through the detector package or stray current through the diamond bulk.

Figure 4.3 shows the I-V curve obtained respectively applying the voltage to the front-side (top) and to the back-side (bottom) electrode.

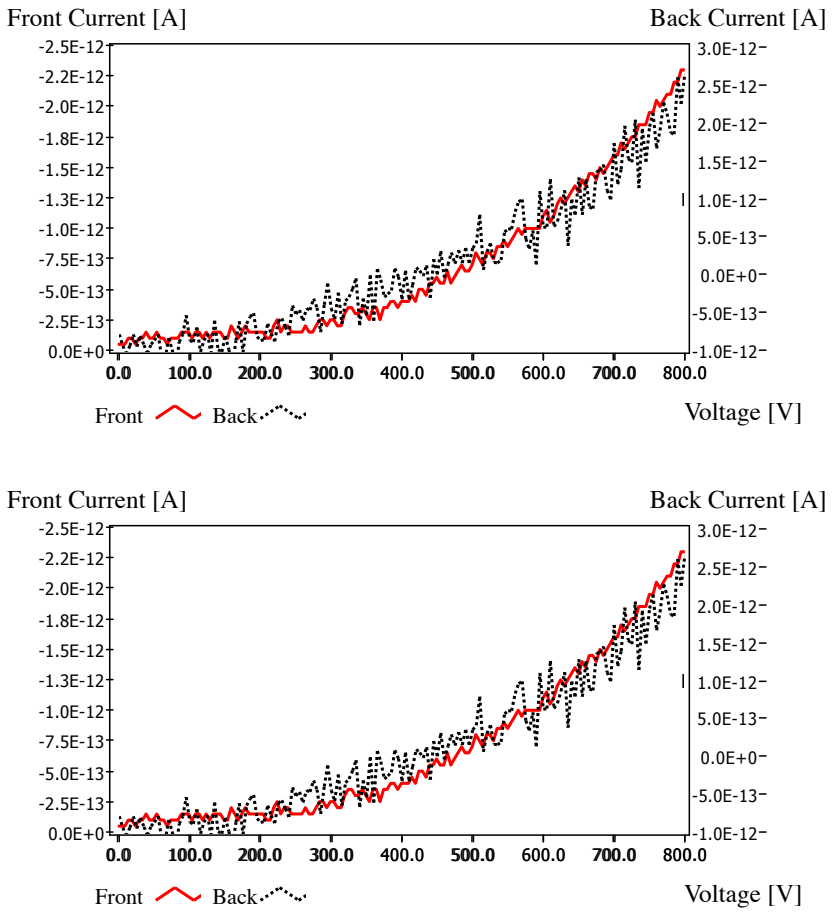

Figure 4.3: I-V characteristics with voltage applied to the front-side (top) and back-side (bottom) electrode. The red line shows the current read from the not biased side, while the dotted black line shows the current read from the same side where the bias voltage is applied.

The typical dark currents measured after the final assembly at 100 V are lower than 1 pA. This value is about three orders of magnitude lower than the current measured during β irradiation in Section 4.4, verifying a clear separation of the signal over the noise. When biasing the front contact, a difference in currents is observed; specifically, I_{front} is higher than I_{back}. The front electrode collects both the current that passes through the diamond (stray current) and the leakage current through the package while the back electrode collects only the current flowing through the diamond. In this way both leakage and stray currents can be estimated. When the front contact is biased, a current between the thin bond wires and the package through the air may be generated, increasing the total output current of the sensor. However, by inverting the polarisation, connecting the bond wires to ground,

no large current changes are usually seen, suggesting that the bond-wire-generated current is negligible. Repeating the same test with opposite polarisation shows a peculiar effect: the I-V characteristic is non-symmetric under polarisation swap.

Differently from silicon devices, which feature a clear orientation due to different doping types, CVD diamonds are expected to be symmetric, which is not observed in the majority our sensors. The observed asymmetry might be ascribed to the crystal growth direction, which is the only known effect that breaks the front-back symmetry of the system.

4.2.2 Characterisation procedure

From the experience of the previous diamond detectors production, we know that the response of diamond sensors may differ from sample to sample for several reasons, such as crystal imperfections from the CVD-growing process or the details of the electrode contact formation. The crystal imperfections can trap or recombine charge carriers generated by irradiation, affecting the charge-collection efficiency at a given bias voltage. In order to assess the main properties of each diamond sensor a suitable characterisation procedure using different radiation sources has been developed. The first part of the procedure, reported in section 4.3, aims at checking the transport properties of the charge carriers and determining the average ionisation energy needed to create an electron-hole pair. The goal is to evaluate the homogeneity of the sensor properties within our sample. In the second part of the procedure I study the stability of the sensor response under steady irradiation, both with β and X radiation, and I measure the current-to-dose-rate calibration factor, as described in section 4.4.3 and 4.5.2. Each part of the procedure is accompanied with a dedicated simulation of the experimental setup, based on the FLUKA software [77], in order to estimate the energy released by impinging radiation in the diamond bulk.

A silicon diode of $(5.0 \times 5.0 \times 0.45)$ mm^3 volume (see Figure 4.4), hosted in a package very similar to that of the diamond sensors, is used as a reference in all the parts of the characterisation.

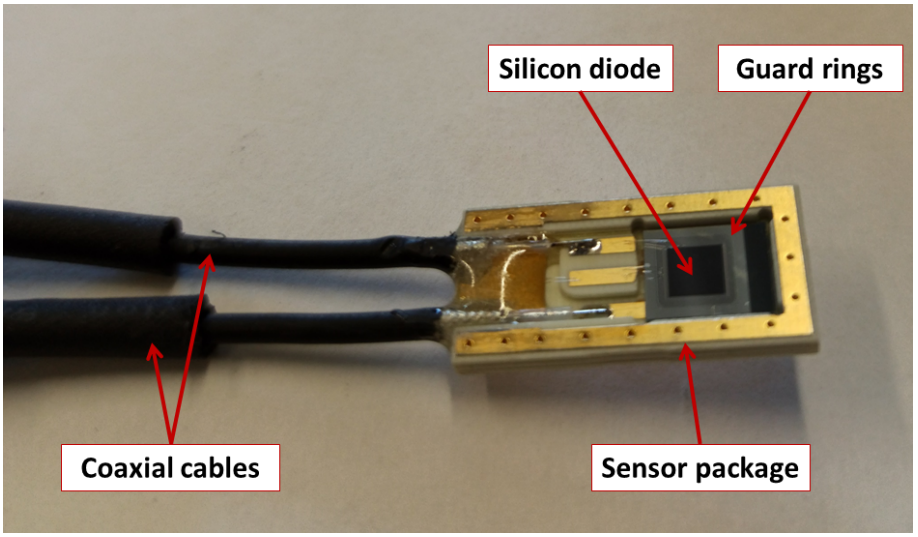

Figure 4.4: Reference silicon diode hosted on a package similar to the one of Fig. 4.1, and the coaxial cables connected to the diode electrodes.

The diode features an n bulk, with a p^+ layer obtained by Boron ion implantation on the front-side, and a n^+ layer for the ohmic contact on back-side. The square-shaped diode is fabricated on a substrate $25.0 \pm 0.1\,\mathrm{mm}^2$ wide and $0.455 \pm 0.010\,\mathrm{mm}$ thick. The diode is

closely surrounded by a p^+ guard ring which delimits the charge collection volume of the central diode, given by an effective area of $12.2 \pm 0.2\,mm^2$ and the depletion thickness. The silicon diode is used in reverse bias condition, applying a positive bias voltage to the n^+ contact, while both the p^+ and the guard rings are connected to ground. For bias voltages higher than 80 V, the diode is fully depleted and the active volume is given by the diode effective area and the substrate thickness.

4.2.3 Radiation sources used in the characterisation procedure

To characterise our detectors I used three different sources with complementary properties, studying each sensor response as a function of different source-detector parameters. In the following the three different sources and their properties are described.

^{241} Am α-source

This source consist of an Americium source with an activity of 5 kBq and a half-life of 432.2 years. The decay is

$$^{241}_{95}\mathrm{Am} \rightarrow ^{237}_{93}\mathrm{Np} + \alpha + \gamma\,. \tag{4.1}$$

The energy spectrum of the α radiation features five main monochromatic peaks within

Energy [MeV]	5.389	5.443	5.486	5.513	5.544
$\mathcal{BR}$ [%]	1.3	12.8	85.2	0.12	0.35

Table 4.1: Energies and branching ratios of the five main peaks of the α-particle from the $^{241}_{95}$Am decay.

155 MeV, whose values and branching fractions are reported in Table 4.1, with an average energy of 5.485 MeV. Since 5.5 MeV α particles have a range of about 15 μm in the diamond crystal, which is small compared to the 500 μm thickness of the sensor, all charge carriers are created close to the impinged surface. The experimental setup used to hold the source in front the detector and collimate the α particles in the centre of the diamond sensor is described in Section 4.3.1.

^{90} Sr β-source

The β source provides electrons from the chain of two subsequent decays

$$^{90}_{38}\mathrm{Sr} \rightarrow ^{90}_{39}\mathrm{Y} + e^- + \bar{\nu}_e\,, \tag{4.2}$$

$$^{90}_{39}\mathrm{Y} \rightarrow ^{90}_{40}\mathrm{Zr} + e^- + \bar{\nu}_e\,, \tag{4.3}$$

with a known energy spectrum, shown in Figure 4.5, up to about 2 MeV and a nominal activity of 3.2 MBq. Being the ^{90}Y half-life (2.7 days) much shorter than that of ^{90}Sr (28.79 years), the ^{90}Y decay rate is *in equilibrium* with its production rate.

Thus, the rate of β electrons emitted from the source is twice the ^{90}Sr activity. The source consists of an ion-exchange organic spherical bead, 1 mm in diameter, with radioactive nuclei uniformly distributed in the volume. The bead is mounted on top of a steel needle embedded in a Plexiglas container. Most of the electrons emitted at lower energy are self-absorbed in the organic bead.

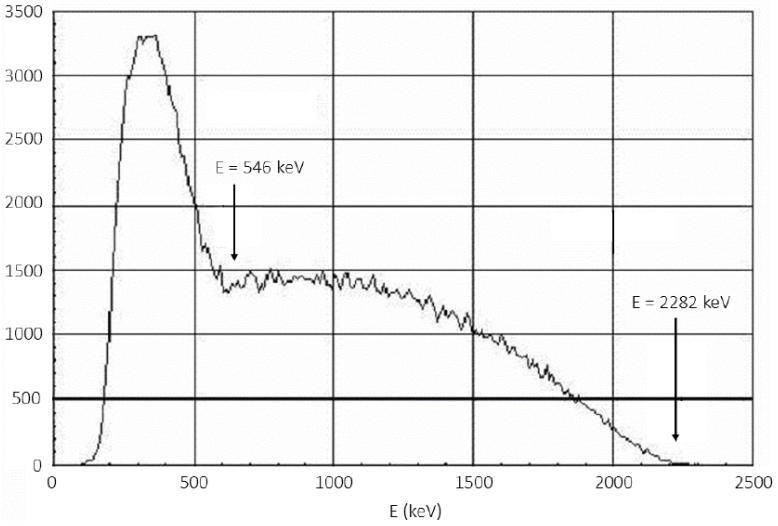

Figure 4.5: Energy spectrum of the emitted electrons from the ^{90}Sr β decay. The first branch of the decay has an energy of 546 keV, while the second branch has a decay energy of 2282 keV.

X-ray source

This source consists of an X-ray tube [78] which emits photons in an energy range from a few keV to 50 keV, by exploiting bremsstrahlung radiation emitted by electrons interacting with a 1.0 μm thick gold target. These electrons are emitted from a tungsten filament by thermionic effect generated with a current (I_{set}), and then accelerated by a voltage difference (V_{set}) between the filament and the gold target. Interacting with the target, electrons decelerate by the emission of bremsstrahlung X-rays in the direction of a berilium window.

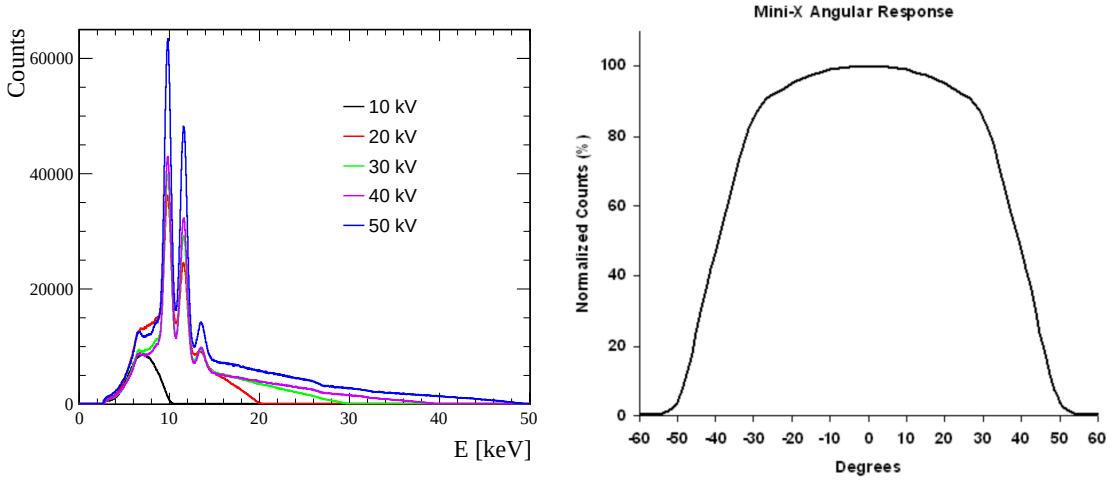

Figure 4.6: (left) X-rays energy spectra for the five voltages V_{set}, measured at a distance of 30 cm from the source in air. The peaks at about 10 keV, 11.5 keV and 13.5 keV correspond to the photon energies of the gold L-shell emission lines. (right) Angular response of the X-ray tube given by specification [78].

The emitted photons have an output spectrum which is the superposition of a continuous component due to the bremsstrahlung radiation and some peaks corresponding to the energy levels of gold atomic shells. The parameters V_{set} and I_{set} can be set via software, and correspond to different energy spectrum and photons flux respectively. Figure 4.6 shows the five energy spectra provided by the instrument, one for each voltage $V_{\text{set}} = \{10, 20, 30, 40, 50\}\,\text{kV}$, and the angular response. The emitted photon flux is almost constant in a cone of $\pm 30°$ centred on the symmetry axis of the tube. The experimental setup is described in Section 4.5.1.

4.3 Characterisation with α radiation

To study the properties of charge carriers in the diamond bulk, I used the transient current technique (TCT) [79]. This technique consists of measuring the shape of the current pulse induced by the carriers drifting under the applied electric field. Since the technique relies on the generation of charge carriers in a limited region of the sensor at a very small depth from the impinged surface, I used the monochromatic source of α particles described in Section 4.2.3, which generates electron-hole pairs very close ($\sim 12\,\mu\text{m}$) to the front electrode.

An uniform electric field is obtained inside the diamond bulk applying a bias voltage between the two electrodes. The current pulse is induced by the drift of charge carriers of one type, depending on the bias polarity, moving through the whole detector thickness to the back-side electrode, while charge carriers of the other type are almost immediately collected at the front-side electrode. As a result, the pulse duration equals the time employed by the selected charge carriers to traverse the detector, assuming an uniform electric field and a carrier lifetime longer than the transit time. From the pulse shape I determined the charge carrier transport properties, separately for electrons and holes.

4.3.1 Experimental setup

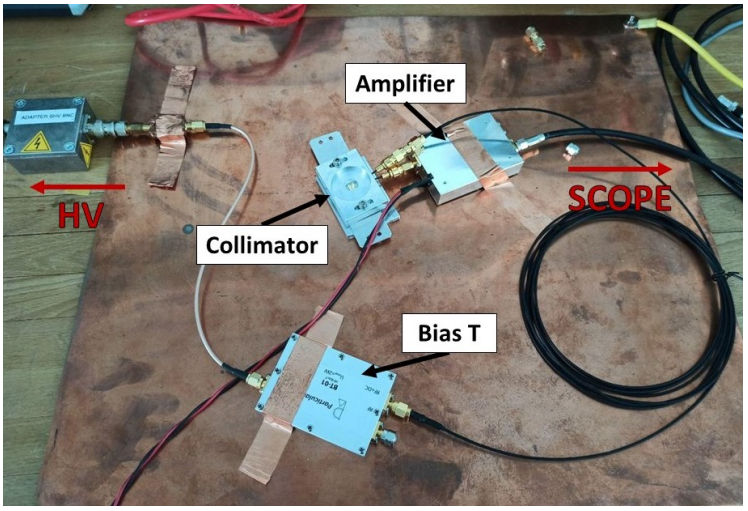

Figure 4.7: Experimental setup for the characterisation with the α radiation. The main components described in the text are identified.

The experimental setup, shown in Figure 4.7, consists of:

- an aluminium support equipped with a plexiglas collimator, which keeps a minimum distance of 3.7 mm between the source and the detector, collimating the α particles on the sensor surface;
- a CAEN DT1471ET [80] power supply, which can supply up to ± 5.5 kV with very low noise. For our measurements the bias voltage is limited in the range from -800 V to $+800$ V, which is the voltage regime used for our particle detectors. The HV is applied at the back-side contact. The other contact is connected to ground;
- a decoupling circuit that enables the connection of high voltage to the detector. This circuit consists of a low pass RC filter and a bias T [81]; the latter is connected directly to the 2.5 m detector cable;
- a current amplifier Particulars AM-02A [82], designed for the use in transient current systems, that amplifies the output current with a nominal gain of 53 dB at 3 GHz bandwidth. The amplifier input is connected to the front-side diamond cable. The nominal input and output impedance is $\sim 50\,\Omega$, matching with the $50\,\Omega$ impedance of the oscilloscope in order to reduce the reflections;
- a LeCroy WavePro 960 [83] digital oscilloscope, with 2 GHz analogue bandwidth at a digitisation rate of 16 GS/s. The scope samples, stores and displays the electric signal at the output of the current amplifier.

The electrical schematics of the set-up used for the measurements is shown in Fig. 4.8.

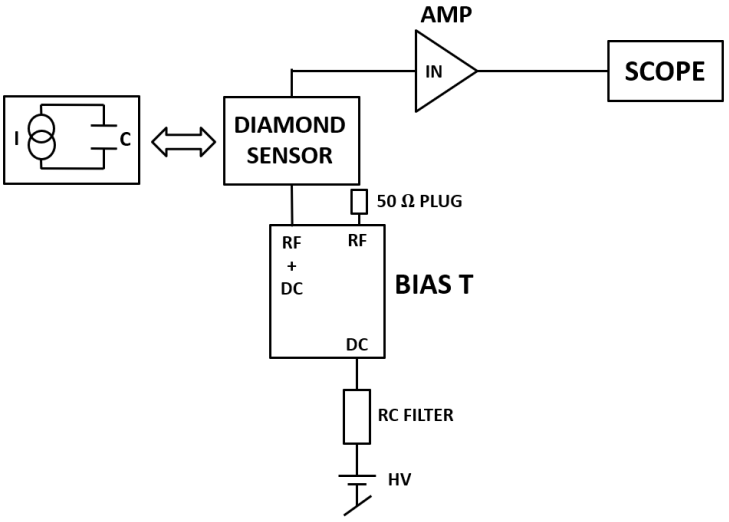

Figure 4.8: Schematic representation of the circuit used for the characterisation with the α radiation. The detector is sketched as a capacitance C and a current source I, the latter provided by the ionisation from the α radiation. The bias voltage is applied on the back-side of the diamond sensor using a bias T, connecting the other side to ground, while the output current is read from the front-side. The current is amplified and the signal is sent to the oscilloscope.

The aluminium support is designed to provide appropriate shielding and allow to position the α source at reproducible distance of 3.7 mm from the front electrode of the

diamond sensor, centred with respect to it. The α particles were collimated by a Plexiglas insert, 2 mm thick, with a circular hole of 1 mm diameter, so that they would hit the sensor well within the electrode area, in a region where edge effects on the electric field can be neglected. Figure 4.9 shows a transverse section of the setup.

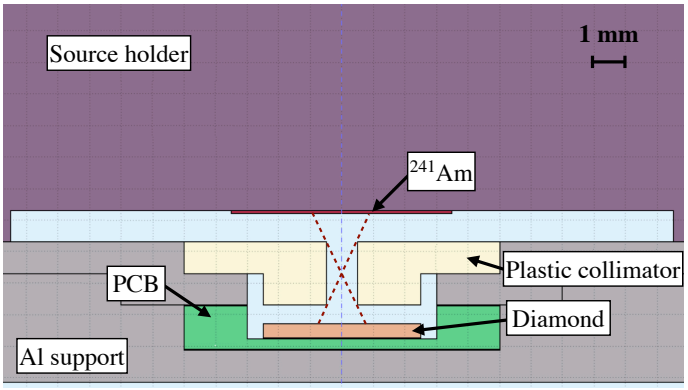

Figure 4.9: Schematic transverse section of the setup used to collimate the α particles on the detector for the TCT measurement. The ^{241}Am is deposited on a circular surface of 7 mm diameter. The red dashed lines show the maximum incident angles of the particle into the detector surface. The distance between the surface of ^{241}Am deposition and the detector is 3.7 mm.

Compared to previous versions, the support has been optimised to collimate the α well within the electrode area, and to minimise the source detector distance, minimising the energy loss by the particles in air.

4.3.2 Characterisation of the experimental setup

Since the induced signals in the sensor are characterised by a fast rise time of the order of 100 ps, the bandwidth of the full experimental setup plays a crucial role. In our case the minimum resolvable rise time is limited by the bandwidth of the 2.5 m micro-coaxial cable, which connects the front-side electrode to the amplifier. In this Section I describe the characterisation of the component which affects mostly our measurements, the 2.5 m micro-coaxial cable, and the absolute calibration of the experimental setup.

With an AGILENT spectrum analyser [84] I measured the attenuation as a function of the frequency of the 2.5 m cable, as shown in Figure 4.10. The trend over frequency might be approximated as a first order low pass with a cut-off frequency of 350 MHz at -3 dB and a roll-off slope of -12 dB per decade. The response can be described by a simple low-pass RC filter: given an input step function with amplitude V_i, for the Kirchhoff's laws the output signal is

$$v_{\text{out}} = V_i(1 - e^{-\omega_0 t}) \tag{4.4}$$

where $\omega_0 = 1/RC$ is the cut-off frequency of the filter.

To assess the impact of the cable on the induced current measured with TCT, I employed a Agilent 81180A pulse generator [85] providing a single square pulse with ~ 1 ns rise time [2] and, with widths and amplitudes similar to the signal induced by charge drift in TCT. The test pulse has been sent though the cable, measuring the output signal with an oscilloscope. Figure 4.11 shows the measured output signal obtained for different test

[2] This is the minimum selected rise time of the instrument.

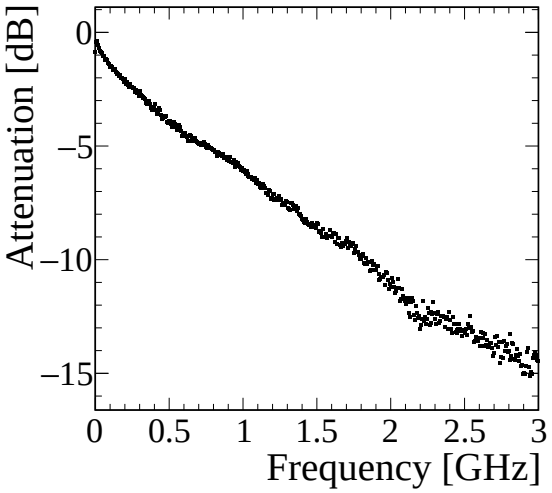

Figure 4.10: Analysis of the attenuation of the 2.5 m microaxial cable in the frequency domain. The measurement is performed using a spectrum analyser with an calibrated signal source integrated in the instrument. The plot shows the value of signal amplitude (dB) as a function of the frequency (GHz). The signal amplitude is obtained subtracting the attenuation of the reference cable from the attenuation measured for the reference cable plus the 2.5 m microcaxial cable.

pulses, varying the pulse amplitude and width. The signals present the shape described by Eq.4.4.

In addition, a dedicated calibration of the whole readout setup is performed to estimate the total gain of the setup and the effect of the readout components on the signal shape. The main goal is to obtain a better accuracy in the measured ionisation energy. Our focus lies on determining the amount of charge generated in the diamond bulk, and the gain factor on the signal amplitude plays a central role. The amplifier-scope readout system, included the 2.5 m cable, has been characterised with test pulses of known amplitude and width. The detector has been replaced with the same pulse generator used for the cable characterisation, providing a single square pulse with fast rise time (about 1 ns), width between 5 ns and 17 ns, and amplitude between 50 mV and 150 mV, simulating the measured signal in TCT measurements. Before sending the test pulse through the readout system, the signal has been attenuated by 46dB using three passive attenuators, in order to have an input signal with the same amplitude of the signal induced by charge drift in the diamond bulk. The total gain on the signal area, which includes the cables attenuation and the gain of the amplifier, is obtained dividing the area of the output signal by the area of the attenuated input signal. The calibration procedure has been performed both for a positive and a negative input signal, simulating the signal induced by electrons and holes.

The amplifier shown an asymmetric gain at 2% level for the two different polarities, and the total gain of the readout system is of 53.4 dB for electrons and 52.7 dB for holes. This asymmetric behaviour might be related to a different saturation output voltage for the two polarities. Since there are no visible reflection, I can suppose that the system has no impedance mismatch between the different components.

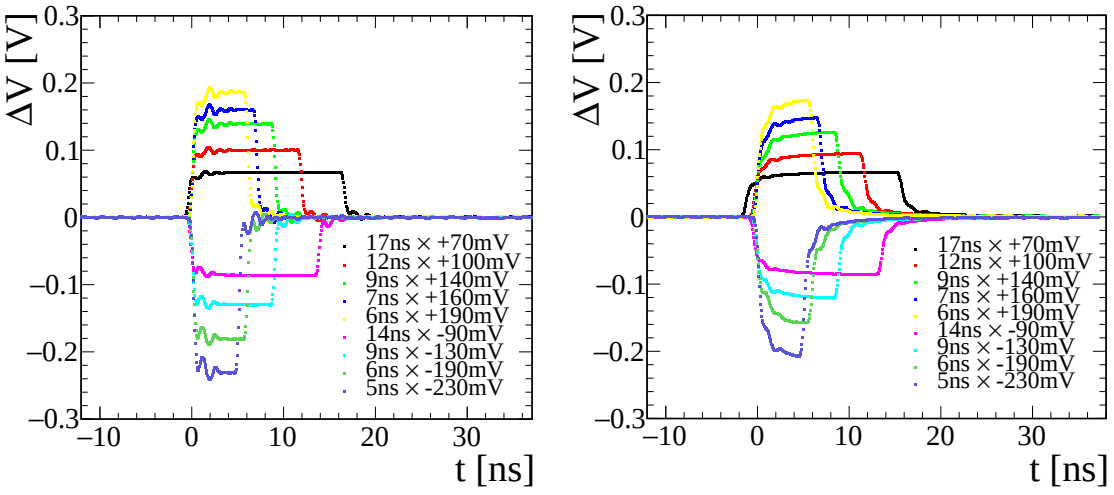

Figure 4.11: Output signals measured without (left) and with (right) a 2.5m micro-coaxial cable, varying the input signal width and amplitude. The legend reports the width and amplitude of each input pulse.

4.3.3 Data taking and analysis of the detector response

The oscilloscope records individual pulses when the pulse amplitude exceeds the trigger threshold. After applying the bias voltage on the back-side, I set the trigger threshold of the oscilloscope without irradiating the diamond sensor, in order to mask the most probable noise-pulse amplitudes and record only signal pulses. This operation has been repeated for each bias voltage set, since the setup is very sensitive to other electrical devices powered near by and the noise amplitude may change during the measurement procedure. The threshold is on average $-58.7\,\mathrm{mV}$ for the positive polarities and $51.3\,\mathrm{mV}$ for the negative ones, with a maximum variation of $5\,\mathrm{mV}$ during the test. The choice of the threshold mostly affect the measurements at lower bias voltages, which corresponds to a lower signal amplitude, limiting the minimum bias voltage to 150 V. After placing the source to irradiate the sensor, the oscilloscope records the signal pulses generated from the α ionisation, an it averages the signal shapes of about 1000 pulses.

Figure 4.12 reports an example of the measured signals, obtained with a positive (blue) and a negative (red) bias voltages, which correspond to electron and hole drift respectively. Thanks to the low source activity of 5 kBq and the collimator placed between the source and the detector, expected the rate of incident α on the active area is about $3\,\alpha/\mathrm{s}$. This value has been estimated assuming the nominal activity and the geometrical efficiency obtained from FLUKA [77] simulation of the experimental setup. The measurement duration is about 10/15 min per voltage setting, and so we can assume that the accumulation of charges underneath the injection contact is low. Since the injected charge is small enough, the field under the contact essentially remains unaltered from its ohmic value and we can assume to measure space-charge-free (SCF) transient curves at all voltages [86].

Assuming an ideal crystal with an uniform electric field E, the charge carriers drift with a constant velocity v_{drift}, and the induced current is given by the Shockley-Ramo theorem [87]

$$i(t) = -q\, v_{\mathrm{drift}} E\,. \tag{4.5}$$

For this ideal situation, the expected signal shape should be rectangular, characterised by

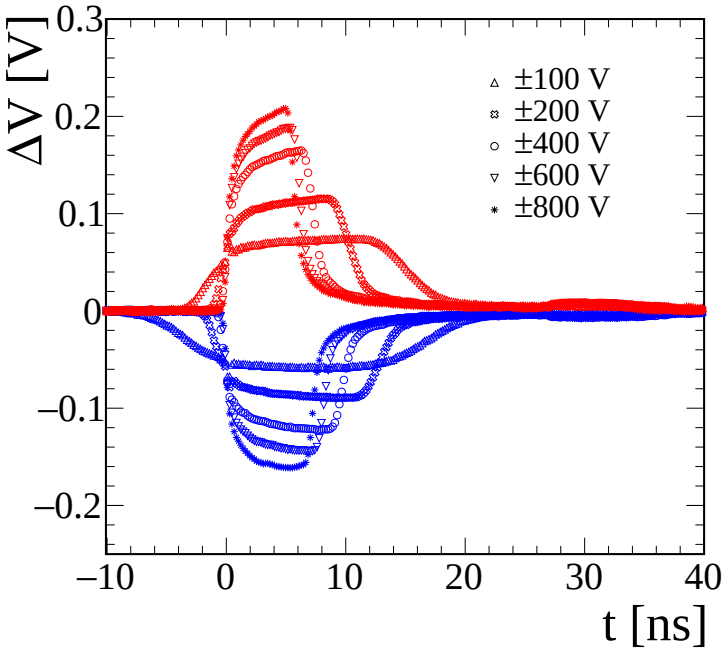

Figure 4.12: TCT signals induced by electrons (blue markers) and holes (red markers), at different bias voltages.

extremely rapid rise and fall times, corresponding to the creation and collection of charge carriers, respectively. Additionally, there should be a flat plateau in the middle of the waveform. The observed signals present instead finite rise and fall time and a non-flat bulk. The signals in Figure 4.12 are characterised by a rising edge which develops an $1 - e^{-\frac{t}{\tau}}$ behaviour and a falling edge with a long exponentially falling tail, mainly related to the readout system, as described in the setup calibration.

The signal rise time is approximately constant for all bias voltages, marking the start of the charge drift, and it has an average value of 600 ps 20-80%. However, the signals measured at a bias voltage of 150 V have a higher rising time due to time jitter: the signal amplitude is closer to the trigger threshold, with a higher impact of noise fluctuations. The falling edge indicates the arrival of the charge carriers at the back electrode. A longer falling time at lower voltages is related to a wider diffusion of the charge carriers as the drift time increases. For bias voltages higher than 200 V the signals present a similar falling edge, since the carriers are faster collected by the electrodes, limiting their diffusion in the bulk.

The majority of the sensors of the new sample presents a non-flat top signal region, far away from the ideal situation, with two different slopes. While one of the two slopes is due to the cut-off frequency of the readout system, the other slope can be ascribed to the presence of a non-negligible net space-charge in the diamond bulk that gives a non-uniform electric field [79]. Assuming a simple case of an uniform distribution inside the diamond bulk, this charge density leads to a linear dependence of the electric field as a function of the position in the bulk, which causes an exponential increase or decrease of the induced current, *i.e.* of the drift velocities.

In particular, an increasing slope is related to a positive charge density, while a decreasing slope to a negative charge density. This effect is called "trap polarisation" and it is

related to the fluence, *i.e.* to the total charge collected, and the bias voltage which generate the electric field into the detector bulk [88]. The effect can be explained by charge-carriers trapping at local defects of the crystal, which can occur either inside the whole diamond bulk or in the interface between the diamond and the metal electrode. The shape of the electric field varies according to the distribution of the charge density, which is influenced by factors such as the type and distribution of traps, trapping and de-trapping times, and the rate at which charge carriers are generated. Specifically, the electron density is greater in proximity to the positive electrode, resulting in a higher concentration of trapped electrons in that region. Similarly, the hole density is higher near the negative electrode, leading to a higher number of trapped holes in that proximity. Consequently, this accumulation of trapped charge carriers generates an internal electric field that opposes the applied high voltage field.

Sequential measurements are performed alternating the bias polarity, to reduce the "trap polarisation" effect [89]. By changing the detector polarity the charge carries start drifting in the opposite direction, neutralising the charge trapped near the electrode, and so removing the polarisation. Nevertheless this approach do not completely remove the effect, which is visible in Figure 4.13 on the left. Another possible approach that decrease the polarisation effect consists in irradiating the sensor with steady β irradiation for a few days, before performing the TCT measurements. A possible solution would be keep the sensor irradiated with β steady irradiation during the TCT, but this was not possible with our experimental setup.

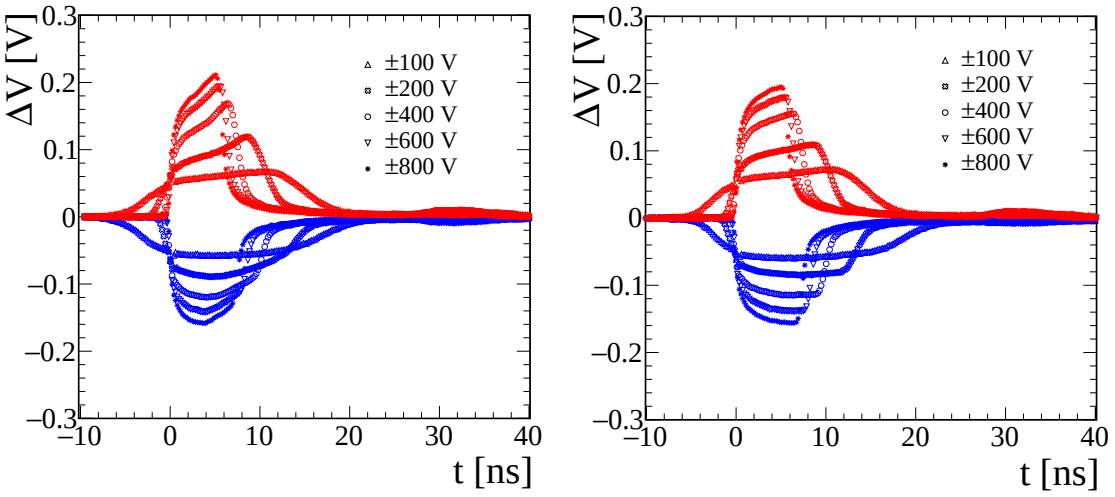

Figure 4.13: TCT signals induced by electrons (blue markers) and holes (red markers), at different bias voltages, measured before (left) and after (right) a β irradiation over several days.

I repeated the measurements for four detectors after a steady β irradiation of 2-3 days. The signal deformation is remarkably reduced after the irradiation, as shown in the right plot of Figure 4.13. The signal shape after the irradiation still shows a slope, far away from the ideal shape with a flat top, since the contribution of the readout system cannot be cancelled. For three detectors out of 4 an increase in the signal integral up to 15% is observed.

4.3.4 Analysis of charge carrier properties

In order to characterise the crystal, I determined the charge-carrier velocity and mobility varying the electric field strength.

A direct measurement of the drift velocity is provided by the measurement of the charge cloud transit time t_c, which is given by the FWHM of the measured pulse. The average drift velocity as a function of the electric field is calculated as

$$v_{\text{drift}}(\epsilon) = \frac{d}{t_c(\epsilon)}\,, \tag{4.6}$$

where d is the crystal thickness, assuming a uniform electric field of strength $\epsilon = |V_{\text{bias}}|/d$ generated by the bias voltage V_{bias}. The drift velocity has a linear dependence with the electric field $v_{\text{drift}} = \mu_0\epsilon$, where μ_0 is the mobility, as predicted by the Drude model of transport properties of electrons in materials [90]. Nevertheless this relation is true only for low field strengths. Increasing the electric field inside the diamond bulk, the charge carriers acquire more energy between the scattering processes, resulting in an higher effective temperature of the lattice. When the velocity approach the thermal velocity, the time between two collision involving charge carriers is no longer constant and the energy is dissipated by the emission of optical phonons. Together with other scattering mechanisms, this effect limits the drift velocity of carriers to a saturation velocity v_{sat} that cannot be exceeded.

In the regime where the drift velocity approaches the saturation velocity [79], it can be described as:

$$v_{\text{drift}}(\epsilon) = \frac{\mu_0\,\epsilon}{1 + \frac{\mu_0\,\epsilon}{v_{\text{sat}}}}\,, \tag{4.7}$$

where μ_0 is the mobility extrapolated to low field-intensity, and v_{sat} is the saturation velocity at high field. Such a saturation has also been observed in semiconductor like silicon. The carrier mobility is obtained as

$$\mu_{e(h)} = \frac{v_{e(h)}}{\epsilon}\,. \tag{4.8}$$

Figure 4.14 shows an example of the measured mobilities (left) and drift velocities (right) as a function of the electric field, calculated separately for electrons and holes. The measured hole mobilities consistently exhibit higher values than those of electrons; in both cases, a decrease of the mobility is observed as the electric-field strength increases. This phenomenon is not universal [91]: for electric-field strengths lower than roughly $0.03\,\text{V}/\mu\text{m}$ or higher than about $10\,\text{V}/\mu\text{m}$, the electron mobilities are higher than those of holes. This phenomenon is ascribed to the band-structure population that is dependent on the field applied. The electron effective mass varies, hence its mobility. I fit the drift velocities of Fig. 4.14 with Eq. 4.7. Both the zero-field mobility and the saturation velocity of holes are higher than those of electrons.

Figure 4.15 reports the distributions of the zero-field mobility and the the saturation velocity measured for the ten diamond detectors. The average values are $v^e_{\text{sat}} = (9.38 \pm 0.09) \times 10^6\,\text{cm/s}$ and $v^h_{\text{sat}} = (13.57 \pm 0.05) \times 10^6\,\text{cm/s}$, and $\mu^e_0 = 2072 \pm 52\,\text{cm}^2/\text{Vs}$ and $\mu^h_0 = 2398 \pm 30\,\text{cm}^2/\text{Vs}$, for electrons and holes respectively. The diamond mobilities and drift velocities measured for the ten diamonds are consistent among them within 7%, which supports the sample homogeneity. Moreover, the values obtained for the ten diamond detectors are consistent with the ones reported in Reference [79]. The differences may be explained by differences in the crystal grow, which implies differences in the defects distribution inside the diamond bulk.

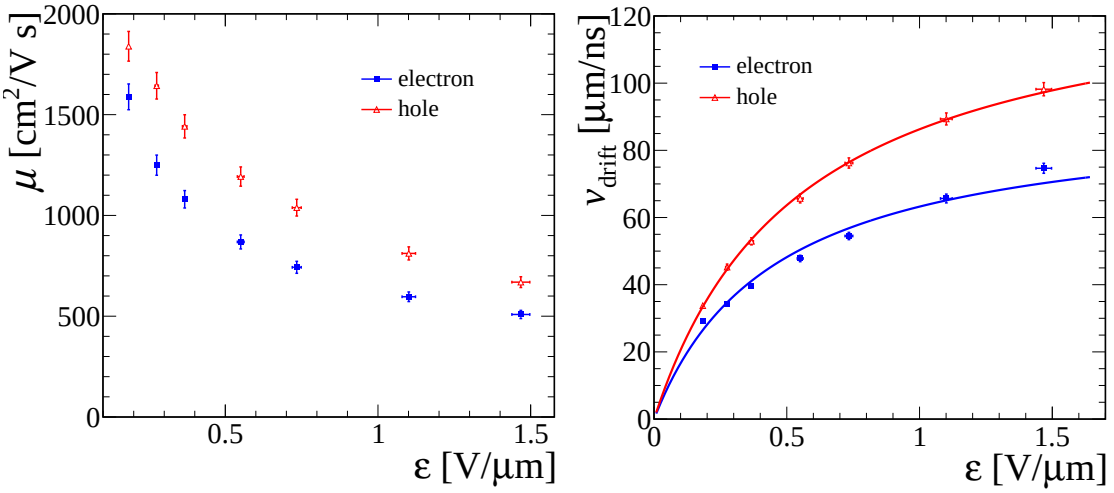

Figure 4.14: Electron and hole (left) mobilities and (right) drift velocities as a function of the electric-field strength. On the right plot, the fit functions defined by Eq. 4.7 are shown.

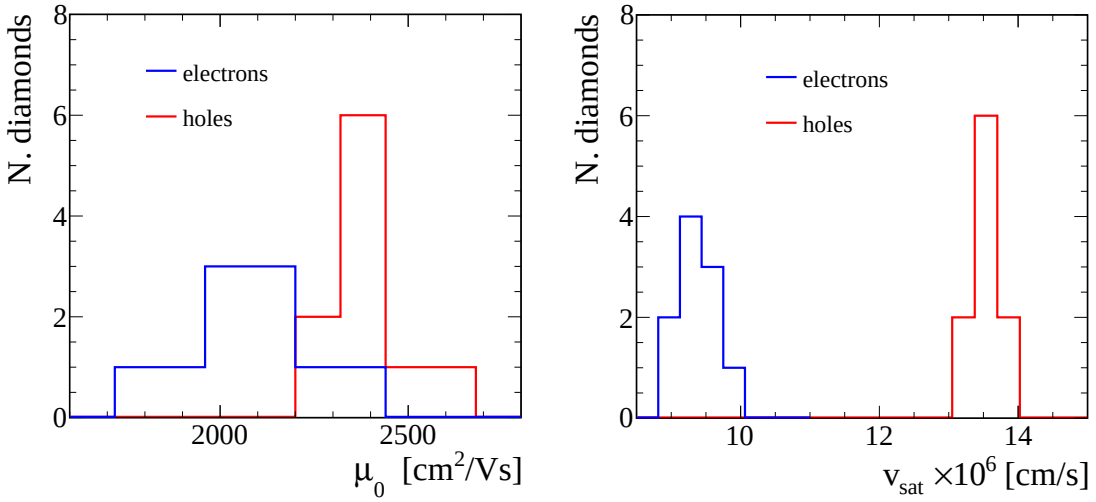

Figure 4.15: Low field mobilities (left) and saturation drift velocities (right), respectively for electrons and holes, measured for the sample of ten diamond detectors. The values are obtained form the fit with Eq. 4.7.

4.3.5 Average energy to create an electron-hole pair

The TCT is also used to determined the mean ionisation energy to create an electron-hole pair. This parameter is obtained by the comparison of the signal pulse with the energy released by the α particle in the diamond bulk. The three main parts of this procedure are described below.

Simulation of α particles interaction with out detector

In order to estimate the mean energy released per α particle in the diamond, I made a dedicated simulation of the experimental setup, which takes into account the geometry of

the detector support, the collimator and the detector itself, the interaction of α particles with all the materials along their path, and the energy released in the active volume of the detector. The simulation exploits the Monte-Carlo simulation FLUKA [77]. Figure 4.16 shows a transverse section of the system geometry as implemented in the simulation and the released energy by α particles along their path.

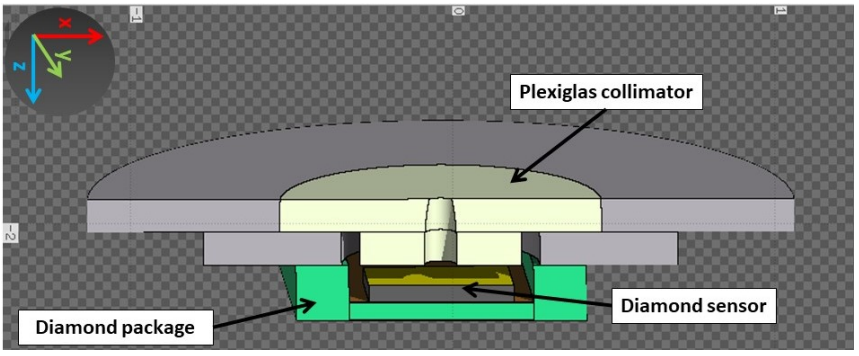

Figure 4.16: 3D section of the simulated setup geometry. The reference frame is chosen so that the x-y plane is parallel to the sensor surface.

The diamond detector is defined in all its parts: the sensor consist in a 540-μm thick diamond crystal with 3 metallic contact layers (Ti+Pt+Au) on both sides. The source is simulated as 0.35 mm-radius disk of Am, which is the active part, deposited on a platinum disk placed behind the source that gives the mechanical support to the source. The α particles are generated with an isotropic angular distribution and the simulation takes into account also of possible back-scattering of the α particle on the support. The source is placed at 0.6 mm from the plexiglas collimator. The energy spectrum of the α particles is simulated with five narrow peaks centred at the corresponding values of Tab. 4.1. For each of the five energy values in the spectrum, I generated a sample with 45×10^6 α particles. Only 0.06% of the simulated particles interact with the active volume of the diamond bulk. For each generated α particle, the simulation gives the energy released inside the detector volume, and also in all materials traversed by the particle along its path. The total distribution of the released energy in the active volume of the detector is obtained by summing the released energies from the 5 samples, each weighted with the branching ratio corresponding to the simulated energy peak.

The irradiated zone is restricted to a circular area with a radius of approximately 1 mm on the diamond surface, a consequence of the collimator's focus. Figure 4.17 (left) shows the x-y section of the diamond and of the released energy on the surface. Most of the energy is released in the centre of the diamond, confirming that the particles are well collimated on the sensor. Figure 4.17 (right) shows instead the relative energy deposited by an α particle, *i.e.* the energy deposited in a finite interval Δz divided by the total energy deposited in the diamond bulk, as a function of the path length z of the particles in the diamond. The zero corresponds to the crossed diamond crystal surface. The energy loss is limited to a depth of about 12 μm, which corresponds to the typical range of α particles in diamond.

A fraction 90.6% of the total energy of the α particle is released on average in the diamond; 4.1% in the metallic contacts, and the remaining energy in air and on the collimator walls. The distribution of the released energy in the diamond bulk is shown in Figure 4.18, which has the a dominant peak centred at 4.9 MeV and long tail at energy lower than 4.8 MeV. Since the fraction of events released an energy lower than 4.8 MeV is

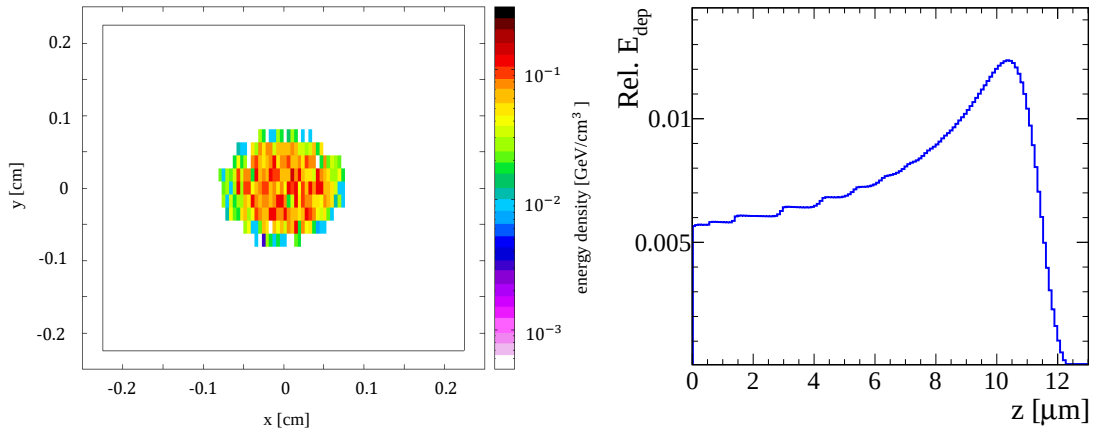

Figure 4.17: (left) Two-dimensional profile illustrating the released energy per unit volume (color scale) deposited on the diamond surface. (right) Relative deposited energy as a function of the α path length within the diamond sensor.

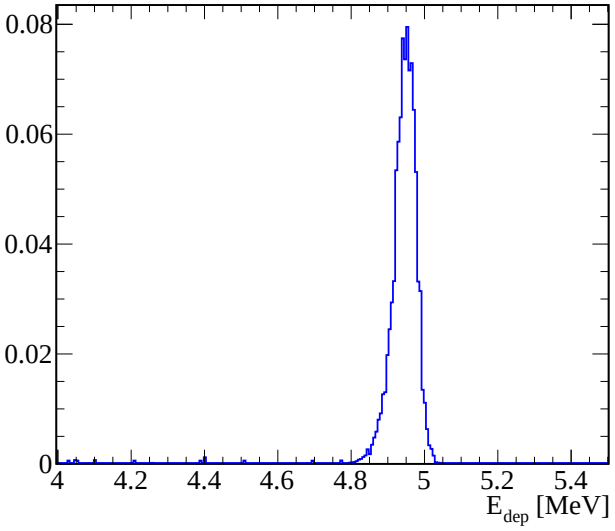

Figure 4.18: Distribution of the released energy in the active volume of the diamond detector. The tail at energies below 4.8 MeV is mainly due to particles losing energy in the air and through interaction with the collimator walls.

about 5% of the total number of α particles interacting with the active volume, I took the most probable value as the mean released energy.

Determination of the mean energy to create an electron-hole pair

The charge collected at the electrode is calculated from the signals-shape average. Given the area A under the signal (in V ns), a coupling impedance $Z_{in} = 50\,\Omega$ and the amplifier gain factor G obtained from the absolute calibration, which has two different values respectively

for electron and hole signals, the collected charge Q is given by

$$Q = G \cdot \frac{A}{Z_{in}} \,. \tag{4.9}$$

Figure 4.19 on the left shows an example of the measured charges as a function of the electric-field strength for electron- and hole-induced signals. The charge values is approx-

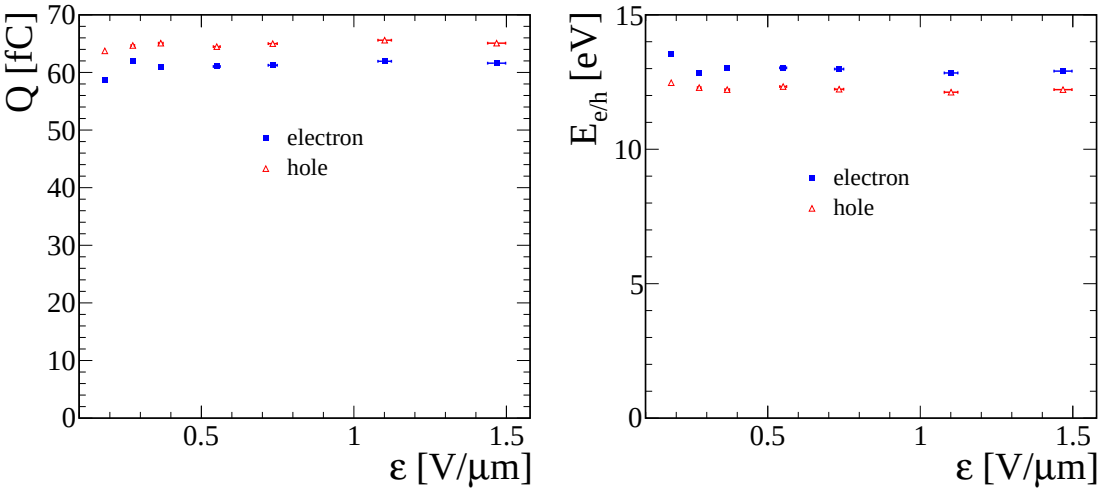

Figure 4.19: Charge (left) and mean ionisation energy (right) as functions of the electric-field strength for electron- and hole-induced signals.

imately constant at electric fields higher than $0.2\,\mathrm{V}/\mu\mathrm{m}$. This implies that the charge is completely collected from the diamond bulk and the charge collection efficiency (CCE) should be assumed to be near 100%. The collection efficiency is higher than 90% even at lower electric field, and so bias voltage applied to the detector.

The average collected charge for the ten diamond sample is of $60.01 \pm 0.34\,\mathrm{fC}$ and $62.95 \pm 0.47\,\mathrm{fC}$ for electron- and hole-induced signal, respectively. The holes measured charge is always $\sim 5\%$ higher than the electrons charge. Assuming a fully efficient-charge collection from the diamond bulk, I evaluate the energy needed to create an electron-hole pair $E_{e/h}$. This is determined by the ratio of the released energy $E_{\mathrm{dep}}^{\mathrm{mean}}$, estimated with simulation, with the number of charge carriers, obtained from the ratio Q/e,

$$E_{eh} = \frac{E_{\mathrm{dep}}^{\mathrm{mean}}\, e}{Q} \,, \tag{4.10}$$

where e is the elementary charge.

Figure 4.19 on the right shows an example of the measured $\epsilon_{e/h}$ as a function of the electric-field strength, for electron- and hole-induced signals. In the example,the values are averaged to obtain

$$E_{eh}^{e} = 12.94 \pm 0.04\,\mathrm{eV} \tag{4.11}$$

$$E_{eh}^{h} = 12.27 \pm 0.03\,\mathrm{eV}\,, \tag{4.12}$$

respectively, where is reported only the statistical uncertainty. No systematic uncertainty is associated to these measurements and the overall uncertainty is perhaps underestimated. The method validation with a silicon diode as a reference is described below. Since the

average ionisation energy determined for the silicon diode is in agreement with the nominal one within $\sim 5\%$, I associated an uncertainty of about 5% to the diamond average ionisation energy. The value measured for electrons and holes are compatible within the systematic uncertainty.

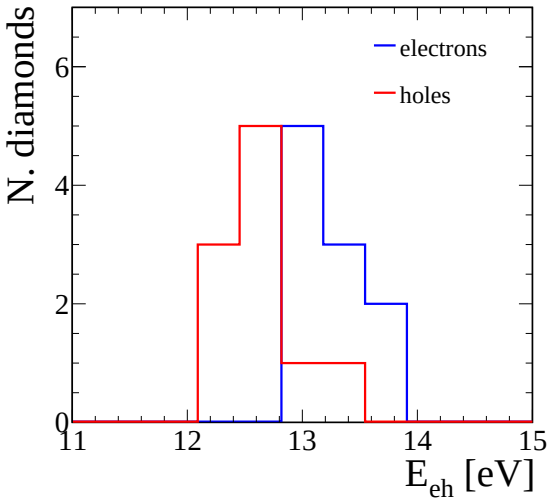

Figure 4.20: Distribution of the average ionisation energy measured for the ten diamond detector, respectively from electrons- (blue) and holes- (red) induced signals.

Figure 4.20 reports the distribution of the measured aver ionisation energy for the ten diamonds detectors, for the signal induced by electrons and holes drift respectively. The average ionisation energy is of 13.26 ± 0.08 eV for electron- and 12.64 ± 0.10 eV for hole-induced signal. The measured values of the ionisation energy are consistent within 6% with the value of 13 eV usually quoted in literature for high-quality diamond sensors [91], with possible variations of the order of 1 eV depending on the quality of the sensors (the lower, the better). Moreover the ionisation energy measured for all the ten new diamond detectors are in good agreement with each other, showing a good sample homogeneity.

Validation of the procedure with a reference silicon diode

I carried out a reference measurement on a silicon diode, described in Section 4.2.3, using the identical setup and analysis technique used for our diamond detector, which aims at validating the measurement of the mean ionisation energy. The α source is mounted on the top of the p^+-implant, and a positive reverse bias is applied to the back-plane, thus providing a measurement of the electron signal.

Figure 4.21 shows the measured signal for different values of bias voltages, V_{bias}, which ranges from 50 V to 250 V. The signal shape changes as a function of the electric field and of the depleted thickness. The measurement has been repeated both without and with the 2.5 m cable between the detector and the amplifier, in order to see the effect of the cable on the signal shape. Adding the cable the signal shape presents a different slope. Moreover a reflection is visible after ~ 30 ns, corresponding to twice the cable length, due to an impedance mismatch between the detector and the amplifier.

Using the same analysis technique described above, I determined the total charge from the integral of the current pulse. This value is compared with the mean released energy in the silicon diode, always obtained with a detailed simulation of the experimental setup

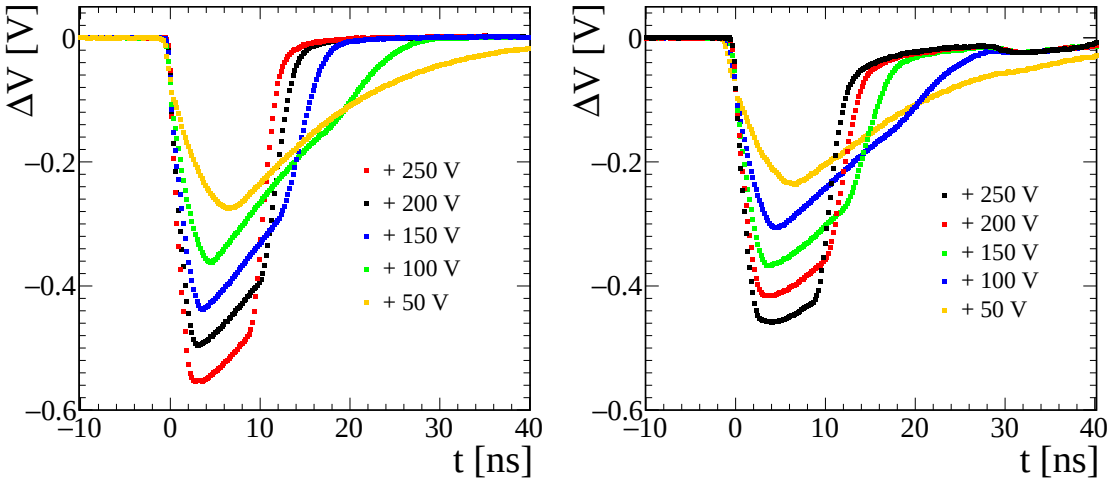

Figure 4.21: Measurement of TCT signals induced by electrons drifting, at different bias voltages, using the identical setup used for diamond detector. Two set of measurement have been performed, without (left) and with (right) a 2.5 micro-coaxial cable between the detector and the amplifier.

in FLUKA. The mean released energy is 5.1 MeV, about 6% higher than the diamond detector since the α loses less energy in the diode electrode. The measured charge as a function of the bias voltage for the two setup configurations is reported in Figure 4.22, showing a difference of 7% for the two setup. This difference is due to a cutoff in time on the measured signal, caused by the longer tail.

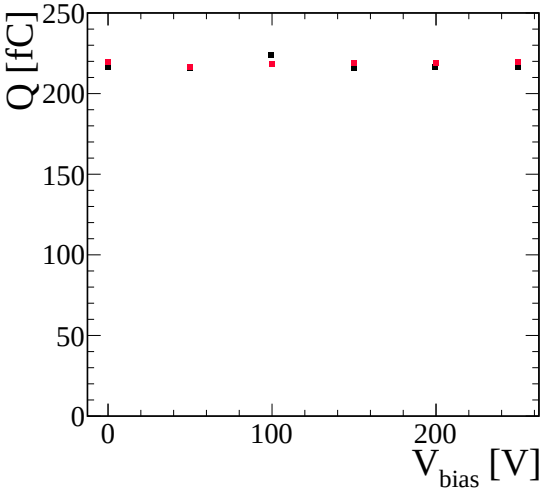

Figure 4.22: Charge as a function of the bias voltage estimated from the induced signal measured with the silicon diode, for the setup configuration without (blue) and with (red) a 2.5 micro-coaxial cable.

For the two sets of measurements, I obtained an average ionisation energy to create an electron-hole pair in silicon of 3.50 ± 0.06 eV and 3.75 ± 0.06 eV, respectively for the setup without and with the 2.5 m cable. Both the results are consistent with the nominal value

of 3.66 eV [92] within 5%.

4.4 Characterisation with β radiation

To characterise the response of the diamond sensors to charged particles, I used the β source described in section 4.2.3. The main goals of this characterisation procedure are to test the stability of the detector's response under a steady irradiation and to determine the optimal operation bias voltage for each detector. The second part of the characterisation is focus on the current-to-dose rate calibration procedure, essential to employ the detector as a dosimeter in our radiation monitoring and beam abort system, described in Section 3.1.1.

4.4.1 Experimental setup and measurements methods

The experimental setup consists of

- a CAEN DT1471ET [93] power supply to provide a bias voltage to the diamond sensors in the range from $-600\,\mathrm{V}$ and $+600\,\mathrm{V}$, with very low noise;
- a 4-channels picoamperometer (model AH501B provided by Sincrotrone Trieste) [94], that measures bipolar currents up to $\pm 11\,\mathrm{mA}$ and has a sampling frequency up to $26\,\mathrm{kHz}$. The device has a dedicated control software which allows to set the current range (three ranges are available: $\pm 2.5\,\mathrm{nA}$, $\pm 6.4\,\mu\mathrm{A}$, $\pm 11\,\mathrm{mA}$), the number of input channels (up to 4), the sampling frequency and the time interval for data averaging, yielding in output the mean value and the standard deviation of the down-sampled current obtained averaging and several other features;
- an aluminium support to host the detector in well defined and reproducible position aligned to the β-source. A $3\,\mathrm{mm}$ thick copper shutter can be placed manually in front of the detector, dumping almost completely the flux of β interacting with the active volume of the detector;
- a stepper motor, controlled via software using an "Arduino" [95], is employed for moving the source support within a $300\,\mathrm{mm}$ range, with steps as fine as $10\,\mu\mathrm{m}$ to adjust the distance between the source and the detector. To ensure precise positioning, a mechanical switch is positioned at the end of the line, designed to stop the stepper motor when the source aligns with the aluminium support of the detector.

As shown in Figure 4.23, both the source and the detector are placed in a $(37 \times 22 \times 22)\,\mathrm{cm}^3$ Plexiglas box with 1-cm-thick walls, that absorb completely the radiation emitted by the β-source and avoids any accidental contact with the source itself. The position of the source respect the diamond detector is changed using a stepper motor driven by an Arduino micro-controller [95]. The origin is known with an accuracy of $0.2\,\mathrm{mm}$. The moving source support plays a pivotal role in the calibration process, since it is possible to change the flux intensity of β radiation on the sensor surface by varying the relative distance between the source and the detector.

In the measurements, the bias voltage is normally applied to the back-side of the diamond sensor, while the other side is set to ground. I measured the output current, induced by charge-carrier drift in the diamond bulk, using the picoammeter connected to the front-side cable, with a sampling time of $1\,\mathrm{s}$.

For each sensor I performed three different sets of measurements, outline in the following.

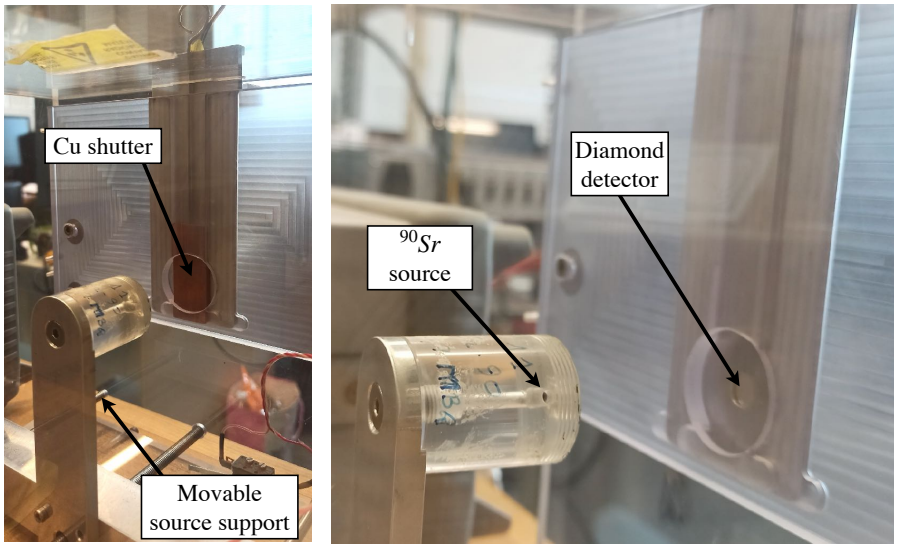

Figure 4.23: Experimental setup for the characterisation with β radiation. The two pictures show the setup with and without the shutter inserted.

Stability measurement: This measurements is performed applying the bias voltage of 100 V, for both the positive and negative polarity. I placed the source at 4.0 mm from the diamond sensor, to guarantee the minimum space necessary to slide the 3.0mm thick copper shutter between the source and the sensor. A dark current measurement is performed by sampling the output current for a period of about 10 minutes, using the shutter to shield the β radiation. Afterwards, the shutter is removed, while I keep sampling the output current. To probe the stable response of each detector, the current is measured for a period of 1-2 days in these conditions.

I-V characteristic: This measurement is performed varying the bias voltage over a ± 600 V range, keeping the source at a fixed distance of 4 mm. I measured the dark current, using the shutter to shield the β radiation, for a period of about 3 minutes. After removing the shutter, the output current given by impinging radiation is measured for a period of about 7 minutes. For each polarity, the measurement is repeated for by increasing the voltage with steps of 1 V in the range $[0; 10]$ V, 10 V in the range $[10; 100]$ V, 50 V in the range $[100; 300]$ V and 100 V in the range $[300; 600]$ V.

I-d measurement: This measurement is performed varying the source-detector distance from 2 mm to 35 mm, applying a fixed bias voltage of ± 100 V. The distances are increased with steps of 0.5, 1.0, 2.0 and 5.0 mm. Also for this set of measurements I measured the dark current placing the shutter between the source and the detector, sampling the current for a period of about 3 minutes. However, at a distance of 2 mm, it is not possible to perform this operation due to insufficient space to place the shutter between the detector and the source. It is assumed that the dark current at the 2 mm distance is the same as that observed in the measurements taken at 4 mm. After removing the shutter, the output current is measured for 5 minutes.

The first two sets aim at verifying the stability of the sensor response to steady irradiation and determine the best operation bias voltage, while the last one is used for the current-to-dose rate calibration. Although the diamond sensor is not sensitive to visible

light, the presence of the aluminium cover diminishes the probability that any incident visible light would generate additional currents in the detectors. The I-d measurement is done also with the silicon diode, used as a reference for the calibration. The silicon diode is operated applying a +100 V reverse bias to the back-side electrode. In this case the sensor is very stable, so a dedicated stability study is not needed; moreover a special care has been kept in order to avoid a long exposure to β radiation that can damage the silicon bulk increasing its leakage current Because the silicon diode is more sensitive to light than the diamond, the presence of the cover in front of the detector is not sufficient to mask it from visible light. For this reason the measurements with the silicon diode are carried out covering the full box with several black cloths, to reduce light contamination to a negligible level which has been verified for each measurement.

4.4.2 Current stability and current-voltage characteristic

Stability

A stable and reproducible response to radiation is crucial for dosimetry and monitoring. I checked the stability in time of the radiation-induced current at the chosen operation voltage, over a time span from ten hours to a few days. The operation voltage for all our diamond detectors is 100 V, chosen looking at the I-V characteristic described below. Figure 4.24 shows an example of current profile obtained from the stability measurement, where I_{diam} is the measured output current and t the irradiation time. The uncertainty associated to each value of the output current is the one measured by the picoamperometer in the acquisition interval of 1 s.

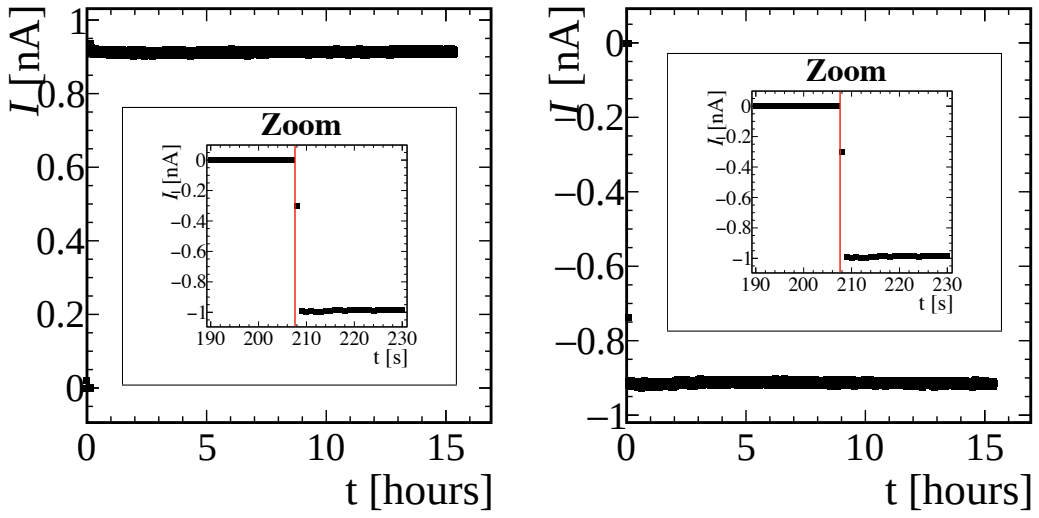

Figure 4.24: Output current I as a function of the irradiation time t. The plot show an example of one of the few diamond sensors with symmetric and stable output current for the two polarities. After removing the shutter, as shown in the zoom, the measured current reaches a stable value in about 1 s. The red line correspond to the time when the shutter has been removed.

All the measurements present an initial value of the output current distributed around zero, corresponding to the dark current measured with the shutter placed between the source and the detector. After manually removing the shutter, the currents suddenly have

nonzero values, reaching about 90% of the value of the current after $\sim 1\,\mathrm{s}$, *i.e.* the time-resolution of the current sampling in these measurements. The zoom in Figure 4.24 show the current transient at the time of the shutter removal, corresponding to the red line. In the ideal case, a stable output current is reached in a very short time, and its absolute values is the same when changing the sign of the bias applied. The measurements performed on the ten diamonds sample show different results for the sensors, and also for the different bias polarisation on the same sensor. Figure 4.25 show a few example of diamond detector a non-ideal behaviour.

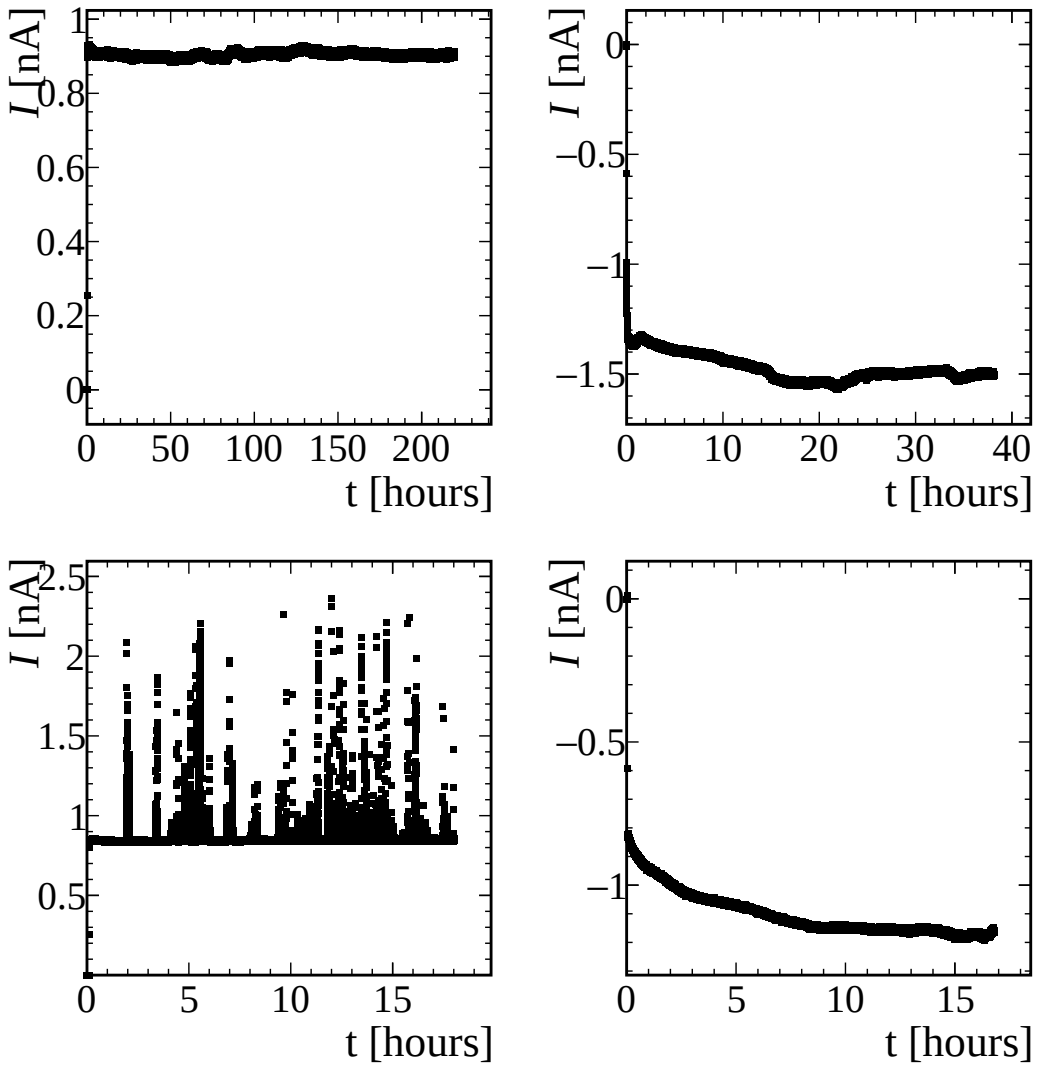

Figure 4.25: Output current I as a function of the irradiation time t. The first row represents the behaviour of a diamond detector with an asymmetric response for the two polarities. The second row shows an example of not stable diamond.

Most of our detectors present an asymmetric response for the two polarities, as shown in the top plots of Figure 4.25. In the example, the measured current for the negative bias voltage (left) takes more than 30 hours to reach a quasi-stable output current and the current is about a factor 1.5 higher than the one measured at $+100\,\mathrm{V}$. Such an asymmetry might depend on subtle surface treatment or on crystal growing effects of the sensor, which

vary from crystal to crystal. The bottom plots present the case of a unstable diamond detector. In the case of a positive bias voltage, the current exhibits sporadic spikes lasting between 10 to 30 s, with values doubling the anticipated current. On the other hand, for the negative voltage, the current displays a more extended transient period, lasting approximately 10 hours, and it remains higher than the expected current level.

Longer transients time to reach a stable output may be seen, as for the measurement in Figure 4.26, where the current reaches a stable value with time duration ranging from tens of seconds to many minutes. We attribute this behaviour to different amounts of crystal

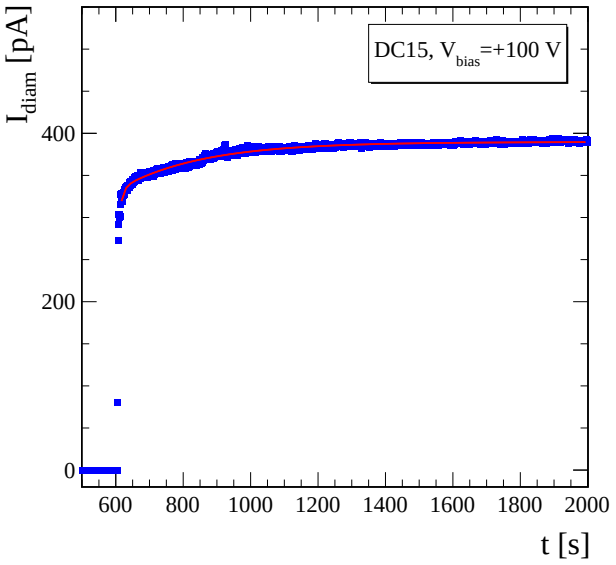

Figure 4.26: Output current I_{diam} as a function of the irradiation time t for one diamond of the previous production, with a bias $V_{\text{bias}} = +100\,\text{V}$ applied. The current profile is fit using Eq. 4.13.

defects, which can introduce variations in the crystal energy levels [96]. The defects, also called *traps*, are located in the band gap and can trap the charge carriers. In the diamond bulk we can distinguish two types of traps: the shallow traps, situated near the valence band or the conduction band, and the deep traps, situated in the central zone of the band gap. These energy levels trap electrons and holes generated by impinging radiation, decreasing the output current. By filling the traps with charge carriers generated by continuous radiation, the output current rises, achieving a stable value when there are no empty traps anymore. This phenomenon is empirically modelled by the following expression

$$I_{\text{diam}}(t) = I_0 \left(1 - w_s\, e^{-\frac{t-t_0}{\tau_s}} - w_d\, e^{-\frac{t-t_0}{\tau_d}}\right) , \tag{4.13}$$

where I_0 is the asymptotic current values; w_s and w_d are the proportions of superficial and deep traps; τ_s and τ_d the corresponding time constants to fill the two categories of traps; and t_0 is the origin time, *i.e.* the start of the irradiation. As shown in Figure 4.26, I fitted the current profile in the transient region using Eq. 4.13, obtaining a long-time constant of 700 s and a short-time constant of 30 s. These two values differs from crystal to crystal.

It is important to emphasise that these transients are examined under conditions of relatively low charge carrier densities. In Chapters 5 and 6, I will present the results of the study of the diamond's transient response under significantly different conditions characterised by high carrier densities.

I-V characteristic

The detector response might depend on the applied bias voltage, and the optimal operation value has to be determined. I measured the current-voltage (I-V) profile under irradiation for each detector after the stability measurement. Increasing the applied bias voltage also the current increases, with a saturation when the full charge collection efficiency (CCE) is reached, as expected for electronic grade sCVD diamond sensors. The ideal I-V profile is characterised by a symmetric profile, where the saturation is achieved for both the polarities. Figure 4.27 illustrates the measured profile for a real diamond detector demonstrating nearly ideal behaviour, hereafter referred to as "ideal".

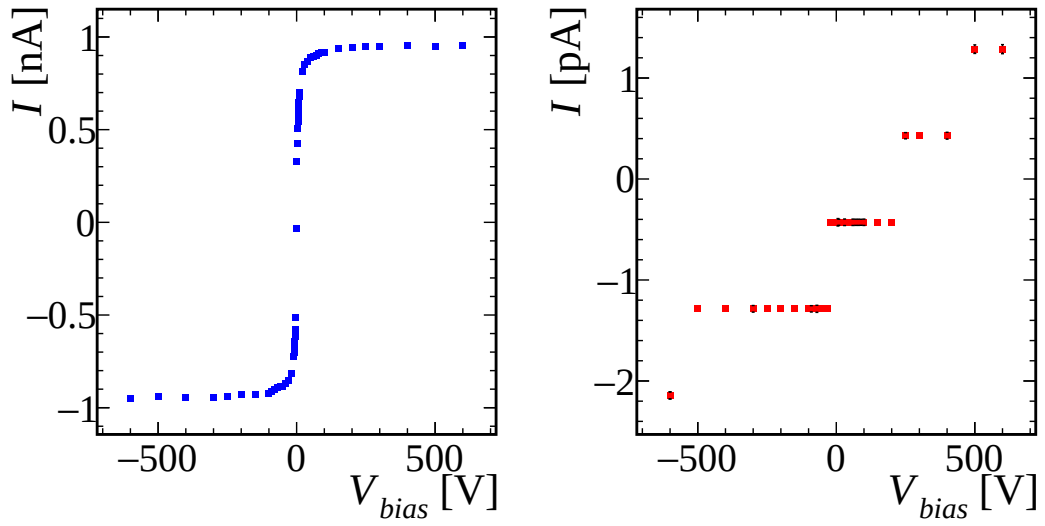

Figure 4.27: I-V characteristic: output current I as a function of the applied bias voltage V_{bias}. The two plots represent respectively the measured current with (left) and without (right) irradiation. The latter is obtained placing a shutter between the source and the detector. The current without irradiation is about three order of magnitude lower than the current with irradiation.

In the range 0–10 V the measured current rises very steeply, reaching about 50% of the plateau value with a bias voltage as small as 2 V, and then slowly saturates increasing the bias voltage. In order to see this fast transition, I sampled the region 0–100 V in finer steps. The saturation current is reached for $|V|$ between 80–100 V, remaining flat up to $|V| = 600$ V. In this plateau region we can assume a charge collection efficiency (CCE) near to 100% for a crystal without imperfections, and higher voltages do not lead to higher currents. For the sensors with an ideal behaviour, also the dark current, measured without irradiation, keeps a value lower than 5 pA.

However, most of the tested diamonds of the new production present an asymmetric I-V profile. Figure 4.28 shows instead an example of a non-ideal behaviour, where for one polarity the current reaches a constant value for $|V|$ typically greater than 90 V, while for the opposite polarity no current saturation is observed. The same asymmetry is also visible for the current-voltage profile measured without irradiation.

A possible hypothesis for this asymmetry could be a crystal asymmetry from the growth process. Moreover, also the features of the diamond-electrode interface can change the diamond response. The latter effect is most likely due to charge injection from the metallic electrodes to the diamond bulk. The metallic contacts are deposited on the crystal surfaces

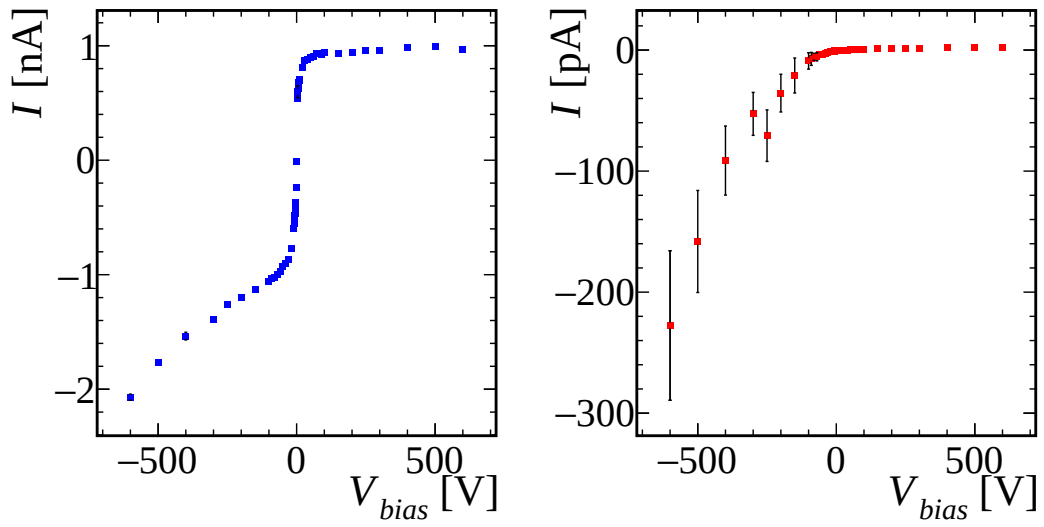

Figure 4.28: Example of I-V characteristic with an asymmetric profile, where output current I as a function of the applied bias voltage V_{bias}. The two plots represent respectively the measured current with (left) and without (right) irradiation. The latter is obtained placing a shutter between the source and the detector.

to extract the charge inside. These contacts can be either blocking or injecting. In the first case the contacts prevent charge injection in the diamond bulk by creating a potential barrier between the contact and the bulk. In the second case, charge injection occurs. The contact has a lower impedance when compared to the series impedance of the diamond bulk. This leads to a higher free carrier density in the vicinity of the contact compared to that in the bulk. Consequently, the contact may inject carriers into the bulk itself [97].

From the I-V characteristic, the bias voltage of $\pm 100\,\mathrm{V}$ is chosen as the optimal operation voltage, in agreement with the value set for the other 28 diamond detectors used for *Phase 3, run 1* in the Belle II radiation monitoring and beam abort system. With this choice, our detectors have a steady-state charge-collection efficiency close to 100% on average. For these sensors I decided to adopt the voltage polarity leading to a saturation of the current. Moreover, on the sensors exhibiting symmetric I-V profiles, I observed a very stable response over time with values constant within 1%. For those with asymmetric I-V profiles, I observed constant current values for the best polarity, with fluctuations no larger than 5%.

4.4.3 Current-to-dose calibration

To employ the diamond detector as a dosimeter, it is necessary to relate the current measured under irradiation to a dose rate. Under a quasi-stationary flux of radiation, the induced current is proportional to the energy released by the radiation in the active volume of the sensor per unit time, and the calibration factor k is defined such that

$$\frac{dD}{dt} \equiv \frac{1}{m}\frac{dE}{dt} = k\,I\,, \tag{4.14}$$

where dD/dt is the dose rate, dE/dt the energy per unit time released by the radiation, m the sensor mass, and I the measured current.

The calibration factor k should be split into two terms, as

$$k \equiv \frac{F}{G}\,, \tag{4.15}$$

where F is a constant factor that depends on the physical properties of the diamond sensor, and G takes into account for the specific response of each detector. Given an active volume of $1.14 \times 10^{-2}\mathrm{cm}^3$ and the diamond density $\rho = 3.52\,\mathrm{g\,cm}^{-3}$, the mass of our sensors is $m = 40.3\,\mathrm{mg}$ and the constant factor F takes the value

$$F \equiv \frac{E_{eh}}{m\,q_e} = 32.3\,(\mathrm{mrad/s})/\mathrm{nA}\,, \tag{4.16}$$

where an average ionisation energy to create electron-hole pairs $E_{eh} = 13\,\mathrm{eV}$ is assumed, in agreement with the measured values reported in Section 4.3.5.

The factor G is a dimensionless constant characteristic of each detector. In the ideal case correspond to the value $G = 1$, which would represent a fully efficient detector, with blocking electrodes [91], and ionisation energy of 13 eV. To determine the value of G, I developed a diamond-to-diode calibration method that compares the diamond response to the one of silicon diode used as a reference.

I exposed the diamond detectors and the reference diode to a source of β radiation, and I determined the ratio of the *signal* current from the diamond detector to the *reference* current from the diode. The characteristic constant G is obtained by comparing the measured *signal/reference* current ratio and that expected from a detailed simulation of the experimental setup, assuming a good knowledge of the diode response. The use of a reference greatly reduces uncertainties associated to the source activity and to the simulation of the setup, that would otherwise limit the accuracy of the calibration procedure.

Measurement of signal-to-reference ratio of currents

The signal-to-reference ratio has been determined comparing the *signal* current from the diamond detector to the *reference* current from the diode, both measured at the same source-detector conditions. I measured the currents with the I-d measurement procedure described in Section 4.29, moving source along a straight line orthogonal to the detector surface and crossing its centre. Figure 4.29 shows an example of the currents measure with the diamond and silicon detectors as a function of the source-detector distance. The current values are determined by taking the mean of the current measured during irradiation and then subtracting the dark current measured in the absence of irradiation. While for diamond detectors the dark current is negligible, it contributes significantly in the measurements with the diode, especially at far source-detector distance.

Both diamond and silicon currents quickly decrease with the distance. At large distances compared to the detector and source size, currents are roughly proportional to d^{-2}, as expected from the variation of the β-electron flux on the detector surface as a function of d, for an almost point-like source. This can be approximately parameterised as

$$I^*_{\mathrm{mis}} = \frac{A}{(d - d_0)^2} + I_0\,, \tag{4.17}$$

where A is a normalisation constant, d_0 is a position offset, and I_0 is a current offset. Such a relation needs a correction to account for the fraction of solid angle subtended by the detector surface and a point-like source at small distances. This is calculated in Ref. [98].

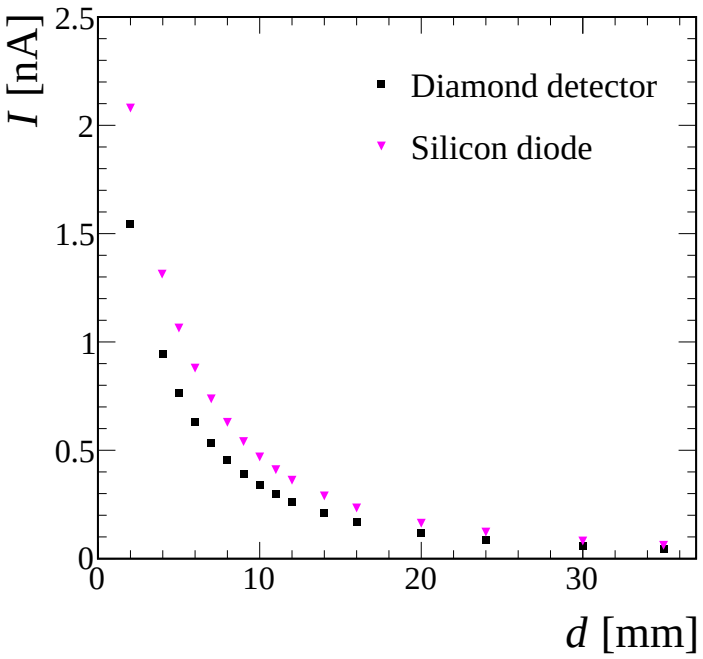

Figure 4.29: Current as a function of source-detector distance. Example of (square markers) the signal current I measured from a diamond detector, and (triangular markers) reference current I_r measured from the silicon diode. The statistical uncertainties are not visible because of their small size compared to that of the markers.

Given such a correction, the output current depends on the distance as

$$I^*_\mathrm{mis} = 4A' \arctan\left(\frac{A_\mathrm{eff}}{2(r-d_0)\sqrt{4(r-d_0)^2+2A_\mathrm{eff}}}\right) + I_0\,, \tag{4.18}$$

where A' is another normalisation constant, and A_eff is the effective surface of the detector.

The signal-to-reference ratio of currents,

$$R \equiv \frac{I(d)}{I_\mathrm{r}(d)}\,, \tag{4.19}$$

is constant versus d, as shown in the Figure 4.30. The flatness of R denotes that the measured values of the source-detector distance are compatible in the two sets of data.

Computation of the expected ratio of currents

The expected signal and reference currents have been computed from the energy released per β electron in the detector volume, E (E_r), obtained by the Monte-Carlo simulation of the full experimental setup. The simulation is implemented using the FLUKA software [77], by implementing a realistic and detailed model of the full setup, from the spherical source to the detectors, with all supports and packaging. This comprehensive model accounts for the full geometry and all materials traversed by the radiation during the simulation.

Figure 4.31 shows a 3D section of the experimental setup, which includes the protective box, the aluminium support for the sensors and the plexiglas support for the source. The active part of the source is modelled as a 0.5 mm radius sphere of ^{90}Sr embedded in a

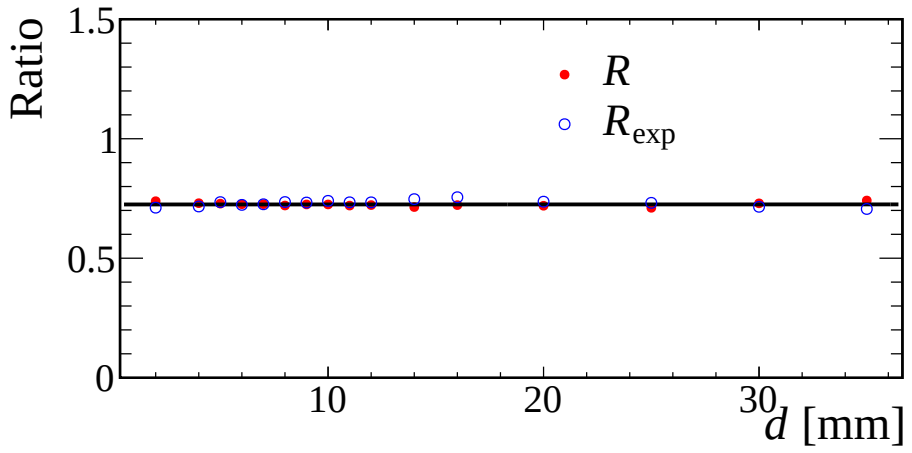

Figure 4.30: The signal-to-reference ratio of currents R compared to the expected ratio R_{exp} from Eq. (4.21). The uncertainties are not visible because of their small size compared to that of the markers.

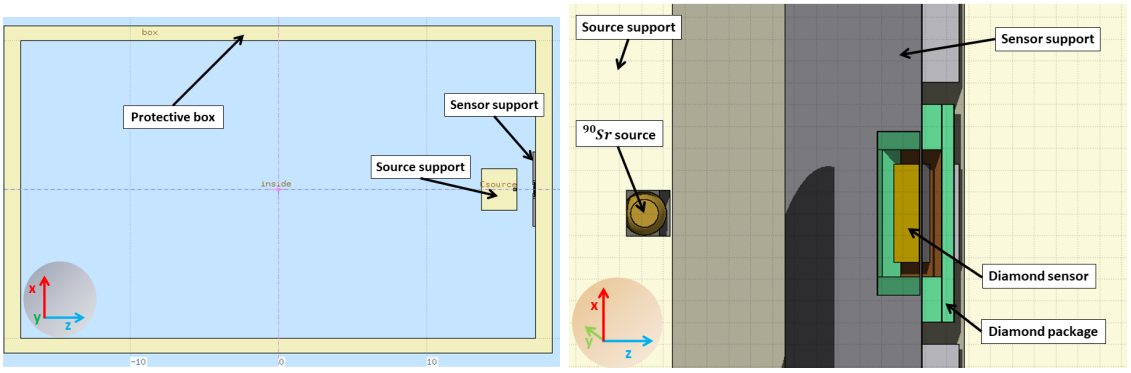

Figure 4.31: Sketch of the experimental setup implemented for the simulation (left) and magnified 3D sketch highlighting the source and the diamond sensor configuration (right).

ceramic sphere and the ^{90}Sr β decay is implemented in FLUKA. I used a simplified model where all energy released in the active volume generates charge carriers. I generated 4.5×10^7 decays at each source-detector distances of the I-d measurements. For each generated decay, the simulation accounts for the energy loss in the crossed materials implemented in the simulation and the energy released inside the detector active volume is saved.

Figure 4.32 shows the distributions of the released energy by β particles in the active volume of diamond (left) and silicon (right) sensors, respectively for the lower (blue) and higher (red) source-detector distances.

In this model, the expected current is expressed as

$$I_{\text{exp}}^{(\text{r})}(d) = 2\,\mathcal{A}\,\frac{E_{(\text{r})}(d)}{E_{eh}^{(\text{r})}}\,q_e\,, \tag{4.20}$$

where the presence of the index "r" identifies the reference-diode quantities; q_e is the charge of the electron; and $\mathcal{A}$ is the ^{90}Sr activity, with the factor 2 to account for the β electrons emitted from ^{90}Sr and ^{90}Y decays. For the diode, I assumed an average ionisation energy $E_{eh}^{\text{r}} = 3.66 \pm 0.03\,\text{eV}$ [92] and a full charge-carrier collection efficiency.

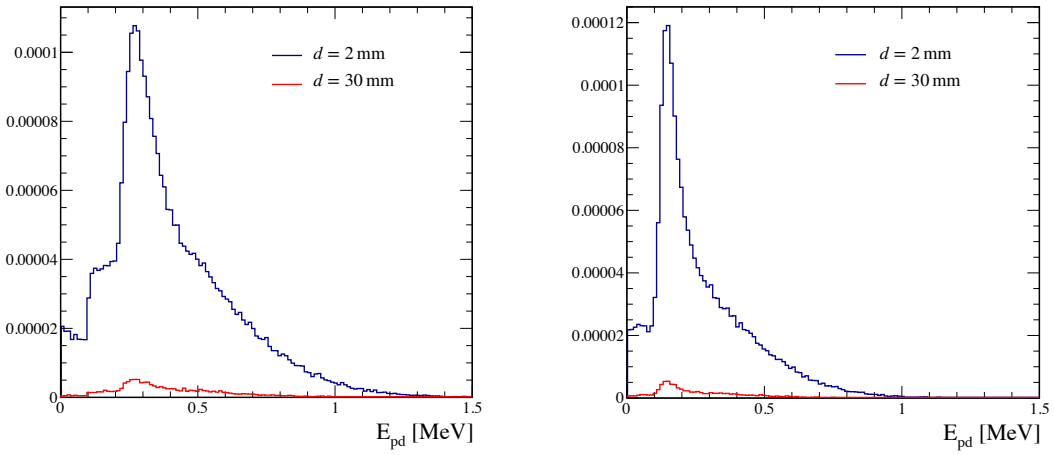

Figure 4.32: Distributions of the released energy by β particles in the active volume of diamond (left) and silicon (right) sensors, respectively for the lower (blue) and higher (red) source-detector distances

The dependence on the source activity cancels out in the ratio of expected currents,

$$R_{\rm exp} \equiv \frac{I_{\rm exp}(d)}{I^{\rm r}_{\rm exp}(d)} = \frac{E(d)}{E_{\rm r}(d)} \frac{E^{\rm r}_{eh}}{E_{eh}}\,, \tag{4.21}$$

which is expected to be constant as a function of d. Any trend versus d can be ascribed to a different offset in the source-detector distance between the measurement with the diamond detector and the diode. In order to observe constant values of R versus d, I corrected the distance introducing a detector-dependent offset, that averages $-0.06\,$mm. This allows for better alignment of the I-d measurement with the diamond detector compared to the reference measurement with the silicon diode. The maximum misalignment is of $0.4\,$mm. This ratio is shown in Figure 4.30, where it is compared with the ratio measured from a diamond detector. The expected and measured values are very close to each other.

Calibration factors

I determine the characteristic constant G for each detector from the ratio

$$\frac{R}{R_{\rm exp}} = \left(\frac{I}{I_{\rm exp}}\right)\left(\frac{I^{r}_{\rm exp}}{I_{r}}\right) = G\,, \tag{4.22}$$

where I assume a precise modelling of the silicon diode (*i.e.* $I_{\rm r} \simeq I^{\rm r}_{\rm exp}$). Figure 4.33 on the left shows the distribution of G determined for the ten diamond sensor of the new production.

The mean value is $\langle G \rangle = 0.97 \pm 0.01$. A value $G = 1$ corresponds on average to fully-efficient detectors, with uniform good-quality crystal ($E_{eh} \approx 13\,$eV assumed for F) and blocking electrodes (since the photoconductive gain is close to unity).

From the measured G, I obtained the calibration factors k reported in Figure 4.33 on the right. On average, the dose rate is about $32.3\,$mrad/s for a measured current of $1\,$nA. The statistical uncertainty on each value of k is negligible with respect to its systematic uncertainty. The values of G and k are listed in the summary Table 4.5.

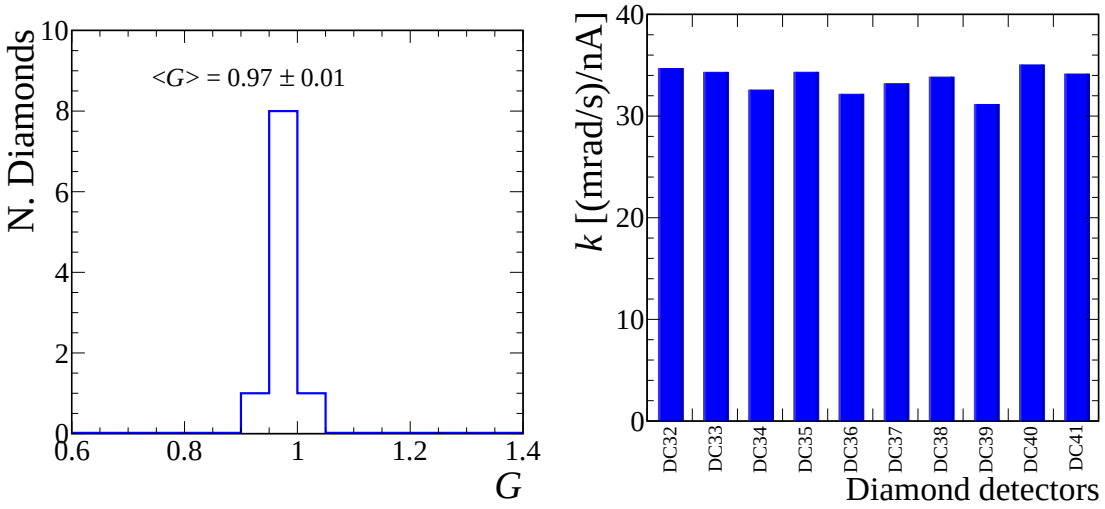

Figure 4.33: (Left) Distribution the of calibration factors G measured from all detectors. (Right) The values of the calibration factor k for each detector.

Systematic uncertainties

I describe here the study I made on the sources of systematic uncertainty that might affect the calibration factor k measured under steady β irradiation.

The largest source of uncertainty is due to possible variations of the signal current due to a transient time to reach a stable value. As discussed in section 4.4.2 most detectors reached a stable output value within 1 s from the start of irradiation, with small fluctuations below 1% under steady irradiation. Some other detectors showed a longer transient time, where the initial values of the current is smaller by approximately 5% than that reached after a certain period of steady irradiation. To account for the different response of the detectors to sudden changes of irradiation conditions, which are expected to occur in the SuperKEKB interaction region, a systematic uncertainty of 5% has been associated to the measurement of the current, which is propagated to the calibration factor.

Another source of uncertainty is related to the reference diode, as I assumed a perfect modelling of its response to obtain G. The estimated current from the diode depends on the ionisation energy, on the charge-collection efficiency, and on the energy released in the active volume. Assuming an uncertainty of 0.03 eV on the ionisation energy, the propagation of this uncertainty to k corresponds to a relative systematic uncertainty of 0.8%. To determine the calibration factor I assumed a fully efficient diode in collecting all generated charge at 100 V bias. This assumption is supported by I-V measurements under irradiation on the diode, and the uncertainty on this assumption can be considered negligible. Since the released energy is proportional to the active volume of the diode used in the simulation, to assess the systematic uncertainty on k, I changed in the simulation the active surface and the depletion thickness by $\pm 0.2\,\mathrm{mm}^2$ and $\pm 10\,\mu$m, respectively, which are the associated uncertainties. These variations corresponds to a minimum and a maximum active volume. For both cases, I computed the released energies as a function of the source-detector distance, and the resulting expected ratio R_{exp} from Eq. (4.21). After taking the difference between each new value of R_{exp} and its nominal value, I considered the largest difference δR_{exp} to assign a relative uncertainty $\delta R_{\mathrm{exp}}/R_{\mathrm{exp}}$. This is propagated to $\delta k/k$ and contributes 4% to the systematic uncertainty.

The same procedure has been used to determine the contribution associated to the

Systematic-uncertainty source	$\delta k/k$ [%]
Current transients and fluctuations	5
Silicon-diode volume	4
Package shielding (diamond detectors)	2
Measurement of source-detector distance	1
Silicon ionisation energy	< 1
Package shielding (diode)	< 1
Simulation approximations and statistic	< 1
Source description	< 1
Total	7

Table 4.2: Relative systematic uncertainties in % on the calibration factor k, obtained for the calibration with β irradiation.

uncertainty on the thickness of the aluminium packaging that impacts the released energy. I varied in simulation the thickness of the aluminium cover by $\pm 5\,\mu$m, which is the uncertainty associated to the cover used in the diode packaging. Other sources that affect the released energy, such as a $0.1\,\mu$m layer of silicon oxide on the surface (the diode area is metallised only around the edge), were estimated and they have a negligible contribution. The aluminium packaging affects the estimation of the released energy in the diamond detectors in a similar fashion as for the diode, and the impact from the uncertainty on its thickness is computed with the same procedure. The resulting systematic uncertainty is $\delta k/k = 2\%$.

The measured values of R are expected to be constant as a function of d, and any trend versus d can be ascribed to a different offset in the source-detector distance between the measurement with the diamond detector and the diode. The distance has been corrected introducing a detector-dependent offset, which align the I-d measurement with the diamond detector to the reference one with the silicon diode. Without the offset correction, the average value of R changes by 1%. This change as a relative systematic uncertainty of 1%.

The value of R_{exp} depends also on the ionisation energy of the diamond detector, on the released energy inside its active volume, and on its charge-collection efficiency. Departures of all these factors from the values assumed in the calculation of the estimated current are accounted for by the characteristic constant G. Moreover, any variation on G due to an uncertainty on the value of the ionisation energy, or that on the detector volume, are counterbalanced by a variation of F in the definition of k in Eq. (4.15). Therefore, these two sources do not enter in the computation of the systematic uncertainty.

Another source that may affect the released energy is the uncertainty on the active volume between the electrodes of the diamond detectors, since the electric field on the edges is not necessarily uniform, affecting the charge collection efficiency. This source has found to be negligible.

As for what concerns the charge-collection efficiency, a departure from the assumed value of 100% is included in the characteristic constant G measured for each detector. A possible source of uncertainty is due to small fluctuations of the voltage provided by the power supply, which presented variations of $\delta V/V \approx 0.5\%$. From the I-V results presented

in section 4.4.2, only sub-percent changes of the efficiency is expected for 0.5 V variation around a 100 V bias. Therefore,the associated systematic uncertainty on k is negligible.

The statistical uncertainty from the size of the simulated samples contributes a negligible uncertainty too. Uncertainties related to other assumptions entering the simulation, such as the transport model used in FLUKA for the β electrons, are found to be smaller than 1%, as these contributions are greatly reduced in the ratio of Eq. (4.21). For the same reason, an imprecise modelling of the β source (material, density, fraction of radioactive nuclei) contributes only a sub-1% systematic uncertainty.

All the relative contributions to the calibration factor systematic uncertainty are summarised in Table 4.2. Summing in quadrature all the contributions I obtain a total relative uncertainty of 7%.

4.5 Characterisation with *X* radiation

The characterisation with X radiation aims to check the response of our diamond detectors to X-rays in a energy range between few keV to 50 keV, to determine calibration factor with a different irradiation source and over a wider range of dose rates and also to compare it with the β source values. Part of this spectrum is interesting because the first layer of PXD is affected by the synchrotron radiation ($\sim$ 10 keV) produced from the SuperKEKB accelerator. These tests also aim to verify that the diamond detectors are sensitive to the softer part of the synchrotron radiation. In the energy range of 0-50 keV, X-rays primarily interact with diamond through the photoelectric effect, where photons are absorbed by inner-shell electrons, creating photo-electrons. This interaction leads to the production of charge carriers in the diamond lattice, generating an electrical current. Compton scattering, though less significant at these energies, can also contribute to charge carrier generation. I study the dependence of the output current on the intensity of the X radiation and its energy, and I determine current-to-dose rate calibration factor, evaluating the systematic uncertainties and comparing the results to the ones obtained with the β radiation.

4.5.1 Experimental setup and measurement methods

The experimental setup is composed of:

- a CAEN DT1471ET [93] power supply to provide a bias voltage to the diamond sensors in the range from -600 V and $+600$ V;
- the 4-channels picoamperometer (model AH501 provided by Sincrotrone Trieste) [94], used also in the characterisation with the β radiation and presented in section 4.4;
- a radiation source provided by the "Amptek Mini X-2", a very compact X-ray tube [78], described in Section 4.2.3;
- an aluminium support for the sensor that align the source and the detector centre, as shown in Fig 4.34. In order to reduce photon backscattering, the detector fixation on the support is made of Plexiglas.

The X-ray tube and the sensor support are placed inside a protective box made of aluminium and lead layers. An ad-hoc support has been designed to centre the detector on the symmetry axis of the tube and place it at a minimal distance of $d = 0.85$ cm from the collimator.

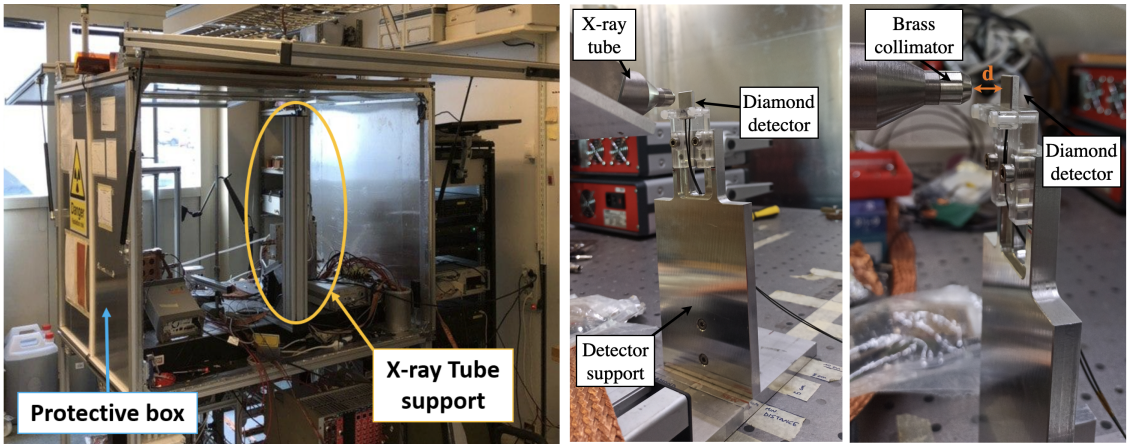

Figure 4.34: Pictures of the apparatus: (left) the protective box and the X-ray source support; (right) the X-ray source and the detector placement.

All measurements are done using two optimal operation bias voltage ±100 V, determined with β characterisation as reported in Section 4.4.3. Same as for β characterisation, the bias voltage is always applied to the back-side of the diamond sensor, while the other side is set to ground. I measured the output current, induced by charge-carrier drift in the diamond bulk, using the picoammeter connected to the front-side cable, with a sampling time of 1 s. The procedure for the measurements is briefly outlined as follows:

Linearity After applying the bias voltage, a measurement of dark current is done sampling the output current from the sensor for a time period of 3 minutes. Then, the X-ray tube is switched on. Setting the voltage V_{set} to a fixed value, the output current is measured for about 10 minutes for different values of I_{set}. This procedure is iterated for two different values of V_{set}, 20 kV and 40 kV, for all the detectors.

The linearity measurements target to check the expected linear relation between the output current and the current I_{set} of the X-ray tube, which is proportional to the intensity of the radiation. The measured current are employed for the calculation of the calibration factors, using the silicon diode as a reference, as explained in section 4.5.2. The silicon diode is used applying a +100 V reverse bias to the back-side electrode. Since the this sensor has a very stable response under a steady irradiation and a long exposure can damage the sensor, I measured the output current with irradiation for a period lower than 3 minutes.

4.5.2 Current-to-dose rate calibration

The calibration factor is determined with the diamond-to-diode calibration method described in Section 4.4.3. The method consists in three different steps:

- measurement of the signal-to reference ratio of currents, determined comparing the *signal* current from the diamond detector to the *reference* current from the diode, both measured at the same source-detector conditions;
- computation of the expected ratio of currents, using the released energy per photon obtained from the simulation of the setup to compute the expected currents;
- determine the characteristic constant G, and so the calibration factor k, from the ratio between the signal-to-reference ration and the expected ratio.

Thanks to this method, the dependence of the photons flux cancels out and the uncertainties related to the source are reduced.

Analysis of the linearity measurements and signal-to-reference ratio

For each sample in the linearity measurements, I calculated the mean output current I_{mean} from the values of current measured with irradiation, and the mean dark current I_{dark} from the currents measured without any radiation. The dark current is generally around $\sim 3\,\text{pA}$ for the diamond detector and around $\sim 10\,\text{pA}$ for the silicon diode. I subtracted the dark current to each value of the mean output current to obtain the current I_m.

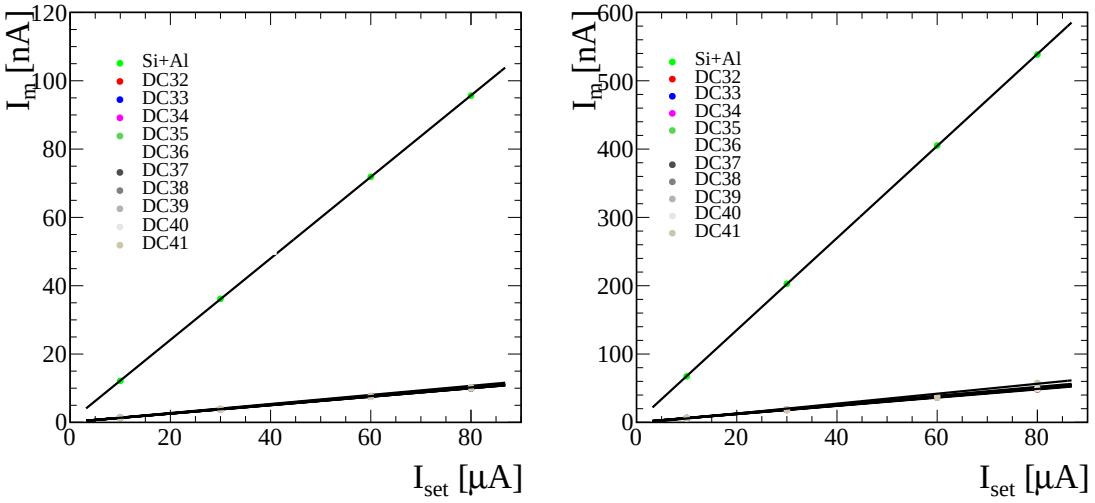

Figure 4.35: Plot of the measured current I_m versus I_{set}, for two different energy spectra, respectively for $V_{\text{set}} = 20\,\text{kV}$ (left) and $V_{\text{set}} = 40\,\text{kV}$ (right). The uncertainties are not visible because of their small size compared to that of the markers.

Figure 4.35 shows the plot of the measured current I_m as a function of I_{set}, both for the diamond detectors and the silicon diode, obtained for two different energy spectra, *i.e.* for a fixed voltage V_{set} of 20 kV and 40 kV on the X-ray tube. A fluctuation of $0.1\,\mu\text{A}$ of the value of I_{set} has been observed during the measurements. This fluctuation is assigned as an uncertainty to I_{set}. A fit with a linear function is done to verify the dependence of I_m on I_{set} and to determine the slope and intercept parameters. The output currents measured in same conditions present similar values for the different diamond sensors.The intercepts parameters of the fits are of the order of a few pA, compatible with zero within uncertainty for most of the cases. Moreover, the current measured with the silicon diode is about eight times higher than that measured with the diamond sensor. This difference is due to the fact that, for the same energy spectrum of incident photons, silicon has a longer attenuation length compared to diamond. This results in a greater number of photons being detected by the silicon diode, leading to a higher measured current.

The signal-to-reference ratio of currents,

$$R \equiv \frac{I(I_{\text{set}})}{I_{\text{r}}(I_{\text{set}})}\,, \tag{4.23}$$

is constant versus I_{set} for both the energy spectra, as shown in the Figure 4.36.

The flatness of R denotes that the measured values of current for the different source intensities are compatible in the two sets of data.

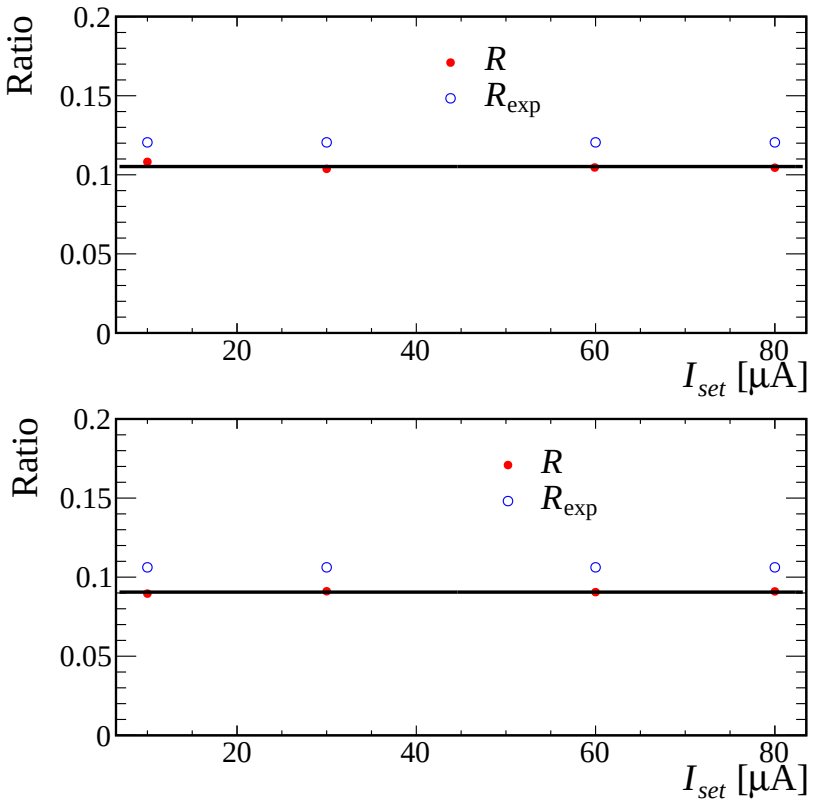

Figure 4.36: The signal-to-reference ratio of currents R compared to the expected ratio R_{exp} from Eq. (4.25), as a function of I_{set}, respectively for $V_{\mathrm{set}} = 20\,\mathrm{kV}$ (top) and $V_{\mathrm{set}} = 40\,\mathrm{kV}$ (bottom).

Computation of the expected ratio of currents

Same as for β calibration, the expected signal and reference currents have been computed from the energy released per photon E_{pp} in the detector volume, E (E_{r}), obtained from the Monte-Carlo simulation of the full experimental setup. The expected current can be defined as

$$I^{(\mathrm{r})}_{\mathrm{exp}}(V_{\mathrm{set}}, I_{\mathrm{set}}) = \Phi(V_{\mathrm{set}}, I_{\mathrm{set}})\, \frac{E^{(\mathrm{r})}_{\mathrm{pp}}(V_{\mathrm{set}})}{E^{(\mathrm{r})}_{\mathrm{eh}}}\, q_{\mathrm{e}}\,, \tag{4.24}$$

where the presence of the index "r" identifies the reference-diode quantities. In the formula $\Phi(V_{\mathrm{set}}, I_{\mathrm{set}})$ is the photon flux, which is proportional to the X-ray tube current I_{set} and varies also with the energy spectrum through V_{set}; E_{pp} is the energy released per photon for the given energy spectrum of the source; E_{eh} is the energy to create a $e^{-}h^{+}$ pair; q_{e} is the elementary charge.

The dependence on the photon flux cancels out in the ratio of expected currents,

$$R_{\mathrm{exp}} = \frac{I_{\mathrm{exp}}(V_{\mathrm{set}})}{I^{\mathrm{r}}_{\mathrm{exp}}(V_{\mathrm{set}})} = \frac{E_{\mathrm{pp}}(V_{\mathrm{set}})}{E^{\mathrm{r}}_{\mathrm{pp}}(V_{\mathrm{set}})}\frac{E^{\mathrm{r}}_{eh}}{E_{eh}}\,, \tag{4.25}$$

which is constant as a function of I_{set}. This ratio is shown in Figure 4.36, where it is compared with the measured signal-to-reference ratio. The expected and measured values are very close to each other.

I estimate the energy released by the X-rays in the diamond sensor and in the silicon diode considering the different energy spectra set by the voltage V_{set} at the source. The estimate of the energy released per photon exploits a simulation in FLUKA [77] of the experimental setup.

The X-ray source is simulated as a focal spot with a diameter of 2 mm and a uniform distribution over an angle of 40°, as shown in the scheme of Figure 4.37 on the right. Figure 4.37 on the left shows a three dimensional draw of the simulated setup. A brass cylindrical collimator is placed immediately after the focal spot, between the source and the detector.

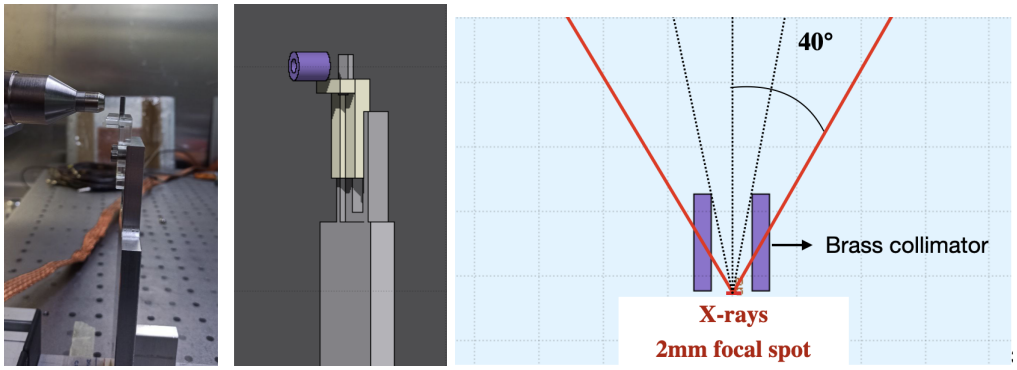

Figure 4.37: (Left) 3-Dimensional draw of the simulated setup and picture of the experimental setup. (Right) Scheme of the simulated X-ray source and the brass collimator place at exit of the X-ray tube.

For each generated photon from the source, the simulation returns the energy released inside the detector volume, taking into account all cross sections for the interaction with the different materials along the path (mainly photoelectric effect and a small fraction of Compton scattering) and the geometrical efficiency.

A weighting method is used to account for the different energy spectra produced by the voltages V_{set} at the source. The range 0–50 keV is split in intervals of equal width (bins), each corresponding to a bin of the histograms of the spectrum in Fig. 4.38. For each bin, 5×10^4 photons are generated with a flat energy distribution in the interval, and the results of the interaction of these photons are saved independently for each detector configuration. The released energies from all photons in a bin are weighted with the content of the bin of the histogram of the source-energy spectrum, which differ for the five values of V_{set}. The resulting distribution of the weighted released energies is normalised to represent the distribution of the energy released per photon, by dividing the integral with the total number of generated photons.

Figure 4.38 reports the distribution of the released energy per photon obtained both for diamond and silicon detectors, respectively for the $V_{\text{set}} = 20$ kV and 40 kV energy spectra of the source. Moreover, the spectrum for the diamond sensor has an higher number of events with energy lower than 1 keV. This is explained by an higher contribution of the Compton scattering in this case, for which photons loose part of their initial energy. The released energy per photon for a given detector configuration, E_{pp}, is calculated by integrating the energies of the corresponding distribution ($\mathrm{d}n/\mathrm{d}E$) shown in Fig. 4.38,

$$E_{\text{pp}} = \int_{E_{\text{min}}}^{E_{\text{max}}} E \, \frac{\mathrm{d}n}{\mathrm{d}E} \mathrm{d}E \, . \tag{4.26}$$

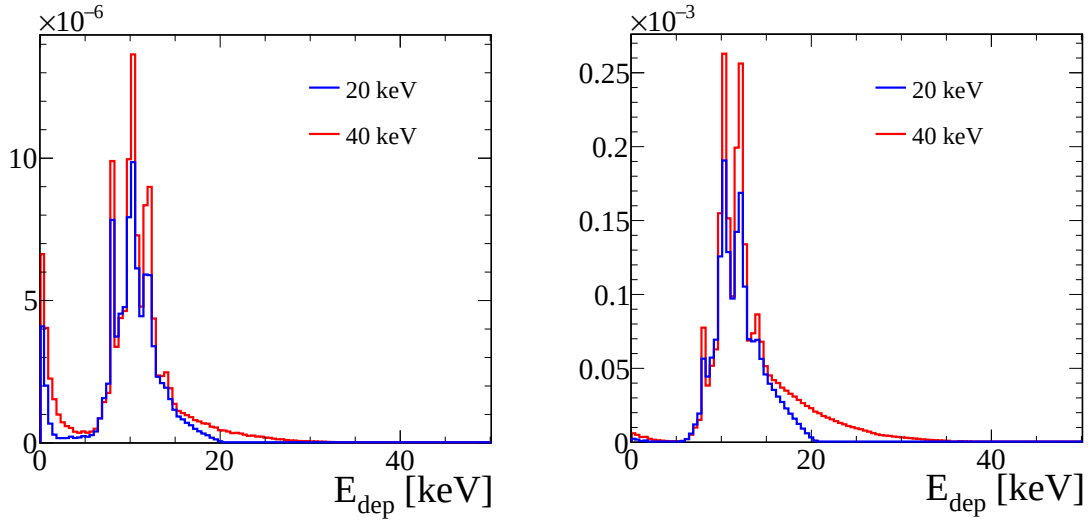

Figure 4.38: Distributions of the released energy per photon resulting of the simulations with the diamond detector (left) and the silicon diode (right), respectively for the spectra at 20 kV and 40 kV.

Current-to-dose calibration

In the same way as in Section 4.4.3, the characteristic constant G for each detector is determined from the ratio

$$\frac{R}{R_{\text{exp}}} = \left(\frac{I}{I_{\text{exp}}}\right)\left(\frac{I^{r}_{\text{exp}}}{I_{r}}\right) = G\,, \tag{4.27}$$

where I assume a precise modelling of the silicon diode (*i.e.* $I_{\text{r}} \simeq I^{\text{r}}_{\text{exp}}$).

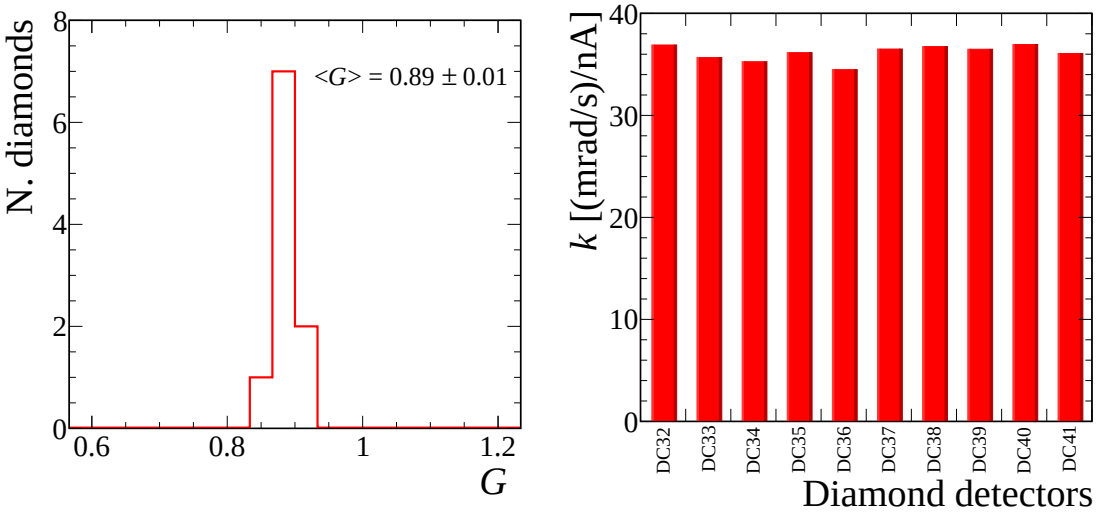

Figure 4.39: Result of the calibration for the energy spectrum $V_{\text{set}} = 20$ kV: (left) distribution the of calibration factors G measured from all detectors; (right) the values of the calibration factor k for each detector.

Figures 4.39 and 4.40 on the left show the distribution of G determined for the ten diamond sensor of the new production, respectively for the two different energy spectra.

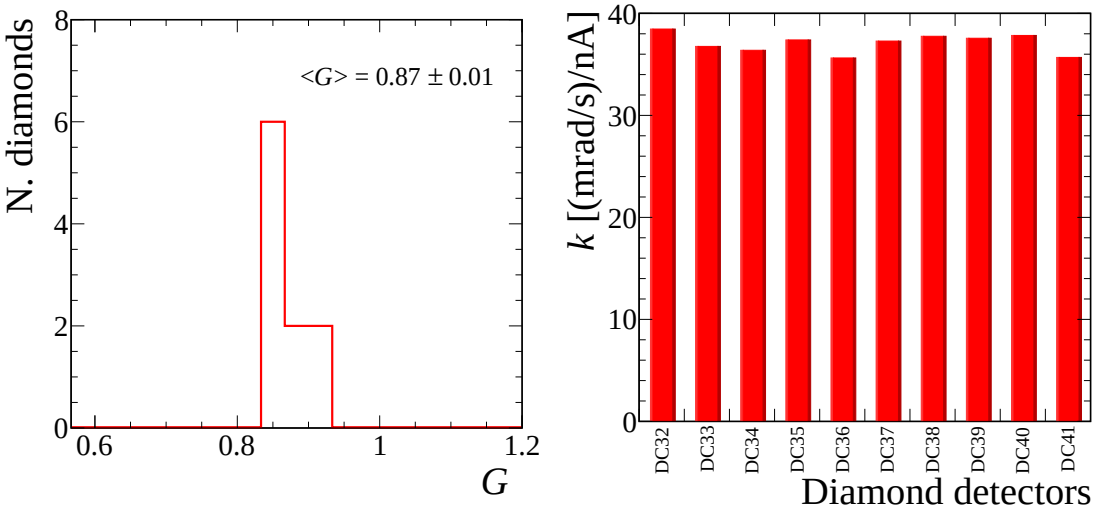

Figure 4.40: Result of the calibration for the energy spectrum $V_{\text{set}} = 40\,\text{kV}$: (left) distribution the of calibration factors G measured from all detectors; (right) the values of the calibration factor k for each detector.

The two values of G obtained for the different spectra are $\langle G \rangle = 0.89 \pm 0.01$ and $\langle G \rangle = 0.87 \pm 0.01$. The two values are compatibles within two standard deviations, but they are about 10% lower than the value of G obtained with β calibration. Nevertheless, the calibration results for the different sources are compatible taking into account also the systematic uncertainty. The calibration factors are obtained multiplying the characteristic constant G times the constant F of Eq. 4.16. The resulting calibration factors for the ten diamond detectors are reported in the right plot of Figures 4.39 and 4.40.

Systematic uncertainty

As for β source, I studied the sources of systematic uncertainty that may affect affect the calibration factor measured under a steady X irradiation. The main sources are reported in Table 4.3.

Systematic-uncertainty source	$\delta k/k$ [%]
Current transients and fluctuations	5
Silicon-diode active area	4
Package shielding and detectors thickness	3
Detector-collimator distance	1
Silicon ionisation energy	< 1
Simulation approximations and statistic	< 1
Source description	< 1
Total	8

Table 4.3: Relative systematic uncertainties in % on the calibration factor k, obtained for the calibration with X irradiation.

The sources related to the diamond detector response and to the property of the material, such as the the silicon ionisation energy, remained the same as determined for β calibration factors presented in Section 4.4.3. The main source of systematic uncertainty is thus related to possible variation in the signal current due to a transient time, which was already explained before.

All the other sources affecting k enter in the estimation of the expected ratio R_{exp}, and so in the released energy per photon through the simulation of the experimental setup.

The dominant uncertainty is the related to the active volume of the diode used in the simulation. I calculated the released energy $E^{(r)}_{\rm pp}(V_{\rm set})$ by varying in the simulation the active surface and the thickness of depleted region of the diode by $\pm 2\,{\rm mm}^2$ and $\pm 10\,\mu$m respectively. These variation correspond to a minimum and maximum active volume. From the computed released energies I determine the relative uncertainty on $R_{\rm exp}$, which correspond to $\delta k/k = 4\%$. Another source is related to the thickness of the layers of silicon, diamond and aluminium in the detector configurations. Any uncertainty due to the electrodes thickness is negligible since these layers are thinner than the sensor volume, and the photons have a very low interaction probability there. To determine this uncertainty I consider the larger difference on the released energy due to an larger or smaller thickness of the sensor and the cover. Since a higher variation of $E_{\rm pp}$ is expected either for an higher sensor thickness and a lower cover thickness, and *vice versa*, the uncertainty is calculated as

$$\Delta E^{\rm det}_{\rm pp} = \max\Big\{\big|E^{\rm det}_{\rm pp}(x_{\rm Si/Di}, x_{\rm Al}) - E^{\rm det}_{\rm pp}(x_{\rm Si/Di} + \Delta x_{\rm Si/Di}, x_{\rm Al} - \Delta x_{\rm Al})\big|\,; \qquad (4.28)$$
$$\big|E^{\rm det}_{\rm pp}(x_{\rm Si/Di}, x_{\rm Al}) - E^{\rm det}_{\rm pp}(x_{\rm Si/Di} - \Delta x_{\rm Si/Di}, x_{\rm Al} + \Delta x_{\rm Al})\big|\Big\}\,,$$

varying in the simulation the thickness of the diamond (silicon) detector and the aluminium cover. I varied the diamond and silicon thicknesses of $\pm 6\,\mu$m and $\pm 10\,\mu$m respectively, while the thickness of the aluminium cover of $\pm 5\,\mu$m. The values of the relative variation of $R_{\rm exp}$ for different configurations for the two spectra are reported in Table 4.4.

	$\delta E/E(V_{\rm set} = 20\,{\rm kV})$	$\delta E/E(V_{\rm set} = 20\,{\rm kV})$
$x_{\rm Di} + \Delta x_{\rm Di}, x_{\rm Al} - \Delta x_{\rm Al}$	2.89 %	2.54 %
$x_{\rm Si} + \Delta x_{\rm Si}, x_{\rm Al} - \Delta x_{\rm Al}$	2.12 %	1.63 %
$x_{\rm Di} - \Delta x_{\rm Di}, x_{\rm Al} + \Delta x_{\rm Al}$	1.42 %	0.99 %
$x_{\rm Si} - \Delta x_{\rm Si}, x_{\rm Al} + \Delta x_{\rm Al}$	1.71 %	0.36 %

Table 4.4: Relative uncertainty on the released energy per photon, obtained for the four different configuration in Eq. 4.28.

The maximum relative systematic uncertainty on the energy is 3%, and so $\delta k/k$ corresponds to 3%. Another systematic source is the source-detector distance: the position of the detector support respect to brass collimator positioned in front of the source target is know with an uncertainty of $\pm 2\,$mm. I varied the source distance in the simulation, obtaining a maximum relative uncertainty on the expected ratio of 1%. This is propagated to $\delta k/k$ and contributes 1% to the systematic uncertainty.

Summing in quadrature all the contributions listed in Table 4.3 I obtain a total relative uncertainty of 8%.

4.6 Summary of the characterisation results and installation on the new beam pipe

The main results of the characterisation of the ten diamond detectors are summarised in Table 4.5. The measured values of the mean ionisation energy are consistent within 3.5% with the value of 13 eV usually quoted in literature for high-quality diamond sensors [91], proof of the crystals high quality and purity. All detectors show a stable response under steady irradiation, both β and X, for at least one of the two polarities. The time necessary to reach a current greater than 90% of the stable current is of the order of 1 s for all ten detectors. All diamonds except one have an asymmetric characteristic curve. Based on the stability results and the measured characteristic curves, I selected the optimum operating bias voltage shown in the Table 4.5, which correspond to the bias voltage applied to the back-side electrode. For each detector I determined the characteristic constant G both with β and X steady irradiation. The calibration factors obtained with β irradiation and used for each diamond detector are reported in the last column of Table 4.5. The values of k obtained from the calibration with X irradiation are consistent within the systematic uncertainties, but 10% systematically higher.

Diamond	α irradiation	β irradiation		k [(mrad/s)/nA]
detector	ϵ_{eh} [eV]*	$V_{\text{bias}}^{\text{op}}$ [V]**	G	
DC32	12.62 ± 0.41	+100	0.982 ± 0.025	32.84
DC33	12.63 ± 0.38	+100	0.931 ± 0.016	34.64
DC34	12.57 ± 0.35	−100	0.938 ± 0.014	34.61
DC35	12.91 ± 0.42	+100	0.945 ± 0.019	34.14
DC36	13.15 ± 0.47	+100	0.949 ± 0.016	33.98
DC37	12.91 ± 0.37	−100	0.931 ± 0.019	34.64
DC38	13.60 ± 0.38	−100	0.972 ± 0.015	33.19
DC39	12.97 ± 0.45	−100	0.957 ± 0.020	33.72
DC40	12.94 ± 0.36	±100	0.937 ± 0.015	34.42
DC41	12.98 ± 0.22	+100	0.928 ± 0.027	34.78

Table 4.5: Summary of the results from the measurement with different irradiation. * average of electron- and hole- mean ionisation energies. ** optimal operation bias voltage applied to the back-side electrode.

Thanks to their stable response all the sensors are suitable to be used in the Belle radiation monitor and beam abort system. In February 2023 I installed eight out of ten diamond detector on the new Belle II beam pipe. Two dedicated tungsten mounting blocks, used to fix the diamond detectors, are positioned on the beam pipe directly in front of the central chamber on both the FWD and BWD sides. The holder allows four diamonds to be fixed on each side by means of a peek plate, as shown in the Figure 4.41. The positions of the diamonds are the same for both sides and are numbered from 0 to 3 for the angles of 35°, 145°, 215° and 325°, defined clockwise with respect to the Belle II reference system. The diamond cover faces the inside of the beam pipe.

I assigned to each diamond a signal cable (SN) from which the output current is read and a high voltage cable (HV) from which the bias voltage is applied to the detector,

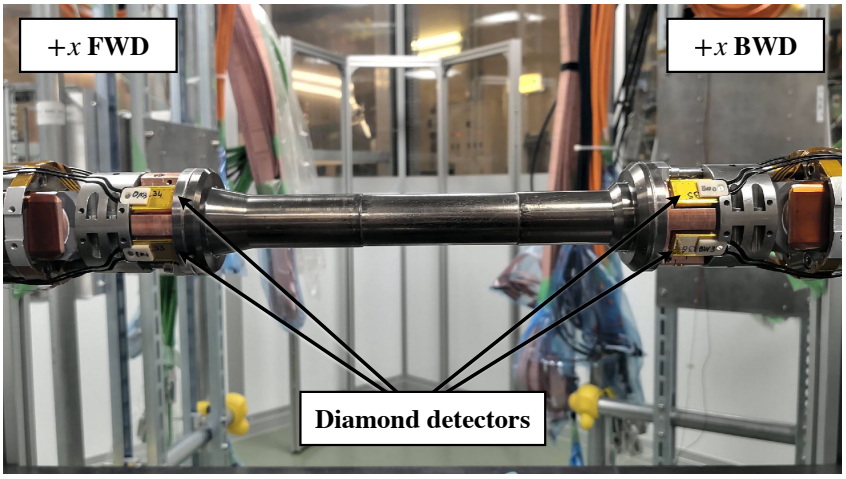

Figure 4.41: Beam pipe $+x$-side with four diamond detectors installed, two on FWD-side and two on BWD-side.

labelling the cables of each diamond detector. Since in the experiment the DCU, described in Section 3.1.3, can only provide a positive bias voltage, I assigned the HV to the back-side when the operating voltage is positive, and to the front-side when the voltage is negative. This is possible because the response of the diamond doesn't change when a positive bias is applied to one electrode or a negative bias to the other.

For each diamond, after installing the detector on the beam pipe, I carried out functional tests to check that the device was working. The tests consists in verifying that the detector dark current and noise is low and check the transient response of the detector by using a β source. The instrumentation used for the tests is similar to the one used in the β and X characterisation procedures:

- the CAEN [93] power supply;
- the AH501B [94] picoamperometer;
- a ^{90}Sr β source with $\sim 2\,\text{MBq}$ activity, deposited with a circular shape on a metal disk. The source has a dedicated holder that allow to easily place the source in front of the detector.

The positioning of the source for testing the diamond is shown in the Figure 4.42 on the left. The plot on the right shows the output current as a function of time. Without the source, the measured current is less than 1pA, whereas when the source is switched on, the current rises instantaneously to approximately 60pA within 2 seconds. Since the flux of β particles crossing the active volume of the detector is rather low, the current measure with the diamond for a source detector distance of few millimetres is much lower than the current measured with our experimental step in Section 4.4.3.

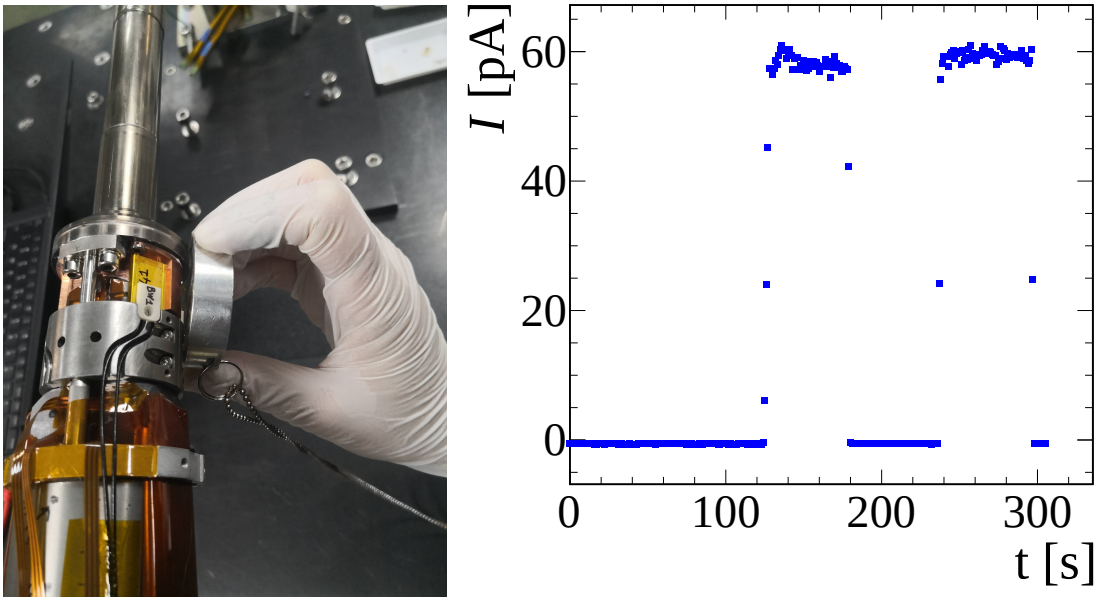

Figure 4.42: (left) ^{90}Sr source placement in front of one of the diamond detectors installed on the beam pipe. (right) Output current as a function of time: the current transient time, when the source is placed in front of the detector is of the order of 1 s.

Chapter 5

Transient response of diamond detectors to sub-picosecond high-intensity electron bunches

In this chapter I describe my investigations of the transient response of our diamond detectors to intense 1 GeV electron bunches. The tests were carried out at the linac of FERMI free-electron laser in Trieste, where a test station for testing small devices such as our diamond detectors was designed and installed. In Section 5.2 I describe the experimental setup and I outline the overall measurement procedure in Section 5.3. A good knowledge of the beam bunch charge and dimensions is crucial to determine the number of electrons incident on the detector and their spatial distribution. These studies also provide an important feedback for operating the machine at lower charge. Section 5.4 shows the beam optimisation studies carried out in successive irradiation campaigns up to the final beam tuning. In sections 5.5 and 5.6 I present the main results of this study. I presented the work described in this Chapter at the conferences [99] and [100].

5.1 Introduction

In Chapter 4 I described the calibration of the detector current to dose-rate response with different radiation sources, for dose rates up to 100 mrad/s, in stationary or quasi-stationary conditions. Nevertheless, the harsh radiation environment at the luminosity frontier requires an investigation of diamond's response to large and fast radiation transients, such as those induced by intense high-energy electron pulses. Thanks to the high mobility of their charge carriers, diamond detectors can generate very fast signals. However, in the case of large ionisation energy deposition in a small volume of the diamond, the large concentration of excess charge carriers in the diamond bulk gives rise to space charge effects [101], that may distort the electric field and affect the signal amplitude, integral and shape.

Specific additional tests are needed in order to assess the transient response to fast and intense radiation bursts, which may lead to non-linear effects in the collection of ionisation charges. For this purpose we studied the diamond's transient response to collimated, sub-picosecond, $\sim$ 1 GeV electron beam bunches, with a bunch charge $\leq$ 100 pC, provided by the linac of FERMI in Trieste [102, 103]. In normal operation FERMI provides bunch charges between 500 and 1000 pC, but for test purpose the charge can be lowered down to $\sim$ 10 pC. To operate in these conditions, specific beam optimisation studies are needed.

As described in Chapter 4.4.3, to determine the current-to-dose-rate calibration factors

of our diamond detectors, I used a radioactive β source providing a steady flux of ionising electrons at MHz rates. Under these conditions the measured current, varying from tens of pA to a few nA, is the time average of current pulses from the individual, well separated ionising tracks with an average time separation > 1000 ns. The charge generated by ionisation, of about 10^4 electron-hole pairs per track, is totally collected: a proof is given by the I-V characteristic curve measured under β irradiation, where a collection efficiency of $\sim 100\%$ is observed for bias voltages higher than 80 V. Therefore, no significant space charge effect is expected to distort or shield the electric field. The linearity of the response of the detector is verified over six orders of magnitude, up to μA currents, using different steady radiations.

However, in the case of large beam losses in the SuperKEKB interaction region, the radiation field can produce signals up to several mA. Assuming a uniform electric field, the current could be defined as

$$I = nq_e v_{\text{drift}} S\,, \tag{5.1}$$

where n is the carrier density, $q_e = 1.6 \times 10^{-19}$ C, $v_{\text{drift}} = \mu E$ and S in the sensor area. For a current of $I = 5$ mA, the ionising carrier concentration in the diamond bulk is $n \simeq 6 \times 10^{10}\,\text{cm}^{-3}$. Under the hypotheses of uniform and slowly varying irradiation, the net space charge accumulated may still be negligible and the electric field approximately uniform.

However, rapidly varying or non-uniform irradiation could produce transient space charge and non-uniform electric field with non-linear effects. As a result, unlike the steady continuous radiation that is well calibrated for our diamond system [72], the dose rate estimated for radiation bursts that have spike-like time dependence might suffer from non-linear effects and lead to an underestimated dose value.

In the irradiation with intense 1 GeV electron bunches at the FERMI e^- linac the detector is subject to extreme transient conditions. Preliminary estimates have been made assuming a bunch charge of 1 pC, corresponding to 6×10^6 electrons, a duration of $\delta t = 1$ ps and a longitudinal and transverse size of $\delta z = 300\,\mu$m and $\sigma_{xy} = 100\,\mu$m respectively, with a flat distribution in the transverse dimension.

Since 1 GeV electrons are minimum ionising particles (MIPs), the approximate stopping power is $\frac{dE}{dx} \simeq 2\text{MeVg}^{-1}\text{cm}^{-2}\,\rho_{\text{diam}} \simeq 7\,\text{MeVcm}^{-1}$. The average energy loss of an incoming electron in the diamond thickness of 500 μm is $\Delta E = 0.35$ MeV; with an average ionisation energy per electron (e) - hole (h) pair of about 13 eV, this corresponds to about 2.7×10^4 e-h pairs injected per incoming electron. Assuming that the beam has a symmetric distribution on the transverse plane, the diamond volume crossed by the beam may be considered cylindrical, where the cross-section radius is related to standard deviation σ_{xy} of the bunch core. Given the sensor thickness $d = 0.5$ mm and the nominal beam size $\sigma_{xy} = 100\,\mu$m, the crossed volume is roughly $V \simeq 1.6 \times 10^{-5}$ cm^3. Therefore a bunch carrying a charge of 1 pC can locally inject e-h concentrations up to about $10^{15}\,\text{cm}^{-3}$ in a limited volume and in a time interval of 1 ps. It is necessary to determine the fraction of the charge generated in the diamond bulk which is collected.

As shown in the left scheme of Figure 5.1, the charges move in the diamond either through diffusion or drift, the latter due to the electric field generated between the two electrodes. The displacement due to diffusion can be considered negligible over a short time interval. When electrons and holes begin to drift in the external electric field towards the two opposite electrodes, an unbalanced negative (positive) space charge appears near the anode (cathode), see Fig. 5.1 on the right, leaving a balanced neutral volume in the diamond bulk.

The unbalanced charges in a thickness L near the two electrodes contribute with an

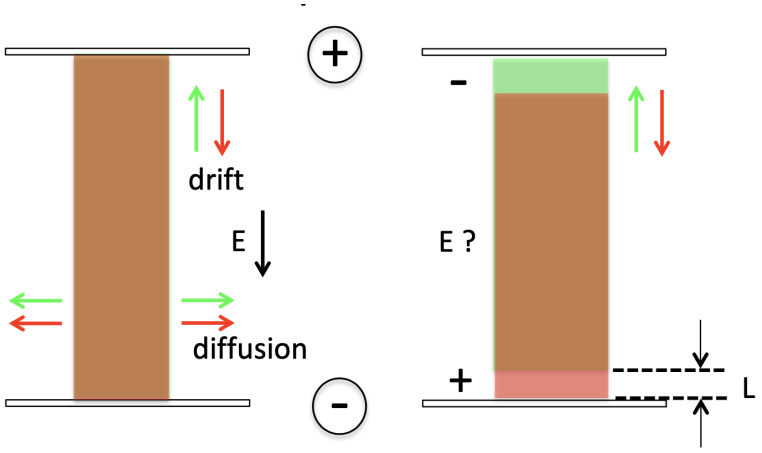

Figure 5.1: Schematic representation of two consecutive phases of charge collection inside a diamond bulk when an electric field E is generated between two electrodes. In the brown volumes, both negative and positive charge carriers are present in equal amounts. The green and red volumes close to the electrodes represent, respectively, the unbalanced concentration of negative and positive charge carriers, which develops in approximately $\mathcal{O}$(ns).

additional "built-in" electric field $2E_i$. When the "built-in" electric field compensates the external electric field, the charge carriers still present in the volume with zero net electric field do not drift. The unbalanced charge near the electrode, quickly (in time of the order of femtoseconds) induces the conductors to rearrange their charges in order to keep a constant potential. To roughly estimate the thickness L needed to produce an approximate opposite "internal" electric field of the same order of the pre-existing "external" one, the charge distribution close to the diamond surface and the corresponding opposite image charge recalled in the metallic electrodes can be approximated as a dipole.

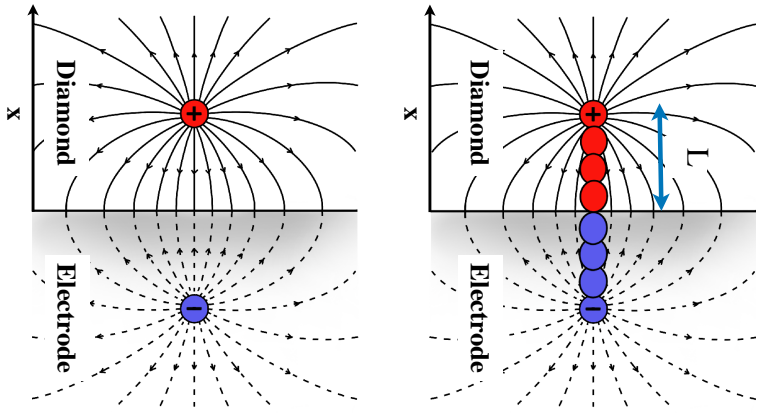

Figure 5.2: Scheme of the dipole approximation process, where the red charge is the one drifting in the diamond bulk and the blue one is the image charge in the electrode.

Assuming that the charges are uniformly distributed along a line in the diamond, and thus also the image charges in the electrode, as shown in Fig. 5.2, the electric field along

the line x is approximated as

$$E = \frac{\lambda L}{4\pi\epsilon_0\epsilon_r}\frac{1}{x}\left(\frac{1}{x-L} - \frac{1}{x+L}\right), \tag{5.2}$$

where λ is the linear charge density, L is the thickness with the unbalanced space charge near the electrodes, necessary to produce a "built-in" E-field of the same order as the pre-existing "external" E-field, ϵ_0 is the vacuum dielectric constant and $\epsilon_0\epsilon_r$ is the diamond dielectric constant. The "built-in" field generated by these charge distributions, added to the external field, changes the distribution of the electrostatic potential: the electric field is initially confined to thin layers close to the electrodes, while in the intermediate volume the electric field is zero. By applying an electric field of $E = 2 \times 10^5\,\mathrm{V/m}$ at the centre of the diamond $x = 250\,\mu\mathrm{m}$, which corresponds to $V_{bias} = 100\,\mathrm{V}$, the thickness L is of the order of tens of microns: it takes $\Delta t = L/v_{\mathrm{drift}}$, of the order of nanoseconds, to create unbalanced space charge distributions by carrier drift.

As shown in Section 4.3, the drift and collection of carriers at the opposite electrodes, for a charge concentration lower then $10^6\,\mathrm{cm}^{-3}$, requires a time interval of the order of only about 10 ns, depending on the bias voltage. In the present case, instead, charge collection occurs by slowly "eating up" the carriers closer to the electrodes where the external field is not shielded by the space charge and the near-dipole field. The current signal can then be expected to have a very long tail, in the microsecond range. Relatively high e-h concentrations are present along the beam path for relatively long times, from nanoseconds to microseconds, immersed in negligible electric field.

Under low charge conditions, recombination lifetimes for sCVD diamonds are on the order of $1\,\mu$s. Radiative recombination via phonons and via defective states in the forbidden band has been extensively studied in the literature [104, 105] by photoluminescence experiments in diamond with laser and electron beams, which produce a similarly high carrier concentration, of the order of 10^{17} cm^{-3}. Based on these results, a significant loss of current signal can be expected due to a substantial amount of carrier recombination due to their persistent high local concentration in the diamond bulk. Heating effects can also be considered. The 'hot' electrons and holes generated by ionisation in the diamond bulk thermalise rapidly, with a time constant of the order of picoseconds, to energy levels close to the conduction and valence bands, transferring energy to lattice vibrations called phonons. Given the distance of 5.5 eV between the conduction and valence bands and the average ionisation energy of 13 eV, a fraction $(13 - 5.5)/13 = 58\%$ of the energy released per bunch crossing $\Delta E_{\mathrm{bunch}} = 3.4 \times 10^{-7}\,\mathrm{J}$ lost by the incoming beam bunch is therefore heat transferred to the lattice. The corresponding temperature increase can be estimated as

$$\Delta T = \frac{58\%\Delta E_{\mathrm{bunch}}}{M}\left(\frac{1}{C_T}\right) = 0.74 \times 10^{-3}\,^{\circ}\mathrm{C}, \tag{5.3}$$

where $M = \rho_{\mathrm{diam}} \cdot V_{\mathrm{diam}} = 4.9 \times 10^{-4}\,\mathrm{g}$ is the mass of the diamond and $C_T \simeq 0.52\mathrm{Jg}^{-1}\,^{\circ}\mathrm{C}^{-1}$ is the specific heat. Under these assumptions, the energy released by 1 pC bunches gives negligible thermal effects.

5.2 Experimental setup

To test the transient response of our detector to intense high-energy electron pulses, the unique properties of the electron beam from the linac of the FERMI free-electron laser can be exploited. In the final section of the linac, a bending and focusing insertion can be activated to deviate the accelerated electrons to a diagnostic beam dump (DBD). Prior

to the beam dump, a vacuum chamber insert was designed, instrumented and installed, together with the FERMI and Elettra colleagues, to measure the beam induced signals of small devices under test (DUT), such as our diamond detectors.

The main components of the experimental setup are described below: the electron beam with its monitoring equipment, the DUT station with our diamond detectors, and the data acquisition systems.

5.2.1 Beam facility

FERMI is an externally seeded XUV free electron laser at the Elettra laboratory in Trieste, Italy [103, 106]. The linac feeding the FERMI free-electron laser can be tuned to provide electron bunches in the energy range from 0.9 to 1.35 GeV, with an energy spread typically from 0.01 % to 0.3 %, a bunch charge from $\sim$ 10 to 1000 pC, a repetition rate up to 50 Hz, sub-picosecond duration, and transverse size down to about 0.1 mm.

The FERMI electron source is a metallic photocathode (polycrystalline copper) illuminated by an intense UV laser at 263 nm, whose pulse shape is chosen to optimise the final beam quality. Since the best measured quantum efficiency of copper at 263 nm is in the range 10^{-5}–10^{-4}, the laser must deliver $\sim 500\,\mu$J to the cathode to produce a ~ 1 nC bunch charge. The first stage gun is specified to provide an output beam energy of $\sim$ 5 MeV at a repetition rate of 50 Hz. A multiple pancake, emittance-compensating solenoid provides focusing to help transport the beam from the gun exit to the entrance of the booster linac structures. The FERMI accelerator is shown schematically in Figure 5.3. It consists of four linacs L1 - L4, two bunch compressors (BC1 and BC2), a laser heater (LH).

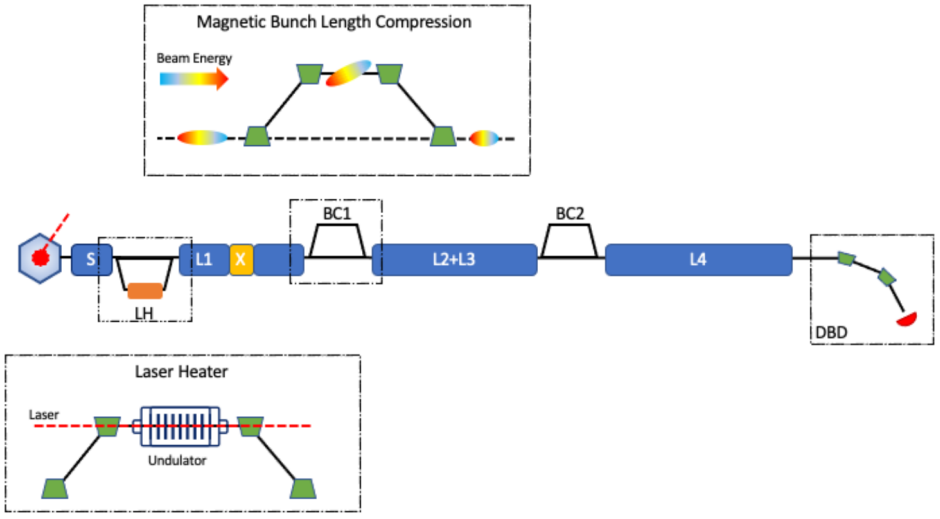

Figure 5.3: Overview of FERMI linac (not to scale). The insets shows the geometry of Laser Heater (lower) and Bunch Lenght Compressor (upper). The Diagnostic Beam Dump is also indicated in the scheme.

The laser heater is a device installed to heat the beam, increasing by a fixed amount the uncorrelated energy spread of the electron beam. The heating is provided by the interaction of the laser with the electron bunch in an undulator, placed in the middle of a

four dipoles chicane. At the output the energy of the electron beam is ~ 100 MeV. The linac is composed of four accelerating sections (L1 to L4) and two bunch compressors (BC1 and BC2) before the transfer section which transports the beam to the two FEL lines, known as a "spreader". The final energy of the electron beam ranges from 0.9 to 1.35 GeV. Bunch compressors are designed to increase the beam peak current. They consist in four-dipole chicanes that exploit the linear chirp introduced by off-crest acceleration, before the first bending magnet, to decrease the path travelled by lower energy particles and increase it for higher energy particles. This strategy shortens the bunch length and, since the charge is conserved, increases the instantaneous current.

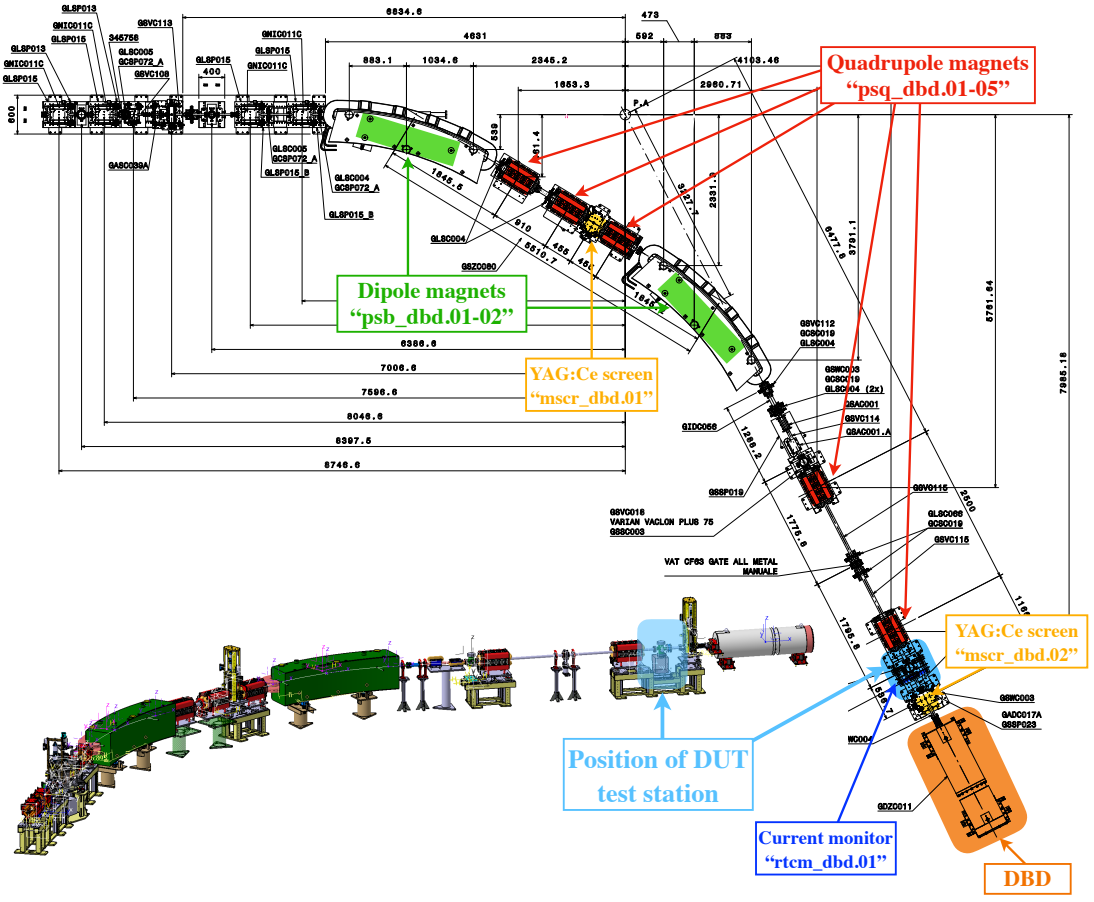

Figure 5.4: The diagnostic beam dump (DBD) insertion at the end of the linac of the FERMI free-electron laser.

To operate the machine in safe condition and optimise the beam parameters, the beamline is equipped with a beam diagnostic system [107]. The photoinjector diagnostic system includes interceptive instrumentation such as YAG:Ce screens [108] for transverse position and profile measurements, and Faraday cups [109] for absolute beam charge measurements. A Cherenkov radiator, coupled to a streak camera, provides an accurate reconstruction of the longitudinal profile and a pepper pot followed by a screen is provided for the transverse emittance measurement [110]. Transverse beam position and charge information is obtained non-destructively using cavity beam position monitors (BPMs) and a current transformer.

In the final section of the linac, the accelerated electrons can be deflected and focused into a Diagnostic Beam Dump (DBD), as shown in Figure 5.5. The beam dump consists of a graphite-aluminium dump, which has a $\sim 99\%$ energy and radiation absorption efficiency. This section is equipped with two dipole bending magnets ("psb_dbd.01-02") and four quadrupole focusing magnets ("psq_dbd.01-05"), which can be used to adjust the direction and focus of the extracted beam. This part of the beamline was modified with additional instrumentation, described in Section 5.2.2, to study the response of devices such as our diamond-based detectors to the FERMI electron beam, taking advantage of its unique properties.

The DUT test station is located approximately 50 cm downstream of the fifth and final quadrupole magnet. A good knowledge of the position, transverse size and charge of the incident beam bunches is required to perform quantitative studies of the response of the DUTs under different beam conditions: a YAG:Ce screen "mscr_dbd.02", located about 50 cm downstream of the DUT station, is used to measure the beam profile, while a beam current transformer "rtcm_dbd.01", located a few centimetres downstream of the station, provides a measurement of the beam charge in front of the DBD. Moreover, an additional YAG:Ce screen "mscr_dbd.01" is used to determine the beam shape before the last bending dipole. Figure 5.5 shows a zoom of the DUT test station position on the mechanical drawing of the FERMI beamline, where the labels correspond to the position of the instrumentation.

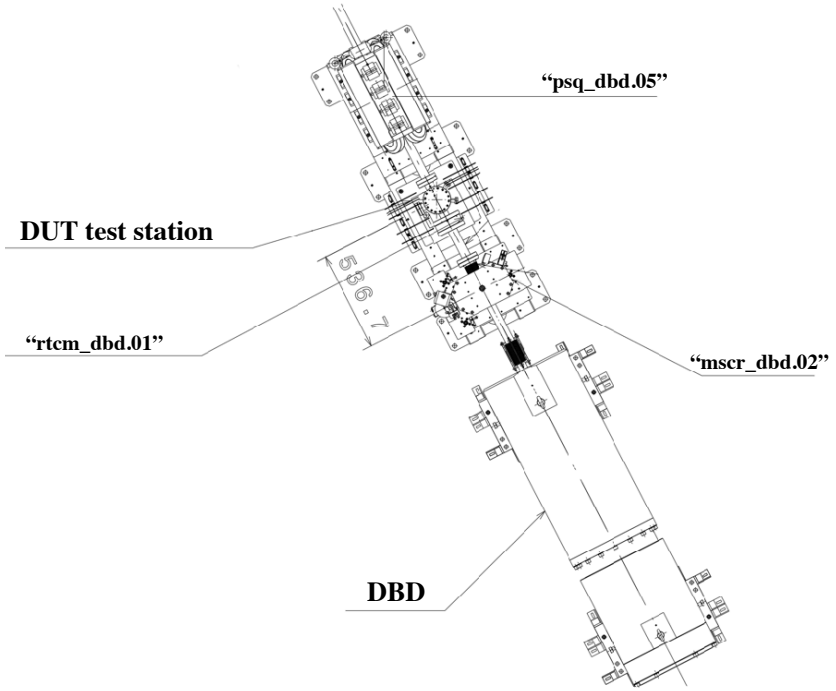

Figure 5.5: Expanded view of the final section before DBD, including the last magnetic element "psq_dbd.05", the DUT test station, and the YAG:Ce fluorescent screen "mscr_dbd.02" and the current transformer "rtcm_dbd.01".

After an initial series of tests summarised in Table 5.1, the setup was improved in the spring of 2023 by adding an additional YAG:Ce screen "mscr_dbd.03" on the test DUT support, thus improving the knowledge of the beam profile at the position of the

detector. A full description of the instrumentation and data acquisition system is given in Section 5.2.4.

Irradiation campaign	Instrumentation
October 2021	DUT
November 2021	DUT, mscr_dbd.01 and rctm_dbd.01
March 2022	DUT, mscr_dbd.02 and rctm_dbd.01
May 2022	DUT, mscr_dbd.02, rctm_dbd.01 and external diamond
June 2022	DUT, mscr_dbd.02, rctm_dbd.01 and external diamond
June 2023	DUT, mscr_dbd.02, mscr_dbd.03 and rctm_dbd.01

Table 5.1: Summary of the instrumentation added in the consecutive irradiation campaigns from October 2021 to June 2023. The labels of the "mscr" beam profile monitors and "rctm" beam current transformers are defined in the text.

5.2.2 DUT test station

The test station is designed to align the support of the detectors to be tested with the direction of the beam. A left-handed reference frame is used in the following: the z axis is

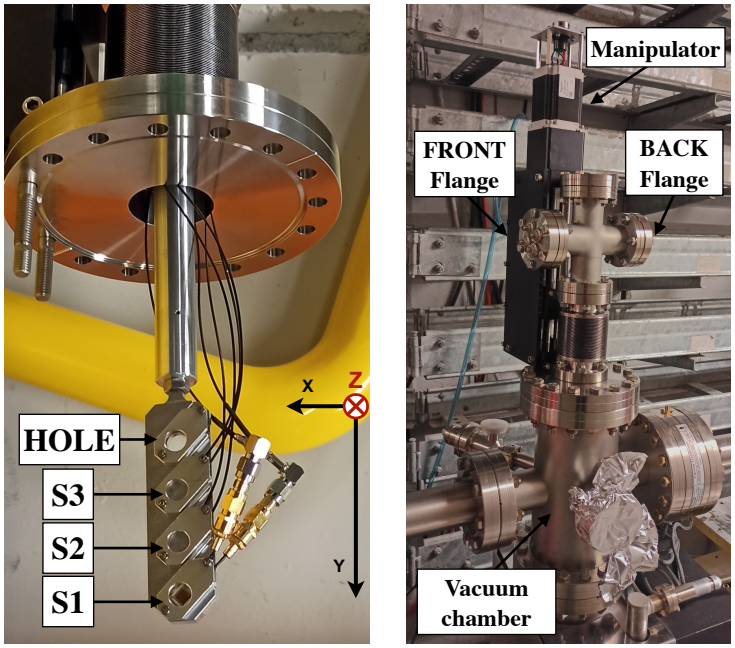

Figure 5.6: (left) The aluminium support holds up to three diamond detectors. Detector labels and reference frame are described in the text. The upper position is left empty to allow the unaltered passage of the beam. (right) The picture shows the test station on the linac beam line. All the components are described in the text.

along the nominal beam direction, the y axis is vertically down and the x axis is horizontal. Up to four devices can be mounted on a mechanical support located in a vacuum chamber on the beam line. The support is made of 8 mm thick aluminium with four circular holes

of 9 mm diameter and centres offset by 21 mm along the vertical direction, corresponding to the sensor positions. The support is connected to a remotely controlled manipulator with a stepper-motor that can move the support vertically in 3.15 μm steps, allowing the sensor to be aligned with the beam along the vertical direction. This also allows vertical beam scanning across detectors. The manipulator is equipped with two switches located at the upper and lower end of stroke. When the guide of the manipulator reaches one of the two switches, the movement is blocked. The position at which the manipulator stops can be adjusted by means of two screws located on the outside of the manipulator.

Figure 5.6 on the left shows the support connected to the manipulator before insertion in the vacuum chamber on the beam line. Three diamond detectors are mounted in the three lower positions, labelled S1, S2 and S3, while the upper position, labelled HOLE,is left empty for beam adjustments. When this HOLE position is selected, the undisturbed beam going through the hole can be tuned and aligned, using the downstream fluorescent screen as beam profile and position monitor.

All detectors are positioned at a 45° angle to the vertical direction of the support, to avoid excessive stress on the cable connection point on the PCB. The detector micro-coaxial cables are shortened to ~ 40 cm to avoid excessive length in the vacuum chamber, soldering an SMA connector to the end of each cable. The connectors are plugged to the feed-through SMA connectors, specific for vacuum applications, installed on the two flanges placed in the upper part of the support. The flanges are designed to accept up to 4 connectors. One of the two flanges, labelled as FRONT, received all the cables connected to the front of the sensor, while the other, labelled BACK, received the cables connected to the back of the sensor.

The bias voltage is applied to the front of the four diamond detectors via three 10 m coaxial cables connected to the FRONT flange connectors. Initially, the three detectors were biased in series with the same power supply. However, initial measurements showed the presence of cross-talk between the detectors and it was decided to power them separately. The back of each detector is instead connected to one of the input channels of the oscilloscope via a 10 m length high quality coaxial cable connected to the BACK flange connectors. These cables are terminated externally with 50 Ω resistors, and the oscilloscope internal high impedance 1 MΩ inputs are selected to accept the large expected signals.

Four diamond detectors are installed in the experimental setup, three of which, labelled DC01, DC15 and DC25, are mounted on the movable support in positions S1, S2 and S3 respectively. The fourth detector, labelled DC00, is mounted externally on the vacuum chamber to monitor beam losses close to the test station. The stepper motor controller, the high voltage power supplies and an oscilloscope are located in a protected position a few metres from the DUT station.

5.2.3 Setup optimisation

In the spring of 2023, the test stand was improved by changing the aluminium support and adding new beam monitoring instrumentation at the DUT position. The new support, shown in Figure 5.7, starting from the top to the bottom, consists of:

- a circular hole of 9 mm diameter that allows the beam to pass unaltered to the fluorescent screen placed ~ 50 cm behind the sample;
- three positions dedicated as detector support, with a circular hole of 9 mm diameter in correspondence with the sensor, labelled as S1, S2 and S3. The detector holder was modified in order to place the sensor horizontal to the vertical direction;

- a YAG:Ce fluorescent screen with a diameter of 22 mm;
- a target with a graduated scale, used for the calibration of the fluorescent screen.

Both the screen and the target are placed on a plane at a horizontal angle of 45° to the electron beam. The scintillation surface of the screen is imaged by a CCD camera located outside the vacuum chamber by means of an in-vacuum mirror which is displaced from the electron beam and tilted so that the optical axis is at normal incidence with respect to the screen surface.

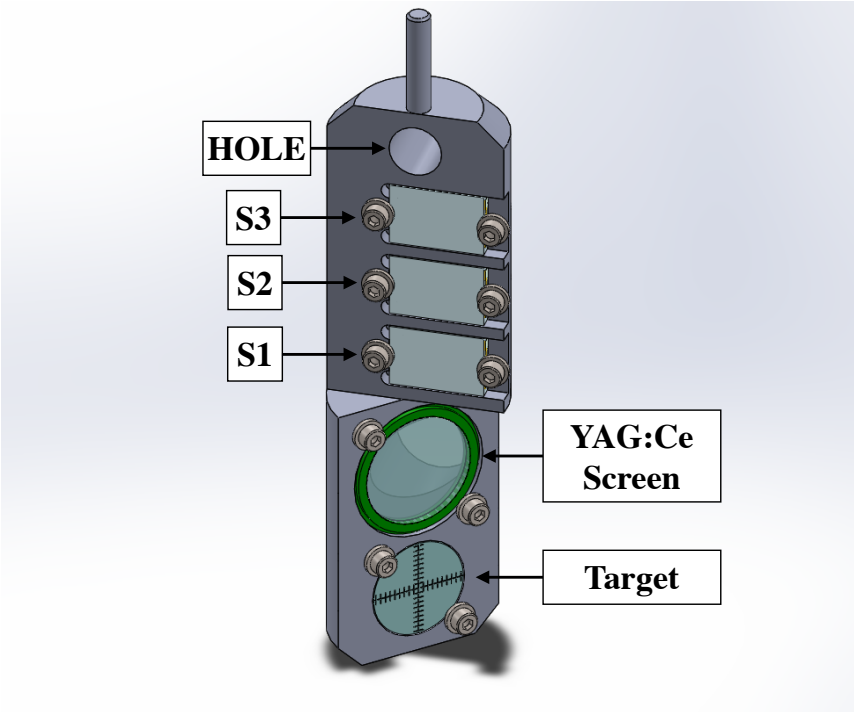

Figure 5.7: CAD drawing of the aluminium support of the optimised setup: the labels show the detectors, fluorescent screen and target positions.

For this experimental setup, two of the three diamond detectors were reinstalled, DC15 and DC25 in positions S2 and S3 respectively. The diamond detector DC01 was replaced by a prototype of SiC detector mounted in position S1, the studies of which are not reported in this work. The detectors are connected to the power supply and the oscilloscope in the same way. In addition, a 50 Ω resistor was added in series with the power supply to reduce the reflection observed in the signals during the previous tests and due to the impedance mismatch between the detector and the power supply. Both the supports were aligned to the beam direction before installing them in the vacuum chamber insertion.

5.2.4 Instrumentation and data collection

The DUT test station is instrumented by:

- a motor control controlling the manipulator and allowing to move the support with steps 3.15 μm;
- two power supplies with HV modules [56] that provide a positive bias voltage up to 1000 V. The power supplies were replaced in the last beam test by a CAEN

DT1471ET [80] power supply, that provides a bias voltage up to 5 kV at very low noise;

- a Teledyne LeCroy HDO9000 oscilloscope [111], used to measure the signal induced on the detector under test. It provides 10 bits analog-to-digital conversion with 2 GHz bandwidth and 10 GS/s sampling rate for 4 channels, with a wide range of mathematical and analysis functions. The oscilloscope records individual pulses when the pulse amplitude exceeds the trigger threshold. A different trigger threshold is set as a function of signal amplitude to reduce signal jitter. The oscilloscope averages the signal shapes of 1000 pulses and the average signal is then stored. The digitised oscilloscope data is transferred to a PC for further analysis.

To optimise the operations, all the instrumentation is set up in order to be remotely controlled.

As described above, additional instrumentation are exploited together with the standard monitoring equipment of the FERMI linac to tune the beam for the DUT tests.

YAG:Ce fluorescent screens [108]: It consists of a 100 μm thick yttrium aluminium garnet cerium doped (YAG:Ce) scintillation screen. Electrons crossing the screen excite the material, which emits light by scintillation. The mechanical properties of the material allow thin screens to be produced down to 0.005mm thick. The maximum emission wavelength is 550 nm, the decay constant is 70 ns and the photon yield at 300 K is $\sim$ 35000 photons/MeV. The visible light from the YAG:Ce screen is then acquired with a CCD camera, providing information on the position and profile of the electron beams. This screen ensures a spatial resolution of better than 10 μm, compatible with the limit of the CCD pixel/sensor size and the optical setup. The screens, with a circular shape of 22 mm diameter, are installed at an angle of 45 degrees to the transverse direction of the beam. The image of the screen surface is transmitted to the CCD camera by means of a vacuum mirror and a series of lenses located between the mirror and the camera. To avoid any degradation of the beam after the screen is positioned, the screen can be inserted when the beam profile measurement is to be performed. The cameras used for the DUT position and DBD screens have a resolution of 15 μm. Since the CCD can capture the entire screen with more than 1400 pixels and an area $\sim 10^4$ times larger than the beam transverse section, it is possible to select a Region Of Interest (ROI) in the acquisition system to reduce the amount of data stored. The intensity measured by each pixel of the camera is proportional to the emitted light, and so to the number of incident electrons, crossing the screen in the position corresponding to the pixel. Since the emitted light is proportional to the charge of the incident beam, in order not to saturate the intensity scale of the CCD camera, a different gain is set varying the beam bunch charge. To compare the imaged screen with the real one, the camera is calibrated using a target with a graduated scale placed at the position of the screen as a reference.

Integrating Current Transformers [112]: The Integrating Current Transformers (ICT) are used for non-destructive measurement of the beam charge with high relative accuracy. They are embedded in flat flanges for direct mounting on the beam tube, with an internal diameter of 60.4 mm for the passage of the beam. The transformer is sensitive to beam charges above about 10 pC, with an accuracy of about 1 pC. In order to be sensitive to lower charges, the gain of the current monitor "rtcm_dbd.01" is reduced.

In order to operate the machine at a repetition rate of up to 50 Hz, a distributed real-time framework is integrated into the control system [113, 114], which provides the capability to measure and manipulate the laser, electron and photon beams, as well as to close synchronised feedback loops on a pulse-to-pulse basis. All relevant monitoring points (*e.g.* electron diagnostics) and control points (*e.g.* power supplies) are synchronised with the bunch trigger and associated to a real-time time stamp called the "bunch number". The diagnostic electronics provides shot-to-shot data to the low-level computers via real-time interfaces [115]; the data is tagged with the bunch number and stored in local circular buffers that can be easily read by high-level applications.

During beam optimisation and focusing at the DUT station, data is recorded by the FERMI control system for offline analysis and documentation. Particular attention is paid to the settings of the dipole and quadrupole magnets of the DBD insertion, to the bunch charge at the linac injection (LH) and at the DUT station from the beam current transformers, and to the beam profile of the fluorescent screen "mscr_dbd.02" downstream of the DUT position. After the optimisation of the setup in March 2023, also the screen "mscr_dbd.03" placed on the DUT holder was implemented in the acquisition system. Before acquiring the images from the screens, the ROI and gain for each camera were selected. In the acquisition process also the the screen parameters, such as pixel-to-space calibration factor, ROI dimensions and gain, are stored. For each beam configuration 1000 shot-to-shot data are stored. The oscilloscope data were recorded separately, storing both the single and average signal for all the three channels used.

5.3 Measurement overview

The measurement procedure should be divided into two parts. The first part is dedicated to beam tuning with the aim of obtaining a beam that is as focused as possible on the detector under test. A measurement of the beam parameters and machine settings is then carried out: using the real time acquisition system I stored 1000 shot-to-shot data of the bunch charge and energy of the beam, both at the injection (LH) and at DBD, the beam profiles and the configuration of all the bending and focusing magnets. The second part of the procedure, once the optimum alignment of the DUT with the beam is found, is devoted to the study of the response of the detector as a function of various parameters. The different sets of measurements are:

Bias voltage scan: Fixing the bunch charge and the beam size, after centrering the beam on the diamond sensor I measured the averaged signal varying the applied bias voltage from 10 V to 300 V. In a few cases the bias is varied up to 600 V for further investigations at higher bias voltage.

Bunch charge scan: Fixing the bias voltage applied to the detector, I measured the average signal varying the bunch charge of the incident beam. The beam size changes varying the bunch charge, especially at low charges below 50 pC.

Beam size scan: Fixing the beam charge and applying a bias voltage $V_{\text{bias}} = 100\,\text{V}$ on the detector, I measured the average signal for four different profiles of the beam.

The analysis and results on detector response are described in Section 5.6.

5.4 Electron beam optimisation

A well-focused beam at the centre of our equipment and a good knowledge of the beam spot incident on the DUT were obtained by progressively improving the instrumentation of the electron beam line. In the following, I chronologically describe the steps followed in the different irradiation campaigns up to the final setup, with all the issues encountered along the way.

In standard operation, the FERMI linac delivers to the transfer line of the FEL 1 ps electron pulses with a bunch charge in the range of 500 to 1000 pC. Under these conditions, it is possible to obtain a highly collimated beam with dimensions of $< 100\,\mu$m in both vertical and horizontal sizes. All diagnostics along the linac are designed to operate in this charge range.

In our measurements, we are interested in investigating a lower charge range, keeping the beam well focused inside the sensitive area of our detectors. However, for lower bunch charges the feedback systems are outside their standard operation range. Moreover, the final section of the beam line, after bending the beam to the DBD, had never been fully equipped to perform measurements of the beam profile. Our beam optimisation consists in focusing the beam at the centre of the sensor with a symmetrical shape, minimising the beam losses along the FERMI linac. Different tools are used in different irradiation campaigns for this purpose. Table 5.1 reports a summary of the instrumentation used in the six consecutive irradiation campaigns from October 2021 to June 2023.

In particular, the beam tuning was progressively improved in the irradiation campaigns, by using the following three tools, which will be discussed in the next paragraphs:

1. the diamond detector response as feedback for the beam position, performing a vertical scan of the DUT varying the vertical position of the support, and a horizontal scan by horizontally bending the beam;

2. the YAG:Ce fluorescent screen "mscr_dbd.02" placed ~ 50 cm downstream the DUT station, looking to the signal measured by the external diamond to minimize the beam losses;

3. the YAG:Ce fluorescent screen "mscr_dbd.03" placed on the optimised setup together with the current transformer after the DUT station.

The final beam optimisation is described in Section 5.4.3.

5.4.1 Diamond response as a feedback

In the first irradiation campaign, the instrumentation consisted in a fluorescent screen "mscr_dbd.01" upstream of the last bending dipole and a current monitor positioned ~ 3 cm after the test station. We used the screen to check the beam size before the final bending to the DBD. After the dipole "psd_dbd.02", in the absence of an additional screen, the current monitor was available to check that all the charge was carried to the test station. Since the preliminary tests showed a clear induced signal on the diamond, described in Section 5.6, whose shape varies with the position of the incident beam, I carried out an initial characterisation of the beam position and shape at the DUT position by looking at the response of our diamond detectors. After placing the diamond in the nominal centre of the vacuum chamber where the DUT test station is located, the magnets in the last section were set in order to maximise the signal amplitude assuming that the signal had maximum amplitude at the centre position of the diamond.

Detector position scan

To determine whether the beam hit our detector, the sensor itself was used as a position monitor. Applying a bias voltage of 10 V and fixing the charge at 10 pC, I measured the induced signal on two diamonds, respectively at positions S2 and S3, by varying the vertical position in 1 mm steps. Figure 5.8 shows the fraction of signal measured with the diamond detector in position S3 (red) and S2 (blue) respectively as a function of the position. The "fraction of signal" is the ratio between the signal amplitude and the maximum signal amplitude measured in the scan, which is assumed to correspond to the diamond centre.

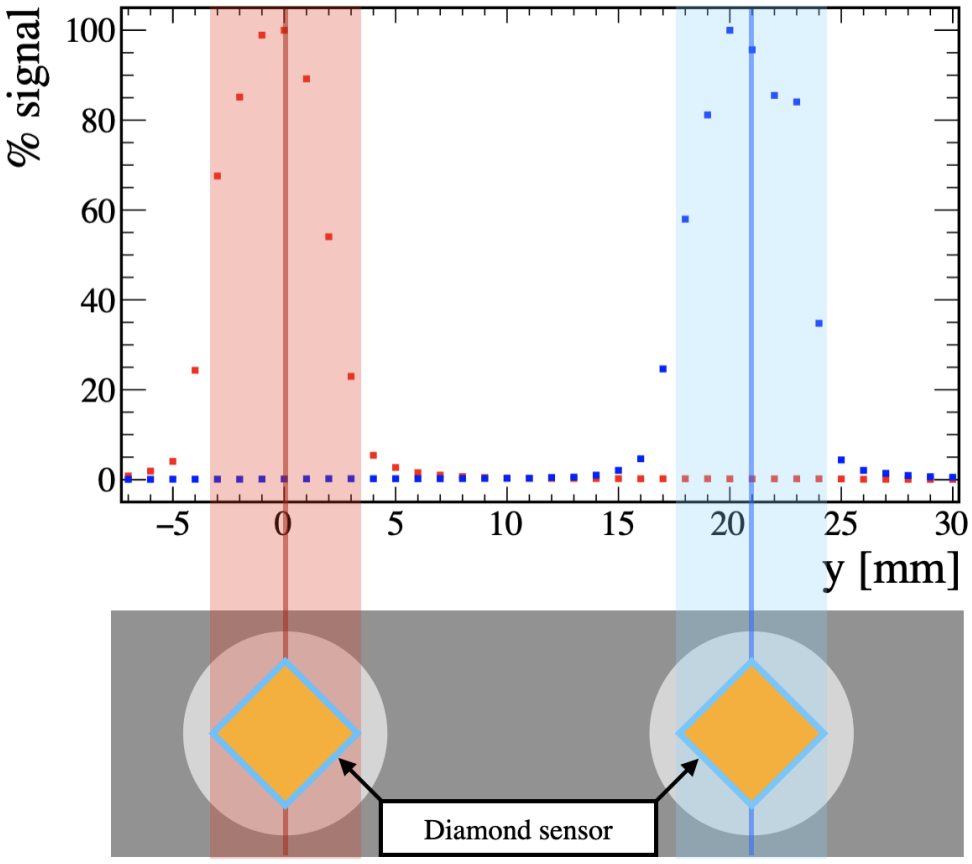

Figure 5.8: Preliminary vertical position scan performed with a bunch charge of 10pC and a bias voltage of 10V. The scheme on the bottom shows the position of the of the beam on the diamond sensor to which corresponds the fraction of signal.

Assuming a beam size of $\sim 100\,\mu$m and an uniform diamond response for beam hitting different position on the crystal, the signal fraction is expected to remain at higher and constant values when the beam is collimated in the active area of the sensor. Since the detectors are mounted on the support with a 45° tilt angle as shown in Figure 5.8, the width of the flat top of the signal amplitude plot might be compared with the vertical diagonal size of the square detector, which is $d = \sqrt{2} \cdot 4.5 = 6.36\,$mm.

However, the amplitude remains close to the maximum for a displacement of only about 2 mm around the centre of the diamond. When the beam is at a distance of more than 3 mm from the centre of the diamond, i.e. outside the active volume of the sensor, the amplitude of the signal is still larger than 20% of the maximum amplitude. The transition of the signal amplitude at the detector edges can be understood as a combination of the

shape of the detector corner and a transverse beam size larger than that measured on the upstream fluorescent screen ($\mathcal{O}(100\,\mu\text{m})$). The diamond was then moved to the centre obtained from the position scan, *i.e.* where the signal has the maximum amplitude. With the detector position fixed, a horizontal position scan was performed, varying the strength of the quadrupoles "spq_dbd.03" and "spq_dbd.04". In this case, the signal amplitude was different from zero and varied by about 15% when the beam was moved by several millimetres in the horizontal direction. This effect may be due to unfocussing the beam by changing the quadrupole parameters; this interpretation could not be verified, since there was no beam image measurement at the DUT.

Expected position scan

To better understand the effect of the shape of the beam width on the vertical scan, I simulated the vertical scan for a beam with a Gaussian spatial distribution on the transverse plane. For each beam position relative to the detector, I generated 10^6 electrons with perpendicular incidence to the diamond surface and with a Gaussian distribution on the transverse plane, and computed the fraction of electrons hitting the diamond. The simulation was repeated by varying the relative position of the beam respect to the diamond with steps of 1 mm. The simulated scan results are shown in Figure 5.9 for four different values of the standard deviation of the Gaussian distribution, assuming a symmetrical beam in the horizontal and vertical direction.

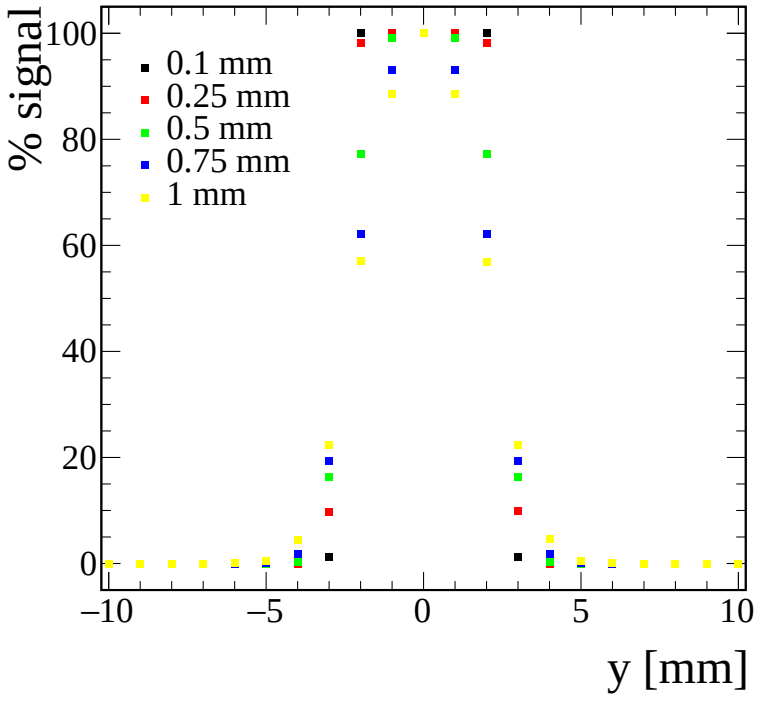

Figure 5.9: Simulated vertical position scan obtained for five different values of the standard deviation, which are reported in the legend. The fraction of electrons hitting the detector are normalised to their maximum value.

The expected response for a beam with a $\sigma_{xy} = 100\,\mu\text{m}$ has a flat top of $\sim 5\,\text{mm}$, compatible with the diagonal of the sensor. For all the five values of the simulated beam

size the fraction of signal at $\sim 3\,\text{mm}$ from the diamond centre is about 20%. Increasing the beam size, the width of the flat top reduces and the transition of the signal near the edges becomes less sharp since a fraction of the beam is outside the crystal boundaries. From the comparison of data and simulation, the measured position scan looks more similar to the simulation results for a beam size of $\sim 1\,\text{mm}$, which is 10 times large than the expected one. Moreover, in the simulation I considered only a symmetric beam shape, that might differ from the real case. However, this simplified simulation only considers the ideal case in which the entire area of the diamond is considered sensitive. Under real conditions, the electrodes have a surface area $4.0 \times 4.0\,\text{mm}^2$ which can be considered the active surface of the crystal: the electric field at the edges is not necessarily uniform and this may have an effect on the charge collection efficiency. This is why it is important to have a collimated beam in the centre of the diamond, the simplest condition in which the electric field can be assumed uniform.

5.4.2 Fluorescent screen downstream DUT

In 2022, the setup was improved by adding a fluorescent screen "mscr_dbd.02" 53.8 cm downstream the location of the test station. The presence of the fluorescent screen after the position of the diamonds, together with the current monitor, made it possible to obtain a more collimated beam and reduce charge losses during transport. When the vertical position of the DUT mechanical support is such that the incoming beam is well centred on the upper "HOLE" position, the beam passes unaltered and reaches the fluorescent screen located $\sim 50\,\text{cm}$ downstream the DUT holder. After fixing the charge, the beam was transported up to DBD and tuned to obtain a symmetrical shape and transverse dimensions of $\sim 100\,\mu\text{m}$ on the fluorescent screen , close to the nominal values of the machine. The beam shape and the horizontal and vertical beam profiles are shown in the left images of Figures 5.10 and 5.11 respectively; a Gaussian fit gives the standard deviations $\sigma_x = 78\,\mu\text{m}$ and $\sigma_y = 100\,\mu\text{m}$ for the horizontal and vertical profiles respectively.

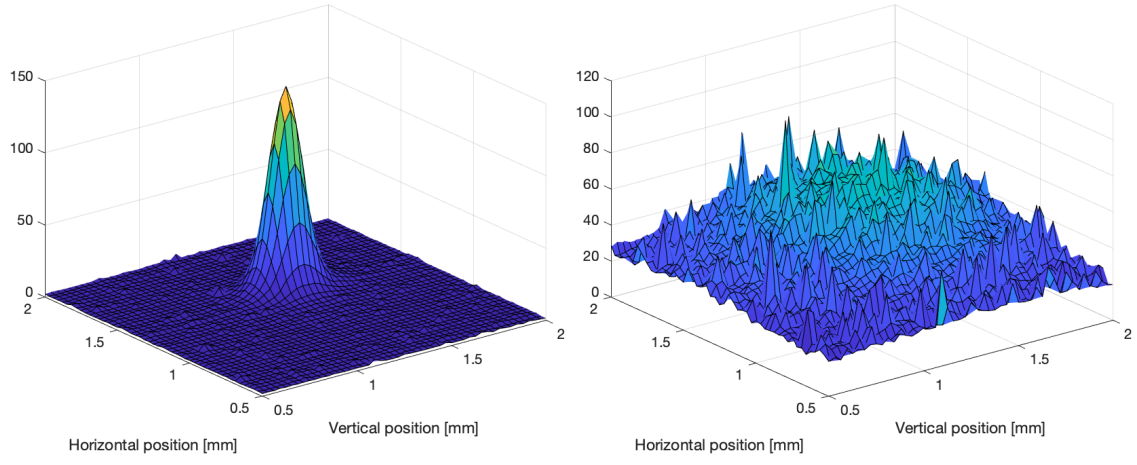

Figure 5.10: 2-D beam profile distribution measured with "mscr_dbd.02", respectively for beam passing through the HOLE (left) and DUT (right) positions. The two images are taken with a different gain of the CCD camera: the vertical scales are not directly comparable.

When the beam hits the aluminium support, the light spot on the fluorescent screen disappears, due to the multiple scattering of electrons in $\sim 1\,\text{cm}$ of aluminium. To verify

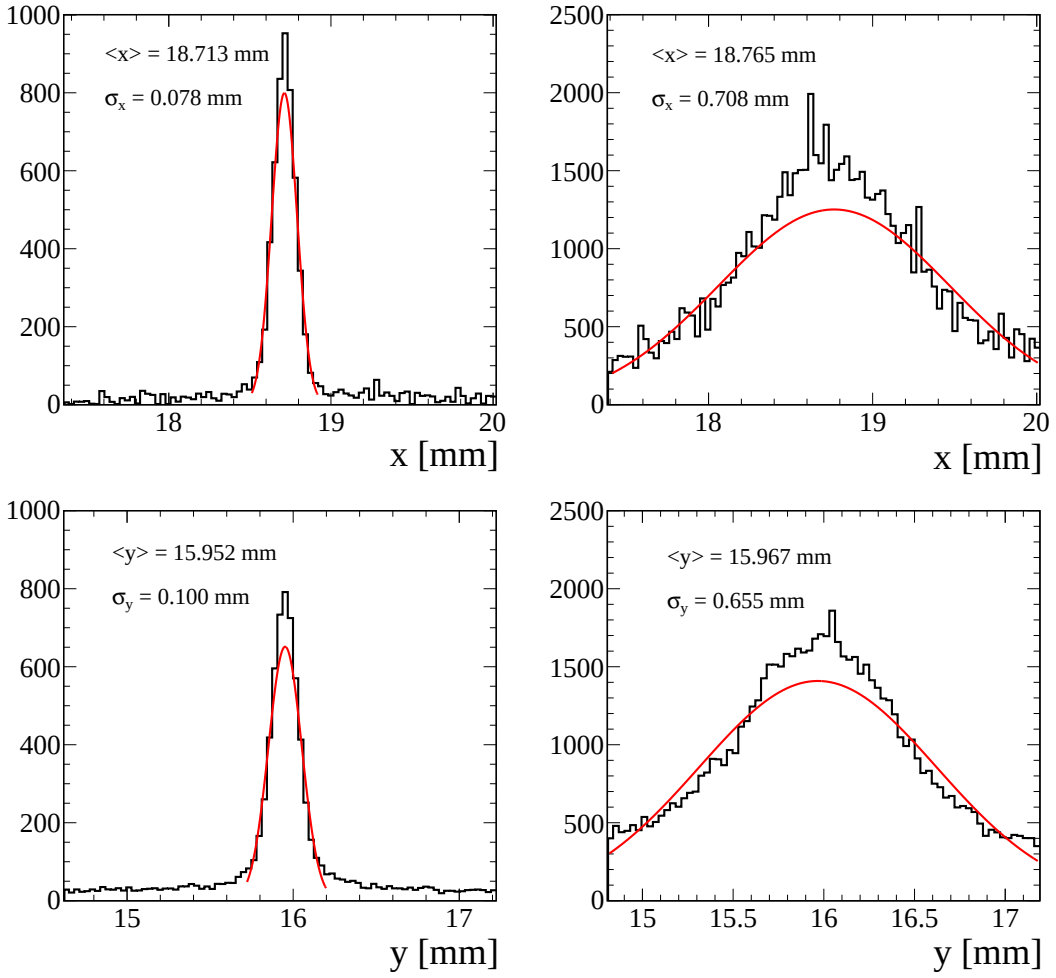

Figure 5.11: Horizontal (top) and vertical (bottom) beam profiles as recorded by the fluorescent screen located downstream the DUT, before DUT insertion (left) and after the DUT insertion (rigth), for an average of 1000 bunch crossing.

that the beam was centred in the middle of the hole along the vertical direction, We moved the support along the vertical direction looking at the image on the screen. The bright spot on the screen disappeared when the beam reached the edge of the hole. This effect was also used to perform a scan of the hole. The beam was widened, as shown in Figure 5.12, so that the horizontal dimension was larger than the width of the hole. In this way, electrons hitting the edge of the hole are multiple-scattered and the corresponding signal on the fluorescent screen is attenuated. An example of the image on the screen for the wider beam is shown in the figure on the left. The arrows indicate the position of the edges. The scan is performed by varying the vertical position of the support.

The plot on the right shows the results of the hole scan, where the points are the distances between the edges measured on the fluorescent screen for each vertical position. From the scan, the hole appears to have an elliptical shape, flattened in the horizontal direction compared to reality. This may be due to divergence of the beam as a result of reduced beam control when the beam is widened in the horizontal direction. From the scan I determined the hole centre in the vertical direction: this was considered as the "zero' position reference for the DUT support.

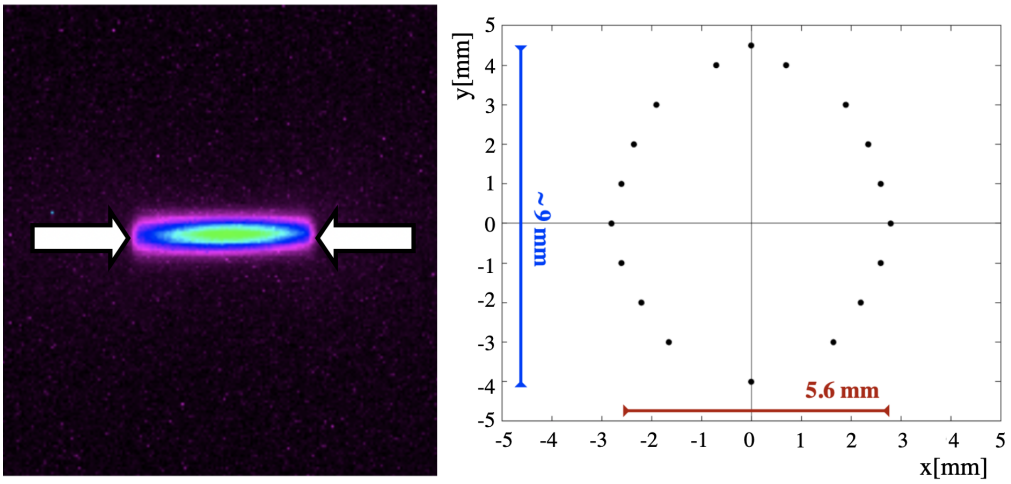

Figure 5.12: Scan of the HOLE of DUT aluminium support, obtained by widening the beam in the horizontal direction and looking at the projection of the hole edges on the fluorescent screen. The picture on the left shows an example of the image at the fluorescent screen, where the arrows point to the hole edges. The plot on the right shows the hole projection resulting from the scan.

Once reached the best collimated beam conditions, I performed a vertical position scan using the diamond as a position monitor. Again, the signal amplitude transition is not sharp as the beam crosses the edges of the crystal. Since the beam size measured at the fluorescent screen position is $\sim 100\,\mu$m, this effect could be due to a non-negligible beam divergence leading to a broadened beam at the position of the diamond. In addition, the beam might have a halo, whose presence might explain by a signal measured both by the adjacent diamond and the diamond positioned outside the vacuum chamber.

Furthermore, the insertion of a diamond detector as DUT, upstream of the fluorescent screen, changes both the shape and intensity of the beam profiles on the screen, as shown in Figure 5.11. The measured profiles at the fluorescent screen are wider after the insertion of the diamond detector. This widening after DUT insertion can be attributed to the combination of two effects: (a) the widening of beam profile at DUT position, due to the beam divergence, and (b) the interactions of the beam electrons by multiple scattering with the detector materials, *i.e.* aluminium cover, sensor with electrodes and PCB. The difference between the horizontal and vertical profiles with the presence of the diamond and without is shown in the Figure 5.10. The position of the beam remains unchanged while the standard deviation increases by a factor of 9 and 7 for the horizontal and vertical direction respectively.

Multiple scattering effect

To separate the effects of beam divergence and multiple scattering, I compared the measurements with a simulation, based on the FLUKA package [77], taking into account the beam size and the electron interactions in the DUT. I generated 3.2×10^8 electrons with 0.906 GeV energy perpendicularly hitting the middle of the detector, with a Gaussian spatial distribution. The simulated beam has different horizontal and vertical standard deviation values, simulated $\sigma_x = 140\,\mu$m and $\sigma_y = 90\,\mu$m respectively.

I simulated the fluorescent screen as a $(6 \times 6)\,\text{cm}^2$ surface placed at a distance of

50 cm from the detector and I recorded the spatial distribution of the electrons incident on the fluorescent screen. I repeated the simulation also for the configuration without the detector, corresponding to the HOLE position. Figure 5.13 shows the comparison between the simulated horizontal and vertical beam profiles, obtained without (red) and with (blue) the DUT 50 cm upstream the fluorescent screen. The widening of the beam is

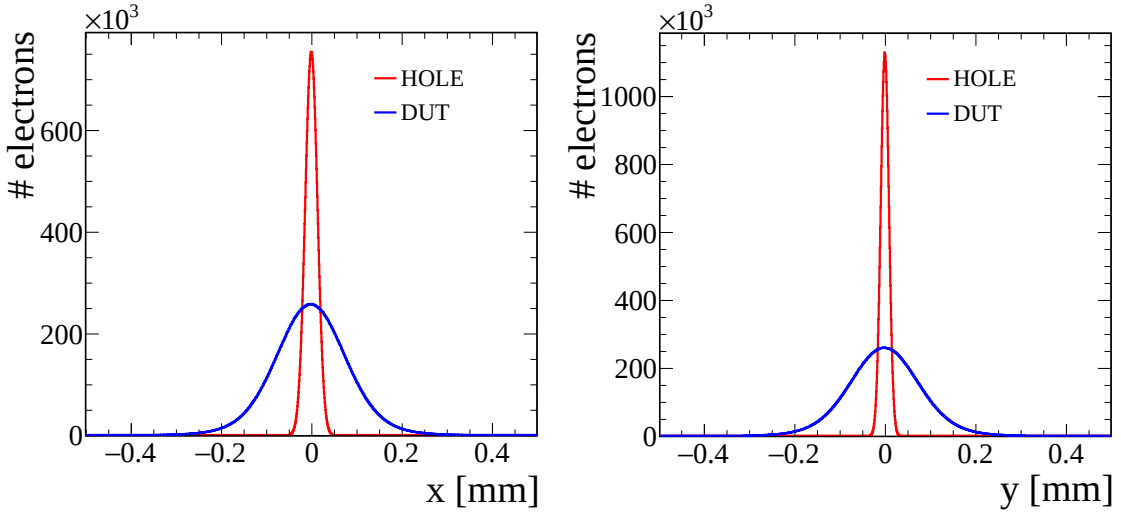

Figure 5.13: Beam horizontal (left) and vertical (right) profiles obtained from the FLUKA simulation of the experimental setup, respectively for a beam passing thought the HOLE position (red) and one of the DUT (blue). The histograms on the left show the results for a beam size $\sigma_x = 140\,\mu$m, while the ones on the right for $\sigma_y = 90\,\mu$m.

about a factor 10, which is close to the one measured by the fluorescent screen after the DUT insertion. The main effect leading to beam widening is multiple scattering. However, the hypothesis of a beam halo or beam divergence cannot be completely discarded since the diamond outside the chamber also gave a non-zero signal. In conclusion, to have a better control of our experimental conditions, it is essential to introduce a system that can measure the shape of the beam at the position of the DUT.

5.4.3 Fluorescent screen on DUT support

The setup was optimised further in 2023, as described in the Section 5.2.3, by adding a fluorescent screen "mscr_dbd.03" on the DUT support. This screen, together with the instrumentation described above, allows to focus the beam in the centre of the diamond. It also makes it possible to measure the beam profile, used in the analysis described in the Section 5.5.

Beam tuning

The beam tuning procedure consists of several steps, and has been improved based on the results and difficulties encountered during the previous irradiation campaigns.

1. With a charge of 500pC, the beam is transported through the linac up to the beginning DBD bending section. With the aid of a fluorescent screen as beam position monitor, a focused beam with a transverse size of $\sim 100\,\mu$m and symmetric shape is obtained.

2. The beam is bent to the DBD and the DUT support is moved so that the HOLE position is placed in the centre of the chamber, such that the beam passes unaltered to hit the screen "mscr_dbd.02". By measuring the charge on the current monitor "rctm_dbd.01" it is verified that all the charge is transferred to the DBD, minimising the beam losses. The fluorescent screen is then used to check that the beam keeps the desired shape and size up to DBD. This last step helps in the final collimation of the beam on the DUT.

3. Once a collimated beam is successfully transported to the DBD, the charge is lowered in steps of 100 pC down to 100 pC and in steps of 10 pC for lower charges. When lowering the charge, the current monitor and fluorescent screen are always available to check that the beam is collimated to DBD.

4. After setting the beam charge, the fluorescent screen "mscr_dbd.03" mounted on the sample support is inserted, positioning it in the nominal centre of the chamber. The position of the beam is adjusted so that it is centred on the screen. This is done by modifying the parameters of the quadrupoles, in particular the last quadrupole at approximately 50 cm before the support.

5. The beam is then focused by looking at the image on the screen to obtain a symmetrical spot with the desired transverse dimension.

At lower charge the intensity of the bright spot on the screen is reduced and it is necessary to change the gain of the CCD camera to measure the beam profile in a more sensitive range. As the gain changes, so does the background noise of the CCD. It is therefore necessary to store the screen image without the beam in order to have a background measurement, to be subtracted from the image measured with the beam.

In the transition from step 2 to step 3, the beam tends to widen and lose its symmetrical shape as the charge is reduced. It is therefore necessary to modify the parameters of the 5 quadrupoles on the DBD line to restore the beam shape. When going from step 3 to step 4, after inserting the fluorescent screen "mscr_dbd.03", I observed that the beam is not centred on the screen but shifted horizontally. It is therefore necessary to modify the parameters of the quadrupoles, and in particular of the last quadrupole "psq_dbd.05" in order to bring the beam back to the centre.

5.5 Beam parameters

In this section I report the results of the measurement of the main beam parameters. A good knowledge of the beam is needed to estimate the total charge injected into the detector by the beam, and to simulate the diamond response, as described in Chapter 6. Once the beam is optimised, the beam data for a total of 1000 consecutive bunches are recorded. In particular, the beam energy at DBD, the beam charge measured in DBD and the images of the fluorescent screen installed on the DUT support have been stored.

In the following I report the results of the analysis of beam parameters obtained for four different bunch charges in the range from 10 pC to 100 pC, with a beam energy of 1.234 GeV. The measured beam parameters are summarised in Table 5.2. In particular, I describe the analysis of the measured data for the bunch charge of 40 pC.

The average bunch charge is obtained from the distribution of the charge measured with the current monitor in DBD. The distributions in Figure 5.14 shown the charge measured with the current monitors placed at the injector (LH) and in DBD respectively.

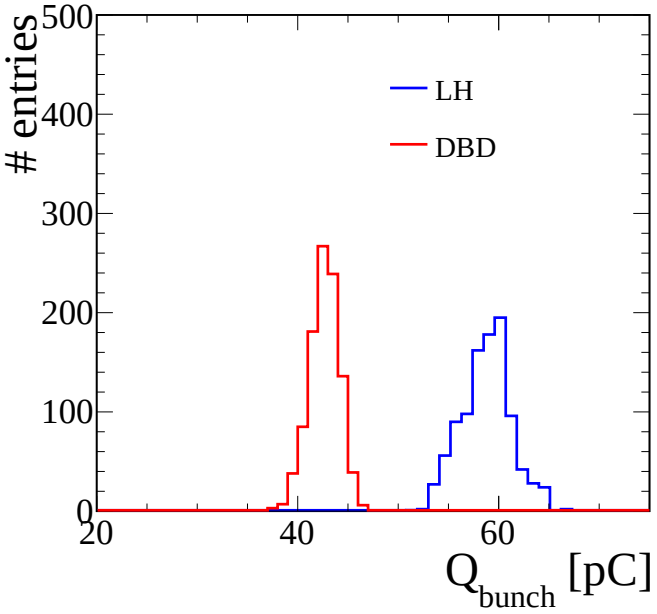

Figure 5.14: Distribution of the bunch charge measured at the injection LH, in blue, and in DBD, in red, for a sample of 1000 bunches.

The measured charge at the injector is always $\sim 30\%$ higher than the charge the measured charge in DBD, due to a charge loss in the transport of the beam up to DBD. For the lowest charge the charge in DBD is $\sim 70\%$ lower than the charge at the injection: this can be explained by an increased loss of charge as we operate the machine at the limit of the sensitivity of the beam diagnostic and feedback instrumentation. Moreover, the distribution of the charge in DBD is narrower due to the better resolution and different sensitivity of the corresponding monitor.

$Q^{\mathrm{LH}}_{\mathrm{bunch}}$ [pC]	$Q^{\mathrm{DBD}}_{\mathrm{bunch}}$ [pC]	σ_x [μm]	σ_y [μm]
96.45 ± 0.04	74.98 ± 0.06	62	98
58.75 ± 0.07	42.14 ± 0.05	67	84
36.41 ± 0.07	27.68 ± 0.03	174	132
23.29 ± 0.06	13.23 ± 0.03	206	195

Table 5.2: Summary of the measured beam parameters for four beam configurations.

The beam transverse size, which is approximately symmetric for the horizontal and vertical directions, is obtained from the analysis of beam profile described below. For the bunch charge of 40 pC, the measurement was repeated for four different transverse beam sizes with the aim of studying how the detector response changes with a larger beam spot on the detector. However, by increasing the spot size it is more difficult to maintain symmetry in the vertical and horizontal dimensions.

Beam profile

The screen images acquired with the CCD camera are converted to a distribution, as shown in Figure 5.15 on the left, where each bin corresponds to a pixel of the camera and the bin content corresponds to the measured light intensity by that pixel.

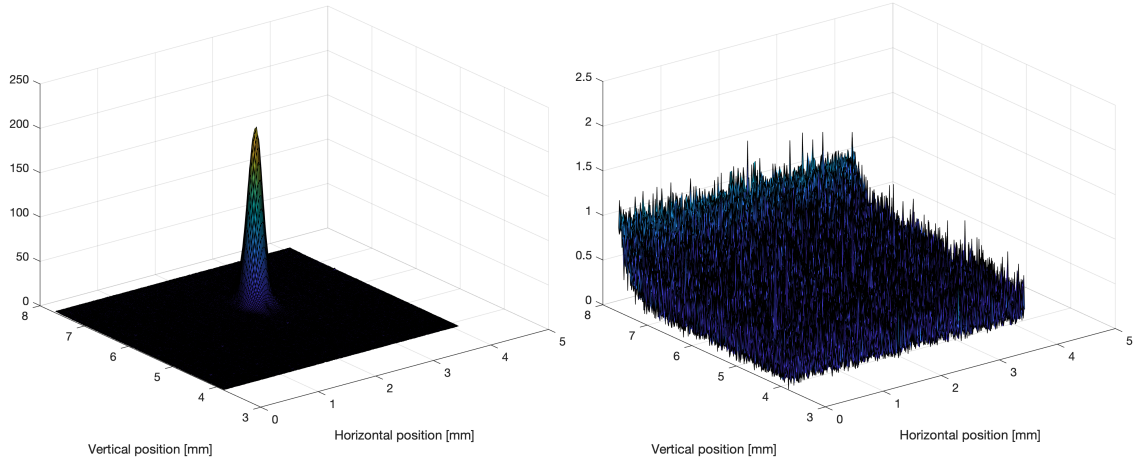

Figure 5.15: (left) Profile of the beam for a bunch charge of 40 pC and (right) the background noise obtained from a single shot image acquired with the CCD camera, for a set gain of 2 dB.

The pixel numbers are converted to a position using the factor $f = 66.5\,\text{pixels/mm}$, corresponding to $\sim 15\,\mu\text{m}$ per pixel both for the vertical and horizontal direction, obtained from a previous calibration of the setup using the target shown in Figure 5.7 as a reference. The bin content is proportional to the number of photons reaching the camera, with an adjustable gain.

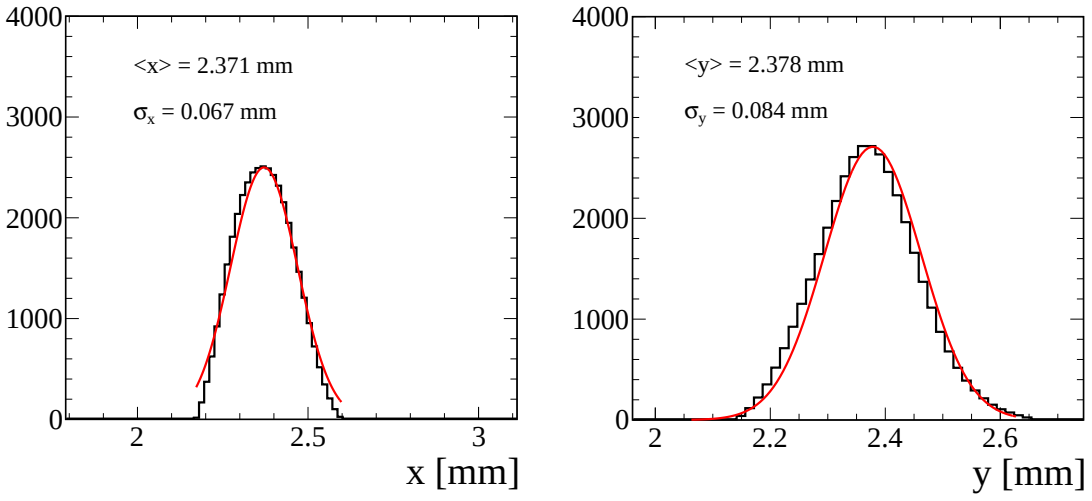

Figure 5.16: Average horizontal (left) and vertical (right) profiles measured for a beam bunch charge of 40 pC.

The measurements at higher bunch charge were performed with the lowest gain value of 2 dB, to minimise the camera saturation; at lower charge the gain were set at 12 dB.

An acquisition of the screen image without beam were done for each gain to determine the background noise of the camera, as shown in Figure 5.15 on the right. Vertical and horizontal profiles, obtained by projecting the distribution for each of the 1000 images, are shown in Figure 5.16. The two distributions are obtained after subtracting the averaged background measured for the same CCD gain. The distribution has a Gaussian shape with flat tails, which are related to the CCD noise and a small fraction of electrons deviated from the main bunch. I fitted the profiles with a single Gaussian to determine the position of the profile and the standard deviation, neglecting the contribution of the tails.

Even if the beam line parameters are fixed, the beam position and shape might change in time. For this reason I fit the individual profiles for each of the 1000 images with a Gaussian distribution, determining the mean position of the centre and the standard deviation both for the vertical and horizontal profile.
In Figure 5.17 the four plots show the profile centre and standard deviation as a function of time for the vertical and horizontal profiles respectively, measured for a bunch charge of 40 pC.

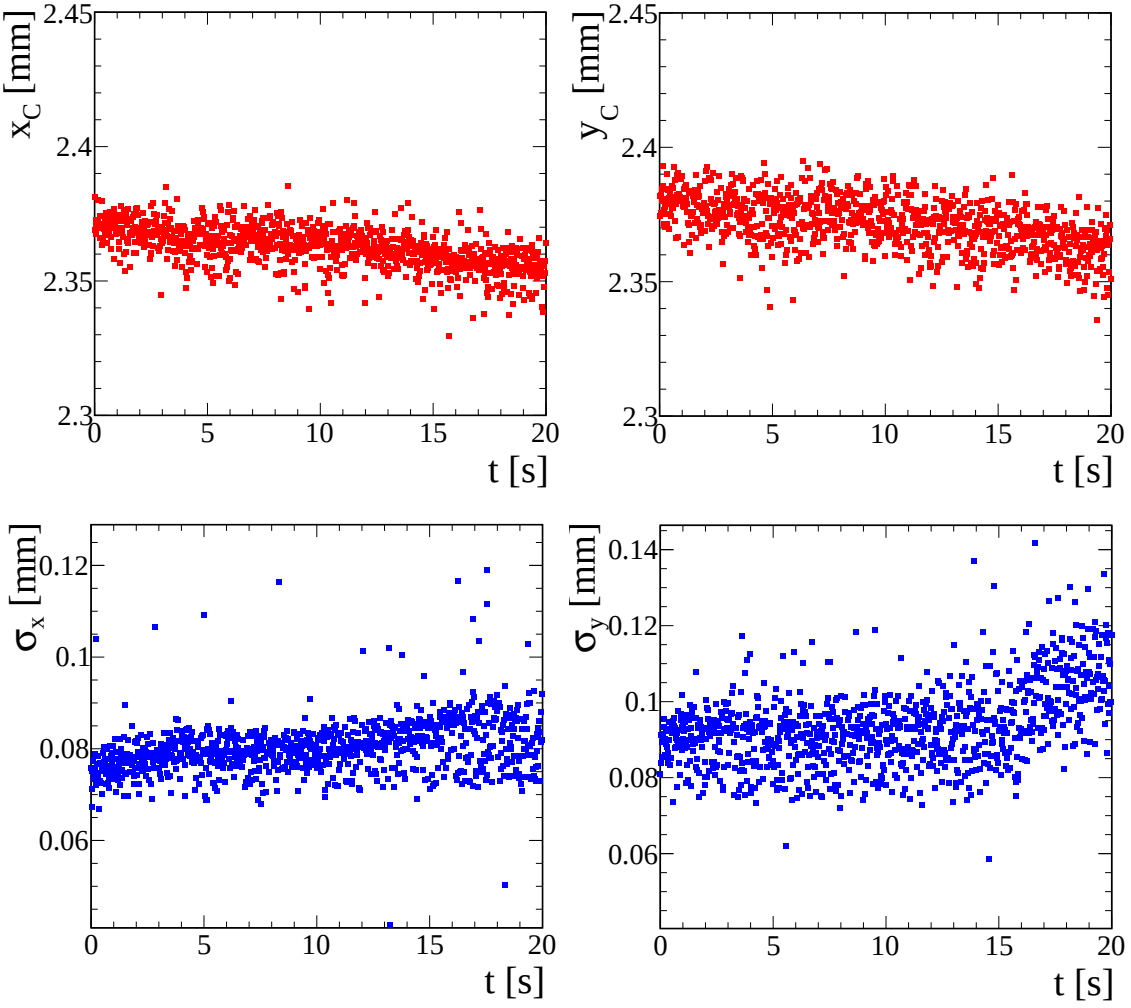

Figure 5.17: Beam profile centre (top) and sigma (bottom) as a function of time, respectively measured for the horizontal (left) and vertical (right) profiles.

Over a time intervals of 20 s, the profile centre fluctuates on average of about 7 μm and

9 μm in the horizontal and vertical projections respectively; also the standard deviation fluctuates in time, on average by $\sim$ 10%, and in a few cases it drifts in time. However, both these effects are included in the average distribution of the 1000 beam profiles, which will be wider than the single profile. The standard deviation obtained from the fit already takes into account the beam widening due to the change in beam position and the beam size over time.

After focusing the beam on the diamond at a fixed charge, a scan of the vertical position is performed to verify the position of the beam in the centre of the diamond and to obtain more information on possible boundary effects. In the optimised support, the detector is no longer tilted at an angle of 45°. If the DUT is moved vertically, the signal is expected to go to zero when the beam is outside the sensitive area of the sensor.

The plot in Figure 5.18 illustrates the fraction of the signal as a function of the distance of the beam from the centre of the diamond. These results are obtained with a bunch charge of 15 pC and a beam size of approximately 200 μm. At the edges of the diamond, roughly 2 mm from the centre, the signal fraction is around 30%. Additionally, outside the boundaries of the crystal, the signal is not zero.

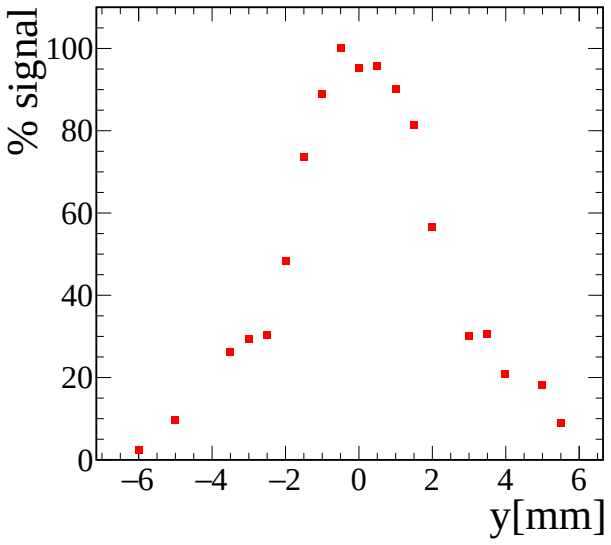

Figure 5.18: Vertical position scan: fraction of signal as a function of the beam position with respect the diamond centre, obtained for a bunch charge of 15 pC, with beam size of $\sim$ 200 μm.

This behaviour can be attributed to the presence of an electron halo surrounding the beam spot, which may not be readily visible on the fluorescent screen due to the limited emitted light outside the sensitivity range of the CCD camera. Since the charge in the halo is significantly smaller than that of the main bunch, the diamond detector may exhibit a different response, potentially collecting a higher number of charges. Consequently, the points at the edges of the diamond may not be directly comparable to those at the centre, potentially indicating a higher charge collection efficiency when the beam is not precisely focused on the detector active area and the charge carriers concentration is reduced significantly.

For a bunch charge of 40 pC the measurements have been repeated for different transverse size of the beam, by changing the quadrupoles current settings. By enlarging the

beam spot it is more difficult to obtained a stable beam focused in the centre of the screen and with a symmetric shape in the vertical and horizontal directions. When de-focused, the beam size becomes asymmetric and tends to separate to multiple bunches. In fact the distribution of the beam profile, for one of the measurements at 40 pC with a horizontal size of $\sim 500\,\mu$m, is characterised by the presence of three separate peaks, as shown in Figure 5.19.

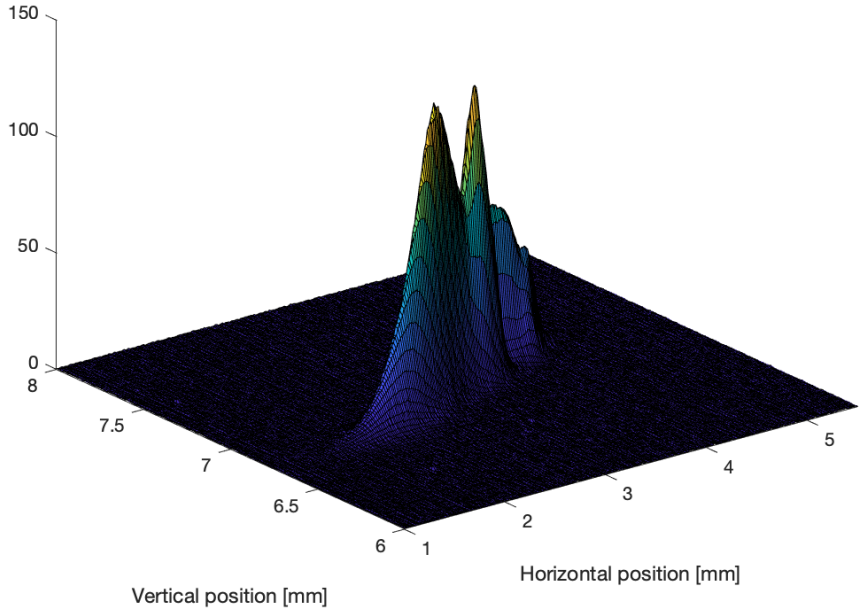

Figure 5.19: Profile of the enlarged beam for a bunch charge of 40 pC at the fluorescent screen. The beam profile presents a three peaks structure.

5.6 Detector signals

In this section I describe the analysis and results of the diamond response studies performed as a function of different parameters with the beam well focused in the centre of the sensor, in particular (a) the detector bias voltage, with fixed beam parameters; (b) the beam bunch charge, with fixed bias voltage; (c) the beam transverse size at the DUT, with fixed detector position and bias voltage. The sensors were always front-biased with positive voltage, while the signal ΔV as a function of time is measured from the back-side electrode. Figure 5.20 shows the simplified circuit of the readout system.

For each configuration of the detector bias voltage and the beam parameters I recorded the averaged signal shape obtained from the average of 1000 single pulses. In the following I discuss the analysis of the measurement performed with the detector DC15 at different beam conditions.

5.6.1 Signals amplitude and shape

During each irradiation campaign I recorded the diamond signals measured with the oscilloscope. Due to the large amount of charge carriers generated in the diamond, the induced current pulse was initially expected to have a maximum amplitude of the order of one ampere. To protect the instrumentation from these very large current pulses, the input

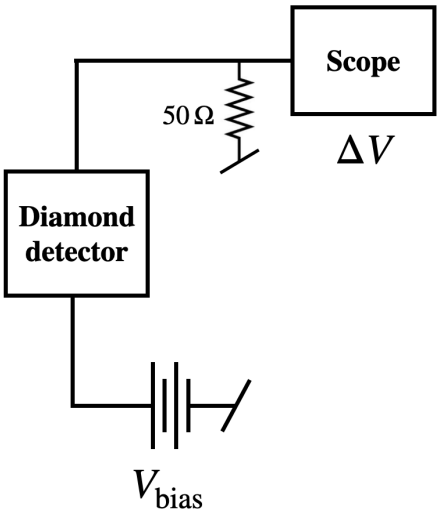

Figure 5.20: Simplified readout circuit with a $50, \Omega$ termination added in parallel to the oscilloscope input.

impedance of the oscilloscope was set to $1\,\mathrm{M}\Omega$ with a $50\,\Omega$ resistor in parallel, as shown in Figure 5.20.

In the initial setup described in Section 5.2.2, the signal shown in Figure 5.21 is characterised by a very fast rise time and an amplitude limited by the bias voltage, the cable impedance and the $50\,\Omega$ termination at the oscilloscope input. This behaviour is a consequence of the initial drop of diamond resistance to a very low value, attributed to the localized high density of charge carriers injected by ionisation along the beam path within the diamond bulk.

When the diamond resistance approaches zero, the induced signal, in a dynamic regime, essentially encounters the cable impedance in parallel with the $50\,\Omega$ termination on the oscilloscope input. Assuming the cable impedance is close to $50\,\Omega$, the signal amplitude at the oscilloscope is estimated using the formula:

$$\Delta V = \frac{Z_{\mathrm{cable}}}{50\,\Omega + Z_{\mathrm{cable}}} V \simeq \frac{1}{2} V\,, \tag{5.4}$$

where V is the signal induced in the diamond. The trailing edge has a rather long tail of the order of hundreds of ns with signal reflections delayed by about 80 ns. They are due to an impedance mismatch at the output of the power supply, which supplies the bias voltage to the diamond detector via a high quality 10 m long coaxial cable.

In June 2023 a $50\,\Omega$ resistor was added in series with the power supply to reduce the impedance mismatch on the bias line and thus the amplitude of the reflected signal. The left plot of Figure 5.22 shows the signal for one of the diamond detectors (DC15) measured in the optimised setup, biased at the reference voltage $V_{bias} = 100\,\mathrm{V}$, which according to our calibrations 4.4.3 with a β source corresponds to about 100% charge-collection efficiency. In this scenario, a relatively low ionisation density is generated within the diamond bulk by a steady state flux of minimum ionising particles. For this measurement the bunch charge in DBD is 28 pC and the spot standard deviations are $132\,\mu$m and $174\,\mu$m for the vertical and horizontal direction respectively.

The signal is characterised by an amplitude of $\sim 13\,\mathrm{V}$, which is a factor 3.5 smaller than the one of the signal measured with the initial setup and a bunch charge of 35 pC. It

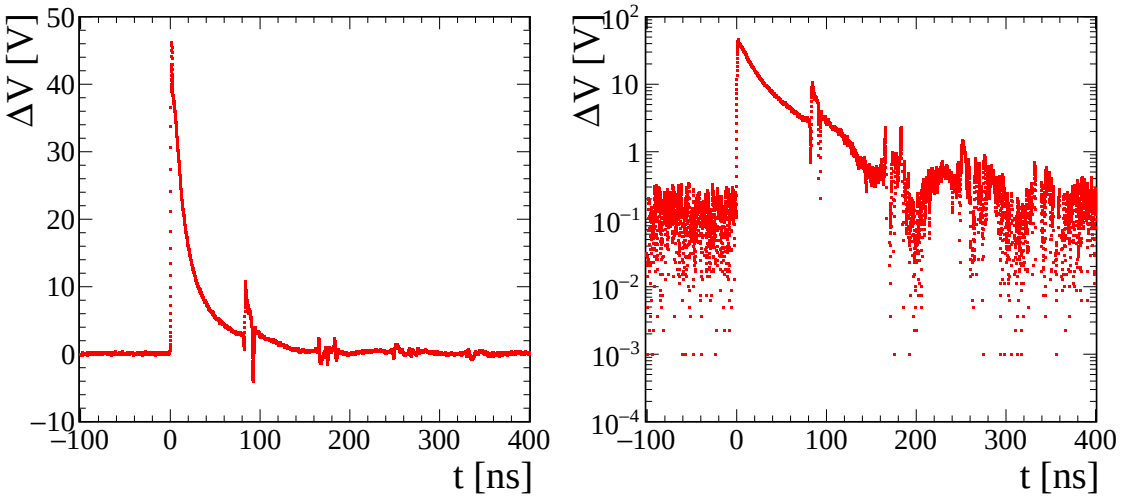

Figure 5.21: Averaged signal measured with DC15 biased at 100 V and a 35 pC bunch charge, during an irradiation campaign with the initial setup. The signal is also shown in logarithmic scale (right)

always has a very fast rise time, of about 500 ps and a tails of hundreds nanoseconds. Also in this case the amplitude of the signal is limited by the bias voltage, the coaxial cable, the 50 Ω termination on the oscilloscope input and the diamond resistance at the hitting time, since this last one initially drops to a very low value when a local high density of charge carriers is injected by ionisation along the beam path in the diamond bulk. The signal rise time is compatible with the bandwidth of the transmitting cables (about 2 GHz). Small signal reflections are still evident with a delay of about 80 ns. The amplitude of the reflected signal experiences a significant reduction following the addition 50 Ω resistance in series to the power supply, which is an evidence of a reduced impedance mismatch. An attempt to quantitatively explain these features is subject of Chapter 6.

Moreover the signal presents a bump, shown in Figure 5.22, that is observed about 100 ns in advance with respect to the signal leading edge, triggering the scope. The bump has a rounded shape with a slow rise time of ~ 50 ns, amplitude of the order of 100 mV and FWHM of about 50 ns. This spurious signal is not related to the readout circuit, but might be associated to the presence of electrons accelerated with a different injection time and a different energy than the main bunch. However, it is not possible to measure separately the spurious signal and the signal induced by the main bunch only by tuning the machine parameters. A possible explanation for this signal is the presence of a *dark current* [116]. The electromagnetic fields in high gradient RF structures can cause electron emission from the metallic walls of the structure. If the emitted electrons are captured and accelerated by the accelerating fields, a so-called *dark current* is induced. This hypothesis is supported by the observation of a bright spot on the DBD fluorescent screen even after the laser is switched off, leaving all RF structures powered. However, we could not quantify this effect on the accelerated beam.

For each averaged signal I determine the maximum amplitude, the integral, the FWHM and the rise time between 20% and 80% of the signal maximum amplitude. From the integral of the signal A_{signal} I determine the collected charge as:

$$Q_{\text{collected}} = \frac{A_{\text{signal}}}{50\,\Omega} \tag{5.5}$$

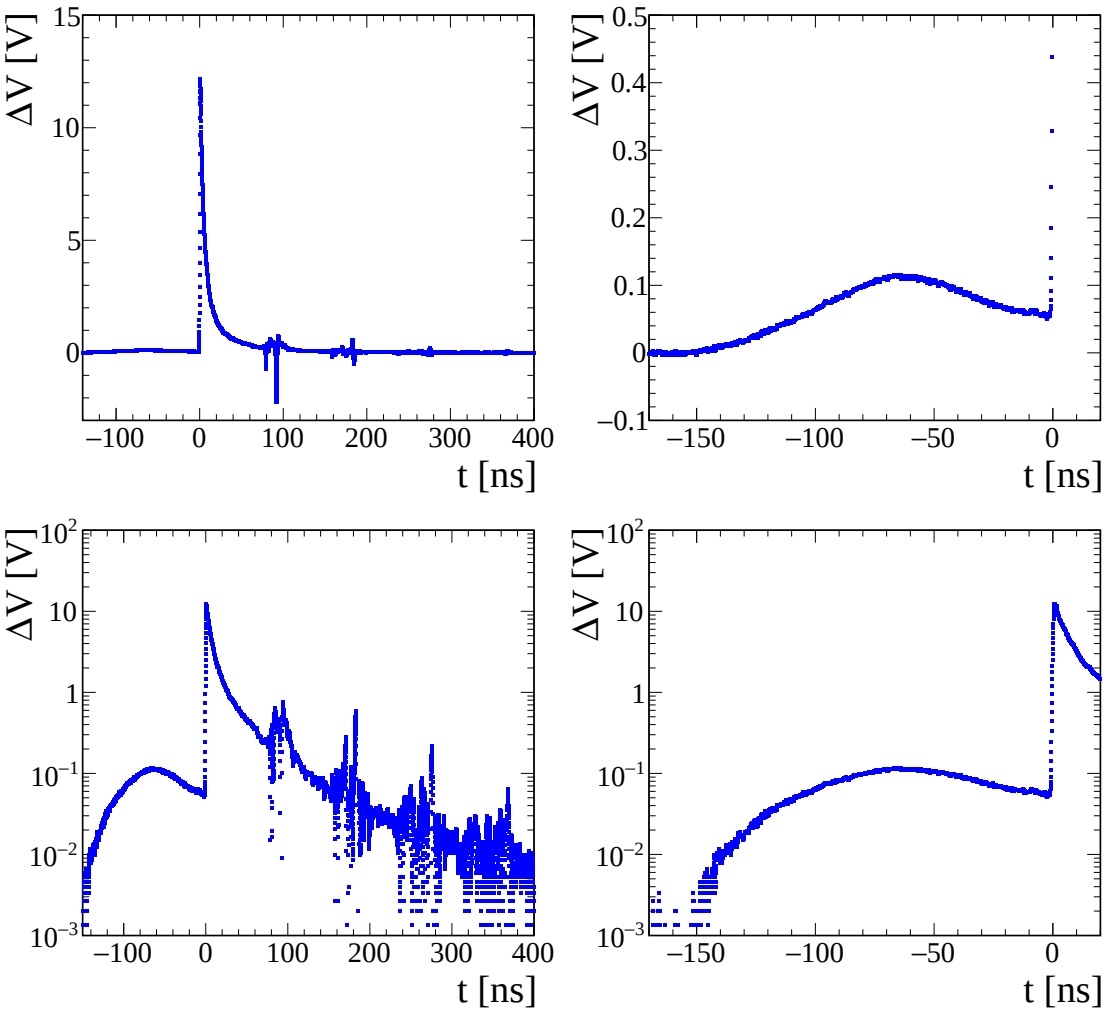

Figure 5.22: (top) On the left the averaged signal measured with DC15, biased at 100 V, for a 30 pC bunch charge. On the right a zoom-in of the average signal for $t < 0\,\mathrm{s}$, before the trigger time. (bottom) The same signals are shown in logarithmic scale.

where 50 Ω is the approximate impedance at the oscilloscope input, given by the termination of the cable. This value is correlated with the total charge injected by ionisation. In the detector characterisation with α particles (see Section 4.3) from a low-intensity α-source, all charge carriers are collected: signal integral and total ionisation charge coincide.

5.6.2 Detector bias-voltage scan

After setting the parameters of the optimised beam at a fixed bunch charge, I performed a bias-voltage scan, varying the bias voltage from 10 V to 300 V. A higher bias voltage is achieved for the lower charge measurement because the signal amplitude didn't saturate the oscilloscope scale. Figure 5.23 shows an example of the measured signals at four different bias voltages, for bunch charge of 40 pC.

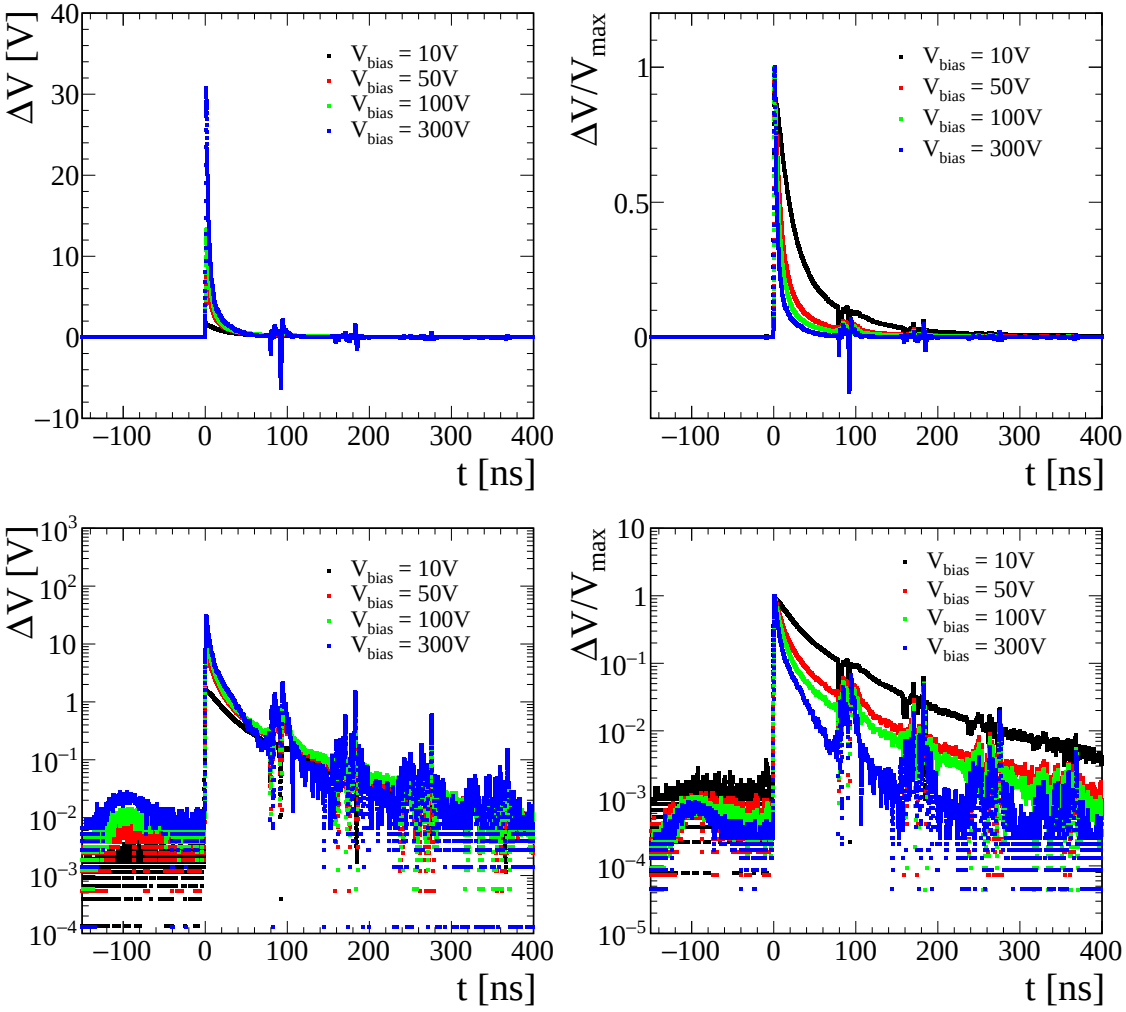

Figure 5.23: (top) Average signals measured with four different bias voltages, for a bunch charge of 40 pC. The signals on the right are re-normalised to the maximum amplitude of the signal. (bottom) The same signals are shown in logaritmic scale.

By increasing the bias voltage the signal amplitude and integral increase, while the FWHM decreases. Re-normalising each signal amplitude by its maximum, as shown in Figure 5.23, the effect of the increasing bias voltage on the signal shape is more evident:

by applying an higher bias voltage the electric field inside the diamond bulk increases, reducing the drift time of the charge carriers in the charge collection process.

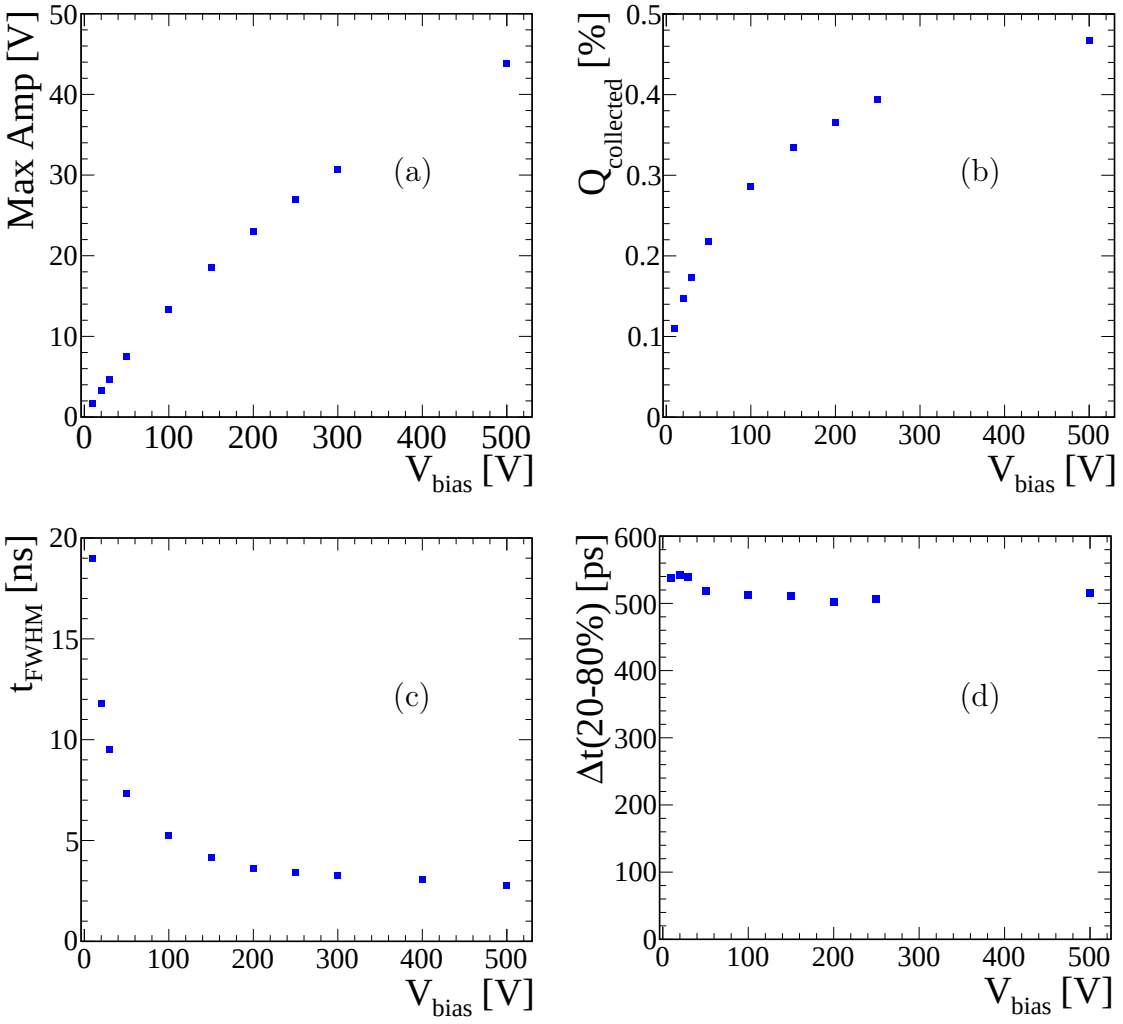

Figure 5.24: Results of the detector bias voltage scan performed for a bunch charge of 42 pC: signal maximum amplitude (a), percentage of collected charge (b), signal t_{FWHM} (c) and signal rise time $\Delta t(20-80\%)$ (d) as a function of the bias voltage V_{bias}.

The dependence of amplitude, fraction of collected charge, FWHM and rise time on bias voltage is shown in Figure 5.24. The fraction of collected charge $Q_{\mathrm{collected}}$ is determined from the ratio of the collected charge and the injected charge generated by ionisation in the diamond as the electron bunch crosses the diamond sensor.

The total ionisation charge produced in the diamond bulk by the electron bunches is estimated using the mean deposit energy by a 1.234 GeV electron in the diamond bulk, obtained with FLUKA [77] simulation of the experimental setup. I simulated the diamond detector, including its 240 μm thick aluminium cover, and a beam of 1.234 GeV electrons hitting its centre. I generated 5×10^6 events, recording the deposited energy E_{dep} in the active volume of the diamond detector. Figure 5.25 shows the Laundau distribution of the deposited energy in the active volume of the diamond, which has a mean value of $E_{\mathrm{dep}} = 0.302$ MeV. This value is close to the value of 0.35 MeV estimated assuming a

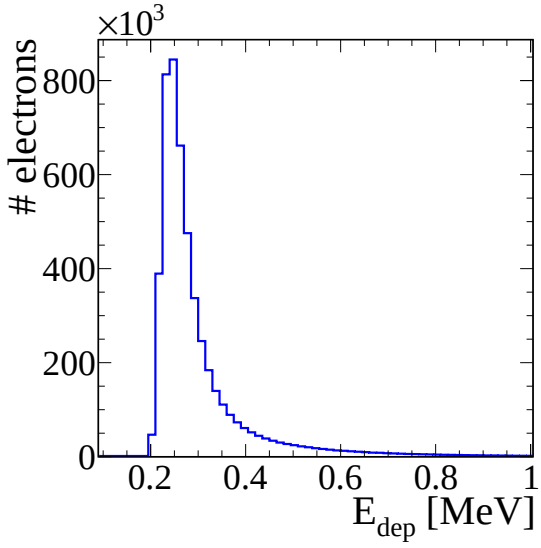

Figure 5.25: Energy deposited by 1.234 GeV electrons in the active volume of the diamond sensor, obtained in FLUKA.

stopping power of $7\,\mathrm{MeV}\cdot\mathrm{cm}^{-1}$ for 1.234 GeV electrons in the diamond [117] and the sensor thickness of 500 μm.

Given that a bunch with a charge of 1 pC has a number of electrons $N_e = 6.24 \times 10^6$, the expected number of electron-hole pairs generated by a bunch of 1 pC is given by

$$N_{eh} = \frac{N_e E_{dep}}{E_{eh}} = 3.75 \times 10^{11}, \tag{5.6}$$

where $E_{eh} = 13\,\mathrm{eV}$ is the mean energy to create an electron-hole pair in diamond. Assuming full charge collection efficiency, each electrode would then collect all the injected charge $Q_{injected} = N_{eh} q_e \simeq 60\,\mathrm{nC}$, where q_e is the elementary charge.

The signal amplitude increases linearly with the bias voltage up to 50 V, then rises more slowly tending to a saturation value. Also the collected charge increases monotonically as a function of the bias voltage. In the present electron beam conditions, the collected charge corresponds to a few ‰ of the total ionisation charge for each bunch crossing and is approaching a saturation value of 0.5% : this is a strong indication of relevant charge carrier losses by recombination in the diamond bulk. Moreover, while the FWHM decreases with the bias voltage, the rise time has a stable value at different bias voltages, with an average value of 520 ps, with a $\sim 10\%$ higher value at low bias voltages: this value is due to the bandwidth limitation, which is dominated by the thin micro-coaxial cable of the diamond detector. Even in presence of a strong recombination inside the diamond volume, the diamond detector has a fast response.

5.6.3 Bunch charge scan

The voltage scan was performed for four different values of the bunch charge: 75.5 pC, 42.5 pC, 28 pC and 13.1pC. Figure 5.26 shows a comparison of the measured signal parameters as a function of bias voltages for the different charge values. The signal amplitude increases with the bunch charge (a), while the rise time (c) slightly decreases at low V_{bias}. For a voltage higher than 50 V the rise time (d) has an average value of 500 ps for all the three charges.

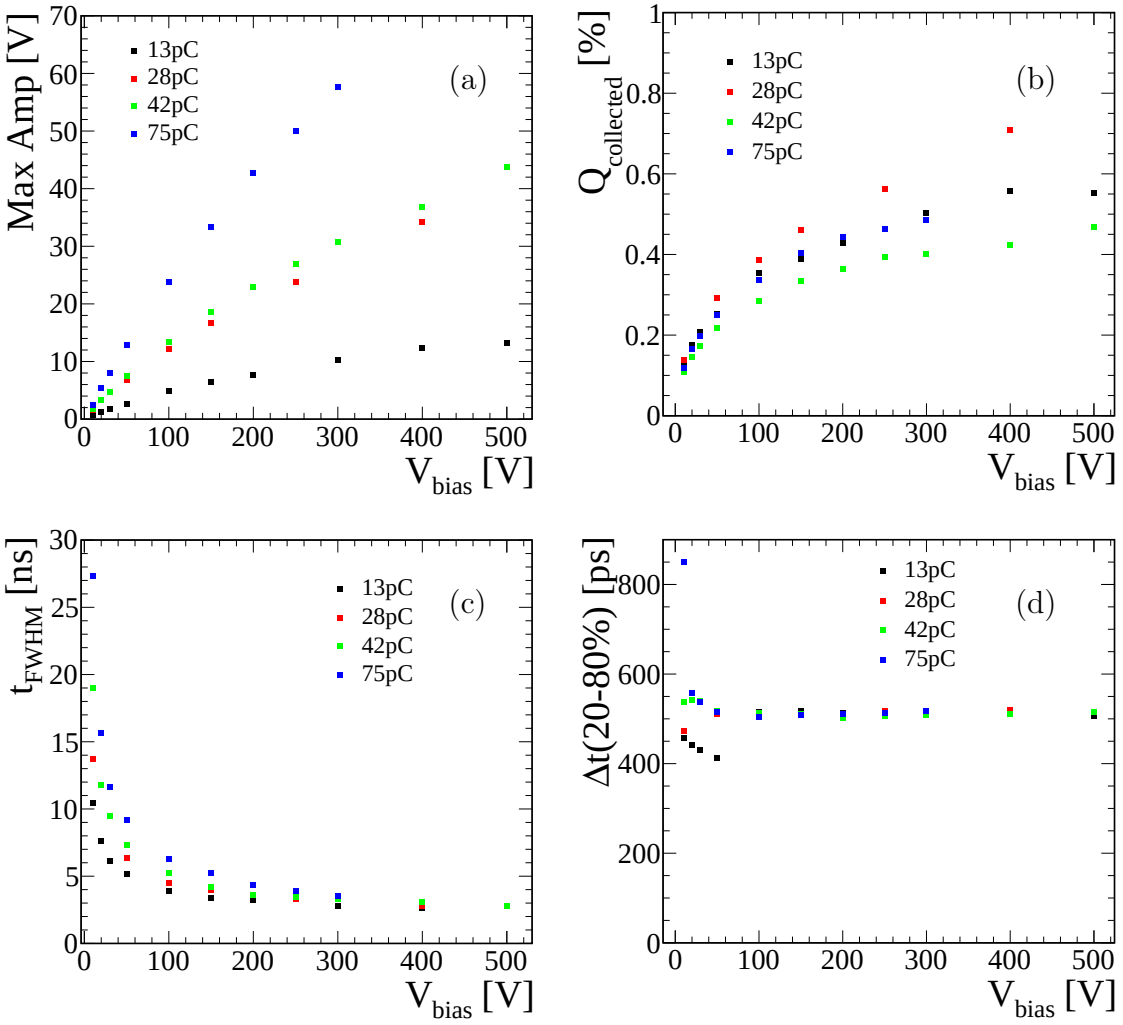

Figure 5.26: Results of the bias voltage scan performed for four different bunch charges (reported in the legend) by varying the detector bias voltage: signal maximum amplitude (a), percentage of collected charge (b), signal t_{FWHM} (c) and signal rise time $\Delta t(20-80\%)$ (d) as a function of the bias voltage.

The fraction of collected charge is lower than 1 % for all the measurements, but the four different data sets are not ordered according to the bunch charge, as seen in Figure 5.26 (b). With less charge injected into the bulk of the diamond, the charge collection efficiency is expected to increase. But the charge collection efficiency is limited by the large charge carrier density in the diamond bulk: it depends also on the volume where this charge is generated. Since while varying the beam bunch charge also the beam transverse size was changing, the charge density generated by the incident beam must be somehow considered.

One way to take the charge carrier density into account is to define an "effective volume" V_{eff} of the collected charge carriers as:

$$V_{\mathrm{eff}} = \frac{Q_{collected}}{q_{injected}} = \frac{Q_{collected}}{\frac{Q_{injected}}{V_{beam}}}, \tag{5.7}$$

where $Q_{collected}$ is the collected charge and $q_{injected}$ is the injected charge density of one carrier type inside the diamond volume, given by the ratio between the injected charge

$Q_{injected}$ and the volume V_{beam} crossed by the beam. The volume crossed by the beam is approximated by the product of the beam transverse section S and the diamond thickness $d = 500\,\mu$m. Since the beam spot is not symmetric for the vertical and horizontal dimension, an elliptical shape is assumed. The transverse section crossed by $\sim 90\%$ of the beam particles is $S = 4\pi(\sigma_x \cdot \sigma_x)$, where σ_x and σ_y are the standard deviations reported in Table 5.2, for the horizontal and vertical beam profiles respectively.

Bunch charge DBD [pC]	Transverse section S [cm^2]	$q_{injected}$ [C cm^{-3}]
74.93 ± 0.06	8×10^{-4}	3.31×10^{17}
42.40 ± 0.05	7×10^{-4}	1.74×10^{17}
28.13 ± 0.03	27×10^{-4}	3.27×10^{16}
13.13 ± 0.03	59×10^{-4}	8.66×10^{15}

Table 5.3: Summary of the measured beam parameters for four beam configurations, used for the bunch charge scan.

The values calculated for the transverse beam section and the injected charge density are reported in Table 5.3. For a collection efficiency of 100%, *i.e.* all the charge generated by ionisation collected, the effective volume would coincide with the volume crossed by the incident beam. This "effective volume" therefore can be interpreted as an indicator of the volume associated with the collected charge. Figure 5.27 shows the effective volume as a

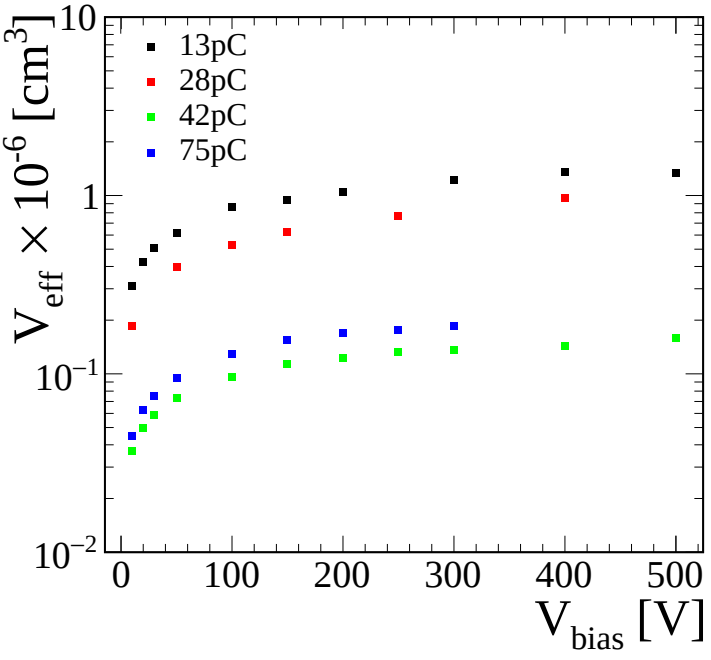

Figure 5.27: Effective volume V_{eff} as a function of the bias voltage for four different bunch charges.

function of the bias voltages for the four different bunch charges. The effective volume V_{eff} is higher for the 13 pC bunch charge, which corresponds to a lower ionising charge density, and monotonically decreases with increasing bunch charges, as expected.

5.6.4 Beam size scan

I also tested the response of the diamond detector with fixed bias voltage of 100 V and fixed bunch charge of ~ 40 pC but different transverse beam distributions at the DUT position. Figure 5.28 shows the the measured signals for three different beam transverse width. Increasing the incident beam width, the signal amplitude and integral increase. Data taken with a fourth beam setting were excluded from the analysis due to uncertainties in the exact beam positioning.

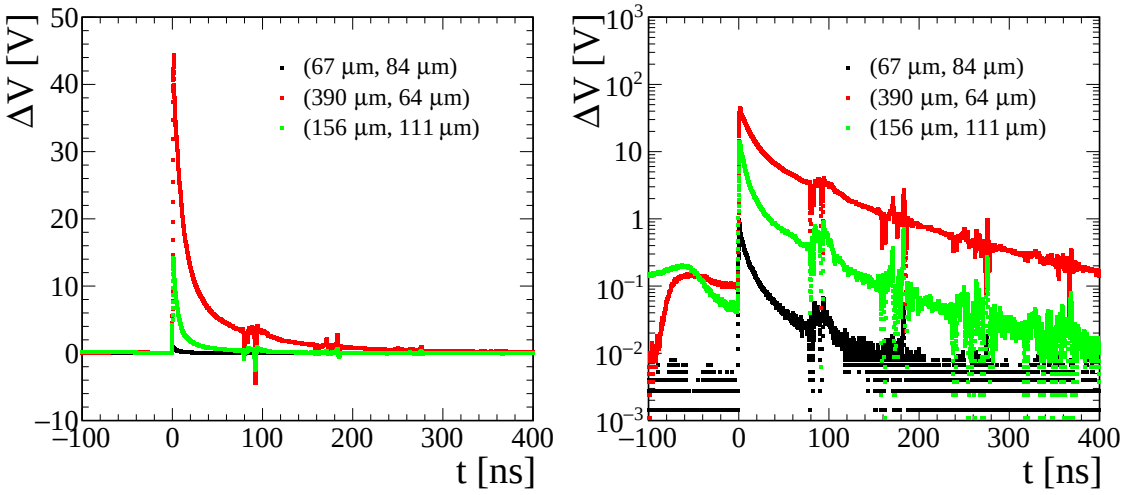

Figure 5.28: Signals from detector DC15 biased at 100 V, for a bunch charge of ~ 40 pC and different beam spots. The legend reports the horizontal and vertical standard deviations of each beam spot.

Table 5.4 reports the measured parameters of the beam, *i.e.* the bunch charge and the transverse section, but also the injected charge carrier concentrations generated inside the diamond bulk and the fraction of collected charge, given by the ratio of the collected charge $Q_{collected}$ and the injected one $Q_{injected}$. The different beam configurations are labelled as B1, B2 and B3.

Beam config.	Q_{DBD} [pC]	S [cm^2]	$q_{expected}$ [C cm^{-3}]	$\%C_{\mathrm{collected}}$
B1	42.14 ± 0.04	8.1×10^{-4}	1.51×10^{13}	2.33×10^{-2}
B2	48.05 ± 0.04	31.4×10^{-4}	4.45×10^{12}	2.01
B3	42.62 ± 0.04	21.8×10^{-4}	5.74×10^{12}	0.35

Table 5.4: Summary of the measured beam parameters for three beam configurations, used for the beam size scan.

The fraction of charge collected increases as the beam widens. This is effect is due to a lower initial charge carrier concentration injected by ionisation, since the volume crossed by the ionising beam is larger. Enlarging the beam transverse size by a factor 4, the charge collection efficiency grows by a factor 10.

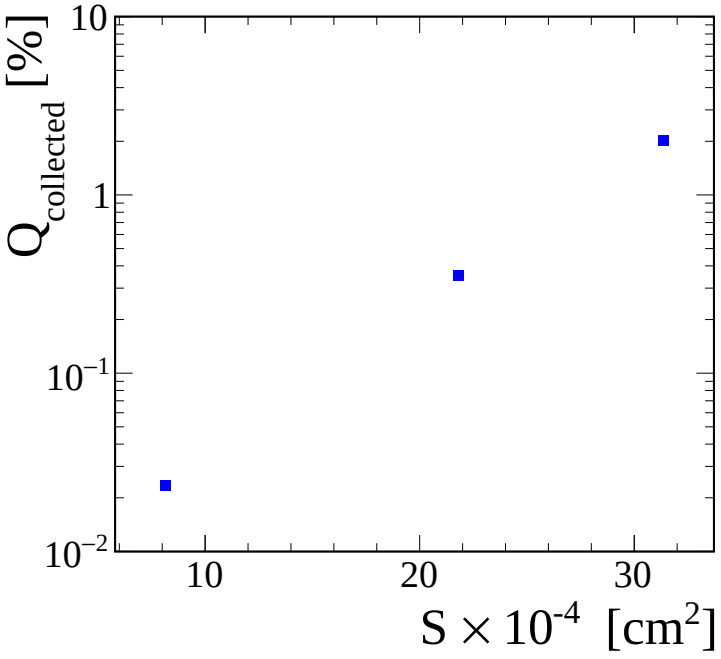

Figure 5.29: Fraction of collected charge as a function of the beam spot transverse section, measured for a bunch charge of ~ 40 pC.

5.7 Summary

The tests described in this Chapter aims at studying the response of our diamond detectors under extreme transient conditions. Our detectors are irradiated with intense 1 GeV electron pulses provided by the linac of the FERMI free-electron laser. In this challenging environment the diamond detector might show a non-linear response due to the high charge carrier density injected in the diamond bulk, which can shield the electric field affecting the signal formation, and so also affect the charge collection process in which charge recombination is no more negligible.

To comprehensively explore these effects, we performed different sets of measurements under various conditions. We systematically varied the bias voltage applied to the diamond detector and the beam parameters, such as the bunch charge and beam spot size. The resulting signals are characterised by an exceptionally fast rise time af ~ 500 ps, amplitudes of the order of ten volts, and long trailing edges spanning hundreds of nanoseconds. Our results are in qualitative agreement with the expectations outlined in Section 5.1. Specifically, I observed that increasing the bias voltage leads to a simultaneous increase in signal amplitude and integral, while the full-width half-maximum (FWHM) decreases. This phenomenon is attributed to the increased electric field within the diamond bulk, which reduces the drift time of charge carriers during the collection process, resulting in greater charge collection. However, as the voltage is further increased, a saturation point is reached with a value of the collected charge significantly lower than 1% for bias voltages exceeding 100 V. This is a clear indication of strong recombination processes occurring within the diamond bulk. Even in presence of a strong recombination inside the diamond volume, the diamond detector has a fast response.

Furthermore, our investigation of the bunch charge scan reveals that both the signal

amplitude and integral increase as the charge of the bunch grows. However, the collected charge is not a function only of the bunch charge, but it depends on the injected charge carrier density. A lower charge carrier density in the diamond bulk would correspond to an higher charge collection efficiency. This expectation is based on the assumption that a reduction in the injected charge would correspond to a diminished shielding effect within the diamond material. In an attempt to quantify these effects, we introduced the concept of an effective volume. The charge collection efficiency is 100% when the effective volume matches the volume crossed by the beam. Lower charge carrier concentration within the diamond bulk results in an increased effective volume, corresponding to higher collection efficiency. This effect is further emphasised by our investigations into varying beam sizes while keeping the beam charge constant. Increasing the beam size consistently resulted in an increase in charge collection efficiency.

A first attempt of a quantitative modelling of signal formation under these extreme conditions in our diamond detectors is outlined in Chapter 6.

Chapter 6

Simulation of the diamond-detector response to ultra-short and intense high-energy electron pulses

In this Chapter I describe a two-step numerical simulation approach to simulate the response of diamond to intense electron bunches. As shown in Chapter 5, when a large ionisation energy is deposited in the diamond bulk in a short time and limited volume, the large concentration of generated charge carriers gives rise to space charge effects that affect the signal formation. The time response of the diamond detector simulated by TCAD-Sentaurus is described Section 6.2, while the external electronic circuit is taken into account by LTspice as discussed in Section 6.3. The approach is validated simulating the diamond response for transient-current-technique (TCT) measurements with α radiation, described in Section 6.4. Finally the comparison between preliminary simulation results and part of the experimental data is reported in Section 6.5. I presented the work described in this Chapter at the conferences [99, 100] and published in [118].

6.1 Introduction

In conditions of low ionisation charge generated inside the diamond detector, when a bias voltage is applied by an external circuit between the two electrodes of the diamond detector, the electric field generated inside the diamond bulk is approximately uniform and the generated electrons and holes drift towards the electrodes, inducing a signal in the external circuit. Thanks to their high charge carrier mobility, diamond detectors can generate very fast signals. However, in the case of large ionisation energy deposition in the diamond bulk, the large concentration of charge carriers may modify the electric field inside the diamond bulk, affecting the signal shape. Also the external circuit contributes to the signal formation. The signal therefore is determined by an interplay between charge carrier transport in the diamond bulk and signal transmission in the external circuit.

This study is motivated by the need to establish a comprehensive model for characterising the time response of diamond detectors under various irradiation conditions, with a particular focus on understanding saturation and non-linearity in the diamond response under extreme radiation conditions. As described in Chapter 5, we tested the diamond detectors with short intense 1 GeV electron pulses in a dedicated test station installed on the FERMI e^- linac diagnostic beam dump. The linac provides electron bunches with a transverse size down to 100 μm and a charge ranging from tens to hundreds of pC. Under

these conditions, a large charge carrier concentration is generated in a limited volume and in a very short time. However, only a small fraction of the generated charge is collected, indication of charge losses during the collection, leading to a non-linear response. Therefore, a simulation of the diamond response to ultra-short and intense high-energy electron pulses is used to better understand how the device works in this regime.

Successful attempts in the diamond devices simulation have been made using Technology Computer-Aided Design (TCAD) software [119] to investigate some properties of diamond devices, e.g., the charge collection efficiency under different bias voltages [120], the transient current caused by single α-particle hit [121]. The TCAD tools capabilities are routinely adopted within the design flow of semiconductor devices, in order to simulate their electrical characteristics as the response to external stimuli. However, device level simulation of diamond detectors has also progressed over the past years.

Moreover, TCAD-Sentaurus and LTspice [122] are widely used simulation programs for semiconductor characteristics and electronic circuits, respectively. The diamond response has been simulated through a two-step numerical simulation using Technology Computer-Aided Design (TCAD-Sentaurus) software to simulate signal formation and LTspice to add the effect of the readout circuit on the signal. TCAD has the capability to include the external circuit in the simulation through "mixed-mode" simulation. However, in our specific case, we were unable to include the complete circuit, in particular a model for coaxial cables. Therefore, we decided to use LTspice for modelling the external circuit. An outline of the TCAD environment and the model use for our device is given in Section 6.2, while the LTspice simulation of the readout circuit is described in Section 6.3.

6.2 TCAD simulation of the diamond response

In this Section, I describe the first step of the simulation process, highlighting the selection of key diamond physical parameters and the choice of models within the TCAD framework. Using TCAD-Sentaurus, a series of sequential processes of the diamond detector are simulated, including the beam-crystal interaction, the creation of electron-hole pairs, the drift of charge carriers, and the evolution of the induced voltage drop on the electrodes: the space-time evolution of the concentration of charge carriers inside the diamond crystal is also obtained.

6.2.1 Sentaurus Technology CAD

Sentaurus TCAD, developed by Synopsys© [119], is a powerful and widely used software suite for Technology Computer-Aided Design (TCAD) simulations in the semiconductor industry. It provides a comprehensive set of tools for simulating and optimizing the performance of semiconductor devices. One of the key features of Sentaurus TCAD is its ability to model charge transport in semiconductor materials with high accuracy. The predictive power of its numerical calculation for the response of semiconductor devices to external electrical, thermal, and optical sources has been verified via numerous applications in the semiconductor industry.

The suite of software tools is composed of several programs specialised to accomplish different tasks of the design flow. *Sentaurus Structure Editor* provides a graphical interface for the 2D or 3D layout design, *Sentaurus Device* is the simulation engine and numerically reproduces the electrical behaviour of devices, even combined in articulated circuits (mixed-mode analysis). The simulation results can be plotted in terms of both macroscopic and microscopic quantities, taking advantage of the *Inspect* and *Sentaurus Visual* modules

respectively.

The simulated domain is a realistic approximation of the actual device, since it is represented by a finite number of points in space (mesh), where the physical characteristic quantities of the device are discretised. Optimisation of the simulation requires the minimum number of mesh elements to reduce the computational load upon the system, whilst maintaining the required level of accuracy of the simulation. The terminal currents, the voltages, and the charges, are computed according to a set of equations that describe the carrier distribution and the conduction mechanisms, in each mesh point. Every simulated device is described by a file which contains information about the geometry of the structure, *i.e.* description of the various regions, boundaries, materials, contacts shape and location, and the doping profiles. These data are strictly associated to the mesh points and the overall file is given as input to the Sentaurus Device tool, which generates an output that can be analysed and plotted.

The charge transport in the device is obtained from a set of fundamentals differential equations, taking into account the overall effects of drift, diffusion, generation and recombination.

Poisson's equation: Poisson's equation relates the electric potential (Φ) to the charge density (ρ) in the semiconductor. It provides the electric field within the material. The equation is:

$$\nabla^2\Phi = -\frac{\rho}{\epsilon}\,, \tag{6.1}$$

where ϵ is the permittivity of the semiconductor material.

Charge continuity equations: These equations describe the rate of change of carrier concentration (electron and hole) with respect to time and position. They account for carrier generation, recombination, and motion due to drift and diffusion. The continuity equations, for electrons and holes respectively, are:

$$\frac{\partial n}{\partial t} = \nabla\cdot(D_n\nabla n) - \nabla\cdot(\mu_n n\nabla\Phi) + G_n - R_n\,, \tag{6.2}$$

$$\frac{\partial p}{\partial t} = \nabla\cdot(D_p\nabla p) + \nabla\cdot(\mu_p p\nabla\Phi) + G_p - R_p\,. \tag{6.3}$$

In the equations n and p are the electron and hole concentrations, D_n and D_p are the diffusion coefficients, μ_n and μ_p are the carrier mobilities, Φ is the electric potential, $G_{n/p}$ represents generation rates, and $R_{n/p}$ signifies recombination rates.

The solutions are obtained via a numerical method: the differential equations are discretised to a first-order approximation, giving rise to a set of algebraic non-linear coupled equations, and then solved iteratively to obtain the carrier concentrations and electric potential at different positions and times within the semiconductor device. The simulation typically considers boundary conditions, material properties, and doping profiles to capture the behaviour of charge carriers in response to applied voltages, external fields, and various semiconductor structures. The method requires also an initial guess of the solution, with several iterations and an adjustment of the guess until an acceptable degree of accuracy is obtained.

6.2.2 Diamond detector model

In the following I describe the model used in the simulation of our diamond detector, with the description of the device geometry, the definition of the material properties and the models used for carrier transport.

Detector geometry

The diamond detector, described in detail in Chapter 4, consists of a $(4.5 \times 4.5 \times 0.5)$ mm^3 high-purity sCVD diamond crystal with two (4.0×4.0) mm^2 electrodes on opposite faces made of Ti+Pt+Au layers $(100 + 120 + 250)$ nm thick. In TCAD it is possible to define a 3D geometry of the device, but this requires considerable computing resources, especially for our diamond detector, which is not very small.

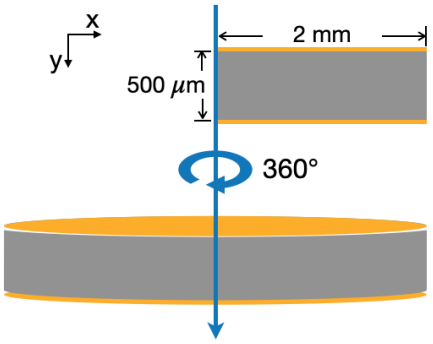

Figure 6.1: Geometry of the diamond detector in TCAD-Sentaurus. To make meshing easier, the thickness of electrodes is set as 10 μm, much thicker than their real dimension. Incident electron bunches traverse the detector along the arrow, which is also the rotation axis.

Since the properties of diamond do not change within the volume, its simple geometry allows the *2D-Cylindrical Model* to be used to describe the sensor geometry, balancing precision and computation time. This model assumes that the behaviour of the device is symmetrical with respect to the azimuthal angle, so that a 3D device can be described in a 2D coordinate system. Figure 6.1 shows a diagram of the 2D geometry of the diamond defined in the simulation and how it can be connected by rotation to the 3D model. The sensor is simulated as 500 μm thick and 2 mm wide, *i.e.* half of the longitudinal section delimited by the two electrodes. The incident electron beam, described in a following paragraph and represented by the blue arrow in the figure, crosses the sensor along one of the two edges. In the 3D model this corresponds to the centre of the sensor.

The mesh is defined with a rectangular shape, whose domain is limited by the length and thickness of the diamond crystal. A mesh 10 times thinner is chosen along the beam path in the sensor, where a larger variation of the charge carrier concentration is expected. The aim is to represent the device as accurately as possible with acceptable computing time. To simplify the mesh, the electrodes are defined as two 10 μm thick aluminium electrodes, which are thicker than in reality. This definition has no effects on the simulation results as the electrodes do not contribute to the device active volume, where the energy is released by the particles.

Diamond material properties

The default values of parameters for the physical properties of diamond in the database of TCAD-Sentaurus are set according to Reference [123]. The main parameters used in the simulation are shown in the Table 6.1 with a brief description.

These values are consistent with the ones quoted in literature, but may vary depending on factors such as material quality and temperature. Some parameters related to charge

Property	Value	Description
Band gap Energy (E_g)	5.47 eV	Energy gap between valence and conduction bands
Dielectric Constant (ε)	5.7	Material ability to store electrical energy
Electron Mobility (μ_n)	2200-2400 $cm^2/V\,s$ *	Electron mobility in the material
Hole Mobility (μ_p)	1900-2200 $cm^2/V\,s$ *	Hole mobility in the material
Refractive Index (n)	2.42 (at 589.3 nm)	Bending of light passing through the material
Thermal Conductivity (κ)	22 W/m K	Heat conduction ability
Density (ρ)	3.52 g/cm^3	Mass per unit volume
Deformation Potential (A and B)	A$\simeq$ 10 eV, B$\simeq$ 1.4 eV	Energy band deformation due to lattice vibrations
Absorption Coefficient (α)	Varies with wavelength and impurity concentration	Rate of light absorption
Surface Recombination Velocity (SRH Lifetime Parameters)	Varies with material quality and surface treatment	Surface carrier recombination parameters
Trapping and Recombination Parameters	Varies based on material quality and impurities	Defect-related carrier trapping and recombination

Table 6.1: Properties of diamond material in TCAD simulations. * these values can have been changed, based on the experimental results obtained in Section 4.3.

transport have been updated to better represent our sensor and they are described in the following paragraph.

Given the extremely low concentration of impurities (nitrogen < 5 ppb; boron < 1 ppb) in the synthetic sCVD diamond crystal with respect to that of the foreseen excess charge carriers generated by the intense electron bunch, the diamond crystal is set as non-doped.

Diamond transport properties

Transport models in TCAD include the mathematical descriptions of carrier movement in semiconductor devices. The most common models are drift-diffusion for steady-state simulations, hydrodynamic for high-speed devices, Monte Carlo for stochastic and detailed carrier transport, the choice of which depends on the device characteristics, the phenomena being studied and the requirements for simulation accuracy.

The *Hydrodynamic* model is employed for carrier transport in the simulation of the diamond detector. The hydrodynamic model [124, 125] is a semi-classical approach that treats charge carriers, including electrons and holes, as a fluid with continuous distributions of charge, velocity and energy. It provides a comprehensive understanding of device behaviour by considering carriers continuity, drift, diffusion and energy transport. The basic equations and formulas used in the hydrodynamic model to simulate carrier transport in semiconductor devices are listed below.

- Continuity equations (Eq 6.2 and 6.3) describe the conservation of charge carriers and ensure that the number of carriers remains constant within the material.

- The drift velocity (v) of charge carriers under the influence of an electric field (E) is described by the formula $v = \mu \cdot E$, where μ represents the carrier mobility.

- Carrier diffusion is described using Fick's first law of diffusion [126]: $J = -D \cdot \nabla n$, where J represents the carrier diffusion current and D is the carrier diffusion coefficient.

- Energy transport equation tracks carrier temperature (T) and energy relaxation, especially in high-field conditions, and it is vital for understanding carrier energy distribution and transport. It is given by:

$$\frac{\partial T}{\partial t} + \nabla \cdot (T \cdot \mathbf{v}) = \nabla \cdot (k \cdot \nabla T) + Q_c \,, \tag{6.4}$$

  where T represents the carrier temperature, $\mathbf{v}$ is the drift velocity, k is the thermal conductivity, and Q_c represents the energy generation rate.

The hydrodynamic model is primarily designed for simulating charge carrier transport in semiconductor materials like silicon. It may not accurately represent the behaviour of carriers in diamond detectors. Diamond detectors exhibit distinctive characteristics, including high breakdown voltage, high radiation hardness, and unique charge carrier transport mechanisms. In diamond detectors, charge carriers can experience extreme electric fields, and the standard mobility models may not accurately capture the carrier behaviour. For this reason, the *HighFieldSaturation* option, which usually describes the mobility of charge carriers in semiconductor materials under high electric field conditions, is enabled to better describe the behaviour of charge carriers in the diamond bulk.

The diamond carriers mobilities reach a maximum value as the electric field strength increases. Under high electric field conditions, carriers can attain maximum drift velocities, and their mobility becomes field-dependent. The *HighFieldSaturation* takes into account of this phenomenon. The drift velocity of charge carriers (v_d) in the presence of high electric field E is described by the formula:

$$v_d(E) = \frac{\mu_0 E}{1 + \frac{\mu_0 E}{v_{sat}}} \,, \tag{6.5}$$

where μ_0 is the intrinsic mobility of the charge carriers extrapolated at low field and v_{sat} is the saturation velocity. This option ensures that the mobility of charge carriers does not increase indefinitely with increasing electric field but instead reaches a saturation value, which is a more accurate representation of carrier behaviour in high-field regions.

The set values of mobility and saturation velocity of charge carriers are updated with the measured values obtained from our detector characterisation [72]. The values of the intrinsic mobility and the saturation velocity for electrons (holes) are $\mu_0 = 1.72 \times 10^3$ cm^2/Vs (2.05×10^3 cm^2/Vs), $v_{sat} = 0.85 \times 10^7$ cm/s (1.29×10^7 cm/s).

The *ElectricField* model is chosen for the driving force, which provides a representation of how the electric field affects the motion of charge carriers (electrons and holes) within our device. The electric field is a critical factor in determining how charge carriers move, drift and contribute to the electrical behaviour of the device. It is concerned with electrostatics, carrier motion, drift, mobility, velocity and current flow, enabling the analysis of devices under different bias conditions, voltage distributions and material properties.

The contact between the diamond bulk and the electrodes is set to ohmic [127, 128]. To accurately measure dose rates with diamond detectors used as radiation monitors, the bias voltage should not be too high, to avoid large fluctuations due to the multiplication of charge carriers in avalanche processes. On the other hand, a sufficient bias voltage is required to guarantee a full charge collection efficiency. In view of these considerations, our diamond system at Belle II is operating with 100 V bias voltage, which corresponds to an electric field intensity 0.2 V/µm. The bias voltage is set to 100 V, which is the operational bias voltage applied on the detector at Belle II and guarantees a full collection efficiency for charge carriers injected up to a concentration of about $10^4\,\mathrm{cm}^{-3}$. The study of the transient response of the diamond device is performed also for other two cases, with 50 V and 150 V bias voltage applied on the electrodes.

Moreover, similar to semiconductor devices, also in diamond several recombination processes occur, affecting the behaviour of charge carriers within the material. Several recombination models are defined in TCAD-Sentaurus, as for example *Shockley-Read-Hall Model*, *Radiative Recombination Model*, and *Exciton Dissociation Model*. The choice of the appropriate recombination model depends on the specific characteristics of the diamond material, the impurity and defect profiles, as well as the operating conditions of the device being simulated. For our simulations, since our experimental measurements are not sufficient to parameterise each process, the Schockley-Read-Hall model has been used in a simplified way, setting most of the parameters to zero. Furthermore, due to the high concentration of charge carriers in the diamond bulk, dedicated models for the recombination at the surface can be neglected.

The Shockley-Read-Hall recombination model is a widely used approach in semiconductor physics and TCAD simulations to describe the recombination of charge carriers (electrons and holes) through defects or traps within the crystal lattice and it is particularly useful for understanding recombination processes in materials with impurities, imperfections, or lattice defects, such as diamond. The recombination rate R_{SHR} is proportional to the product of the electron and hole concentrations and the density of available traps. It is described by the following equation:

$$R_{\mathrm{SRH}} = \frac{n \cdot p - n_i^2}{\tau_{\mathrm{SRH}}}\,, \tag{6.6}$$

where n and p are the electron and hole concentrations respectively, n_i is the intrinsic carrier concentration, which depends on the temperature and τ_{SRH} is the SRH lifetime, *i.e.* a measure of how quickly carriers recombine through the SRH process.

The SHR model relies on the principle of detailed balance, where in thermal equilibrium, the rate of generation of charge carriers (due to light absorption, for instance) is equal to the rate of recombination. It also depends on the properties of the defects and traps within the material. Defect states or traps are energy levels in the energy band gap that can capture either electrons or holes, leading to recombination. The concentration and energy levels of these traps play a significant role in determining the recombination rate. Moreover, the intrinsic carrier concentration (n_i) and the SRH lifetime (τ_{SRH}) are temperature-dependent parameters. Changes in temperature affect the rate of recombination through the SRH process. In the simulation only the lifetime is set, for a fixed temperature. Lifetimes of both types of charge carriers are reported as 2 µs in the handbook [129] from the producer Element Six Ltd. However, measurements by several groups using diamond crystals from Element Six Ltd give diverse results ranging from tens of nanoseconds to one microsecond [79, 130–132]. In the following the lifetime is set to $\tau_{\mathrm{SRH}} = 50\,\mathrm{ns}$, but results for three different lifetimes are obtained, as described in Section 6.5.

6.2.3 Electron beam simulation

The FERMI electron beam, used in our studies and described in Chapter 5, is characterised by $\sim 1\,\text{GeV}$ electron bunches of 1 ps duration, with variable bunch charge ranges from 10 to 100 pC and a size of about $100\,\mu\text{m}$. In particular, the beam defined in the simulation has a bunch charge of 35 pC and a dimension $\sigma_x = 120\,\mu\text{m}$.

The electron beam is simulated in TCAD using the *HeavyIon* irradiation model, which is able to describe the interactions of a charged particle passing through a device. The definition of the beam in the model is given by several parameters, such as the charged particle type and the particle energy, its angle of penetration and the spatial distribution, and the relation between the energy loss, or linear energy transfer (LET), and the number of pairs created. LET is a term used in dosimetry to describe the action of radiation upon matter: how much energy an ionising particle transfers to the material per unit distance [μm]. The latter can be express both as an energy deposited both as the charge generated by the particle in the material. In our simulation the LET is defined as a charge generated per unit distance. The HeavyIon model is generally employed in transient simulations where both microscopic and macroscopic quantities can be monitored: at this stage the total charge density and the instant generation rate, due to the impinging ionisation particle.

The simulated incident electron beam traverses the diamond crystal along the axis, $x = 0$, with the starting time of the injection set to 1 ns. To obtain a beam as close as possible to the measured experimental conditions, the beam is implemented with a Gaussian radial distribution with a standard deviation of $120\,\mu\text{m}$. The beam energy is fixed at 0.9 GeV, while the charge of the single packet is included in the LET calculation.

When crossing the diamond volume electrons of about 1 GeV undergo scattering with the diamond atoms, causing ionisation and excitation. Additionally, the fast-moving electron may emit bremsstrahlung radiation, which is electromagnetic radiation produced when the electron is deflected by the strong electric fields of atomic nuclei. This process generates high-energy gamma rays. Due to the thinness of the detector, bremsstrahlung photons barely interact with the diamond crystal: the average deposited energy by bremsstrahlung photons is $\sim 10\,\text{keV}$ per incoming electron. Therefore, only the energy released by ionisation is considered to be responsible for the generation of charge carriers.

The linear energy transfer (LET) is given by:

$$LET = \frac{S(E) \cdot N_e \cdot q_e}{E_{eh}}\,, \tag{6.7}$$

where $S(E)$ is the stopping power for diamond, N_e is the number of electrons in one bunch, q_e is the elementary charge and $E_{eh} = 13\,\text{eV}$ is the average energy to create an electron-hole pair in diamond. The stopping power $S(E)$ is determined from the mean released energy by $\sim 1\,\text{GeV}$ electrons in the diamond detector, obtained with the FLUKA simulation of the experimental setup described in Section 5.6.2. The mean value of the energy loss is 0.302 MeV, which correspond to a stopping power $S(E) = 6\,\text{MeV} \cdot \text{cm}^{-1}$, given the sensor thickness of $500\,\mu\text{m}$. In addition, the assumption of collision stopping power is compatible with the value quoted in a recent study [133], for 0.9 GeV electrons: assuming the density of diamond $3.5\,\text{g/cm}^{-3}$, the diamond stopping power is $S(E) = 7.0$ MeV·cm^{-1}. This value agrees with the NIST database [117] and it is close to the value obtained with simulations. Given the value $S(E) = 6\,\text{MeV} \cdot \text{cm}^{-1}$ and the number of electrons in a bunch of 35 pC $N_e = 2.18 \times 10^8$, the linear energy transfer is $LET = 1630\,\text{pC}/\mu\text{m}$.

6.2.4 Signal formation

To perform the device simulation, an external circuit must be specified using the "mixed-mode" TCAD feature. This option offers only a limited choice of models of circuit elements, in particular for coaxial cables; the computing time is also severely affected by the complexity of the external circuit. For this reason, we adopt a two-step approach with a simplified external circuit in TCAD. The simplified circuit, shown in Figure 6.2, consists of a DC bias voltage source V_{bias} connected to one electrode, while the other electrode is connected to ground via a load resistor R.

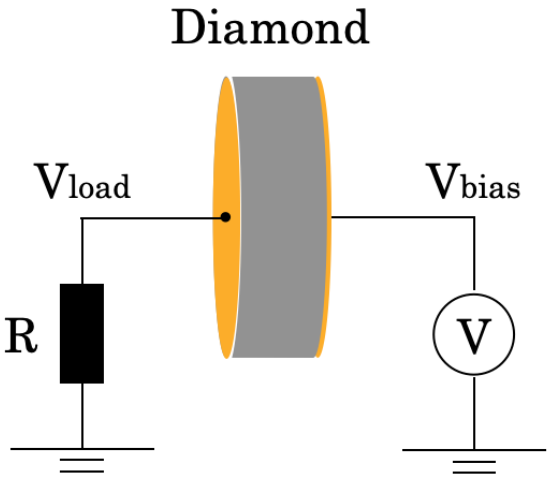

Figure 6.2: Sketch of the diamond detector in the TCAD-Sentaurus "mixed-mode" simulation. One electrode is biased by a voltage source V_{bias}, the other is connected to the ground via a load resistor $R = 50\,\Omega$.

The simulation gives as output the time evolution of the voltage $\mathrm{V}_{\text{load}}(t)$ across the load resistor, of the charge carrier concentration in the diamond bulk and of the electric field inside the crystal.

Figure 6.3 shows the time evolution of the load voltage $V_{\text{load}}(t)$ for three different bias voltages: V_{load} increases up to almost V_{bias} immediately after the beam crossing with a fast rise time of about 300 ps. The three signals present an almost flat top, whose duration decreases by increasing the bias voltage. The traversing electron beam injects a large concentration of electron-hole pairs of about $10^{17}\,\mathrm{cm}^{-3}$ along the beam path. Due to the high concentration of charge carriers, the diamond temporally becomes a conductor and the voltage difference ($\mathrm{V}_{\text{bias}} - \mathrm{V}_{\text{load}}$) across the two electrodes drop almost to zero.

Driven by the external electric field, the two types of charge carriers separate and move in opposite directions. Thin layers of only one type of unbalanced charge carriers are formed near the two electrodes; their net charge, together with the opposite charge induced on the electrodes, is sufficient to establish an internal electric field that can cancel the external field as sketched in Figure 6.4. This screening blocks the drift of charge carriers in the diamond bulk, as expected and discussed in Section 5.1. V_{load} then decreases slowly, with a decay time of the order of 100 ns.

The concentration of electrons in the diamond bulk is shown in Figure. 6.5, 1 ns after the beam crossing. A symmetrical distribution is obtained for holes. The concentration near the beam position remains close to the initial $10^{17}\ cm^{-3}$ for rather long time.

Figure 6.6 shows the time evolution of the concentration of negative and positive charge

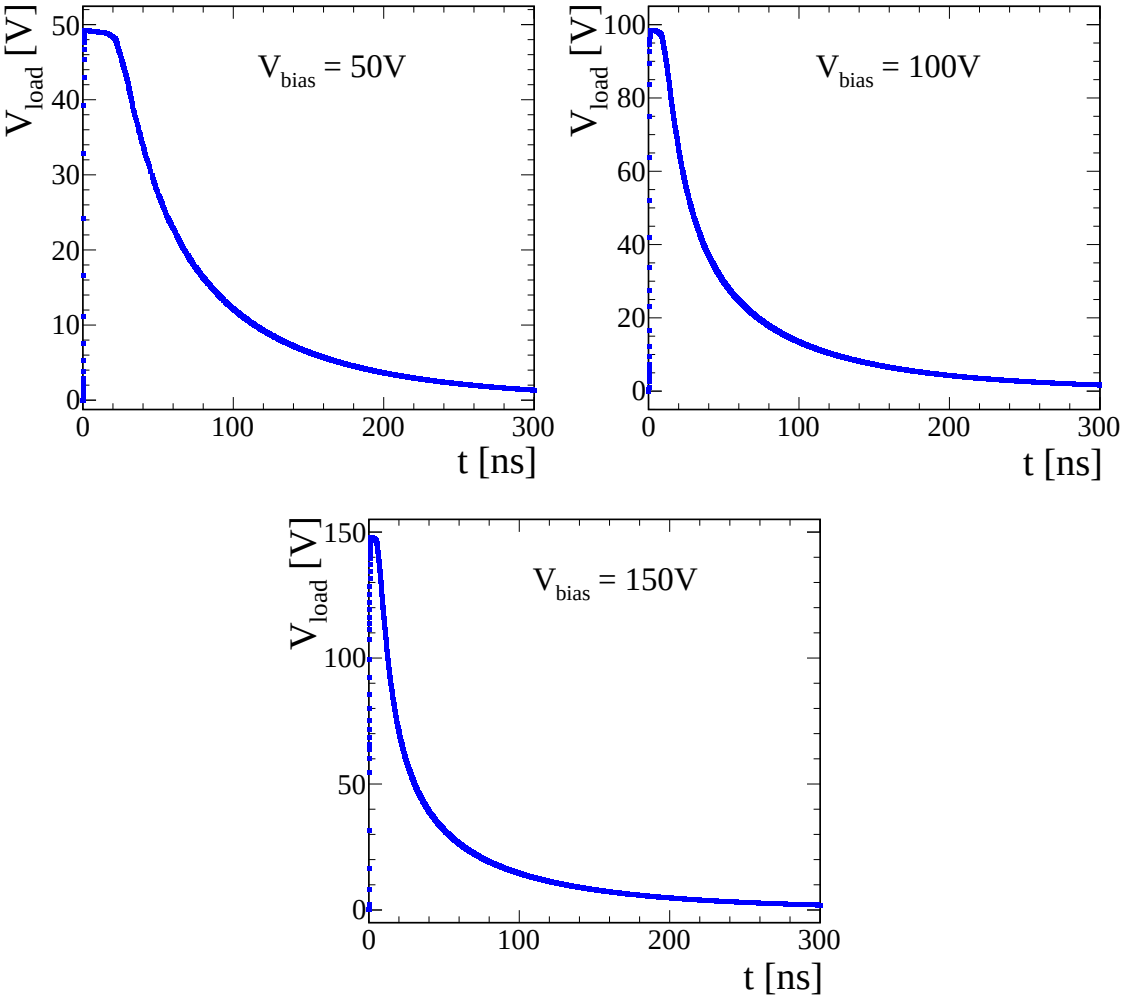

Figure 6.3: Voltage of the electrode connected to the ground across the 50 Ω load resistor as a function of time, $V_{load}(t)$. The bias voltage is applied to the other electrode. The plots show the simulation output for the bias voltage values of 50 V, 100 V and 150 V.

carriers near the trajectory of the incident electron bunches. The charges are slowly collected by the electrodes and the density of charge carriers between the two electrodes near the beam trajectory is still of the order of $10^{16}\,\mathrm{cm}^{-3}$ after 100 ns.

At this high charge concentration, excitonic recombination with phonons takes place [134], a process in which an exciton, *i.e.* a bound pair of an electron and a hole attracted to each other by the electrostatic Coulomb force, interacts with lattice vibrations, or phonons, in the diamond crystal. This interaction causes the exciton to lose energy, eventually leading to the recombination of the electron and hole. This recombination process is not explicitly considered in the SHR recombination model implemented in TCAD and described in Section 6.2.2.

For this reason the value of lifetime in simulation is set to 50 ns, an empirical value consistent with the observed signal decay time and compatible with contributions from excitonic recombination.

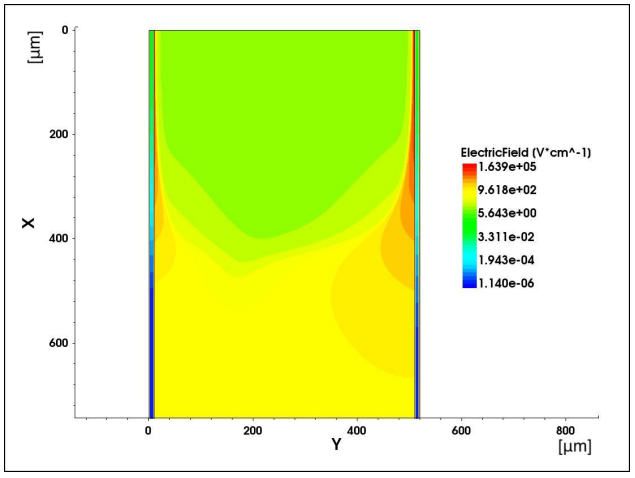

Figure 6.4: A zoom-in plot of the magnitude of electric field in the diamond bulk near the trajectory of incident electron bunches. As already defined in Figure 6.1, the y axis is perpendicular to the electrodes located at $y = 0$ and $y = 500\,\mu$m. The x coordinate is the radial distance from the diamond central axis located at $x = 0$ (top). As discussed in the text, the green region is screened and has a relatively low magnitude of electric field. This is the simulated result of $V_{bias} = 100$ V, at 20 ns after irradiation. Similar distributions are obtained for the cases of 50 V and 150 V bias voltages.

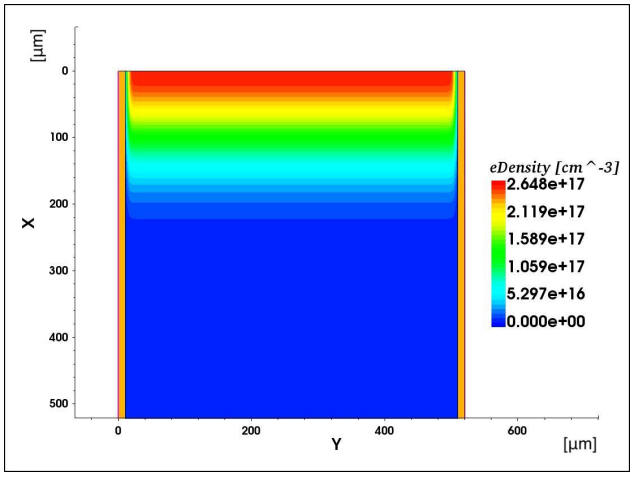

Figure 6.5: A zoom-in plot of the concentration of negative charge carriers (electrons) in the diamond bulk near the trajectory of incident electron bunches at time $t = 1$ ns after the beam crossing. The coordinates x and y are defined as in Figures 6.1 and 6.4, the 3-D diamond detector and its properties are obtained by rotation around the $x = 0$ axis. The beam bunches are crossing the crystal along $x = 0$. The bias voltage in this case is 100 V. Similar distributions are obtained for bias voltage values of 50 V and 150 V.

6.3 LTspice readout circuit

TCAD-Sentaurus package has an embedded SPICE (Simulation Program with Integrated Circuit Emphasis) utility, which is often integrated to provide circuit-level simulation capabilities in the "mixed-mode" operation. This integration allows users to model and simulate

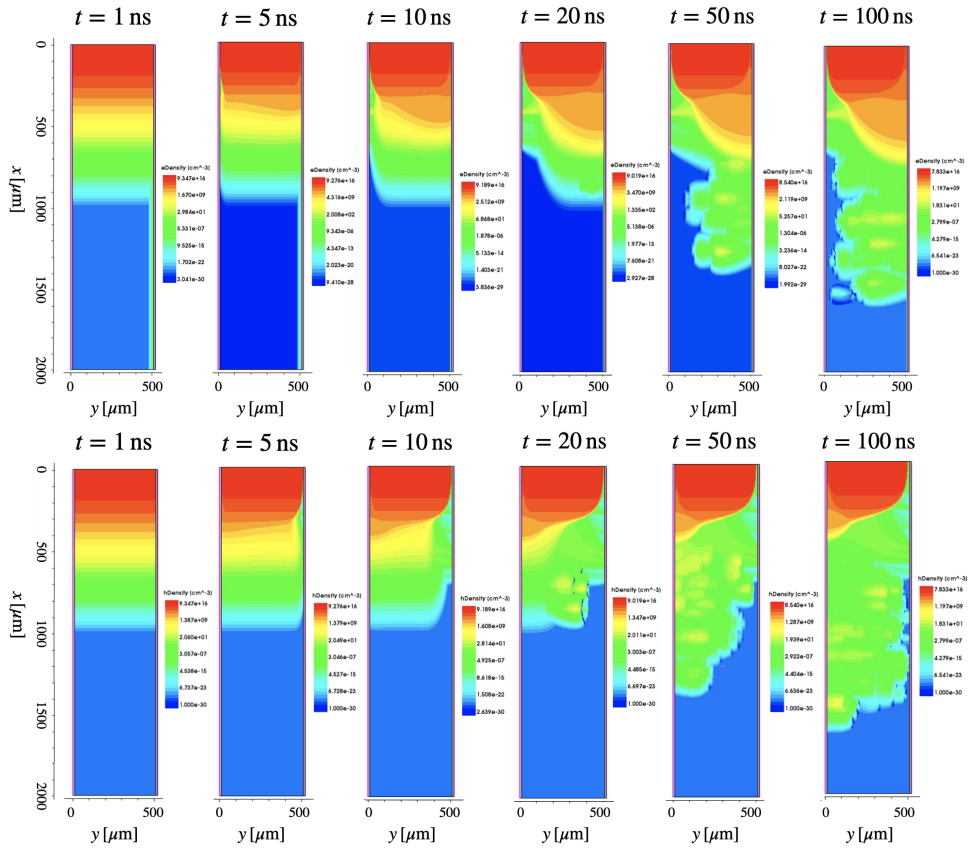

Figure 6.6: Time evolution of the concentration of electrons (top) and holes (bottom) in the diamond bulk, near the trajectory of incident electron bunches, obtained for a bias voltage of 100 V. From the left to the right the time after beam bunch crossing is 5 ns, 10 ns, 20 ns, 50 ns and 100 ns. x and y coordinates are defined as in Figure 6.4.

the electrical behaviour of semiconductor devices, components, and external circuits, while taking into account the physical and material properties defined within the TCAD framework. However, its functionalities and models are not adequate to fully take into account the effect of transmission cables, which plays a leading role in dealing with fast pulses. The available computing resources and execution time turn out to be incompatible with the implementation of a realistic description of our circuits in TCAD "mixed-mode".

To overcome these limitations, LTspice, the most widely used SPICE software in the industry, is employed in a second step of the simulation workflow. LTspice [122], which is a SPICE-based electronic circuit simulation software developed by Linear Technology, is used to model the detector and readout circuit. It operates through a schematic editor, allowing users to design circuits using an extensive component library, including resistors, capacitors, semiconductors, and more, and to visualise and analyse the simulation results.

In the following I describe the circuit model, and in particular the model used to represent the diamond detector. The voltage signal obtained in the previous step with TCAD-Sentaurus serves as an input to the LTspice simulation as for the voltage source and a variable resistor models the conduction in the irradiated diamond.

6.3.1 Diagram of the circuit

In the initial experimental setup, described in Chapter 5, a bias voltage is applied between the electrodes of the diamond, and the signal induced by the charge drifting in the diamond bulk is read at the oscilloscope input, across a line-terminating resistor.

The elements entering the circuit of the readout system are shown in Figure 6.7:

- a power supply [56] provides the bias voltage up to one of the two electrodes of the diamond sensor. It is characterised by an output circuit with a resistance $R_3 = 4.7\,\mathrm{k\Omega}$ and a capacitance $C_3 = 30\,\mathrm{nF}$;
- a Teledyne LeCroy HDO9000 oscilloscope [111] is used to measure the signal induced on the detector under test. The oscilloscope features an input capacitance of $C_1 = 20\,\mathrm{pF}$. Additionally, a $50\,\Omega$ resistor R_1 is introduced externally in parallel to provide impedance matching of the connected cables. The oscilloscope input impedance is set to 1 MΩ, to prevent high-current damage of the input circuit of the oscilloscope; it is considered negligible;
- two 10 m long coaxial cables, labelled "S_04162_B-01", are connected respectively to the power supply and the oscilloscope. The cable parameters are $R = 0.8\,\Omega\cdot\mathrm{m}$, $L = 200\,\mathrm{nH\cdot m}$ and $C = 80\,\mathrm{pF\cdot m}$;
- two 40 cm long micro-coaxial cables, "MicroCoax_CERN", connect the coaxial cables to the diamond electrodes. The cable parameters are $R = 1\,\Omega\cdot\mathrm{m}$, $L = 312\,\mathrm{nH\cdot m}$ and $C = 125\,\mathrm{pF\cdot m}$;
- the diamond detector, represented by the components in the left dashed box, is modelled as a voltage source V_2 and a resistor R_2 in parallel with the detector capacitance C_2.

Since the properties of the cables affect the shape of the signal, they are defined using the *Transmission Line Model*, which is used to simulate the behaviours of transmission lines, like coaxial cables or microstrip lines, in electronic circuits. It considers line parameters such as characteristic impedance, propagation delay, and attenuation, allowing for an accurate representation of signal transmission effects.

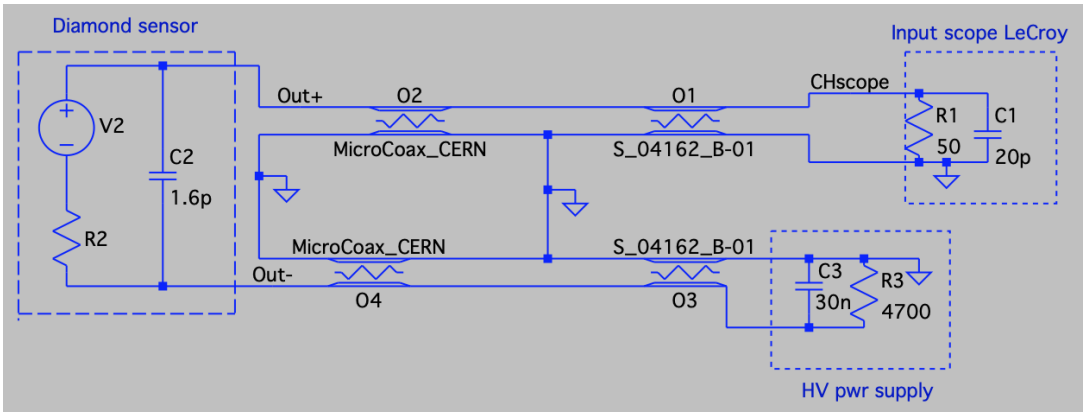

Figure 6.7: Equivalent circuit for diamond detector irradiated by ultra-short and intense high-energy electron pulses. The diamond detector is represented via the components in the dashed box on the left.

The bias voltage provided by the power supply is included in the voltage source V_2.

To model the diamond detector in LTspice, we have to choose whether to represent it as a current source or a voltage source within the equivalent circuit. This choice depends on the unique characteristics of the detector and the system in which it operates. Typically, a semiconductor detector generates a current response when subjected to incident radiation or other external stimuli. Under such circumstances, it is often modelled as a current source. This modelling choice is intrinsically tied to the nature of the power supply providing the bias voltage to the detector. When the power supply is capable of rapidly and efficiently maintaining the potential difference between the two electrodes of the detector, the semiconductor device tends to function as a current source. In this mode, it supplies a relatively constant current output, which is a common configuration when the power supply can readily adapt to the detector's dynamic needs.

On the contrary, if the power supply exhibits slower charging dynamics, or if its capacity is insufficient relative to the signal generated by the device, the system can be regarded as being in a "closed" configuration. In such cases, the energy dissipated as charge carriers traverse through the semiconductor bulk results in a noticeable voltage drop across the detector's electrodes. Consequently, when the system operates under these conditions, it is appropriate to represent the semiconductor device, such as a diamond detector, as a voltage source in the circuit model. In this mode, the device essentially induces a voltage response due to the energy losses associated with charge carrier movements.

The output voltage as a function of time, obtained from the TCAD simulation, is given in input to LTspice for the diamond detector voltage source, and the time window region for the simulation has been thus defined from 0 ns to 300 ns, to be consistent with the considerations described above.

The diamond detector is represented as a voltage source together with a resistance R_2 in series and a capacitor C_2 in parallel. This configuration serves as a simplified model to take into account both the voltage drop V_2 and the effective resistance R_2 across the detector as a function of time. V_2 and R_2 are taken from the output of the TCAD simulation as described in the next Section 6.3.2.

The capacitance of the diamond detector is:

$$C_2 = \frac{\epsilon_0 \cdot \epsilon_r \cdot S}{d} = 1.6 \text{ pF}, \tag{6.8}$$

where d and S are the thickness and the cross-sectional area of the diamond crystal, ϵ_0 is the vacuum permittivity, and $\epsilon_r = 5.7$ is the dielectric constant of sCVD diamond. Since diamond changes its electrical properties as a function of time, a model for diamond resistivity is defined in the next paragraph.

6.3.2 Diamond resistance

In the absence of radiation, diamond behaves as an insulator, exhibiting a resistivity $\rho > 10^{11}\,\Omega \cdot \text{cm}$. This high resistivity is characteristic of pure diamond and prevents the flow of electrical current. However, the electrical properties of diamond can change when exposed to ionising radiation. When irradiated by intense electron bunches, a high concentration of charge carriers is generated within the diamond bulk, effectively changing the electrical properties of the material. This irradiation-induced presence of charge carriers instantaneously transforms the material from an insulator to a conductor, causing a rapid drop in its resistivity to very low values.

Assuming that diamond behaves as an intrinsic semiconductor, its resistivity ρ depends on both electron and hole concentrations (n and p) and on their respective mobilities (μ_n

and μ_p); it can be approximated as:

$$\rho = \frac{1}{q_e \cdot (n\mu_n + p\mu_p)} \,. \tag{6.9}$$

In our case, the concentrations of electron and hole are equal and correspond to the total number of e-h pairs N_{eh} generated in the bulk by the impinging radiation, divided by the volume crossed by the electron bunches $V_{\text{crossed}} = d \cdot S$, where d is the diamond thickness and S is the transverse section of the beam path.

The resistance is therefore given by

$$R = \frac{d}{S} \cdot \rho = \frac{d^2}{q_e \cdot (N_{eh}\mu_n + N_{eh}\mu_p)} \,, \tag{6.10}$$

where the section S cancels.

Assuming for simplicity that the e-h pairs are confined with a uniform average concentration in a cylindrical volume corresponding to the ionisation by the incoming beam, using the value of mobility in Section 6.2.2, Equation 6.10 leads to $R \approx 1\ \Omega$ for the resistance of diamond right after irradiation, for a number of e-h pairs $N_{eh} \sim 10^{13}$ corresponding to a a bunch charge of 35 pC.

As the charge carriers are collected, the resistance increases and returns to the initial value. The change in resistance over time can be estimated from the time evolution of the voltage on the electrode $\mathrm{V_{load}(t)}$ and the current I(t) obtained from the TCAD simulation:

$$R(t) = \frac{V_{\text{bias}} - V_{\text{load}}(t)}{I(t)} \,. \tag{6.11}$$

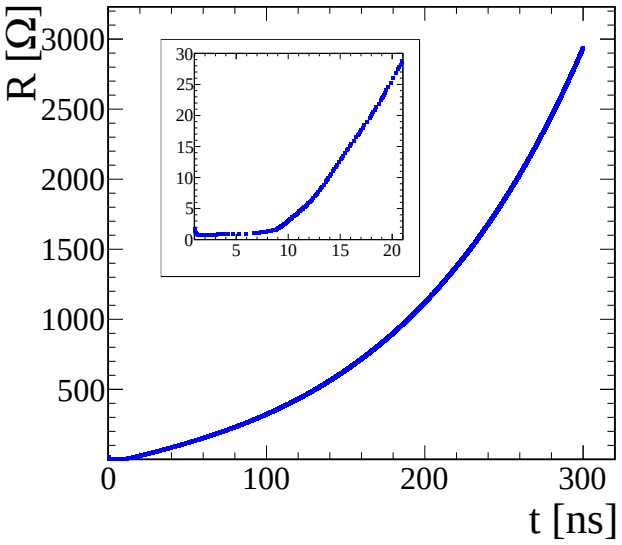

Figure 6.8: Resistance of the diamond detector obtained from TCAD simulation for the case of $\mathrm{V_{bias}} = 100$ V. The inset shows that the value starts out at about 1 Ω.

Figure 6.8 shows the resistance as a function of time obtained from the simulation for 35 pC electron bunches, in which the value of resistance initially is about 1 Ω then starts to increase after about 10 ns. This change in resistance over time is an important ingredient of the signal formation.

6.4 Validation of the simulation approach

A validation of the two-step simulation approach is based on the study of a well-understood process, to test in particular the model adopted for our diamond detector. The measurements performed with the transient-current-technique (TCT), described in Section 4.3, are compared with simulations. These measurements aim at studying the transport properties of charge carriers in the diamond bulk.

In the TCT measurements, monochromatic α particles with an average energy of 5.486 MeV deposit all their energy in $\sim 12\,\mu$m near the crossed electrode. A current pulse is induced by the drift of charge carriers of one type, depending on the bias polarity, through the whole detector thickness to the opposite electrode. The signal has a rectangular shape, with fast rise time and fall time, and a duration which equals the time employed by the charges to traverse the detector. In these measurements the short cables have reduced impact on the signal shape.

In the TCAD simulation, the only modification made is the adjustment of the source definition. The energy deposition from α particles in the detector is computed using a comprehensive simulation of the experimental setup, as outlined in Section 4.3.5. On average, α particles deposit approximately 4.97 MeV of energy within the diamond, which accounts for 90.6% of their initial energy. The linear energy transfer (LET) in the diamond bulk due to α particles is approximated using a step function to represent the simulated energy deposition distribution, illustrated in Figure 4.17. The LET is defined by dividing the $12\,\mu$m range of α particles within our sensor into 5 steps. In the first $8\,\mu$m, the LET have a constant of 3.1fC/μm, while it increases for deeper points, reaching a peak value of 8.7fC/μm at a depth of $10\,\mu$m. The current $I(t)$ induced by electron drift, obtained from the first-step TCAD simulation for a bias voltage of +150 V, is shown in Figure 6.9.

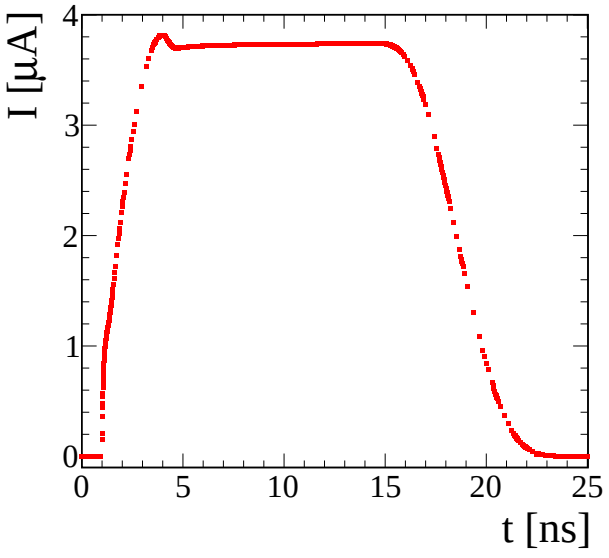

Figure 6.9: Time evolution of the current signal $I(t)$ from α particles (TCT measurement), simulated with TCAD alone.

The signal has an approximately rectangular shape, with an amplitude of $\sim 4\,\mu$A. One type of charge carrier is collected by the nearby electrode swiftly in a time of the order of few ns, corresponding to the small initial peak in the current signal, while the other type

of charge carrier drifts through the entire thickness of the diamond crystal, determining the width of the signal.

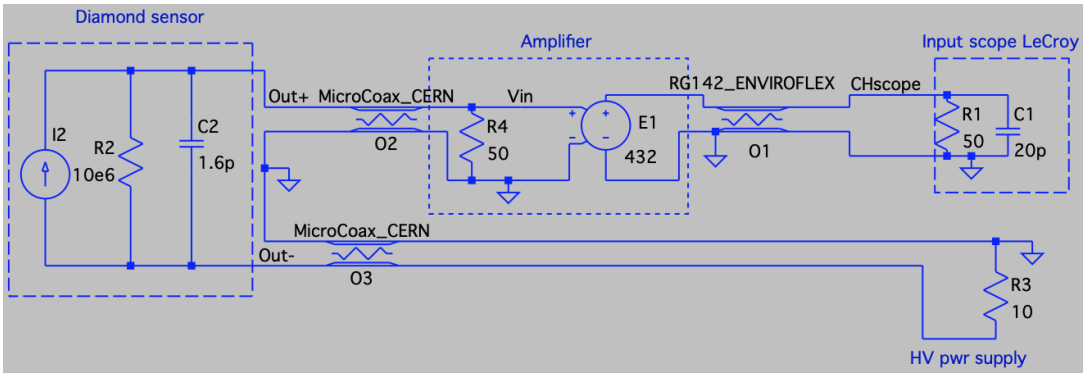

Figure 6.10: Equivalent circuit for TCT measurement of diamond charge carriers transport properties in LTspice. The diamond detector is represented via the components in the left dashed box; the current source, which is the result of TCAD simulation, already includes the active part of the HV power supply.

The LTspice circuit diagram takes into account the TCT experimental setup, as illustrated in Figure 6.10. The circuit consists of the following components:

- a power supply, CAEN DT1471ET [93], providing a ±150 V bias voltage to one of the electrodes. Its output impedance is represented by a 10 Ω resistor;
- an oscilloscope, LeCroy WAVEPRO960 [83], with an input circuit featuring a 50 Ω resistance (R_1) and 20 pF capacitance (C_1);
- an RF amplifier, Particulars Am-02A [82], inserted between the diamond detector and the oscilloscope. The measured amplifier gain is 53.4 dB for positive-polarity signals (electron-induced current) and 52.7 dB for negative-polarity signals (hole-induced current). The amplifier 3 GHz bandwidth does not limit the setup bandwidth: it can be represented by a voltage-dependent voltage source with a fixed gain, assuming no loss on high-frequency components;
- two short 1 cm micro-coaxial cables with the same characteristics as described previously;
- a 3 m-long coaxial cable, "RG142_ENVIROFLEX," connecting the amplifier and the oscilloscope, with parameters $R = 0.025\,\Omega\cdot$m, $L = 226\,$nH$\cdot$m and $C = 94.5\,$pF$\cdot$m;
- the diamond detector.

Due to the relatively small number of charge carriers liberated in the TCT measurement, the current pulse has an amplitude below the current limit provided by the power supply, and the diamond sensor can be treated as a current source. Additionally, the diamond circuit is modified to include a parallel resistor, $R_2 = 1\,\text{M}\Omega$, which replicates the diamond resistance under these irradiation conditions. It also features a parallel capacitor with a value of $C_2 = 1.6\,$pF.

Figure 6.11 shows the voltage across the oscilloscope input as a function of time, induced by electrons (black) or holes (green) drift. These results are obtained for a bias voltage of

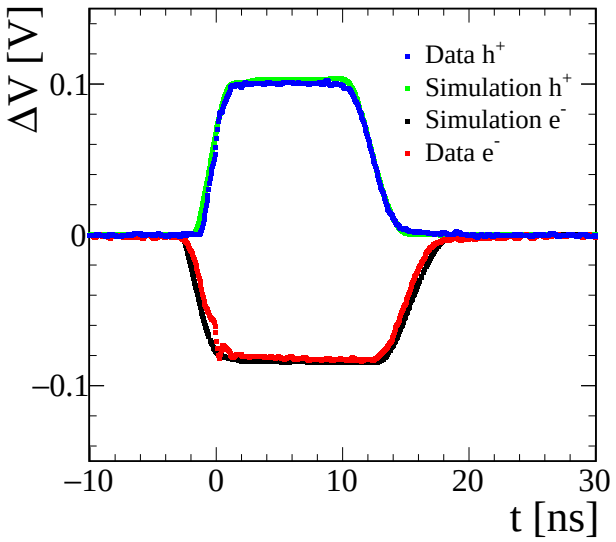

Figure 6.11: Voltage observed by the oscilloscope as a function of time. Upper half: hole-induced signals; lower half: electron-induced signals. The experimental data (blue and red curves) of the TCT measurement are from Reference [72]. The green and black curves are the results of the two-step simulation.

150 V. The respective measured pulses for electrons (red) and holes (blue) are also shown. The remarkable agreement between the numerical simulation and the measurements, in terms of both pulse amplitude and width, confirms that the charge carrier transport process and the effects of the electronic circuit on signal propagation, as revealed by the simulation, accurately describe the experimental data.

6.5 Comparison of the simulation results with the experimental data

After the validation of the two-step simulation method in comparison with TCT measurements, characterised by low-intensity irradiation, my main goal is to asses its capability to predict the response of diamond detectors to the ultra-short, high-intensity electron beam bunches described in Chapter 5, starting with the data collected in an irradiation campaign with the initial FERMI-DBD setup described in Sections 5.2.2 and 5.6.1 and Figure 5.21. The measured signals are also shown in Figure 6.12 by the curves in red, for three values of the applied bias voltage: 50 V, 100 V and 150 V.

The curves in blue represent the simulated signals at the oscilloscope input defined in LTspice circuit simulation, as described in Section 6.3, obtained for the corresponding bias voltages of 50 V, 100 V and 150 V. The amplitude of the signal, as observed on the oscilloscope across the 50Ω load, is influenced by the impedance of each component in the circuit, including the diamond sensor, oscilloscope, HV power supply, and cables. Notably, the low resistance of the diamond detector immediately after irradiation, owing to the high concentration of mobile charge carriers, combined with the impedance of the other circuit elements, determines a signal amplitude approximately equal to half of the bias voltage $V_{\text{bias}}/2$.

In both data and the simulated signal, the maximum amplitude is approximately half

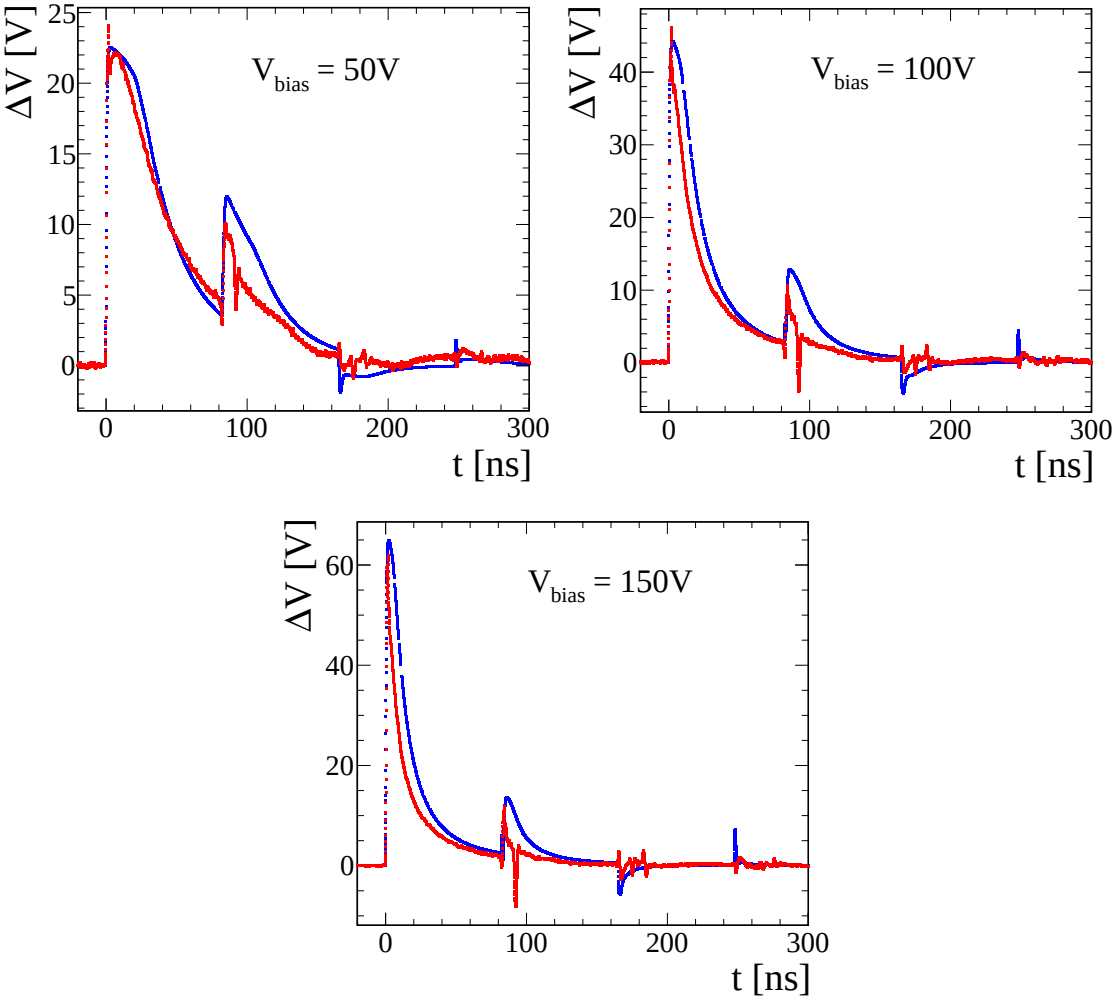

Figure 6.12: Voltage across the 50 Ω load, as a function of time. The three plots show the response of the diamond detector to 35 pC electron bunches, respectively with 50 V, 100 V and 150 V bias voltages. Blue curves indicate the results of simulations with carrier lifetime set to 50 ns, and red curves indicate the results of measurements.

the applied bias voltage, and there are periodic reflections occurring every 85 ns, which correspond to delays determined by the length of the cables. In the current experimental layout, the HV power supply has a relatively low impedance for fast signals. The time variable impedance of the diamond detector does not match the impedance of the cables as well. Due to these impedance mismatches, reflections appear as secondary peaks. These reflections are reduced by a more symmetrical layout, *e.g.* increasing the impedance of the HV power supply by inserting a 50 Ω resistor in series during the irradiation campaign with the optimised setup, described in Section 5.2.3.

The long tail of the signal can be explained by the screening effect of space charges as discussed in Section 6.2.4, which delays the collection of charge carriers at the electrodes. Since the charge density in the diamond bulk is influenced by the recombination process, the tail is expected to depend on the recombination lifetime.

The simulated signals are shown in Figure 6.13 for three values of the recombination lifetime, 20 ns (green), 50 ns (blue) and 100 ns (black) respectively. When using a lower value for the recombination lifetime, the tail of the signal, which is originated by the

shielding effect of the electric field on charge collection, exhibits a steeper decline as a result of charges in the diamond bulk recombining more rapidly. Conversely, for a recombination lifetime of 100 ns, the tail of the signal has a slower decline. The choice of recombination time depends on the dominant recombination mechanisms, which can vary based on factors such as charge carrier concentration, temperature, and time. A recombination time of 50 ns appears a reasonable compromise to represent the measured data, aligning more closely with experimental observations at different values of the bias voltage V_{bias}. The signal amplitude, on the other hand, is less influenced by variations in the recombination time, as expected.

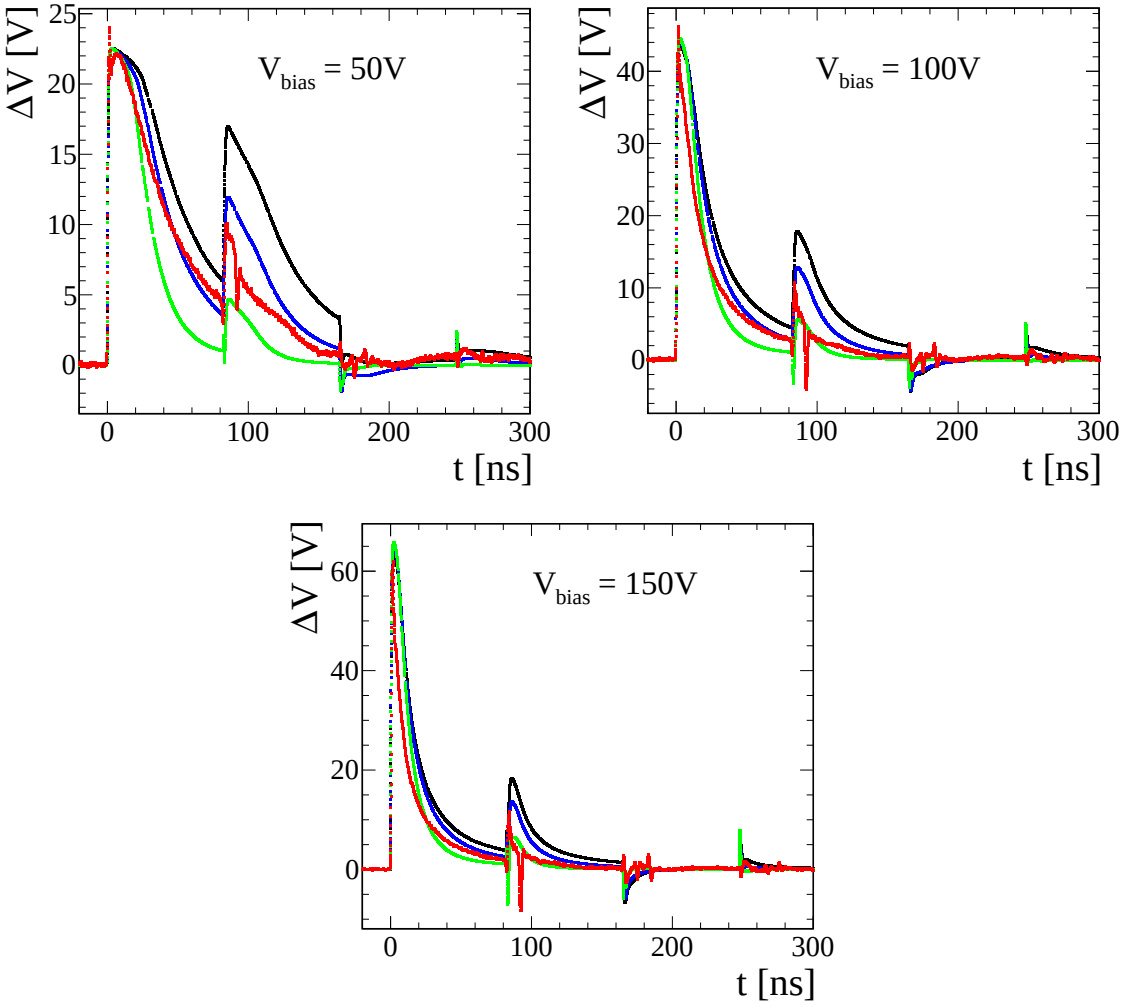

Figure 6.13: Simulated voltage across the 50 Ω load, as a function of time, observed by the oscilloscope. The three plots show the response of the diamond detector to 35 pC electron bunches with 50 V, 100 V and 150 V bias voltages. Red curves indicate the results of measurements while the other three curves are the results of simulations with carrier lifetime set to 20 ns (green), 50 ns (blue) and 100 ns (black).

6.6 Summary and future developments

The two-step simulation of the diamond response described in this Chapter is based on the Sentaurus TCAD and LTspice packages.

After validation by comparison with signals from α-particles in TCT measurements, the simulation of the diamond device and of the external circuit predicts several features of the detector response to high-intensity electron beam bunches, in the data recorded at the initial setup of the FERMI-DBD test stand, described in Chapter 5. Quantitative results from simulations confirm the expected mechanisms outlined in Chapter 5. In particular, the signal rise time, peak amplitude and reflections due to impedance mismatching are well reproduced. However, the trailing edge of the signal is only approximately reproduced by a fixed recombination lifetime of 50 ns. A more accurate match between simulation and data in this respect may require a more refined recombination model, which may be the subject of future development.

As described in Chapter 5, more diamond irradiation data are available from the optimised FERMI-DBD setup, at different values of detector bias voltage, electron beam bunch charge, and transverse beam size. Due to limited time and computing resources, it was not possible to extend the simulations to cover these conditions. However, this additional data will provide an interesting testing ground for this method in the future.

Summary

The thesis is dedicated to the extensive characterisation of the diamond detectors used in the radiation monitoring and beam abort system of Belle II. To maximise the particle-production rates, high beam intensities are needed, corresponding to a higher beam-induced background. These detectors play a crucial role in ensuring the safe and efficient operation of the accelerator SuperKEKB and the protection of the Belle II detectors, in particular the innermost silicon vertex detector. I assembled, characterised and calibrated the diamond detectors for the update of the Belle II radiation monitor system. In February 2023, I successfully installed eight of these detectors onto the new beam pipe during a long shutdown period.

The full characterisation procedure involves the use of three different radiation sources to assess the main properties of each diamond sensor, which may differ from crystal to crystal. This approach allows the evaluation of various aspects, starting with the measurement of carrier transport properties, the determination of the average ionisation energy and the assessment of sample homogeneity. A first part of the procedure aims at checking the transport properties of charge carriers, determining the average ionisation energy and evaluating the homogeneity of the tested sample. The second part is focused on studying the response under two different types of steady radiation, β and X, and determining the current-to-dose rate calibration factor, a fundamental parameter crucial to the effective use of these detectors within our radiation monitoring system. The calibration is refined under steady-state irradiation using a silicon diode as a reference, reducing systematic uncertainties associated with the radiation source.

The study shows a good homogeneity within the sample, with mean ionisation energy consistent within 3.5% with the value of 13 eV quoted in literature. This result underlines the high quality and purity of the crystals. All the detectors show a stable response under steady irradiation, reaching a stable current in a short time, with a charge collection efficiency near to 100%. The calibration factors are obtained, with β and X steady irradiation, over a current range from few pA to tens of nA. Our diamond detectors exhibits a linear response over a wide range of current values, covering dose rates typical of our experimental conditions. However, other aspects that must be studied on these well-calibrated detectors are the non-linear effects during radiation bursts, leading to potential underestimation of dose values.

To investigate the transient response under extreme conditions, we designed and installed a dedicated test stand in a vacuum chamber along the diagnostic beam dump line of the linac of the FERMI free-electron laser. This facility provides 1 GeV ultra-short, high-intensity electron bunches with adjustable bunch charge and spot size. The experimental setup was optimised during several irradiation campaigns. Under these extreme conditions, the high carrier concentration in the diamond bulk induces a space charge effect, shielding the electric field, and affecting signal formation and consequently the charge collection process. The tests are carried out under different conditions, varying the bias voltage applied

to the diamond detector and the beam parameters, such as bunch charge and spot size. The measured signal is characterised by a fast rise time, but even with increasing bias voltage, the collected charge is always significantly lower than 1%: this is clear evidence of strong recombination in the diamond bulk. We observe that the collected charge is a function of the carriers concentration in the bulk diamond: a lower concentration corresponds to a higher charge collection efficiency.

We quantitatively model the signal formation under these extreme conditions using a two-step numerical simulation approach, employing the Sentaurus TCAD and LTspice packages. The simulation results accurately replicate the rise time, peak amplitude, and signal reflections caused by impedance mismatches observed in the data collected with the initial setup at FERMI. The choice of recombination model significantly influences the simulation of the signal trailing edge: further study with alternative recombination models is an interesting theme for future developments. The limited time and computing resources available did not allow to extend the simulation to match the conditions of the optimised setup. The data acquired with the optimised setup will provide an interesting opportunity to further test this model.

In a broader context, this work not only ensures the reliability and accuracy of radiation monitoring at Belle II, but also contributes to our knowledge of the response of diamond detectors under extreme conditions, which is relevant to other high-energy physics experiments.

Acknowledgements

I would like to express my sincere gratitude to the members of the electronic division and the FERMI team at Elettra Sincrotrone Trieste for their invaluable contributions to the research presented in Chapters 5 and 6 of this thesis. Their expertise, support, and collaboration have been crucial for the successful completion of this project.

Bibliography

[1] M. Kobayashi and T. Maskawa, *$\mathcal{CP}$-violation in the renormalizable theory of weak interaction*, Prog. Theor. Phys. **49** (1973) 652–657.

[2] M. Gell-Mann, *A Schematic Model of Baryons and Mesons*, Phys. Lett. **8** (1964) 214–215.

[3] J. J. Aubert *et al.*, E598, *Experimental Observation of a Heavy Particle J*, Phys. Rev. Lett. **33** (1974) 1404–1406.

[4] J. E. Augustin *et al.*, SLAC-SP-017, *Discovery of a Narrow Resonance in e^+e^- Annihilation*, Phys. Rev. Lett. **33** (1974) 1406–1408.

[5] S. W. Herb *et al.*, E288, *Observation of a Dimuon Resonance at 9.5-GeV in 400-GeV Proton-Nucleus Collisions*, Phys. Rev. Lett. **39** (1977) 252–255.

[6] N. Cabibbo, *Unitary symmetry and leptonic decays*, Phys. Rev. Lett. **10** (1963) 531–533.

[7] A. J. Bevan *et al.*, Belle and BaBar Collaborations, *The physics of the B factories*, Eur. Phys. J. **C74** (2014) 3026.

[8] K. Akai, K. Furukawa, and H. Koiso, SuperKEKB, *SuperKEKB Collider*, Nucl. Instrum. Meth. A **907** (2018) 188.

[9] T. Nozaki, *The KEK B factory and the BELLE detector*, Nucl. Phys. B Proc. Suppl. **50** (1996) 288–295.

[10] Y. O. et al., *Accelerator design at SuperKEKB*, Prog. Theo. Exp. Phys. **2013** (2013) 03A011.

[11] Y. Ohnishi, SuperKEKB, Belle II, *SuperKEKB Luminosity Quest*, JACoW **eeFACT2022** (2023) 1–6.

[12] D. Zhou, K. O. Y. Funakoshi, and Y. Ohnishi, *Luminosity performance of SuperKEKB*, `arXiv:2306.02692 [physics.acc-ph]`.

[13] P. Raimondi, D. N. Shatilov, and M. Zobov, *Beam-Beam Issues for Colliding Schemes with Large Piwinski Angle and Crabbed Waist*, `arXiv:physics/0702033`.

[14] M. A. Furman, *Hourglass effects for asymmetric colliders*, Conf. Proc. C **910506** (1991) 422–424.

[15] N. Ohuchi *et al.*, *Design study of superconducting magnets for the SuperKEKB interaction region*, in *Proceedings PAC 2005*, p. 2470. 2005.

[16] T. Abe *et al.*, Belle II Collaboration, *Belle II Technical Design Report*, ArXiv e-prints (2010) , arXiv:1011.0352.

[17] N. Taniguchi, Belle II Collaboration, *Central Drift Chamber for Belle-II*, JINST **12** (2017) no. 06, C06014.

[18] K. Inami and I. Belle, *TOP counter for particle identification at the Belle II experiment*, Nuclear instruments and methods in physics research section A: accelerators, spectrometers, detectors and associated equipment **766** (2014) 5–8.

[19] S. Iwata *et al.*, *Particle identification performance of the prototype aerogel RICH counter for the Belle II experiment*, PTEP **2016** (2016) no. 3, 033H01, arXiv:1603.02503 [physics.ins-det].

[20] V. Aulchenko *et al.*, *Electromagnetic calorimeter for Belle II*, J. Phys. Conf. Ser. **587** (2015) no. 1, 012045.

[21] A. Abashian *et al.*, Belle Collaboration, *The K-L/mu detector subsystem for the BELLE experiment at the KEK B factory*, Nucl. Instrum. Meth. **A449** (2000) 112–124.

[22] Belle-II, F. Forti, *Snowmass Whitepaper: The Belle II Detector Upgrade Program*, in *Snowmass 2021*. 3, 2022. arXiv:2203.11349.

[23] P. Lewis *et al.*, *First Measurements of Beam Backgrounds at SuperKEKB*, Nucl. Instrum. Meth. A **914** (2019) 69–144, arXiv:1802.01366.

[24] Z. J. Liptak *et al.*, *Measurements of beam backgrounds in SuperKEKB Phase 2*, Nucl. Instrum. Meth. A **1040** (2022) 167168, arXiv:2112.14537.

[25] The momentum acceptance is defined as the maximum energy excursion that an accelerated particle can have before it is lost from the machine.

[26] The equation that describes the scattering probability is known as Bruck's formula and it is derived in H. Bruck, *Circular Particle Accelerators*. Los Alamos Scientific Laboratory, 1st ed., 1972.

[27] H. Wiedemann, *Particle Accelerator Physics*. Springer Cham, 01, 2015.

[28] L. Vitale, *The Belle II Silicon-strip Vertex Detector*, in *Vertex 2014*, p. 017. 2015.

[29] A. Natochii *et al.*, *Measured and projected beam backgrounds in the Belle II experiment at the SuperKEKB collider*, Nucl. Instrum. Meth. A **1055** (2023) 168550, arXiv:2302.01566 [hep-ex].

[30] *SuperKEKB Design Report, Chapter 5*, http://www-superkekb.kek.jp/documents.html.

[31] C. Marinas, DEPFET, *The Belle II pixel detector: high precision with low material*, Nucl. Instrum. Meth. **A731** (2013) 31–35.

[32] H. Schreeck, *Commissioning and first data taking experience with the Belle II pixel vertex detector*. PhD thesis, Gottingen U., II. Phys. Inst., 2020.

[33] P. Avella, *DEPFET sensors development for the Pixel Detector (PXD) of Belle II*, JINST **9** (2014) no. 01, C01057.

[34] K. Adamczyk *et al.*, Belle-II SVD, *The design, construction, operation and performance of the Belle II silicon vertex detector*, JINST **17** (2022) no. 11, P11042, arXiv:2201.09824.

[35] C. Irmler *et al.*, *Origami chip-on-sensor design: Progress and new developments*, JINST **8** (2013) C01014.

[36] L. L. Jones, M. J. French, Q. Morrissey, A. Neviani, M. Raymond, G. Hall, P. Moreira, and G. Cervelli, *The APV25 deep submicron readout chip for CMS detectors*, Conf. Proc. C **9909201** (1999) 162–166.

[37] R. Thalmeier *et al.*, Belle-II SVD, *Series production testing and commissioning of the Belle II SVD readout system*, Nucl. Instrum. Meth. A **958** (2020) 162942.

[38] B. Verlaat *et al.*, *The ATLAS IBL CO_2 cooling system*, JINST **12** (2017) no. 02, C02064.

[39] G. Lindström, *Radiation damage in silicon detectors*, Nucl. Instrum. Meth. A **512** (2003) 30–43.

[40] G. Lutz *et al.*, *Semiconductor radiation detectors*. Springer, 2nd ed., 1999.

[41] H. Schreeck *et al.*, *Effects of gamma irradiation on DEPFET pixel sensors for the Belle II experiment*, Nucl. Instrum. Meth. A **959** (2020) 163522, arXiv:2109.10879.

[42] B. A. *et al*, *The BaBar detector: Upgrades, operation and performance*, Nucl. Instrum. Meth. A **729** (2013) 615–701.

[43] L. Zani *et al.*, Belle-II SVD, *The Silicon Vertex Detector of the Belle II experiment*, Nucl. Instrum. Meth. A **1038** (2022) 166952, arXiv:2206.11648 [physics.ins-det].

[44] T. I. Meyer, *PIN photodiodes for radiation monitoring and protection in the BABAR Silicon Vertex Tracker*, Int. J. Mod. Phys. **A16S1C** (2001) 1084–1086.

[45] V. Re *et al.*, *Radiation damage studies for the BaBar Silicon Vertex Tracker*, Nucl. Instrum. Meth. A **549** (2005) 11 – 15.

[46] D. Zontar, *Radiation monitoring at Belle*, Nucl. Instrum. Meth. **A501** (2003) 164–166.

[47] S. F. Kozlov *et al.*, *Preparation and Characteristics of Natural Diamond Nuclear Radiation Detectors*, IEEE Transactions on Nuclear Science **22** (1975) no. 1, 160–170.

[48] C. Canali *et al.*, *Electrical properties and performances of natural diamond nuclear radiation detectors*, Nuclear Instruments and Methods **160** (1979) no. 1, 73 – 77.

[49] For a consistent derivation of a radiation hardness parameter that reflects the diamond radiation hardness capabilities see V. Grilj and others, *The evaluation of radiation damage parameter for CVD diamond*, Nucl. Instrum. Meth. B **372** (2016) 161–164.

[50] M. Guthoff, *Radiation Damage to the diamond-based Beam Condition Monitor of the CMS Detector at the LHC*. PhD thesis, KIT, Karlsruhe, 2014.

[51] P. Bergonzo *et al.*, *Particle and radiation detectors based on diamond*, Phys. Status. Solidi A **185** (2001) 167–181.

[52] S. Koizumi *et al.*, *Physics and applications of CVD diamond*. Wiley, 1st ed., 2008.

[53] J. C. Angus *et al.*, *Growth of diamond deed crystals by vapor deposition*, Journal of Applied Physics **39** (1968) no. 6, 2915–2922.

[54] R. Muller and T. I. Kamins, *Device electronics for integrated circuits*. Wiley, 3rd ed., 2002.

[55] *Cyclone V FPGA*, `https://www.intel.com/content/www/us/en/products/details/fpga/cyclone/v.html`.

[56] *HV module*, `https://www.xppower.com/portals/0/pdfs/SF_CA_Series.pdf`.

[57] *Analog Devices AD9653*, `https://www.analog.com/media/en/technical-documentation/data-sheets/AD9653.pdf`.

[58] *Analog Devices LTC6268*, `https://www.analog.com/media/en/technical-documentation/data-sheets/AD9653.pdf`.

[59] B. L. *et al.*, *Design of High Dynamic Range Preamplifiers for a Diamond-Based Radiation Monitor System*, JACoW **IBIC2022** (2022) 216–219.

[60] *Murata thermistor NCP15XV103E03RC*, `https://www.murata.com/en-sg/products/productdetail?partno=NCP15XV103E03RC`.

[61] B. Hallgren, H. Boterenbrood, H. J. Burckhart, and H. Kvedalen, *The embedded local monitor board (ELMB) in the LHC front-end I/O control system*, in *7th Workshop on Electronics for LHC Experiments*, pp. 325–330. 9, 2001.

[62] *Steinhart-Hart coefficients for NTC thermistor*, `https://www.ametherm.com/thermistor/ntc-thermistors-steinhart-and-hart-equation`.

[63] M. Esposito *et al.*, *Fiber Bragg Grating sensors to measure the coefficient of thermal expansion of polymers at cryogenic temperatures*, Sens. Actuators A **189** (2013) 195–203.

[64] *Micron Optics Optical Sensing Interrogator sm225*, `http://micronoptics.ru/uploads/library/documents/Datasheets/Micron%20Optics%20sm225.pdf`.

[65] *Micron Optics ENLIGHT Optical Sensing Analysis software*, `http://micronoptics.ru/sensing_software.html`.

[66] *Vaisala sensors*, `https://www.vaisala.com/`.

[67] *Nokeval sensors*, `https://nokeval.com/en/`.

[68] *Alpha Moisture humidity sensors*, `http://www.amsystems.co.uk/`.

[69] *Michell Instruments dew point sensors*, `http://www.michell.com/uk/category/dew-point-transmitters.php`.

[70] *Modicon M340 Schneider electric*, https://www.se.com/it/it/product-range/1468-modicon-m340/.

[71] L. Bosisio *et al.*, *In-depth characterisation of diamond sensors for dosimetry in beam-loss monitoring*, Nucl. Instrum. Meth. A **1045** (2023) 167587.

[72] G. Bassi *et al.*, *Calibration of diamond detectors for dosimetry in beam-loss monitoring*, Nucl. Instrum. Meth. A **1004** (2021) 165383.

[73] S. Bacher *et al.*, *Performance of the diamond-based beam-loss monitor system of Belle II*, Nucl. Instrum. Meth. A **997** (2021) 165157.

[74] *Element Six (UK) Ltd.*, http://www.e6.com/.

[75] *CIVIDEC Instrumentation GmbH*, https://cividec.at/.

[76] *Rogers Corporation*, http://www.rogerscorp.com/.

[77] A. Ferrari, P. R. Sala, A. Fasso, and J. Ranft, *FLUKA: A multi-particle transport code (Program version 2005)*. CERN Yellow Reports: Monographs. CERN, 2005.

[78] Amptek, Inc., *Mini-X2 User Manual*, https://www.amptek.com/products/x-ray-sources/mini-x2-ray-tube.

[79] H. Pernegger *et al.*, *Charge-carrier properties in synthetic single-crystal diamond measured with the transient-current technique*, Journal of Applied Physics **97** (2005) no. 7, 073704.

[80] Caen, *CAEN DT1471ET*, 7, 2015. https://www.caen.it/products/dt1471het/.

[81] Particulars, *Particulars Bias-T*, 8, 2015. http://www.particulars.si/downloads/ParticularsBias-T-Manuals.pdf.

[82] Particulars, *Particulars wide band current amplifiers*, 8, 2015. http://www.particulars.si/downloads/ParticularsAmps-Manuals.pdf.

[83] LeCroy, *LeCroy Wavepro 960*, 3, 2002. http://www.w2hx.com/x/LeCroy/WavePro960/LECROY-WAVEPRO$%$20960-Datasheet.pdf.

[84] *AGILENT N9320B spectrum analyser*, https://www.keysight.com/us/en/product/N9320B/rf-spectrum-analyzer-bsa-9-khz-3-ghz.html?&cc=IT&lc=ita.

[85] *AGILENT 81180A 4.2 GSa/s Arbitrary Waveform Generator,*, https://www.keysight.com/gb/en/support/81180A/42-gsas-arbitrary-waveform-generator.html.

[86] R. S. Sussmann, *CVD diamond for electronic devices and sensors*. Wiley, 1st ed., 2009.

[87] W. Shockley, *Currents to conductors induced by a moving point charge*, J. Appl. Phys. **9** (1938) 635–636.

[88] M. Rebai *et al.*, *Time-stability of a Single-crystal Diamond Detector for fast neutron beam diagnostic under alpha and neutron irradiation*, Diamond and related materials **61** (2016) 1 – 6.

[89] M. Guthoff *et al.*, *Radiation damage in the diamond based beam condition monitors of the CMS experiment at the Large Hadron Collider (LHC) at CERN*, Nucl. Instrum. Meth. A **730** (2013) 168–173.

[90] H. Ibach and H. Lüth, *"Free" Electrons in Solids*. Springer Berlin Heidelberg, Berlin, Heidelberg, 2009.

[91] E. Berdermann, *Diamond for particle and photon detection in extreme conditions*, Comprehensive Hard Materials **3** (03, 2014) 407–467.

[92] F. Scholze, H. Rabus, and G. Ulm, *Mean energy required to produce an electron-hole pair in silicon for photons of energies between 50 and 1500 eV*, Journal of Applied Physics **84** (1998) no. 5, 2926–2939.

[93] *CAEN DT5521HM high voltage supply*, `http://www.caen.it`.

[94] Elettra Sincrotrone Collaboration, *AH501B Picoammeter*, `http://ilo.elettra.trieste.it/index.php?page=_layout_prodotto&id=394&lang=en`.

[95] *Arduino:*, `https://www.arduino.cc`.

[96] P. Bergonzo *et al.*, *Improving diamond detectors: a device case*, Diamond and Related Materials **16** (2007) no. 4, 1038 – 1043.

[97] K. C. Kao, *Dielectric phenomena in solids*. Elsevier, 1st ed., 2004.

[98] G. Bassi, *Radiation monitor with diamond sensors for the Belle II experiment at SuperKEKB*, laurea thesis, Trieste U., 2018.

[99] S. Bassanese *et al.*, *Diamond detectors' response to intense high-energy electron pulses*, Nucl. Instrum. Meth. A **1047** (2023) 167801.

[100] *Characterisation of the transient response of diamond and SiC detectors with short intense electron pulses*, `https://indico.cern.ch/event/1264216/contributions/5548174/`.

[101] P. Tove and W. Seibt, *Plasma effects in semiconductor detectors*, Nucl. Instrum. Meth. **51** (1967) no. 2, 261–269.

[102] Elettra Sincrotrone Collaboration, *Elettra Sincrotrone webpage*, `https://www.elettra.trieste.it/`.

[103] E. Allaria *et al.*, *The FERMI free-electron lasers*, Journal of Synchrotron Radiation **22** (May, 2015) 485–491.

[104] E. I. Lipatov *et al.*, *Pulsed Cathodoluminescence of Natural and Synthetic Diamonds Excited by Nanosecond and Subnanosecond Electron Beams*, Cathodoluminescence. Rijeka, Croatia: InTech (2012) 51–70.

[105] E. I. Lipatov, D. E. Genin, and V. F. Tarasenko, *Recombination Radiation in Synthetic and Natural Diamonds Exposed to Pulsed UV Laser Radiation*, Russian Physics Journal **58** (2015) no. 7, 911–922.

[106] C. Bocchetta *et al.*, *FERMI@Elettra FEL Conceptual Design Report, Sincrotrone Trieste*, Trieste, Italy (2007) .

[107] L. Badano *et al.*, Sincrotrone Elettra Trieste, *The Beam Diagnostics System for the FERMI@ elettra Photoinjector*, .

[108] Sincrotrone Elettra Trieste, A. Abrami *et al.*, *Intra undulator screen diagnostic for the FERMI@Elettra FEL*, 2013.

[109] S. Bassanese *et al.*, *Characterisation of fast Faraday cups at the ELETTRA Linac*, in *DIPAC 2003*, pp. 113–115. 5, 2003.

[110] J. Power, *Slit scattering effects in a well aligned pepper pot*, in *Proceedings of the 2003 Particle Accelerator Conference*, vol. 4, pp. 2432–2434 vol.4. 2003.

[111] *Datasheet of HDO9000*, `https://cdn.teledynelecroy.com/files/pdf/hdo9000-oscilloscope-datasheet.pdf`.

[112] *In-flange integrating current transformer*, . model: ICT- CF6"60.4-40-UHV-05:1, CF100, 60.4 mm ID.

[113] M. Lonza *et al.*, *The control system of the FERMI@Elettra free electron laser*, Proceedings of ICALEPCS2009, Kobe, Japan (2009) .

[114] M. Lonza *et al.*, *Status report on the FERMI@Elettra control system*, Proceedings of ICALEPCS2011, Grenoble, France (2009) .

[115] E. Allaria, E. Ferrari, E. Roussel, and L. Vidotto, *REALTA and pyDART: A Set of Programs to Perform Real Time Acquisition and On-Line Analysis at the FERMI Free Electron Laser*, in *16th International Conference on Accelerator and Large Experimental Physics Control Systems*, p. THPHA044. 2018.

[116] R. Assmann, F. Decker, M. Seidel, R. Siemann, and D. Whittum, *Observation of dark-current signals from the S-band structures of the SLAC linac*, vol. 1, pp. 500 – 502 vol.1. 06, 1997.

[117] M. Berger *et al.*, *Stopping-Power & Range Tables for Electrons, Protons, and Helium Ions*, Tech. Rep. NISTIR 4999, National Institute of Standards and Technology, Gaithersburg, MD, July, 2017.

[118] Y. Jin, P. Cristaudo, and A. Gabrielli, *Simulation of the response of a diamond-based radiation detector to ultra-short and intense high-energy electron pulses*, Nucl. Instrum. Meth. A **1052** (2023) 168259, `arXiv:2210.14690`.

[119] *Synopsys TCAD*, `https://www.synopsys.com/silicon/tcad.html`.

[120] A. Morozzi *et al.*, *Polycrystalline CVD diamond device level modeling for particle detection applications*, J. Instrum. **11** (2016) no. 12, C12043.

[121] M. J. Kholili, *Study on Diamond Detector to Develop Its Numerical Model and Charge Amplification Structure*. PhD thesis, Graduate University for Advanced Studies (SOKENDAI), 2019.

[122] *LTspice, Analog Devices*, `https://www.analog.com/en/design-center/design-tools-and-calculators/ltspice-simulator.html`.

[123] *Diamond properties*, `http://www.ioffe.ru/SVA/NSM/Semicond/Diamond/index.html`.

[124] N. Aluru, K. Law, A. Raefsky, P. Pinsky, and R. Dutton, *Numerical solution of two-carrier hydrodynamic semiconductor device equations employing a stabilized finite element method*, Computer Methods in Applied Mechanics and Engineering **125** (1995) no. 1, 187–220.

[125] N. Aluru, A. Raefsky, P. Pinsky, K. Law, R. Goossens, and R. Dutton, *A finite element formulation for the hydrodynamic semiconductor device equations*, Computer Methods in Applied Mechanics and Engineering **107** (1993) no. 1, 269–298.

[126] Z. Zalevsky and I. Abdulhalim, *Chapter 1 - Physical Background*. Micro and Nano Technologies. William Andrew Publishing, Oxford, 2010.

[127] T. Tachibana, B. E. Williams, and J. T. Glass, *Correlation of the electrical properties of metal contacts on diamond films with the chemical nature of the metal-diamond interface. II. Titanium contacts: A carbide-forming metal*, Phys. Rev. B **45** (1992) 11975.

[128] Y. Wang *et al.*, *Ohmic contacts and interface properties of Au/Ti/p-diamond prepared by r.f. sputtering*, Surf. Interface Anal. **29** (2000) no. 7, 478–481.

[129] *CVD Diamond Handbook*, `https://e6cvd.com/media/wysiwyg/pdf/E6_CVD_Diamond_Handbook_A5_v10X.pdf`.

[130] M. Pomorski *et al.*, *Development of single-crystal CVD-diamond detectors for spectroscopy and timing*, Phys. Status Solidi (A) **203** (2006) no. 12, 3152–3160.

[131] K. Konishi, I. Akimoto, H. Matsuoka, *et al.*, *Low-temperature mobility-lifetime product in synthetic diamond*, Appl. Phys. Lett. **117** (2020) no. 21, 212102.

[132] J. Isberg *et al.*, *High Carrier Mobility in Single-Crystal Plasma-Deposited Diamond*, Science **297** (2002) no. 5587, 1670–1672.

[133] J. M. Fernández-Varea *et al.*, *Electronic stopping power of diamond for electrons and positrons*, Phys. Med. Biol. **66** (2021) 165003.

[134] M. G. Donato *et al.*, *Exciton condensation in homoepitaxial chemical vapor deposition diamond*, J. Appl. Phys. **106** (2009) no. 5, 053528.